

Orthopädische Klinik und Poliklinik, Universitätsmedizin Rostock
(Direktor: Prof. Dr. med. Wolfram Mittelmeier)

**Biomechanische Charakterisierung neuartiger
Hybridwerkstoffe für Knieendoprothesen basierend auf
Oxidkeramiken und Titan/Niob/Tantal-Legierungen**

Kumulative Dissertation

zur Erlangung des akademischen Grades
Doctor rerum humanarum (Dr. rer. hum.)

an der Medizinischen Fakultät der Universität Rostock

vorgelegt von

Jan-Oliver Saß, M.Sc.

geb. am 18.11.1994 in Rathenow
aus Rostock

Rostock, November 2024

Dekan: Prof. Dr. med. B. Krause

1. Gutachter: Prof. Dr. med. Dipl.-Ing. Rainer Bader
Forschungslabor für Biomechanik und Implantattechnologie, Orthopädische
Klinik und Poliklinik, Universitätsmedizin Rostock

2. Gutachter: Prof. Dr.-Ing. Hermann Seitz
Lehrstuhl für Mikrofluidik, Universität Rostock

3. Gutachter: Prof. Dr. Dipl. -Ing. (FH) Matthias Woiczinski
Experimentelle Orthopädie / Forschung, Waldkliniken Eisenberg GmbH

Datum der Einreichung: 15.11.2024

Datum der Verteidigung: 08.07.2025

Inhaltsverzeichnis

1	Einleitung	1
1.1	Grundlagen der Knieendoprothetik.....	1
1.2	Aseptische Implantatlockerung.....	1
1.3	Multifunktionale Hybridwerkstoffe.....	2
1.4	β -Titanlegierungen.....	2
1.5	Motivation und Zielstellung.....	3
2	Materialien und Methoden	4
2.1	Charakterisierung additiv gefertigter Ti/Nb/Ta Legierungen.....	4
2.1.1	Materialien und Probenfertigung.....	4
2.1.2	Mikrostrukturelle und mechanische Charakterisierung.....	4
2.1.3	Statistische Auswertung.....	4
2.2	Charakterisierung der Ti-Nb35-Ta6/ATZ Hybridwerkstoffe.....	5
2.2.1	Materialien und Probenfertigung.....	5
2.2.2	Strukturelle und mechanische Charakterisierung.....	6
2.2.3	Statistische Auswertung.....	6
2.3	Computergestützte Analyse einer Ti-Nb35-Ta6/ATZ Femurkomponente.....	6
2.3.1	Modellannahmen, Materialkennwerte und Diskretisierungsstrategie.....	6
2.3.2	Rand- und Kontaktbedingungen für die zementfreie Implantation.....	8
2.3.3	Rand- und Kontaktbedingungen für die zweibeinige Kniebeuge.....	8
2.3.4	Auswertung.....	9
3	Ergebnisse	10
3.1	Charakterisierung additiv gefertigter Ti/Nb/Ta Legierungen.....	10
3.2	Charakterisierung der Ti-Nb35-Ta6/ATZ Hybridwerkstoffe.....	12
3.3	Computergestützte Analyse einer Ti-Nb35-Ta6/ATZ Femurkomponente.....	14
3.3.1	Untersuchung der zementfreien Implantation.....	14
3.3.2	Untersuchung der zweibeinigen Kniebeuge.....	15
4	Diskussion	16
4.1	Charakterisierung additiv gefertigter Ti/Nb/Ta Legierungen.....	16
4.2	Charakterisierung von Ti-Nb35-Ta6/ATZ Hybridwerkstoffen.....	17
4.3	Computergestützte Analyse einer Ti-Nb35-Ta6/ATZ Femurkomponente.....	19
4.4	Limitationen und Ausblick.....	20
5	Zusammenfassung	21
	Literaturverzeichnis	22
	Verwendete Originalarbeiten zur kumulativen Dissertation	29
	Abbildungsverzeichnis	I
	Tabellenverzeichnis	II
	Abkürzungsverzeichnis	III
	Lebenslauf	IV
	Liste der Originalarbeiten und Konferenzbeiträge	VI
	Danksagung	IX
	Erklärung	X

1 Einleitung

1.1 Grundlagen der Knieendoprothetik

Die Gonarthrose ist mit Schmerzen, Funktionseinschränkungen und einer Reduzierung der Lebensqualität der betroffenen Patienten:innen verbunden [1]. Zu den Therapieansätzen zählt unter anderem eine Operation mit Implantation einer Knieendoprothese [1]. Die Fallzahl dieses Eingriffs betrug im Jahr 2023 229.551 und ist damit eine der am häufigsten durchgeführten Operationen in Deutschland [2]. In 87,1 % der Fälle wurde dabei eine bikondyläre Knieendoprothese implantiert [3]. Dieses Implantatsystem besteht aus einer tibialen Komponente (Tibiatray), einem Inlay und einer Femurkomponente [1]. Laut Deutschem Endoprothesenregister werden Femurkomponenten auf Basis einer Kobalt-Chrom-Molybdän (Co-Cr-Mo) Legierung bei 99,9 % (90,8 % unbeschichtet, 9,1 % beschichtet) der primären Eingriffe verwendet und die intraoperative Fixation erfolgt zumeist mit Knochenzement [3]. Trotz einer hohen Überlebensrate der Knieendoprothesen von bis zu 82 % nach 25 Jahren [4] nimmt die Zahl der Revisionsoperationen aufgrund steigender Implantationen zu [5]. Für den Zeitraum von 2020 bis 2050 wird in Deutschland eine weitere Zunahme der Primäreingriffe von 43 % prognostiziert [6]. Erforderliche Revisionsoperationen sind mit höherer Komplikationsrate, verminderter Überlebensrate der Implantate und mit höherer Unzufriedenheit der Patienten:innen verbunden [6,7]. Einer der Hauptgründe für eine Revision ist die aseptische Implantatlockerung [3].

1.2 Aseptische Implantatlockerung

Aseptische Implantatlockerungen werden zum Teil auf materialspezifische Faktoren zurückgeführt. Zu diesen zählen unerwünschte biologische Reaktionen auf freigesetzte Abrieb- und Korrosionsprodukte sowie die periimplantäre Knochenresorption in Folge einer Spannungsabschirmung (engl. *stress shielding*) [8–10].

Im Kniegelenk entstehende Abriebpartikel (Metall- oder Polyethylenpartikel) und Korrosionsprodukte, d. h. Metallionen wie Co^{2+} und Cr^{3+} führen an der Grenzfläche zwischen den Implantatkomponenten und dem Knochen zu einer Herauf- bzw. Herunterregulation proinflammatorischer Zytokine und Chemokine. Diese Mediatoren beeinflussen über Signalmechanismen die Funktionen der Zellen [9–16]. Dabei kann eine Osteolyse resultieren, die nachweislich einer aseptischen Implantatlockerung vorausgeht [10].

Oxidkeramiken, wie z. B. Aluminiumoxid-verstärkte Zirkonoxidkeramik (ATZ) oder Zirkonoxid-verstärkte Aluminiumoxidkeramik (ZTA) sind vielversprechende Verbundkeramiken, die Abrieb und Korrosion reduzieren [17,18]. In der Hüftendoprothetik werden in Deutschland bereits mehr als 90 % der Operationen mit einem keramischen Kopf durchgeführt [3]. Dabei wurde eine signifikante Reduktion ($p < 0,01$) der Abriebrate von $0,063 \text{ mm} \times \text{Jahr}^{-1}$ (Co-Cr-Mo Legierung) auf $0,047 \text{ mm} \times \text{Jahr}^{-1}$ (Oxidkeramik) beobachtet [19]. In der Knieendoprothetik werden derzeit weniger als 0,1 % der Femurkomponenten auf Basis einer Oxidkeramik eingesetzt [3]. Keramische Knieendoprothesen zeigen gute klinische Ergebnisse [18], jedoch auch ein sprödes Materialverhalten und eine damit verbundene Gefahr von intra- [20] und postoperativen [21] Implantatbrüchen.

Ein weiterer materialspezifischer Faktor für die aseptische Implantatlockerung ist die Spannungsabschirmung des periprothetischen Knochens [22]. Der durch mechanische Reize gesteuerte Knochenumbau [23,24] wird nach der Implantation einer Knieendoprothese in Richtung Knochenresorption verschoben [22,25]. Dies wird auf die reduzierte mechanische Beanspruchung des periprothetischen Knochens zurückgeführt [25–27], die durch die Diskrepanz der mechanischen Eigenschaften, insbesondere der Elastizität der Implantatmaterialien im Vergleich zum umliegenden Knochen begründet ist (Elastizitätsmodul Co-Cr-Mo: $\approx 241 \text{ GPa}$ [25], Oxidkeramik: $\approx 260 \text{ GPa}$ [28], Knochen: $\leq 20 \text{ GPa}$ [29–31]). Neben der oben aufgeführten partikel- und metallioneninduzierten Osteolyse kann auch die Abnahme der periprothetischen Knochendichte durch die Spannungsabschirmung zur aseptischen Implantatlockerung beitragen [10,22,27].

Materialspezifische Ansätze für die Reduktion der Spannungsabschirmung beschreiben Implantatwerkstoffe mit höherer Elastizität wie Polyetheretherketon (PEEK) [26], beschichtete Titanwerkstoffe [25,27] oder hybride Titan/Keramik Werkstoffe [32,33]. Diese Ansätze wurden in experimentellen bzw. computergestützten Untersuchungen [25,26,33] sowie zum Teil in klinischen Studien [27] verifiziert.

1.3 Multifunktionale Hybridwerkstoffe

Multifunktionale Hybridwerkstoffe kombinieren Oxidkeramiken mit Titanwerkstoffen [33]. Ziel dieses Ansatzes ist es, die jeweiligen vorteilhaften Eigenschaften, d. h. die hohe Abrieb- und Korrosionsbeständigkeit der Oxidkeramik und hohe Elastizität und Osteokonduktivität von Titanwerkstoffen zu kombinieren. Dabei werden gleichzeitig spezifische Limitationen wie die Sprödigkeit der Oxidkeramik und die geringe Abriebbeständigkeit der Titanwerkstoffe reduziert [33,34]. Fertigungsoptionen sind beispielsweise das Spark Plasma Sintern von funktional gradierten Titan/Keramik Werkstoffen [35–39] oder das Fügen von Titan- und Keramikkomponenten mittels der Glaslottechnologie [34,40].

Die Glaslottechnologie wurde für die Herstellung eines Dentalimplantates auf Ti/ZrO₂ Basis [41] und darauf aufbauend für eine bikondyläre Knieendoprothese [40] beschrieben. Die Verbindung der Werkstoffe erfolgt durch das Auftragen eines silikatischen Glaslotes und einem anschließenden Brennvorgang, der zu einer stoff- und formschlüssigen Verbindung führt [34,42]. Die experimentelle Studie von Mick et al. [34] untersuchte den Ti-Al6-V4/ATZ Hybridwerkstoff für endoprothetische Implantate und beschrieb eine Biegefestigkeit von 118 MPa, woraus eine potenzielle Anwendbarkeit der Werkstoffverbindung mittels Glaslottechnologie abgeleitet wurde. Die in dieser Studie verwendete Ti-Al6-V4 Legierung ist derzeit der Standard für endoprothetische Implantatkomponenten auf Basis von Titan [3], weist jedoch Limitationen hinsichtlich der mechanischen Kompatibilität zum Knochen auf, da Ti-Al6-V4 einen Elastizitätsmodul von ca. 110 GPa [43] besitzt. Alternativen stellen β -phasige Titanlegierungen dar, da diese einen deutlich niedrigeren Elastizitätsmodul bzw. höhere Elastizität aufweisen können [44–46].

1.4 β -Titanlegierungen

β -Titanlegierungen zeigen aufgrund ihrer kubisch raumzentrierten Kristallstruktur eine höhere Elastizität [46]. Es wurden biokompatible und β -stabilisierende Legierungselemente zur Herstellung und Charakterisierung binärer (Ti/Nb [44,47]), ternärer (Ti/Nb/Ta [48–51], Ti/Nb/Zr [45,52]) und quartärer (Ti/Nb/Ta/Zr [53–55]) Titanlegierungen verwendet. Ternäre Ti/Nb/Ta Legierungen zeigten vielversprechende Eigenschaften für biomedizinische Anwendungen, wie z. B. Biokompatibilität [49] und Korrosionsbeständigkeit [50].

Neben den mechanischen Eigenschaften sind die Herstellungsverfahren für Implantatwerkstoffe hochrelevant. In diesem Zusammenhang ermöglicht die additive Fertigung eine größere Designfreiheit des Implantates, die Herstellung funktionalisierter Oberflächen sowie die Herstellung patientenspezifischer Implantate [56–58]. In diesem Kontext wurde gezeigt, dass Ti-Nbx-Ta6 ($x = 20, 27, 35$ Gew.-%) Legierungen durch Laserstrahlschmelzen aus legierten Metallpulvern hergestellt werden können und Zugfestigkeiten von bis zu $802,0 \pm 3,0$ MPa (Ti-Nb20-Ta6) aufweisen. Darüber hinaus zeigten die additiv gefertigten Proben ohne weitere thermische Nachbehandlung ein duktileres Verformungsverhalten mit einer Bruchdehnung von bis zu $26,0 \pm 1,3$ % (Ti-Nb27-Ta6) [48].

Durch die additive Fertigung von β -Titanlegierungen können die mechanischen Eigenschaften durch die resultierende anisotrope Mikrostruktur in gewissen Grenzen eingestellt werden [47,51,59,60]. Diesbezüglich zeigte Pilz et al. [47] die Abhängigkeit der Elastizität von der Fertigungsrichtung am Beispiel von Ti-Nb42 und Lauhoff et al. [51] die Abhängigkeit der Festigkeit und Duktilität von Ti-Nb27-6Ta von Prozessparametern bzw. dem Energieeintrag während der Fertigung. Dementsprechend sind bei der Untersuchung additiv gefertigter β -Titanlegierungen neben der chemischen Zusammensetzung ebenfalls die Prozessparameter und die Fertigungsorientierung zu berücksichtigen.

1.5 Motivation und Zielstellung

Die aseptische Implantatlockerung der Femurkomponente einer bikondylären Knieendoprothese wird zum Teil auf materialspezifische Faktoren der verwendeten Co-Cr-Mo Legierungen zurückgeführt [8–10]. Freigesetzte Metallpartikel und -ionen stimulieren die Knochenresorption [9–16]. Darüber hinaus führt die Diskrepanz zwischen der Elastizität des Werkstoffes und des humanen Knochens zu einer periprothetischen Spannungsabschirmung [22]. Diese Faktoren reduzieren die periprothetische Knochendichte und tragen somit zur Implantatlockerung bei. Oxidkeramiken und β -Titanlegierungen sind in diesem Kontext relevante Werkstoffe, um die aseptische Implantatlockerung reduzieren zu können, da diese eine hohe Abrieb- und Korrosionsbeständigkeit bzw. eine hohe Elastizität und Osteokonduktivität aufweisen. Die Verwendung dieser Werkstoffe als Monolith ist jedoch durch individuelle Eigenschaften, wie Sprödigkeit und hohe Steifigkeit (Oxidkeramik) bzw. geringe Abriebbeständigkeit (β -Titanlegierungen) limitiert.

Die Glaslottechnologie stellt einen Ansatz dar, um einen multifunktionalen Hybridwerkstoff aus einer Oxidkeramik und einer β -Titanlegierungen (z. B. Ti/Nb/Ta Legierungen) zu fertigen [40]. Dieser Ansatz kombiniert die sehr gute Abrieb- und Korrosionsbeständigkeit der Oxidkeramik mit der hohen Elastizität und den osteokonduktiven Eigenschaften der Ti/Nb/Ta Legierungen. In einschlägigen Vorarbeiten wurden Ti-Al6-V4/ATZ Hybridwerkstoffe [34] sowie additiv gefertigte Ti-Nbx-Ta6 ($x = 20, 27, 35$ Gew.-%) Legierungen [48] untersucht. Die Untersuchung der mechanischen Eigenschaften der Ti/Nb/Ta Legierungen in Abhängigkeit von der Fertigungsrichtung und dem Niob-Gehalt sowie die Integration dieser Legierungen in einen Hybridwerkstoff am Beispiel endoprothetischer Implantate wurden bislang noch nicht durchgeführt. Weiterhin wurde das Konzept der hybridwerkstoffbasierten Knieendoprothese bisher nur als Idee beschrieben [40], jedoch erfolgte keine experimentelle oder computergestützte Untersuchung des Implantats unter relevanten Lastfällen.

Ziel der vorliegenden Arbeit war es daher, multifunktionale Hybridwerkstoffe aus einer ATZ Keramik und einer Ti/Nb/Ta Legierung für die Verwendung in der Femurkomponente einer bikondylären Knieendoprothese biomechanisch zu charakterisieren. Aus sich daraus ergebenden Forschungsarbeiten resultierten die Publikationen [I], [II] und [III].

Hierbei wurden zuerst additiv gefertigte Ti-Nbx-Ta6 ($x = 20, 27, 35$ Gew.-%) Legierungen mikrostrukturell und mechanisch charakterisiert. Dabei wurde in [I] neben der chemischen Zusammensetzung der Legierungen auch die Fertigungsrichtung ($0^\circ, 45^\circ, 90^\circ$) während des Laserstrahlschmelzens betrachtet. Neben dichten Proben wurden für eine mögliche physikalische Funktionalisierung der Implantatoberfläche offen-poröse Strukturen aus Ti-Nb20-Ta6 hergestellt und mechanisch charakterisiert.

Aufbauend auf den Ergebnissen aus [I] wurde die Ti-Nb35-Ta6 Legierung durch ein silikatisches Glaslot mit einer ATZ Keramik zu einem multifunktionalen Hybridwerkstoff verbunden [II]. Zylindrische Hybridwerkstoffproben wurden hinsichtlich ihrer mechanischen Eigenschaften durch statische und dynamische Schertestungen analysiert. Anschließend wurde die Verbindungstechnologie auf einen simplifizierten Funktionsdemonstrator der Femurkomponente einer Knieendoprothese übertragen, der im Rahmen biomechanischer Untersuchungen (dynamische Gangzyklen gefolgt von Belastung bis zum Bruch durch ein Flexions-Extensionsmoment) charakterisiert wurde.

Abschließend wurde eine computergestützte Analyse durchgeführt, um eine Femurkomponente aus dem Hybridwerkstoff Ti-Nb35-Ta6/ATZ in den relevanten Lastfällen der zementfreien Implantation und der zweibeinigen Kniebeuge untersuchen zu können [III]. Innerhalb dieser Simulationen sollte das Bruchrisiko während der Implantation sowie die Knochen-Implantat-Interaktion während der Kniebeuge betrachtet werden. Die Materialparameter von Ti-Nb35-Ta6 wurden aus [I] übernommen. Zusätzlich wurden analog zur Methodik in [I] offen-poröse Ti-Nb35-Ta6 Proben charakterisiert und diese als Oberflächenstrukturierung des Implantates in die Analyse integriert.

2 Materialien und Methoden

2.1 Charakterisierung additiv gefertigter Ti/Nb/Ta Legierungen

2.1.1 Materialien und Probenfertigung

In [1] wurden Ti-Nbx-Ta6 ($x = 20, 27, 35$ Gew.-%) Legierungen nach der Methodik von Johannsen et al. [48] additiv mittels Laserstrahlschmelzen gefertigt. Dazu wurden legierte, sphärische Metallpulver (TANIOBIS GmbH, Goslar, Deutschland) verwendet. Die in Johannsen et al. [48] beschriebenen Prozessparameter führten zu Proben mit einer Dichte $> 99,9\%$ und einer homogenen Elementverteilung.

Für die mechanische Charakterisierung wurden zylindrische Proben in Anlehnung an Schulze et al. [44] gefertigt. Dabei wurde die Fertigungsausrichtung ($0^\circ, 45^\circ, 90^\circ$; siehe Abb. 1A) variiert. Weiterhin wurden offen-poröse Ti-Nb20-Ta6 und Ti-Al6-V4 (Referenz) quaderförmige Proben mit einer kubisch flächenzentrierten Gitterstruktur gefertigt. Die gefertigten Proben sind in Abb. 1B und C dargestellt und weiterführende Details wurden in [1] beschrieben.

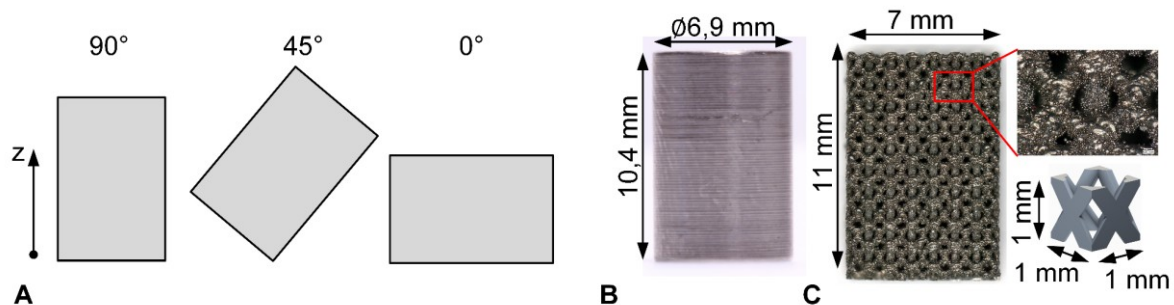


Abbildung 1. Übersicht der additiv mittels Laserstrahlschmelzen gefertigten Proben: A) Darstellung der Fertigungsrichtungen $0^\circ, 45^\circ, 90^\circ$ (z: Aufbauachse), B) zylindrische Proben für die Kompressionsversuche der Ti-Nbx-Ta6 ($x = 20, 27, 35$ Gew.-%) Legierungen und C) offen-poröse Proben aus Ti-Nb20-Ta6 oder Ti-Al6-V4 sowie die kubisch flächenzentrierte Einheitszelle.

2.1.2 Mikrostrukturelle und mechanische Charakterisierung

Die Mikrostruktur der Ti/Nb/Ta Legierungen in Abhängigkeit vom Niob-Gehalt und der Fertigungsrichtung wurde mittels Elektronenrückstrahlmikroskopie (SEM JSM6490, Jeol, Tokio, Japan) untersucht. Die zylindrischen und offen-porösen Proben wurden im Kompressionsversuch (zylindrische Proben: 100 kN Landmark®, MTS Systems Corporation, Eden Prairie, MN, USA; offen-poröse Proben: Z050-50kN, Zwick Roell, Ulm, Deutschland) mit einer Geschwindigkeit von $0,005 \text{ mm} \cdot \text{s}^{-1}$ bis zum Bruch oder 1.900 MPa belastet. Der Kompressionsmodul (C in GPa), die Dehngrenze ($\sigma_{C,0,2}$ in MPa), die Kompressionsfestigkeit (UCS in MPa) und die Bruchdehnung (ε_B in %) wurde bestimmt. Als Querschnitt der offen-porösen Proben wurde für die Berechnung der Gesamtquerschnitt der Probe herangezogen (49 mm^2) und die daraus resultierende Steifigkeit der Gesamtprobe im weiteren als Kompressionsmodul bezeichnet. Darüber hinaus wurde die zulässige elastische Dehnung (engl. *elastic admissible strain*, EAS) ermittelt, die als Indikator für die mechanische Funktionalität eines Implantatwerkstoffs definiert wurde und als Verhältnis zwischen der Dehngrenze zu dem Elastizitätsmodul berechnet wurde [45]. In [1] wurde für diese Berechnung der Kompressionsmodul herangezogen. Die Bruchflächen der Proben nach dem Kompressionsversuch wurden mittels Rasterelektronenmikroskopie (SEM, MERLIN® VP Compact, Carl Zeiss Microscopy Deutschland GmbH, Oberkochen, Deutschland) untersucht.

2.1.3 Statistische Auswertung

Die statistische Auswertung erfolgte mit IBM SPSS Statistics v29 (IBM Corporation, Armonk, NY, USA). Die Ergebnisse der Kompressionsuntersuchungen von $n = 5$ Proben für jede Gruppe wurden mit dem Mann-Whitney-U-Test auf Signifikanz (Signifikanzniveau $p < 0,05$) geprüft. Paarweise Vergleiche wurden für jede Legierung in Abhängigkeit der Druckrichtung und für jede Druckrichtung entsprechend dem Niob-Gehalt durchgeführt.

2.2 Charakterisierung der Ti-Nb35-Ta6/ATZ Hybridwerkstoffe

2.2.1 Materialien und Probenfertigung

Die Fertigung des Ti-Nb35-Ta6/ATZ Hybridwerkstoffes erfolgte in [II] mit einem silikatischen Glaslot (DCMhotbond fusio-12, DCM Dental Creative Management GmbH, Rostock, Deutschland) mit den Hauptbestandteilen: SiO_2 (63 - 67 Gew.%), Al_2O_3 (6 - 9 Gew.%), K_2O (6 - 9 Gew.%) und Na_2O (6 - 9 Gew.%). Der Wärmeausdehnungskoeffizient und die Schmelztemperatur des Glaslots betragen $10 \times 10^{-6} \times \text{K}^{-1}$ und $450 \text{ }^\circ\text{C}$ (Angaben von DCM Dental Creative Management GmbH). Der Hybridwerkstoff wurde aus additiv gefertigtem Ti-Nb35-Ta6 (Prozessparameter nach [I] bzw. Johannsen et al. [48]) und mittels Schlickerguss hergestellter ATZ Keramik (Fa. Koebel Engineering, Dachsen, Schweiz) gefertigt. Die verwendeten Ti-Nb35-Ta6 Probekörper wurden für 4 h bei $1.200 \text{ }^\circ\text{C}$ im Vakuum ausgelagert und wiesen danach im relevanten Temperaturbereich einen Wärmeausdehnungskoeffizienten von $8,2 - 9,3 \times 10^{-6} \times \text{K}^{-1}$ (Angabe von TANIOWIS GmbH) auf. Im Rahmen eigener Voruntersuchungen wurde festgestellt, dass diese Temperung der Ti-Nb35-Ta6 Legierung notwendig ist, um thermische Eigenspannungen nach der Glaslötung zu reduzieren. Die ATZ Keramik war durch einen Wärmeausdehnungskoeffizienten von $7,8 - 8,1 \times 10^{-6} \times \text{K}^{-1}$ (Angabe von Fa. Koebel Engineering) charakterisiert.

Die Fertigung der Ti-Nb35-Ta6/ATZ Hybridprobekörper wurde in [II] detailliert beschrieben und basierte teilweise auf eigenen Vorarbeiten [61,62] sowie den Herstellerangaben des Glaslotes. Es wurde ein standardisiertes Protokoll angewendet, das die Probenvorbereitung (Reinigung mit Ethanol im UV-Bad und Sandstrahlen der Oberflächen mit Al_2O_3 Partikeln) und das Brennen des Hybridwerkstoffes bei $820 \text{ }^\circ\text{C}$ (Aufheiz- und Abkühlrate: $20 \text{ K} \times \text{min}^{-1}$, Haltezeit 300 s) definiert. Innerhalb der Untersuchungen wurde der äquivalent hergestellte Hybridwerkstoff Ti/ATZ aus kommerziellem Reintitan und der gleichen ATZ Keramik als Referenzwerkstoff verwendet, da die Glaslottechnologie initial für ein Dentalimplantat entwickelt wurde [41] und Reintitan dort als Standardwerkstoff etabliert ist.

Die mechanischen Untersuchungen erfolgten mit zylindrischen Scherzugproben ($\varnothing 19,05 \text{ mm}$, Abb. 2A) und Funktionsdemonstratoren der Femurkomponente einer Knieendoprothese (Abb. 2B). Das Design der Funktionsdemonstratoren wurde auf den Flexionsbereich des Tibiofemoralgelenkes beschränkt und entsprach dem 120° Segment eines Zylinders mit einem Außendurchmesser von 60 mm. Weiterhin wurde die Titankomponente mit 0,1 mm dicken Abstandshaltern versehen, um einen homogenen Lötspalt zu gewährleisten. Details der Konstruktion sind in [II] dargestellt.

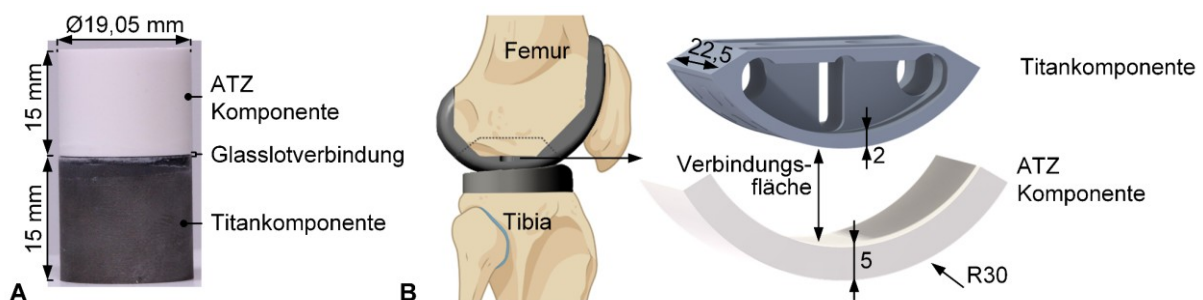


Abbildung 2. Übersichtsdarstellung der A) Hybridproben für die Schertestung und B) des Funktionsdemonstrators der Gleitflächen des Tibiofemoralgelenkes der Femurkomponente einer bikondylären Knieendoprothese (Angaben in mm).

Im Gegensatz zu den Scherzugproben erfolgte die Glaslotverbindung der Funktionsdemonstratoren in einem sequenziellen Prozess aus der Sprühbeschichtung der Komponenten mit dem Glaslot, Brennen der einzelnen Komponenten und Polieren der Verbindungsflächen. Dieser Vorgang wurde wiederholt, bis der Raum zwischen den Abstandshaltern auf der Titankomponente vollständig mit Glaslot gefüllt war und diente der Reduzierung eingeschlossener Fehlstellen im Glaslot. Eine umfassende Beschreibung des Prozesses erfolgte in [II].

2.2.2 Strukturelle und mechanische Charakterisierung

Die Glaslotverbindung des Ti-Nb35-Ta6/ATZ Hybridwerkstoffes wurde innerhalb der Scherzugsproben und der Funktionsdemonstratoren durch Rasterelektronenmikroskopie (SEM JSM6490, Jeol, Tokio, Japan) und Rückstreuelektronenmikroskopie (X-Flash SEM 4010, Bruker Nano GmbH, Berlin, Deutschland) strukturell und chemisch analysiert.

Die mechanische Charakterisierung der Hybridwerkstoffe erfolgte in statischen Scherzugsversuchen (Zwick 50kN RetroLine, Zwick Roell, Ulm, Deutschland) mit einer Belastungsgeschwindigkeit von $2,5 \text{ mm} \times \text{min}^{-1}$ bis zum Bruch [63] sowie in dynamischen Scherzugsversuchen (ElectroForce 3510, TA Instruments – Waters LLC, Eden Prairie, MN, USA) zwischen 1 und 10 MPa bei 10 Hz für 10^7 Zyklen [64]. Zusätzlich zu den unbehandelten Proben der Hybridwerkstoffe wurden statische Scherzugsversuche mit beschleunigt gealterten Proben (0,5 MPa, 70 °C, 14 Tage; durchgeführt von Endolab Mechanical Engineering GmbH, Riedering, Deutschland) vorgenommen. Daraus ergaben sich Gruppe 1: Ti-Nb35-Ta6/ATZ (statisch), Gruppe 2: Ti/ATZ (statisch), Gruppe 3: Ti-Nb35-Ta6/ATZ gealtert (statisch), Gruppe 4: Ti/ATZ gealtert (statisch), Gruppe 5: Ti-Nb35-Ta6/ATZ (dynamisch) und Gruppe 6: Ti/ATZ (dynamisch), wobei in Klammern der mechanische Test definiert ist.

Analog zu [II] umfasste die biomechanische Charakterisierung der Funktionsdemonstratoren zwei aufeinander folgende Untersuchungen. Die Proben wurden initial in einem 6-Freiheitsgrade-Gelenksimulator (VIVO™, Advanced Mechanical Technology, Watertown, MA, USA) mit 10.000 Gangzyklen gemäß der ISO-Norm 14243-3:2014 [65] belastet. Anschließend wurde das maximal ertragbare Flexions-Extensionsmoment dieser Proben in einer biaxialen Prüfmaschine (Instron® 8874, Instron GmbH, Darmstadt, Deutschland) bei einer Belastungsgeschwindigkeit von $0,1 \text{ }^\circ \times \text{s}^{-1}$ bestimmt. Im Anschluss an die mechanischen Testungen wurde eine Bruchflächenanalyse durch ein Laser-Scanning- (VK-X250) und Digitalmikroskop (VHX-6000, beide Mikroskope: Keyence Corporation, Osaka, Japan) durchgeführt.

2.2.3 Statistische Auswertung

Die statistische Analyse wurde mit IBM SPSS Statistics v29 (IBM Corporation, Armonk, NY, USA) durchgeführt, wobei $p < 0,05$ als Signifikanzniveau verwendet wurde. Die Ergebnisse der Scherzugsversuchen von jeweils $n = 5$ Proben pro Gruppe wurden mit dem Mann-Whitney-U-Test auf signifikante Unterschiede geprüft. Für die Ergebnisse der Funktionsdemonstratoren wurde keine statistische Analyse durchgeführt, da nur $n = 3$ Proben pro Gruppe zur Verfügung standen.

2.3 Computergestützte Analyse einer Ti-Nb35-Ta6/ATZ Femurkomponente

2.3.1 Modellannahmen, Materialkennwerte und Diskretisierungsstrategie

Die computergestützte Untersuchung einer hybridwerkstoffbasierten Femurkomponente einer Knieendoprothese umfasste die Lastfälle der zementfreien Implantation und der zweibeinigen Kniebeuge [III]. Die Modellierung der quasi-statischen Finite-Elemente (FE) Modelle erfolgte in Abaqus v2022 (Dassault Systèmes, Providence, RI, USA). Basierend auf den Arbeiten [I] und [II] wurde Ti-Nb35-Ta6/ATZ als Hybridwerkstoff untersucht und mit Ti-Al6-V4/ATZ sowie monolithischer ATZ Keramik und Co-Cr28-Mo6 verglichen. Für die Modelle wurde der CT-Scan eines humanen Femurs (männlich, 83 Jahre alt, Körpergewicht 61 kg) mit Mimics 25.0 (Materialise NV, Leuven, Belgien) segmentiert und in Geomagic Studio 2013 (Geomagic Inc., Morrisville, NC, USA) entsprechend einer geometrieorientierten Flächenrückführung zu 3D-Volumenmodellen rekonstruiert [66]. Die Verwendung der radiologischen Daten wurde durch die Ethikkommission der Universitätsmedizin Rostock bewilligt (A 2019-0164). Die virtuelle Implantation einer kreuzbänderhaltenden Knieendoprothese (Columbus®, Aesculap AG, Tuttlingen, Deutschland) erfolgte gemäß den chirurgischen Leitlinien.

Das etablierte Implantatdesign der Femurkomponente wurde in Creo Parametrics 6.0.3.0 (PTC Inc., Boston, MA, USA) zu einem biphasischen Design (Titan- und Keramikkomponente) modifiziert. Die Glaslotverbindung der Hybridwerkstoffe wurde durch eine vollständig eingeschränkte Kontaktbedingung der Verbindungsflächen modelliert. Die Titankomponente wies eine konstante Dicke von 3 mm auf. Weiterhin wurde die Titankomponente so konstruiert, dass die Simulation einer 1 mm dicken, offen-porösen Oberfläche ermöglicht wurde. Die offen-poröse Oberfläche wurde im FE Modell durch die Modifikation der Elastizität nachgebildet, die in experimentellen Kompressionsuntersuchungen ermittelt wurde. Die Gitterstruktur wurde analog zu der Methodik in [I] aus Ti-Nb35-Ta6 gefertigt und gleichermaßen wie in [I] mechanisch charakterisiert.

Die modellierten linear-elastischen Materialeigenschaften sind in Tab. 1 zusammengefasst. Während der Kniebeuge artikulierte die Femurkomponente mit dem passenden Tibia-Inlay aus ultrahochmolekularem Polyethylen (UHMW-PE), für das ein linear-elastisches, plastisches Materialverhalten (Dehngrenze: 25 MPa [67]) angenommen wurde. Der Knochen wurde als heterogenes Material modelliert [26,29,30,66]. Die Hounsfield Units (HU) aus dem CT-Scan wurden knotenpunkt-basiert als virtuelle Temperaturwerte im FE Modell unter Verwendung eines Python-basierten Abaqus Plug-ins zugewiesen [66]. Die HU wurden über eine phantombasierte Kalibrierfunktion (QRM, Moehrendorf, Deutschland) mit der Knochendichte korreliert, entsprechend der Methodik von Schileo et al. [68]. Weiterhin wurde der dichteabhängige Elastizitätsmodul nach Rho et al. [29] berechnet, wobei die spezifischen Funktionen für die Kortikalis und Spongiosa des distalen Femurs verwendet wurden.

Tabelle 1. Übersicht der linear-elastischen Materialeigenschaften des Knochens, der Femurkomponenten und des Tibia-Inlays [III].

Material	Elastizitätsmodul [GPa]	Querkontraktionszahl []	Quelle
Knochen			
Kortikalis	$-6,142 \times 0,014 \times \rho$	0,4	Rho et al. [29]
Spongiosa	$0,82 \times \rho^{1,27}$		
Femurkomponente			
Co-Cr28-Mo6	241	0,3	Galas et al. [25]
ATZ	261	0,27	Vogel et al. [28]
Ti-Al6-V4	110	0,3	Niinomi et al. [43]
Ti-Al6-V4 offen-porös	8,8	0,3	Publikation [III]
Ti-Nb35-Ta6*	63,8	0,3	Publikation [I]
Ti-Nb35-Ta6 offen-porös	5,2	0,3	Publikation [III]
Tibia-Inlay			
UHMW-PE	0,239	0,35	Sauer et al. [67]

ρ : ash density (Knochendichte), *gemittelter Kompressionsmodul von den Fertigungsrichtungen 0° , 45° , 90° aus [I]

Die Diskretisierung der Modelle erfolgte mit quadratischen Tetraederelementen (C3D10). Die Elementgrößen wurden durch Konvergenzanalysen bestimmt. Betrachtet wurde die Änderung der maximalen Spannung in der Femurkomponente während der zementfreien Implantation und die Dehnungsenergie im distalen Femur während der zweibeinigen Kniebeuge. Als Konvergenzkriterium wurde eine Änderung der Ergebnisgrößen von weniger als 5 % [69] im Vergleich zum nächst feineren Netz mit etwa doppelter Elementanzahl festgelegt. Details der Konvergenzanalyse sowie die Parameter der definierten Vernetzung sind in [III] ausführlich dargestellt.

2.3.2 Rand- und Kontaktbedingungen für die zementfreie Implantation

Der Aufbau und die Randbedingungen der zementfreien Implantation sind in Abb. 3A sowie detailliert in [III] dargestellt. In Anlehnung an die einschlägige Literatur [45,46] wurde ein Übermaß von 1 mm in anterior-posteriorer Richtung zwischen Knochen und Implantat angenommen. Die Simulation erfolgte basierend auf der Methode von Behramani et al. [70], bei der Oberflächenknotenpunkte des Knochens (Sekundäroberfläche) inkrementell in Richtung der Implantatoberfläche (Hauptoberfläche) verschoben werden. Zusätzlich wurde das Implantat um 0,5 mm nach distal verschoben, um das superior-inferiore Übermaß aufzulösen. Diese Translation wurde auf einen gekoppelten Referenzpunkt (F_{RP}) angewendet. Der proximale Knochenabschnitt wurde während der gesamten Simulation über einen gekoppelten Referenzpunkt (K_{RP}) fest eingespannt. Der Kontakt zwischen Implantat und Knochen wurde reibungsfrei simuliert.

2.3.3 Rand- und Kontaktbedingungen für die zweibeinige Kniebeuge

Der Modellaufbau und die Randbedingungen für die zweibeinige Kniebeuge sind in Abb. 3B dargestellt und im Detail in [III] beschrieben. In einer eigenen Vorarbeit wurde eine Methode zur kombinierten muskuloskelettalen Mehrkörpersimulation (MMKS) und FE Simulation erarbeitet [71] und in der Publikation [III] angewandt. Die Dynamik und Kinematik des Tibiofemoral- und Patellofemoralgelenkes während einer aktiven Kniebeuge wurde mit einer MMKS unter Berücksichtigung wirkender Muskel- und Bandkräfte basierend auf Keibach et al. [72] berechnet. Anschließend wurden die Kinematik sowie die axialen Gelenkkräfte des Tibiofemoral- und Patellofemoralgelenkes durch eine Koordinatentransformation auf Knochenreferenzpunkte (K_{RP} und K_{PF}) in das FE Modell übertragen und als translatorische und rotatorische Freiheitsgrade oder Kräfte implementiert. Für die Auswertung der volumetrischen Spannungsabschirmung im periprothetischen Knochen wurden fünf Bereiche (engl. *regions of interest*, ROI) im distalen Femur definiert [54,55].

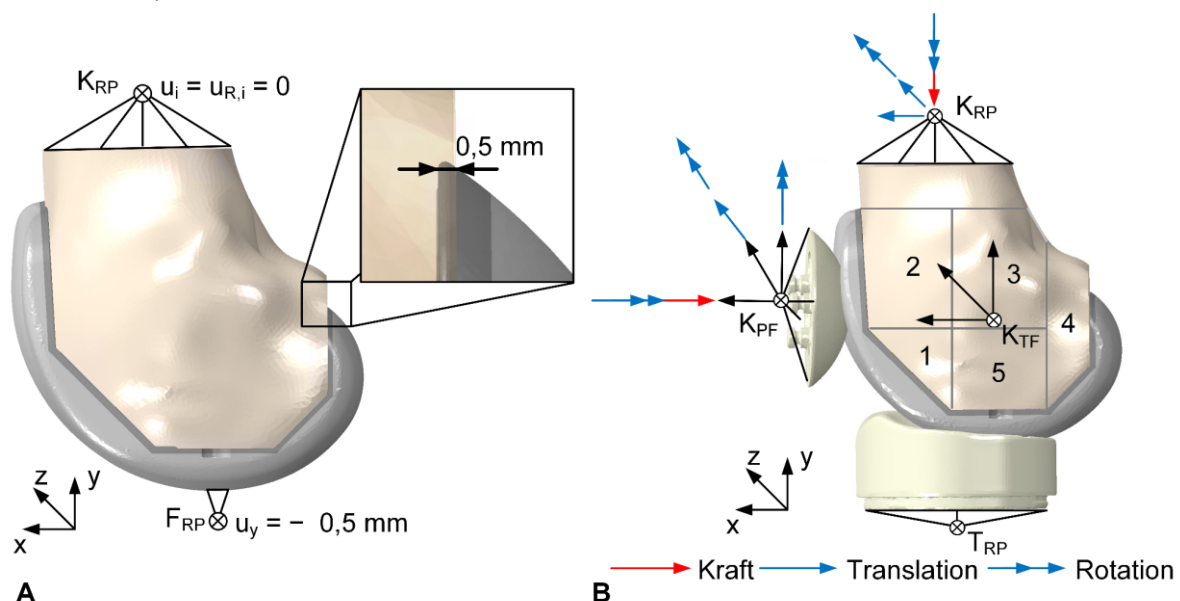


Abbildung 3. Darstellung der Randbedingungen der Finite-Elemente Modelle: A) zementfreie Implantation (K_{RP} : Knochenreferenzpunkt (fest eingespannt), F_{RP} : Referenzpunkt der Femurkomponente (Translation von 0,5 mm in y Richtung; restliche Freiheitsgrade nicht eingeschränkt), Anwendung der Reduktion einer initialen Oberflächendurchdringung von 0,5 mm, B) zweibeinige Kniebeuge (K_{RP} : Knochenreferenzpunkt (Freiheitsgrade aus der muskuloskelettalen Mehrkörpersimulation), T_{RP} : Referenzpunkt des Tibia-Inlays (fest eingespannt), K_{TF} : Koordinatensystem des tibiofemorales Gelenkes, K_{PF} : Koordinatensystem des patellofemorales Gelenkes, wobei Freiheitsgrade der Patellakomponente auf den Koordinatenursprung aufgebracht wurden und aus der muskuloskelettalen Mehrkörpersimulation entnommen wurden) und Kennzeichnung definierter Bereiche für die Auswertung der Dehnungsenergiedichte (Knochen ROI 1 bis 5). Die Referenzpunkte sind kinematisch mit den gekennzeichneten Flächen der Modellkomponenten gekoppelt. Die Richtungen entsprechen der anterior-posterioren Richtung (x), der superior-inferior Richtung (y) und der medio-lateralen Richtung (z).

2.3.4 Auswertung

Während der Simulation einer zementfreien Implantation wurde die maximale Spannung in der Femurkomponente berechnet. Bei hybridwerkstoffbasierten Femurkomponenten wurde diese Berechnung für jede Materialkomponente separat durchgeführt. Aufgrund der unterschiedlichen intrinsischen Materialeigenschaften (spröde oder duktil) wurde für die ATZ Keramik die maximale Hauptnormalspannung und für Co-Cr28-Mo6 und die Titanlegierungen (Ti-Nb35-Ta6 oder Ti-Al6-V4) die maximale von Mises Spannung als Auswerteparameter herangezogen. Während der aktiven Kniebeuge wurde zudem die relative Änderung der Dehnungsenergiedichte im Vergleich zur ATZ-Femurkomponente in den definierten Knochenbereichen in Abhängigkeit des Flexionswinkels analysiert. Die Dehnungsenergiedichte wurde als Stimulus für den Knochenumbau beschrieben [57,58] und bereits verwendet, um den Einfluss des Implantatmaterials auf die volumetrische Spannungsabschirmung des periprothetischen Knochens zu untersuchen [55].

3 Ergebnisse

3.1 Charakterisierung additiv gefertigter Ti/Nb/Ta Legierungen

Der Niob-Gehalt und die Fertigungsausrichtung beeinflussten die Mikrostruktur der additiv gefertigten Ti/Nb/Ta Legierungen [1] (siehe Abb. 4). Im Gegensatz zu Ti-Nb27-Ta6 und Ti-Nb35-Ta6 zeigte das Gefüge von Ti-Nb20-Ta6 plättchenartige Ausscheidungen. Bei Proben in 90° Fertigungsausrichtung waren längliche, säulenförmige Korngrenzen zu erkennen, die entlang der Aufbaurichtung während der additiven Fertigung orientiert waren.

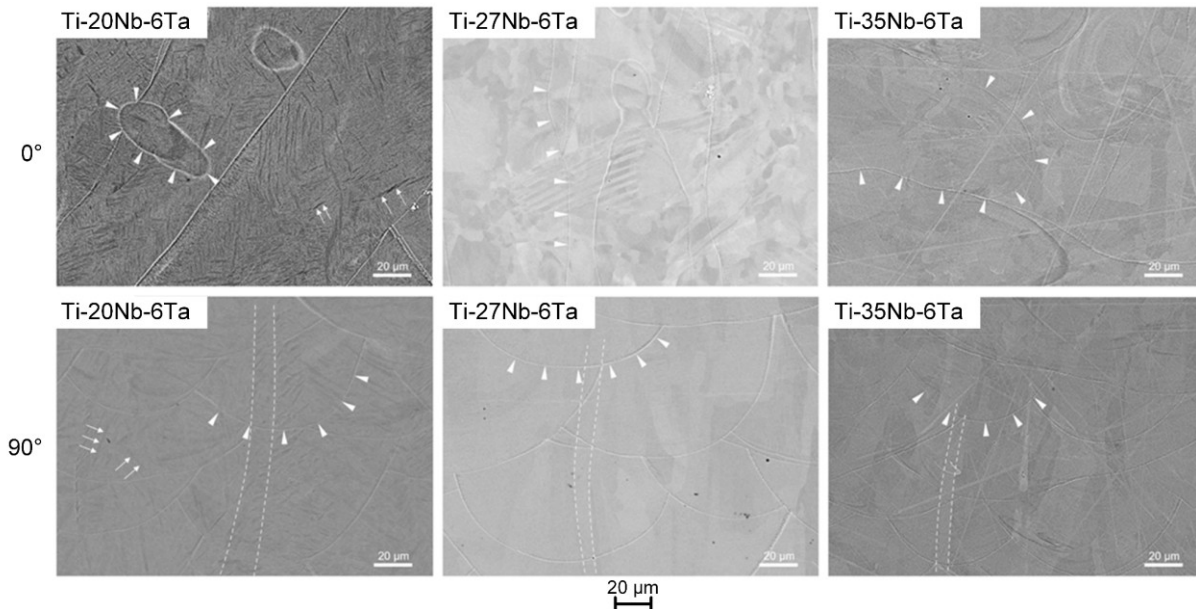


Abbildung 4. Rückstreuerelektronenanalyse von Ti-Nbx-Ta6 ($x = 20, 27, 35$ Gew.-%) Legierungen, die additiv mittels Laserstrahlschmelzen in 0° (oben) und 90° Fertigungsausrichtung (unten) hergestellt wurden. Plättchenartige Strukturen (nur Ti-Nb20-Ta6), längliche, säulenförmige Körner (bei 90°) und Schmelzbadgrenzen sind durch weiße Pfeile, gestrichelte Linien bzw. weiße Dreiecke hervorgehoben.

Repräsentative Spannungs-Dehnungs-Kurven der Ti/Nb/Ta Legierungen sind in Abb. 5A dargestellt. Die Proben zeigten ein duktileres Werkstoffverhalten und Ti-Nb20-Ta6 bzw. Ti-Nb27-Ta6 versagten in 45° zur einwirkenden Kompressionskraft. Ti-Nb35-Ta6 Proben zeigten kein Versagen bis 1.900 MPa Kompressionsspannung bzw. ca. 48 % plastischer Dehnung. Die offen-porösen Proben aus Ti-Nb20-Ta6 oder Ti-Al6-V4 versagten ebenfalls in 45° zur einwirkenden Kompressionskraft. Die ermittelten Festigkeiten lagen unterhalb der dichten Proben, wobei insbesondere Ti-Nb20-Ta6 ein duktileres Versagensverhalten zeigte. Elektronenmikroskopische Aufnahmen der Bruchflächen von Ti-Nb20-Ta6 in 0° und 45° Fertigungsausrichtung sind in Abb. 5B und 5C dargestellt. Diese wiesen Merkmale von Verformungsbrüchen (Wabenstrukturen) und Sprödbrüchen (Spaltflächen) auf. Die übrigen Bruchflächen konnten nicht untersucht werden, da die Bruchteile aneinanderhafteten, obwohl makroskopisch das Versagen erkennbar war.

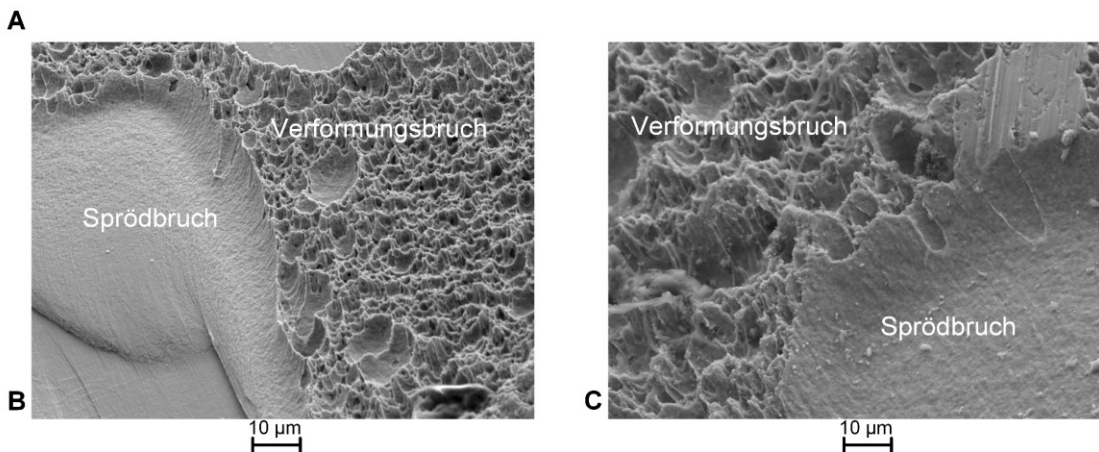
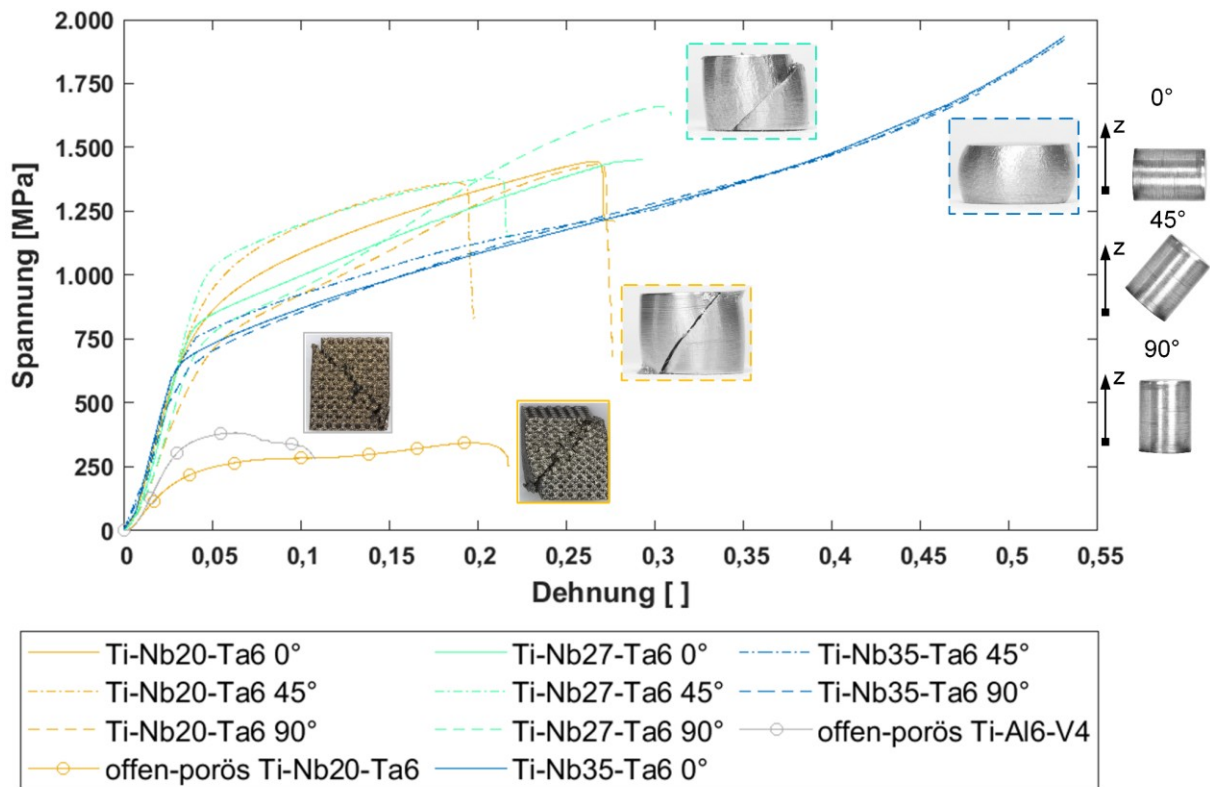


Abbildung 5. Darstellung A) repräsentativer Spannungs-Dehnungs-Kurven der durch Laserstrahlschmelzen additiv gefertigten Ti-Nbx-Ta6 ($x = 20, 27, 35$ Gew.-%) Legierungen in 0°, 45° und 90° Fertigungsausrichtung (z: Aufbaurichtung) und der offen-porösen Ti-Nb20-Ta6 und Ti-Al6-V4 Proben, B) beispielhafte elektronenmikroskopische Aufnahmen der Bruchflächen von Ti-Nb20-Ta6 Proben in B) 0° und C) 45° Fertigungsausrichtung sowie Kennzeichnung der spezifischen Bruchmuster des Verformungsbruchs (Wabenstruktur) und des Sprödbruchs (Spaltflächen).

Sowohl die Druckausrichtung als auch der Niob-Gehalt beeinflussten signifikant die mechanischen Eigenschaften der Titanlegierungen. Die ermittelten mechanischen Kennwerte sind in Tab. 2 dargestellt. Für jede Legierung ist der Kompressionsmodul und die Dehngrenze in Abhängigkeit von der Fertigungsausrichtung wie folgt geordnet: $90^\circ < 0^\circ < 45^\circ$. Dementsprechend zeigte Ti-Nb20-Ta6 in 90° die höchste zulässige elastische Dehnung. Die Kompressionsfestigkeit und Bruchdehnung von Ti-Nb20-Ta6 und Ti-Nb27-Ta6 waren minimal bei 45° Fertigungsausrichtung und die Kennwerte stiegen mit zunehmendem Niob-Gehalt an. Des Weiteren zeigten Ti-Nb20-Ta6 und Ti-Nb27-Ta6 in der 45° Fertigungsausrichtung die niedrigste mechanische Festigkeit und die geringste Bruchdehnung, während zwischen 0° und 90° nur geringe Unterschiede auftraten. Ti-Nb35-Ta6 zeigte ein abweichendes Verhalten. Die maximale Dehngrenze wurde bei 45° ersichtlich. Unabhängig von der Fertigungsausrichtung wurde kein Versagen bis zur maximalen Kompressionsspannung von 1.900 MPa beobachtet.

Eine detaillierte Beschreibung der Ergebnisse basierend auf der statistischen Auswertung ist in [I] dargestellt.

Offen-poröse Ti-Nb20-Ta6 Proben wiesen einen signifikant geringeren Kompressionsmodul auf als offen-poröse Ti-Al6-V4 Proben ($p = 0,008$), während sich das Verhältnis von Dehngrenze und Elastizität nicht signifikant unterschied ($p = 0,222$).

Tabelle 2. Zusammenfassung der mechanischen Eigenschaften (C: Kompressionsmodul, $\sigma_{c,0,2}$: Dehngrenze, UCS: Kompressionsfestigkeit, ε_B : Bruchdehnung, EAS: Relation von Elastizität zur Dehngrenze) der durch Laserstrahlschmelzen additiv gefertigten Ti-Nbx-Ta6 ($x = 20, 27, 35$ Gew.-%) Legierungen in Abhängigkeit des Niob-Gehaltes und der Fertigungsausrichtung (FA) sowie die Eigenschaften der offen-porösen Proben aus Ti-Nb20-Ta6 und Ti-Al6-V4.

Nb [Gew.-%]	FA [°]	C [GPa]	$\sigma_{c,0,2}$ [MPa]	UCS [MPa]	ε_B [%]	EAS []
Zylindrische Proben (Dichte > 99.9 %)						
20	0	69,0(2,7)	670,1(6,3)	1.467,8(37,1)	29,9(1,9)	0,97(0,03)
	45	73,2(10,6)	751,8(15,6)	1.374,6(30,2)	25,3(1,7)	1,05(0,17)
	90	43,1(2,6)	619,1(2,0)	1.453,3(21,0)	30,2(1,7)	1,44(0,09)
27	0	74,9(2,5)	787,3(76,1)	1.629,1(191,8)	34,9(5,5)	1,05(0,11)
	45	87,9(5,4)	954,4(13,6)	1.389,6(23,9)	18,8(0,3)	1,09(0,07)
	90	51,7(2,1)	695,1(49,1)	1.673,6(55,7)	30,8(5,1)	1,35(0,11)
35 ^a	0	64,5(1,1)	636,7(8,2)	-	48,1(0,3)	0,99(0,02)
	45	72,6(2,5)	693,4(3,1)	-	48,1(0,1)	0,96(0,03)
	90	54,2(2,9)	597,2(17,0)	-	48,1(0,3)	1,12(0,02)
Offen-poröse Proben						
Ti-Nb20-Ta6		8,7(1,0)	179,2(4,5)	351,7(7,5)	22,5(1,0)	0,48(0,07)
Ti-Al6-V4		16,7(3,2)	312,0(20,0)	381,7(2,0)	7,63(1,9)	0,53(0,08)

^{a)} Kein Bruch der Probe bis 1.900 MPa Kompressionsspannung

3.2 Charakterisierung der Ti-Nb35-Ta6/ATZ Hybridwerkstoffe

Die strukturelle und chemische Analyse der Schnittfläche einer Ti-Nb35-Ta6/ATZ Probe ist in Abb. 6 dargestellt. Das Glaslotverfahren führte zu einer homogenen Verbindung mit einer Spaltdicke von ca. 100 μm [II]. Im Glaslot wurden sphärische Poren mit Durchmessern im einstelligen Mikrometerbereich beobachtet. Die Elementverteilung im Glaslot zeigte eine lokale Anreicherung von Aluminium an der Grenzfläche zwischen Glaslot und Ti-Nb35-Ta6. Neben diesen Eigenschaften bestand das Glaslot aus einer homogenen Matrix aus SiO_2 , K_2O und Na_2O sowie weiteren Oxiden, die für eine bessere Übersicht nicht aufgeführt sind.

Scherzugsprobe

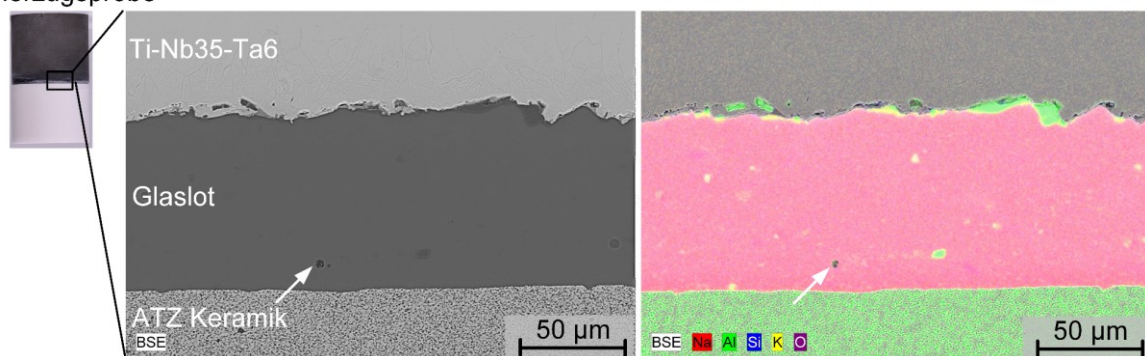


Abbildung 6. Elektronenmikroskopische Struktur- und Elementanalyse der Grenzfläche des durch ein silikatisches Glaslot gefügten Ti-Nb35-Ta6/ATZ Hybridwerkstoffes, wobei Ti-Nb35-Ta6 additiv durch Laserstrahlschmelzen gefertigt wurde. Es werden die Elemente Sauerstoff, Kalium, Silizium, Aluminium und Natrium als Hauptbestandteile des Glaslotes dargestellt.

Die statische Scherfestigkeit der Ti-Nb35-Ta6/ATZ und Ti/ATZ Proben (Gruppe 1 vs. Gruppe 2) betrug $26,4 \pm 4,2$ MPa bzw. $38,2 \pm 14,4$ MPa ($p = 0,117$). Demgegenüber betrug die statische Scherfestigkeit der beschleunigt gealterten Ti-Nb35-Ta6/ATZ und Ti/ATZ Proben (Gruppe 3 vs. Gruppe 4) $32,1 \pm 1,4$ MPa bzw. $44,1 \pm 9,7$ MPa ($p = 0,075$). Gealterte Ti-Nb35-Ta6/ATZ Proben zeigten eine signifikant höhere Scherfestigkeit als ungealterte

Ti-Nb35-Ta6/ATZ Proben ($p = 0,016$). Beide Hybridwerkstoffe (Gruppe 5 und 6) überstanden 10^7 Zyklen während einer dynamischen Scherbelastung zwischen 1 MPa und 10 MPa ohne Versagen der Glaslotverbindung.

Innerhalb der frakturierten Scherzugsproben wurde ein Mischversagen im Titanwerkstoff (kohäsives Versagen) und im Glaslot (adhäsives Versagen) in unterschiedlichen Anteilen beobachtet. Kohäsives Versagen war als graue Materialablagerung auf der ATZ-Komponente sichtbar (Abb. 7A). Darüber hinaus wurde beobachtet, dass Proben mit überwiegend kohäsivem Versagen höhere Scherfestigkeiten aufwiesen als Proben, die vorwiegend im Glaslot versagten. Die Porenbildung beeinträchtigte die Verbindung der Werkstoffe und führte zu Fehlstellen in der Lötverbindung [II]. Diese Fehlstellen waren zufällig über die Oberfläche verteilt und sphärisch (Abb. 7B) oder bildeten eine vernetzte bzw. verzweigte Struktur (Abb. 7C).

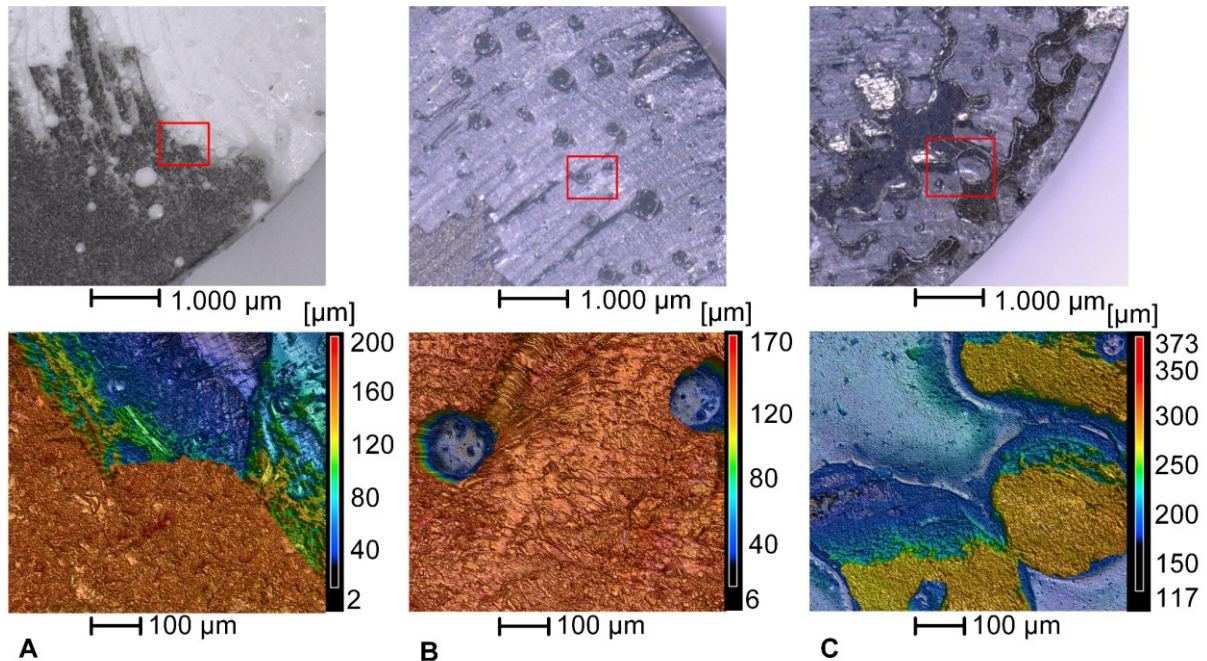


Abbildung 7. Mikroskopische Analyse der Bruchflächen der durch die Glaslottechnologie gefertigten Hybridwerkstoffe: A) keramische Bruchfläche einer Ti/ATZ Probe für die Verdeutlichung des kohäsiven und adhäsiven Mischversagens, B) Ti-Nb35-Ta6 Bruchfläche einer Ti-Nb35-Ta6/ATZ Probe für die Verdeutlichung der sphärischen Poren im Glaslot und C) Reintitan Bruchfläche einer Ti/ATZ Probe zur Verdeutlichung einer vernetzten oder verzweigten Struktur der Fehlstellen im Glaslot.

Die Glaslotverbindung des Ti-Nb35-Ta6/ATZ Funktionsdemonstrators wies einen homogenen Fügespalt mit vereinzelt Poren im Glaslot auf, wie sie bereits bei den gelöteten zylindrischen Proben beobachtet wurden.

Alle Funktionsdemonstratoren zeigten kein Versagen innerhalb der dynamischen Gangbelastung über 10.000 Zyklen. Die maximalen Flexions-Extensionsmomente der Funktionsdemonstratoren betragen $40,7 \pm 2,2$ Nm (Ti-Nb35-Ta6/ATZ) und $18,4 \pm 3,8$ Nm (Ti/ATZ). Vergleichbar mit dem Bruchverhalten der Scherzugsproben wurde ein kohäsives und adhäsives Mischversagen beobachtet.

3.3 Computergestützte Analyse einer Ti-Nb35-Ta6/ATZ Femurkomponente

3.3.1 Untersuchung der zementfreien Implantation

Die maximale Spannung während der zementfreien Implantation wurde im lateralen, posterioren Radius der Femurkomponenten ermittelt (Abb. 8). In Abb. 8 werden darüber hinaus die unterschiedlichen Spannungsverteilungen der Femurkomponenten aus Ti-Nb35-Ta6/ATZ mit und ohne offen-poröser Oberflächenstruktur und der monolithischen ATZ-Femurkomponente dargestellt [III].

Die maximale Hauptnormalspannung in der monolithischen ATZ-Femurkomponente betrug 1568,9 MPa und die maximale von Mises Spannung in der Femurkomponente aus Co-Cr28-Mo6 1290,6 MPa. Die maximale Hauptnormalspannung in der ATZ-Komponente wurde für die Femurkomponenten aus einem Hybridwerkstoff auf 367,6 MPa (- 76,6 %) für Ti-Al6-V4/ATZ, auf 560,9 MPa (- 64,3 %) für Ti-Al6-V4/ATZ mit offen-poröser Oberflächenstruktur, auf 474,9 MPa (- 69,7 %) für Ti-Nb35-Ta6/ATZ und auf 648,4 MPa (- 58,7 %) für Ti-Nb35-Ta6/ATZ mit offen-poröser Oberflächenstruktur reduziert. Die maximalen von Mises Spannungen in den Implantatkomponenten auf Basis der Titanlegierungen betragen 758,2 MPa (Ti-Al6-V4/ATZ), 636,5 MPa (Ti-Al6-V4/ATZ mit offen-poröser Oberflächenstruktur), 506,2 MPa (Ti-Nb35-Ta6/ATZ) und 411,1 MPa (Ti-Nb35-Ta6/ATZ mit offen-poröser Oberflächenstruktur). Die maximale von Mises Spannung in der offen-porösen Oberflächenschicht betrug 52,6 MPa und 84,2 MPa für Ti-Nb35-Ta6 bzw. Ti-Al6-V4.

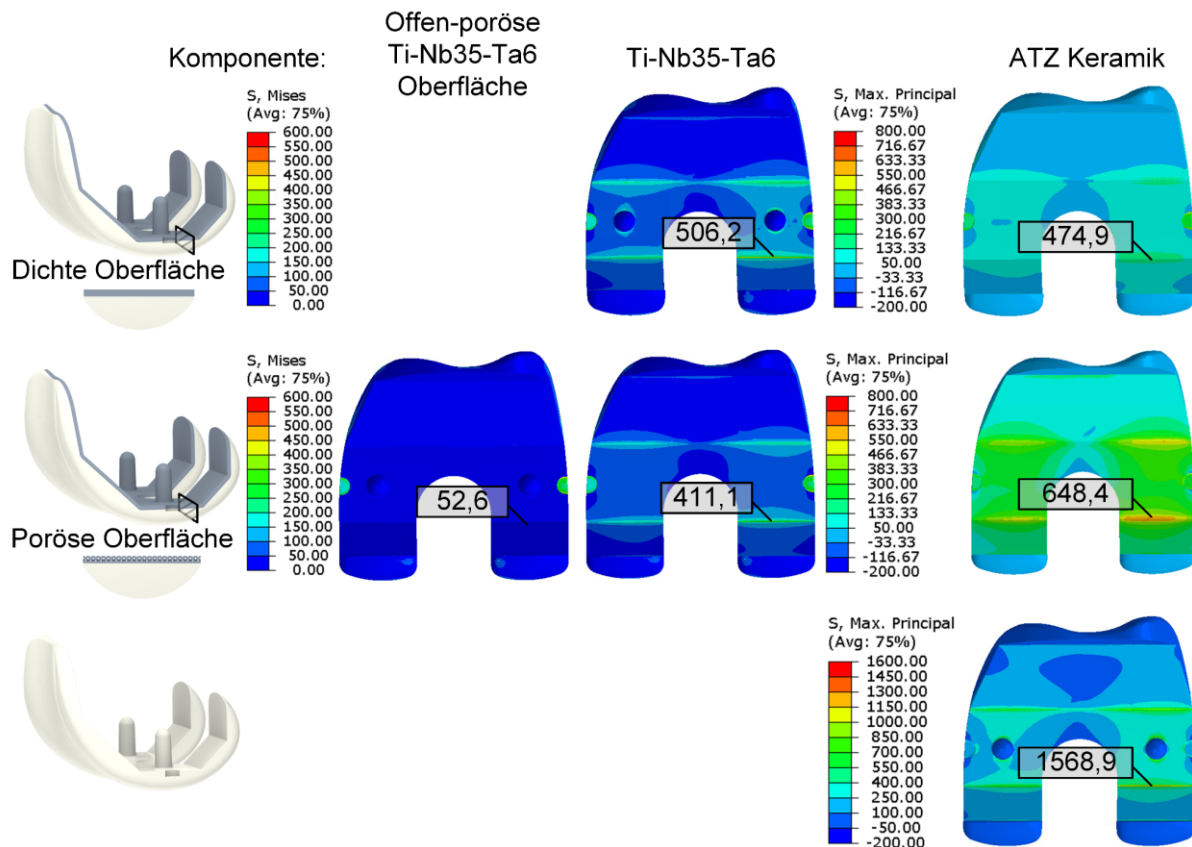


Abbildung 8. Spannungsverteilungen (Werte angegeben in MPa) der zementfreien Implantation der Femurkomponenten aus Ti-Nb35-Ta6/ATZ Hybridwerkstoffen mit bzw. ohne offen-poröser Oberflächenstruktur und aus monolithischer ATZ Keramik (Referenz). Gekennzeichnet sind die maximalen Spannungen während der simulierten Implantation.

3.3.2 Untersuchung der zweibeinigen Kniebeuge

Die Dehnungsenergiedichte in allen definierten Knochenbereichen nahm bei höheren Flexionswinkeln und damit einhergehenden höheren axialen Gelenkkräften zu [III]. Die relativen Änderungen der Dehnungsenergiedichte (Δ SED) als Indikator für die Spannungsabschirmung sind in Abb. 9 dargestellt. Dabei werden die verschiedenen Knochenbereiche (ROI 1 bis 5) in Abhängigkeit des Implantatwerkstoffes und des Flexionswinkels im Vergleich zur monolithischen ATZ Keramik betrachtet.

Zwischen der Femurkomponente aus monolithischer ATZ Keramik oder Co-Cr28-Mo6 wurden geringe Unterschiede bezüglich der Dehnungsenergiedichte ersichtlich. Die Hybridwerkstoffe führten zu einer Zunahme der Dehnungsenergiedichte in allen Bereichen des distalen Femurs. Die Zunahme war am stärksten für die Bereiche ROI 1 und ROI 5 ausgeprägt. Bei maximaler Flexion erhöhte sich die Dehnungsenergiedichte im Bereich ROI 1 um 25,7 % (Ti-Al6-V4/ATZ), 70,3 % (Ti-Al6-V4/ATZ mit offen-poröser Oberflächenstruktur), 43,7 % (Ti-Nb35-Ta6/ATZ), 82,5 % (Ti-Nb35-Ta6/ATZ mit offen-poröser Oberflächenstruktur) und 4,8 % (Co-Cr28-Mo6) im Vergleich zu monolithischer ATZ Keramik. Entsprechend beeinflusste neben der Titanlegierung auch die Oberflächenstrukturierung die Dehnungsenergiedichte.

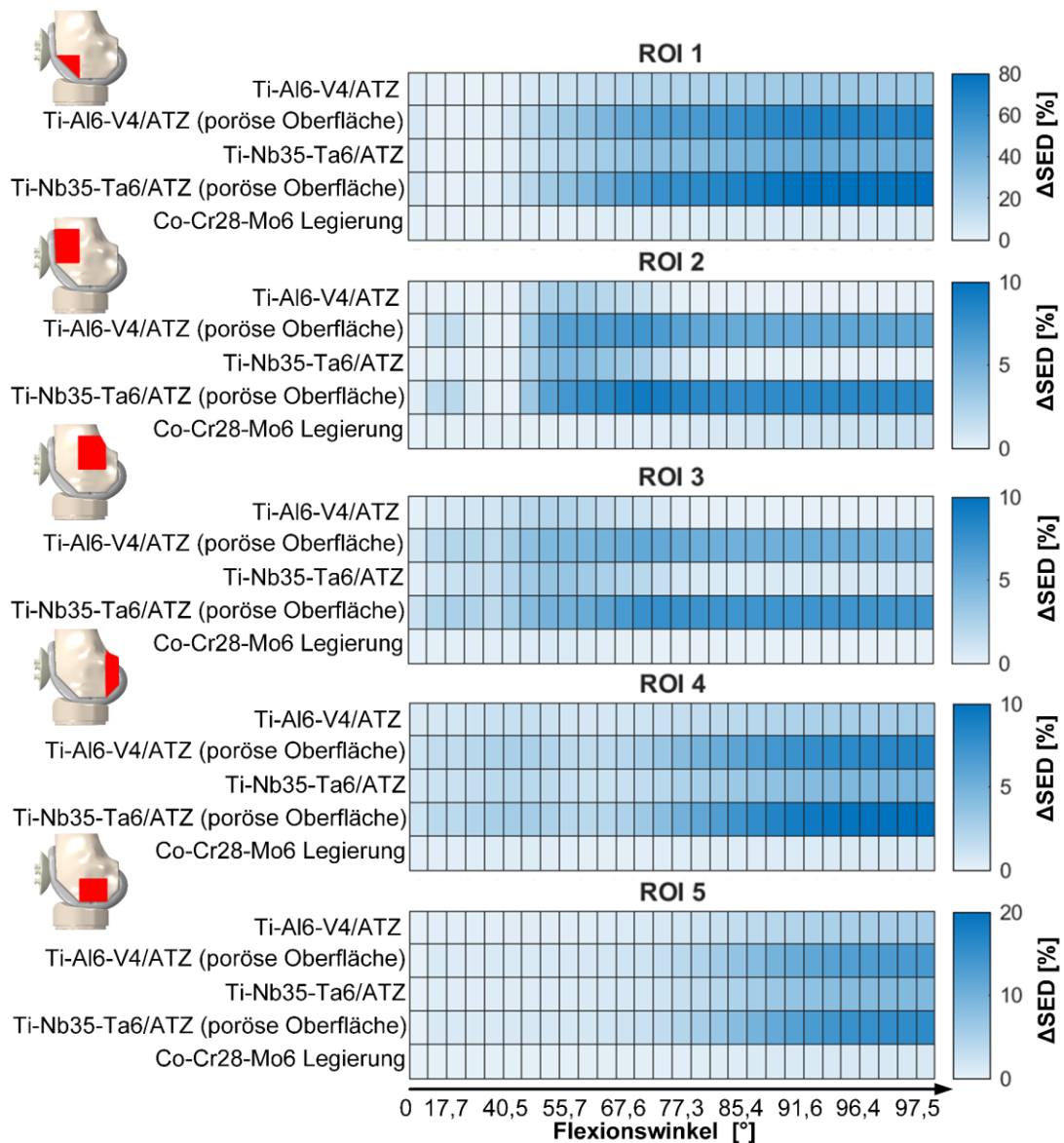


Abbildung 9. Temperaturfelder der relativen Änderung der Dehnungsenergiedichte (Δ SED [%]) für die verschiedenen Knochenregionen (ROI 1 bis 5, rot gekennzeichnet) im Vergleich zur Femurkomponente auf Basis einer monolithischen ATZ Keramik als Funktion des Implantatwerkstoffes (Hybridwerkstoff aus Ti-Al6-V4/ATZ und Ti-Nb35-Ta6/ATZ mit dichter bzw. offen-poröser Oberflächenstruktur sowie monolithischem Co-Cr28-Mo6).

4 Diskussion

Die aseptische Implantatlockerung der Femurkomponente einer bikondylären Knieendoprothese wird zum Teil auf materialspezifische Faktoren zurückgeführt [8–10]. Derzeit werden in Deutschland mehr als 99 % der implantierten Femurkomponenten aus einer Co-Cr-Mo Legierung gefertigt [3]. Freigesetzte Metallpartikel und -ionen sowie Polyethylenpartikel führen über eine zellbiologische Kaskade zur Osteolyse des periprothetischen Knochens [9–16]. Des Weiteren führt die Diskrepanz zwischen der Elastizität des Knochens und des Implantatwerkstoffes zu einer Spannungsabschirmung des periprothetischen Knochens, die ebenfalls mit einer Osteolyse einhergehen kann [22,25–27,32]. Die resultierende Knochenresorption trägt dabei zur aseptischen Implantatlockerung bei [10]. Zur Vermeidung dieser Prozesse wurden multifunktionale Hybridwerkstoffe beschrieben, die die vorteilhaften Eigenschaften von Oxidkeramiken und Titanwerkstoffen vereinen [33–39]. Dabei sind insbesondere biokompatible, hochelastische β -Titanlegierungen (z. B. Ti/Nb/Ta) relevant, um die derzeitigen Limitationen von Ti-Al6-V4 zu verbessern. Allerdings war der Zusammenhang der mechanischen Eigenschaften von Ti/Nb/Ta Legierungen in Abhängigkeit von der Fertigungsrichtung während eines additiven Fertigungsprozesses und dem Niob-Gehalt sowie die Integration dieser Legierungen in einen Hybridwerkstoff am Beispiel endoprothetischer Implantate bislang unzureichend untersucht. Ziel dieser Arbeit war es daher, einen multifunktionalen Hybridwerkstoff aus einer ATZ Keramik und einer Ti/Nb/Ta Legierung im Hinblick auf den möglichen Einsatz in der Femurkomponente einer bikondylären Knieendoprothese zu evaluieren. Dazu wurden zunächst additiv gefertigte Ti/Nb/Ta Legierungen experimentell charakterisiert [I], die anschließend in einen multifunktionalen Hybridwerkstoff aus einer ATZ Keramik und einer Ti/Nb/Ta Legierung integriert wurden [II]. Die Verbindung der Werkstoffe erfolgte durch ein silikatisches Glaslot. Darüber hinaus wurde eine hybride Knieendoprothese innerhalb einer computergestützten Analyse unter relevanten Lastfällen (zementfreie Implantation und zweibeinige Kniebeuge) biomechanisch charakterisiert [III].

4.1 Charakterisierung additiv gefertigter Ti/Nb/Ta Legierungen

In [I] erfolgte die mechanische Charakterisierung additiv gefertigter Ti-Nbx-Ta6 ($x = 20, 27, 35$ Gew.-%) Legierungen. Die additive Fertigung wurde durch Laserstrahlschmelzen in verschiedenen Fertigungsrichtungen ($0^\circ, 45^\circ, 90^\circ$) durchgeführt. Zusätzlich wurden offenporöse Ti-Nb20-Ta6 Proben charakterisiert. Der Kompressionsmodul der Ti/Nb/Ta Legierungen lag zwischen $43,1 \pm 2,6$ GPa (Ti-Nb20-Ta6, 90°) und $87,9 \pm 5,4$ GPa (Ti-Nb27-Ta6, 45°) und somit deutlich unter dem Elastizitätsmodul von Ti-Al6-V4 (110 GPa [43]). Die offenporösen Ti-Nb20-Ta6 Proben zeigten einen Kompressionsmodul von $8,7 \pm 1,0$ GPa, was im Bereich des humanen Knochens liegt [30,31,73].

Die höhere Elastizität wird auf die Mikrostruktur der Ti/Nb/Ta Legierungen zurückgeführt [46], die in Abhängigkeit des Niob-Gehaltes rein β -phasig (Ti-Nb35-Ta6), ein Mischkristall aus β -, ω - und α' -Phasen (Ti-Nb27-Ta6) oder eine orthorhombische α' -Martensitphase war [48]. Durch das Laserstrahlschmelzen werden längliche, säulenförmige β -Körner entlang der Baurichtung gebildet [47,51,74], was auch anhand der elektronenmikroskopischen Aufnahmen zu erkennen war [I]. Bei der additiven Fertigung wird das epitaktische Kristallwachstum durch die Bewegung des Schmelzbades beeinflusst, die wiederum von der räumlichen und zeitlichen Variation des Temperaturgradienten abhängt. Dies kann zur Programmierung einer bevorzugten kristallografischen Orientierung mit gewünschten Eigenschaften genutzt werden [59]. Die höchste Elastizität eines additiv gefertigten Bauteils wird durch eine Orientierung der $\langle 001 \rangle$ Kristallrichtung parallel zur Belastungsrichtung erreicht [47]. Entsprechend ist in Übereinstimmung mit den Ergebnissen von Pilz et al. [47] die Elastizität in Abhängigkeit von der Fertigungsrichtung wie folgt geordnet: $45^\circ > 0^\circ > 90^\circ$.

Folglich konnte eine potenzielle Verbesserung der Kompatibilität bezüglich der Elastizität der untersuchten Ti/Nb/Ta Legierungen mit dem humanen Knochen nachgewiesen werden.

Darüber hinaus zeigten die Ergebnisse, dass die Elastizität der Ti/Nb/Ta Legierungen durch die Orientierung der Mikrostruktur in gewissen Grenzen eingestellt werden kann [I].

Neben dem Kompressionsmodul ist die Festigkeit des Werkstoffs ein entscheidender Faktor. Die Dehngrenze der untersuchten Legierungen lag zwischen $597,2 \pm 17,0$ MPa (Ti-Nb35-Ta6, 90°) und $954,4 \pm 13,6$ MPa (Ti-Nb27-Ta6, 45°) und die Kompressionsfestigkeit zwischen $1.374,6 \pm 30,2$ MPa (Ti-Nb20-Ta6, 45°) und $1.673,6 \pm 55,7$ MPa (Ti-Nb27-Ta6, 90°), wobei die Ti-Nb35-Ta6 Proben bis 1.900 MPa Kompressionsspannung nicht frakturierten. Weiterhin zeigten alle Legierungen ein duktileres Verhalten mit Bruchdehnungen $> 18,8 \pm 5,1$ %. Die Anwendbarkeit der Ti/Nb/Ta Legierungen hinsichtlich der Festigkeit muss individuell gemäß den spezifischen Normen geprüft werden und kann somit anhand der durchgeführten Untersuchungen nicht abschließend verifiziert werden. Die zulässige elastische Dehnung lag zwischen 0,96 % und 1,44 % und zeigt damit ein vergleichbares Verhältnis aus Dehngrenze und Elastizität wie andere β -Titanlegierungen und Ti-Al6-V4 [43–45,47,75].

Es wurde eine Abhängigkeit der Festigkeit und Duktilität von der Fertigungsausrichtung festgestellt. Das Deformationsverhalten additiv gefertigter Proben wird neben dem Gleiten einzelner Atomebenen durch die geringe Kristallgröße, das Auftreten von Schmelzbadgrenzen und der zellularen Struktur beeinflusst [60,76]. Im Zusammenhang mit den komplexen Verformungsmechanismen anderer β -Titanlegierungen [60] wird die Abhängigkeit der Festigkeit und Duktilität mit der individuellen Mikrostruktur in Verbindung gebracht. Eine detaillierte Untersuchung des Verformungsverhaltens, vergleichbar mit der von Liu et al. [60] durchgeführten Studie lag jedoch nicht im Fokus der Arbeiten in [I], sollte aber in zukünftigen Untersuchungen betrachtet werden.

Ergänzend zu den mechanischen Untersuchungen wurden in [I] die Biokompatibilität und die osteogenen Eigenschaften der Ti/Nb/Ta Legierungen untersucht. Für alle untersuchten Titanlegierungen konnten Marker der osteogenen Differenzierung und keine zytotoxischen Reaktionen nachgewiesen werden. Dementsprechend wurde in [I] neben der mechanischen Kompatibilität auch auf zellbiologischer Ebene die Eignung der Ti/Nb/Ta Legierungen als Implantatwerkstoff im Knochenkontakt nachgewiesen.

4.2 Charakterisierung von Ti-Nb35-Ta6/ATZ Hybridwerkstoffen

In [II] wurde aufbauend auf den Ergebnissen aus [I] ein Hybridwerkstoff aus einer ATZ Keramik und Ti-Nb35-Ta6 mit der Glaslottechnologie hergestellt. Der Verbund wurde mechanisch charakterisiert und auf den Erkenntnissen aufbauend wurden Funktionsdemonstratoren einer Knieendoprothese entwickelt sowie biomechanisch analysiert. Aus den Ti/Nb/Ta Legierungen wurde aufgrund von Voruntersuchungen Ti-Nb35-Ta6 ausgewählt, das im Verbund mit der ATZ Keramik die höchste Festigkeit erreichte. Die statische Scherfestigkeit des Ti-Nb35-Ta6/ATZ Hybridwerkstoffes ($26,4 \pm 4,2$ MPa) unterschied sich nicht signifikant von der Referenz (Ti/ATZ), und die beschleunigte Alterung hatte keinen negativen Einfluss auf die Scherfestigkeit. Darüber hinaus wiesen alle Proben eine ausreichende Ermüdungsfestigkeit auf, um 10^7 Zyklen dynamischer Scherbelastung bis 10 MPa zu widerstehen.

Der Einsatz von hybriden Implantatwerkstoffen auf Basis einer Glaslotverbindung darf nicht zu einer mechanischen Schwächung des Implantates führen. Bei zementfrei fixierten Implantaten bestimmt die Knochen-Implantat-Festigkeit die Belastbarkeit bis zur Implantatlockerung. Untersuchungen ergaben Knochen-Implantat-Festigkeitswerte zwischen 0,5 MPa und 19,7 MPa [77–82]. Darüber hinaus wurden in der Norm zur Bewertung der Scherfestigkeit von titanbasierten Plasmaspritzschichten 20 MPa als Mindestanforderung definiert [83]. Auf Basis der angenommenen Vergleichbarkeit der verwendeten Glaslotverbindung wurden 20 MPa als Mindestanforderung an die Scherfestigkeit definiert und eingehalten. Während der physiologischen Belastung einer Knieendoprothese in-situ wird der Hybridwerkstoff jedoch durch eine superponierte Zug-, Scher- und Druckbelastung beansprucht [82], welche in der idealisierten Scherbelastung in [II] nicht abgebildet wurden. Entsprechend ist die angenommene Mindestanforderung in relevanten Lastfällen zu verifizieren.

Mikroskopische Untersuchungen der Bruchflächen zeigten, dass die Festigkeit des Hybridwerkstoffes durch adhäsives Versagen an der Grenzfläche zwischen Glaslot und Titanwerkstoff sowie durch kohäsives Versagen des Glaslots bestimmt wird, was ebenfalls in vergleichbaren Studien beschrieben wurde [34,84,85]. Ti/Nb/Ta Legierungen bilden Oxidschichten an der Oberfläche (z. B. TiO_2 , Nb_2O_5 und Ta_2O_5) [50,86] und die Reaktion der Oberflächenschicht mit dem Glaslot ist entscheidend für den Stoffschluss [34,42]. Spezifische Studien zur Wechselwirkung von Ti/Nb/Ta Legierungen mit den Oxidverbindungen des Glaslots sind derzeit nicht veröffentlicht und waren auch nicht im Fokus der Arbeit [II], sodass die Reaktion der Grenzschicht nur auf SiO_2 und Al_2O_3 bezogen werden kann. Hey et al. [87] beschrieben in diesem Zusammenhang die Bildung von Ti_5Si_3 durch die Reaktion von SiO_2 mit Titan unter Verwendung eines vergleichbaren Glaslotes. Darüber hinaus beschrieben Travessa et al. [88] in einer Studie über die Diffusionsbindung von Al_2O_3 und Reintitan, dass Al_2O_3 bei $800\text{ }^\circ\text{C}$ in Gegenwart von Titan zu einer intermetallischen Ti_3Al -Verbindung reagiert. Dabei diffundiert Sauerstoff in das Titan und es kommt zu einer Anreicherung aluminiumreicher Verbindungen an der Grenzfläche, was auch in [II] beobachtet wurde. Im Gegensatz dazu wurde keine chemische Reaktion von Ti/Ta Legierungen [89,90] oder reinem Niob [91] mit Al_2O_3 beschrieben. Aus den Ergebnissen der Fraktografie und der einschlägigen Literatur wird angenommen, dass der Stoffschluss zwischen dem Glaslot und Ti-Nb35-Ta6 durch die Reaktion von Titan mit SiO_2 und Al_2O_3 resultierte. Zusätzlich wurde aus den Versuchsergebnissen ersichtlich, dass der durch die Oberflächentopografie erzeugte Formschluss die Scherfestigkeit beeinflusst. Dies wurde daraus abgeleitet, dass in den Scheruntersuchungen kein signifikanter Unterschied zwischen Ti-Nb35-Ta6/ATZ und Ti/ATZ festgestellt wurde, jedoch ein 2,2-fach höheres ertragbares Flexionsmoment der Funktionsdemonstratoren aus Ti-Nb35-Ta6/ATZ. Die Fertigungsstrategie führte dazu, dass Funktionsdemonstratoren aus Ti-Nb35-Ta6/ATZ und Ti/ATZ eine Mittenrauheit von $5,8 \pm 2,0\text{ }\mu\text{m}$ bzw. $1,9 \pm 0,3\text{ }\mu\text{m}$ aufwiesen. Dementsprechend stellt die Oberflächentopografie einen Faktor für die Optimierung der Verbindungsfestigkeit dar.

Die Übertragung der Glaslottechnologie auf komplexe Implantatgeometrien ist für die Entwicklung einer bikondylären Knieendoprothese entscheidend. Im Zuge dieser Arbeit wurde die Machbarkeit an einem simplifizierten Funktionsdemonstrator überprüft, der den Flexionsbereich einer unilateralen Kondyle abbildet. Die hybriden Funktionsdemonstratoren überstanden 10.000 Gangzyklen nach ISO 14243-3:2014 [65] und wiesen maximal ertragbare Flexionsmomente von $40,7 \pm 2,2\text{ Nm}$ (Ti-Nb35-Ta6/ATZ) bzw. $18,4 \pm 3,8\text{ Nm}$ (Ti/ATZ) auf.

Die 10.000 Gangzyklen dienten als erstes Bewertungskriterium für die biomechanische Leistungsfähigkeit der Funktionsdemonstratoren. Diese Zyklenzahl reicht jedoch nicht aus, um die Ermüdungsfestigkeit unter physiologischer Belastung nachzuweisen. Die ISO-Norm 14243 für die Verschleißuntersuchung von Knieendoprothesen schreibt beispielsweise 5×10^6 Zyklen vor, die etwa fünf Jahren klinischer Belastung entsprechen. Neben der Dauerbelastung wurde daher das maximal ertragbare Flexions-Extensionsmoment bestimmt. Bei instrumentierten bikondylären Knieendoprothesen wurden Flexionsmomente von $25,9\text{ Nm}$ beim Gehen und bis zu $59,1\text{ Nm}$ beim Treppensteigen ermittelt [92]. Damit liegt das maximal ertragbare Flexionsmoment der Funktionsdemonstratoren unterhalb der in Implantaten gemessenen maximalen Flexionsmomente, jedoch wurden diese für bikondyläre Knieendoprothesen ermittelt. Die Vergleichbarkeit ist limitiert, da die Belastung innerhalb der biomechanischen Untersuchung von dem simplifizierten, unilateralen Funktionsdemonstrator aufgenommen wurde. Daraus ergibt sich, dass die Glaslottechnologie das Potenzial für eine ausreichende Verbindungsfestigkeit bietet, jedoch eine genaue Untersuchung des Einflusses aller Fertigungsparameter sowie die Übertragung auf ein gesamtes Implantatdesign erforderlich ist, um die Anwendbarkeit zu verifizieren.

Zusätzlich zu den mechanischen Eigenschaften ist die Zytotoxizität der Hybridwerkstoffe ein entscheidender Faktor für die Verwendung als Implantatwerkstoff. Aus diesem Grund wurden in [III] zusätzlich biologische Untersuchungen mit humanen Osteoblasten in einem indirekten

Eluationstest durchgeführt. Die Ergebnisse zeigten, dass die Eluate von Ti-Nb35-Ta6/ATZ Proben die Vitalität humaner Osteoblasten nicht beeinträchtigten, während Co-Cr28-Mo6 Proben die Zellproliferation und die Stoffwechselaktivität verringerten. Im Gegensatz zu Co-Cr-Mo Legierungen, bei denen freigesetzte Ionen unerwünschte biologische Reaktionen hervorrufen können [13,93–95] sind das Glaslot und die ATZ Keramik vergleichsweise biokompatibel [96]. Darüber hinaus wurde in [I] gezeigt, dass auf Ti/Nb/Ta Legierungen kultivierte Osteoblasten vital sind und eine osteogene Differenzierung induziert wird. Des Weiteren sind Ti/Nb/Ta Legierungen hochgradig korrosionsbeständig [50,86], womit von einer geringen Ionenfreisetzung auszugehen ist. In Übereinstimmung mit diesen früheren Erkenntnissen wurde gezeigt, dass der Ti-Nb35-Ta6/ATZ Hybridwerkstoff experimentell keine zytotoxischen Wirkungen zeigte und damit als Implantatwerkstoff verwendet werden kann.

4.3 Computergestützte Analyse einer Ti-Nb35-Ta6/ATZ Femurkomponente

Aufbauend auf den Studien [I] und [II] wurde in [III] das beschriebene Konzept einer hybridwerkstoffbasierten Femurkomponente innerhalb einer computergestützten Untersuchung mittels FE Simulation auf ein etabliertes Implantatdesign übertragen und während der zementfreien Implantation und einer zweibeinigen Kniebeuge analysiert. Bei der zementfreien Implantation wurde die mechanische Beanspruchung der Implantatkomponenten evaluiert. Die zweibeinige Kniebeuge wurde basierend auf einer sequenziellen MMKS-FE Simulation durchgeführt und es wurde die relative Änderung der Dehnungsenergie-dichte im distalen Femur in Relation zur monolithischen ATZ-Femurkomponente betrachtet. Neben der Variation des Hybridwerkstoffes (Ti-Nb35-Ta6/ATZ vs. Ti-Al6-V4/ATZ) wurden die mit dem Knochen interagierenden Oberflächen der Titankomponenten ohne und mit einer 1 mm dicken, offen-porösen Strukturierung modelliert. Die Materialparameter der offen-porösen Oberflächenschicht wurden entsprechend der in [I] beschriebenen mechanischen Charakterisierung berücksichtigt.

Die zementfreie Implantation bietet Vorteile gegenüber der zementierten Implantation [97], führt jedoch intraoperativ zu einer hohen Belastung der Femurkomponente durch die Übermaßpassung zwischen Knochen und Implantat. Für keramische Femurkomponenten sind kritische Hauptnormalspannungen von bis zu ca. 2.000 MPa während der Implantation beschrieben [20]. Dabei wurde in dieser Studie die zementierte Implantation mit verschiedenen Resektionsfehlern betrachtet. Da die zementfreie Implantation auf einem Übermaß zwischen Knochenlager und Implantat beruht [70,98], ist von einer vergleichbar hohen Beanspruchung durch das Aufbiegen der Femurkomponente auszugehen.

In [III] wurde eine maximale Hauptnormalspannung von 1.568,9 MPa in der monolithischen ATZ-Femurkomponente ermittelt. Für ATZ Keramiken wurden eine maximale Biegefestigkeit von 1.394 MPa [99] und maximale biaxiale Festigkeiten von 1.636 ± 302 MPa [100] beschrieben, sodass die maximale Hauptspannung in einem kritischen Bereich des Materialversagens lag. Dies deutet auf ein intraoperatives Bruchrisiko hin. Unter Verwendung der Hybridwerkstoffe wurde eine Spannungsreduktion zwischen 58,7 % und 76,6 % in der Keramikkomponente ermittelt. Die Reduktion war abhängig von der Steifigkeit der Titankomponente. Der multifunktionale Hybridwerkstoff reduziert somit potenziell das intraoperative Bruchrisiko der ATZ Keramik. Neben der Elastizität der Werkstoffe (Ti-Nb35-Ta6 vs. Ti-Al6-V4) sind auch die Wandstärke der Titankomponente und die Strukturierung der Oberfläche entscheidend für die Spannungsreduktion in der ATZ Komponente.

Die Spannungsabschirmung des periprothetischen Knochens wird durch die veränderte Lastübertragung auf den distalen Femurknochen nach Implantation einer Knieendoprothese hervorgerufen [22,25,101]. Implantatmaterialien mit einer geringeren Elastizität als der Knochen führen dazu, dass die Kräfte überwiegend von den Implantatkomponenten und nicht vom umliegenden Knochen getragen werden [25]. Nach dem Wolff'schen Gesetz [23] führt die veränderte Knochenbelastung zu einer beanspruchungsinduzierten Knochenresorption [24]. Aufgrund der höheren Elastizität der Titanlegierungen reduzierten die hybriden

Femurkomponenten die Spannungsabschirmung des periprothetischen Knochens im Vergleich zu monolithischer ATZ Keramik oder Co-Cr28-Mo6 Legierung. Frühere Studien untersuchten den Einfluss des Implantatmaterials auf die Spannungsabschirmung [25,33,102] und beschrieben äquivalente Beobachtungen. Insbesondere der anteriore Bereich des distalen Femurknochens (ROI 1 und 5) zeigte eine ausgeprägte Zunahme der Dehnungsenergiedichte. In diesen Bereichen wird klinisch eine Reduktion der Knochendichte nach Implantation einer Femurkomponente auf Basis einer Co-Cr-Mo Legierung beobachtet [27,101,103]. Damit verdeutlichen die in [III] erhobenen Ergebnisse die in [I] und [II] herausgearbeiteten Vorteile der Hybridwerkstoffe auf Basis hochelastischer Ti/Nb/Ta Legierungen auf die Knochen-Implantat-Interaktion am Beispiel einer Femurkomponente für Knieendoprothesen. Die additive Fertigung ermöglicht dabei die Generierung offen-poröser Oberflächen, die die Knochen-Implantat-Interaktion weiter verbessern können.

4.4 Limitationen und Ausblick

Die vorgestellten Untersuchungen unterliegen Limitationen, die in den jeweiligen Publikationen [I-III] detailliert dargestellt sind.

In [I] wurden elektronenmikroskopische Messungen durchgeführt, um den Einfluss der Fertigungsrichtung während des Laserstrahlschmelzens auf die Mikrostruktur zu charakterisieren. Eine detailliertere Analyse ist jedoch notwendig, um den Einfluss des Niob-Gehaltes und der Fertigungsrichtung auf das Deformationsverhalten zu charakterisieren und somit die anisotrope Fertigung optimal für den Designprozess ausnutzen zu können. Unter Berücksichtigung dieser Limitationen sollten zukünftige Studien den Zusammenhang zwischen diesen Parametern und der Mikrostruktur detailliert untersuchen.

Zu den Limitationen in [III] zählt das randomisierte Auftreten von Poren im Glaslot, welche eine Kerbwirkung induzieren. Dies führte beispielsweise zu einer signifikanten Zunahme der Scherfestigkeit gealterter Ti-Nb35-Ta6/ATZ Proben im Vergleich zu unbehandelten Proben, welche nicht mit den übrigen Beobachtungen oder der einschlägigen Literatur begründet werden kann und daher auf den zufälligen Fehler der Fehlstellen im Glaslot zurückgeführt wird. Im Rahmen der Fertigung der Funktionsdemonstratoren wurde ein Prozess entwickelt (sukzessives Aufbringen und Abschleifen der Glaslotschicht), der die Porenformierung reduziert, aber nicht vollständig verhindert. Die Poren beruhen auf eingeschlossenem Gas, das möglicherweise aus der Verdampfung der polymer basierten Trägersuspension der Glaslotpaste während des Brennens stammt. Weiterführende Studien sollten weitere Ansätze zur Verbesserung der Glaslotverbindung sowie die Übertragung der Erkenntnisse auf ein gesamtes Implantatdesign anstreben.

In [III] wurden im Rahmen der Modellbildung Vereinfachungen getroffen, die die Ergebnisse beeinflussen. Die Glaslotverbindung wurde durch einen numerischen Ansatz eingeschränkter Kontaktflächen berücksichtigt und nicht durch eine volumetrische Modellierung des Glaslotes. Die Untersuchung der Beanspruchungen im Glaslot und in den Grenzflächen ist jedoch ein kritischer Punkt, da wie in [II] beschrieben von einem Versagen innerhalb des Glaslotes oder der Grenzflächen auszugehen ist. Aus [II] ergibt sich, dass sich an der Grenzfläche zwischen Glaslot und Ti-Nb35-Ta6 eine Diffusionsschicht bildet, deren Materialeigenschaften derzeit unbekannt sind und somit keine verlässliche Modellierung möglich ist. Darüber hinaus wurde keine experimentelle Validierung der Ergebnisse durchgeführt. Daher müssen die absoluten Werte mit Einschränkung interpretiert werden. Die erzielten Simulationsergebnisse stimmen jedoch mit der einschlägigen Literatur überein [20,25,26,33]. Dementsprechend sollten die im Rahmen der vorgelegten Arbeit durchgeführten computergestützten Modellierungen als vergleichende Untersuchungen der verschiedenen Implantatmaterialien und als eine erste Evaluation des neuartigen Hybridwerkstoffes angesehen werden. Zukünftige Studien sollten sich auf verschiedene Aspekte konzentrieren, u.a. die experimentelle Validierung, das für die Primärstabilität erforderliche Übermaß, der Einfluss von Designspezifikationen (z. B. Wandstärke und Geometrie der Titankomponente, Ausprägung der Glaslotschicht) und patientenspezifischer Faktoren (z. B. Knochenqualität, Implantatgrößen).

5 Zusammenfassung

Die aseptische Lockerung der Femurkomponente einer bikondylären Knieendoprothese wird zum Teil durch materialspezifische Faktoren (Partikel bzw. Metallionen-induzierte Osteolyse und mechanische Spannungsabschirmung) bedingt. Die vorgelegte kumulative Dissertation, basierend auf Forschungsarbeiten, die zu den Publikationen [I-III] führten, befasste sich daher mit der experimentellen und computergestützten Untersuchung einer Femurkomponente einer bikondylären Knieendoprothese auf Basis eines multifunktionalen Hybridwerkstoffes. Das Ziel dieses Ansatzes ist es, materialspezifische Faktoren der aseptischen Implantatlockerung zu reduzieren. Der Hybridwerkstoff basierte auf der Verbindung einer ATZ Keramik und einer additiv gefertigten Ti/Nb/Ta Legierung durch ein silikatisches Glaslot. Es wurden zunächst mittels Laserstrahlschmelzen additiv gefertigte Ti-Nbx-Ta6 ($x = 20, 27, 35$ Gew.-%) in Abhängigkeit der Fertigungsrichtung ($0^\circ, 45^\circ, 90^\circ$) mechanisch charakterisiert [I]. Dabei wurden neben dichten Proben offen-poröse Proben für eine potenzielle Implantatoberfläche gefertigt und charakterisiert. Auf den Ergebnissen aus [I] aufbauend wurde Ti-Nb35-Ta6 in den Hybridwerkstoff Ti-Nb35-Ta6/ATZ integriert und untersucht [II]. Dazu wurden zunächst statische und dynamische Scherzugstestungen durchgeführt und darauf aufbauend Funktionsdemonstratoren der Gleitfläche des Tibiofemoralgelenkes biomechanisch evaluiert. Innerhalb einer nachfolgenden computergestützten Untersuchung der hybriden Femurkomponente unter relevanten Lastfällen (zementfreie Implantation und zweibeinige Kniebeuge) erfolgte eine Funktionsanalyse der Knochen-Implantat-Interaktion [III].

Die Ti-Nbx-Ta6 ($x = 20, 27, 35$ Gew.-%) Legierungen wiesen in Abhängigkeit des Niob-Gehaltes und der Fertigungsrichtung einen Kompressionsmodul zwischen $43,1 \pm 2,6$ GPa und $87,9 \pm 5,4$ GPa auf und offen-poröses Ti-Nb20-Ta6 einen Kompressionsmodul von $8,7 \pm 1,0$ GPa. Diese Abhängigkeit der mechanischen Eigenschaften von der Fertigungsrichtung wurde mit der anisotropen Mikrostruktur in Verbindung gebracht und ermöglicht die Einstellung der mechanischen Eigenschaften durch die Prozessparameter. In [I] wurde aus den mechanischen und weiterführenden biologischen Untersuchungen die Eignung der Ti/Nb/Ta Legierungen für einen Implantatwerkstoff im Knochenkontakt nachgewiesen. Zudem wurde in [II] gezeigt, dass die Glaslottechnologie geeignet ist, multifunktionale Hybridwerkstoffe aus einer ATZ Keramik und einer Ti-Nb35-Ta6 Legierung zu fertigen. Die auf Ti-Nb35-Ta6/ATZ basierenden Funktionsdemonstratoren der Gleitfläche des Tibiofemoralgelenkes zeigten eine suffiziente mechanische Belastbarkeit über 10.000 Gangzyklen sowie ein maximal ertragbares Flexions-Extensionsmoment von $40,7 \pm 2,2$ Nm. Weiterhin zeigte der Hybridwerkstoff im Vergleich zu Co-Cr-Mo Legierungen keine zytotoxische Wirkung, weshalb eine Verminderung des Risikos einer metallionen-bedingten Osteolyse zu erwarten ist. Innerhalb der computergestützten Untersuchung wurde gezeigt [III], dass die Hauptnormalspannung in der ATZ Komponente in einer hybridwerkstoffbasierten Femurkomponente während der zementfreien Implantation bis zu 76,6 % (Ti-Al6-V4/ATZ) verringert wird. Dies reduziert das intraoperative Frakturrisiko der spröden Implantatkomponente. Zudem wurde das Potenzial einer reduzierten Spannungsabschirmung durch die erhöhte Dehnungsenergiegedichte von bis 82,5 % (Ti-Nb35-Ta6/ATZ mit offen-poröser Implantatoberfläche) im periprothetischen Knochen während der zweibeinigen Kniebeuge verdeutlicht. Die Knochen-Implantat-Interaktion wurde sowohl durch die verwendete Titanlegierung als auch die Oberflächenstrukturierung beeinflusst.

Zusammenfassend konnte in der vorliegenden Arbeit gezeigt werden, dass mittels der Glaslottechnologie multifunktionale Hybridwerkstoffe aus einer ATZ Keramik und einer Ti/Nb/Ta Legierung für Femurkomponenten einer bikondylären Knieendoprothese gefertigt werden können. In den Hybridwerkstoffen werden die sehr gute Abrieb- und Korrosionsbeständigkeit der ATZ Keramik mit der hohen Elastizität und den ausgezeichneten osteokonduktiven Eigenschaften der Ti/Nb/Ta Legierungen vereint, wodurch materialspezifische Einflussfaktoren auf die Entstehung einer aseptischen Implantatlockerung in der Gelenkendoprothetik vermindert werden könnten.

Literaturverzeichnis

- [1] D.C. Wirtz, H. Reichel, G. Matziolis, T. Pfitzner (Eds.), Endoprothetik des Kniegelenkes, Springer Berlin Heidelberg, Berlin, Heidelberg, 2023.
- [2] Statistisches Bundesamt, Die 20 häufigsten Operationen insgesamt (OPS 5), 2023. <https://www.destatis.de/DE/Themen/Gesellschaft-Umwelt/Gesundheit/Krankenhaeuser/Tabellen/drg-operationen-insgesamt.html> (zuletzt geprüft am 02.10.2024).
- [3] A. Grimberg, J. Lützner, O. Melsheimer, M. Morlock, A. Steinbrück, Arthroplasty Register Germany (EPRD) - Annual Report 2023: Mit Sicherheit mehr Qualität, EPRD Deutsche Endoprothesenregister, Berlin, 2023.
- [4] J.T. Evans, R.W. Walker, J.P. Evans, A.W. Blom, A. Sayers, M.R. Whitehouse, How long does a knee replacement last? A systematic review and meta-analysis of case series and national registry reports with more than 15 years of follow-up, *Lancet* (London, England) 393 (2019) 655–663. [https://doi.org/10.1016/S0140-6736\(18\)32531-5](https://doi.org/10.1016/S0140-6736(18)32531-5).
- [5] P.L. Lewis, O. Robertsson, S.E. Graves, E.W. Paxton, H.A. Prentice, A. W-Dahl, Variation and trends in reasons for knee replacement revision: a multi-registry study of revision burden, *Acta Orthopaedica* 92 (2021) 182–188. <https://doi.org/10.1080/17453674.2020.1853340>.
- [6] K. Deere, M.R. Whitehouse, S.K. Kunutsor, A. Sayers, A.J. Price, J. Mason, A.W. Blom, How long do revised and multiply revised knee replacements last? An analysis of the National Joint Registry, *The Lancet. Rheumatology* 3 (2021) e438-e446. [https://doi.org/10.1016/S2665-9913\(21\)00079-5](https://doi.org/10.1016/S2665-9913(21)00079-5).
- [7] M. Weber, T. Renkawitz, F. Voellner, B. Craiovan, F. Greimel, M. Worlicek, J. Grifka, A. Benditz, Revision Surgery in Total Joint Replacement Is Cost-Intensive, *BioMed Research International* 2018 (2018) 8987104. <https://doi.org/10.1155/2018/8987104>.
- [8] M.D. Jones, C.L. Buckle, How does aseptic loosening occur and how can we prevent it?, *Orthopaedics and Trauma* 34 (2020) 146–152. <https://doi.org/10.1016/j.mporth.2020.03.008>.
- [9] S.B. Goodman, J. Gallo, Periprosthetic Osteolysis: Mechanisms, Prevention and Treatment, *Journal of Clinical Medicine* 8 (2019). <https://doi.org/10.3390/jcm8122091>.
- [10] J. Gallo, S.B. Goodman, Y.T. Konttinen, M.A. Wimmer, M. Holinka, Osteolysis around total knee arthroplasty: a review of pathogenetic mechanisms, *Acta Biomaterialia* 9 (2013) 8046–8058. <https://doi.org/10.1016/j.actbio.2013.05.005>.
- [11] Y. Jiang, T. Jia, P.H. Wooley, S.-Y. Yang, Current research in the pathogenesis of aseptic implant loosening associated with particulate wear debris, *Acta Orthopaedica Belgica* 79 (2013) 1–9.
- [12] S. Yang, K. Zhang, F. Li, J. Jiang, T. Jia, S.-Y. Yang, Biological responses of preosteoblasts to particulate and ion forms of Co-Cr alloy, *Journal of Biomedical Materials Research. Part A* 103 (2015) 3564–3571. <https://doi.org/10.1002/jbm.a.35501>.
- [13] A. Jonitz-Heincke, M.-L. Sellin, A. Seyfarth, K. Peters, B. Mueller-Hilke, T. Fiedler, R. Bader, A. Klinder, Analysis of Cellular Activity Short-Term Exposure to Cobalt and Chromium Ions in Mature Human Osteoblasts, *Materials (Basel)* 12 (2019). <https://doi.org/10.3390/ma12172771>.
- [14] A. Jonitz-Heincke, J. Tillmann, A. Klinder, S. Krueger, J.P. Kretzer, P.J. Høl, A.C. Paulus, R. Bader, The Impact of Metal Ion Exposure on the Cellular Behavior of Human Osteoblasts and PBMCs: In Vitro Analyses of Osteolytic Processes, *Materials (Basel)* 10 (2017). <https://doi.org/10.3390/ma10070734>.
- [15] K. Lochner, A. Fritsche, A. Jonitz, D. Hansmann, P. Mueller, B. Mueller-Hilke, R. Bader, The potential role of human osteoblasts for periprosthetic osteolysis following exposure to wear particles, *International journal of molecular medicine* 28 (2011) 1055–1063. <https://doi.org/10.3892/ijmm.2011.778>.
- [16] G.J. Atkins, D.R. Haynes, D.W. Howie, D.M. Findlay, Role of polyethylene particles in peri-prosthetic osteolysis: A review, *World Journal of Orthopedics* 2 (2011) 93–101. <https://doi.org/10.5312/wjo.v2.i10.93>.

- [17] D. Shekhawat, A. Singh, M.K. Banerjee, T. Singh, A. Patnaik, Bioceramic composites for orthopaedic applications: A comprehensive review of mechanical, biological, and microstructural properties, *Ceramics International* 47 (2021) 3013–3030. <https://doi.org/10.1016/j.ceramint.2020.09.214>.
- [18] P. Bergschmidt, M. Ellenrieder, R. Bader, D. Kluess, S. Finze, B. Schwemmer, W. Mittelmeier, Prospective comparative clinical study of ceramic and metallic femoral components for total knee arthroplasty over a five-year follow-up period, *The Knee* 23 (2016) 871–876. <https://doi.org/10.1016/j.knee.2016.06.001>.
- [19] K.C. Mertz, J. Yang, B.C. Chung, X. Chen, C.K. Mayfield, N.D. Heckmann, Ceramic Femoral Heads Exhibit Lower Wear Rates Compared to Cobalt Chrome: A Meta-Analysis, *The Journal of Arthroplasty* 38 (2023) 397–405. <https://doi.org/10.1016/j.arth.2022.09.008>.
- [20] D. Kluess, P. Bergschmidt, I. Mueller, W. Mittelmeier, R. Bader, Influence of the distal femoral resection angle on the principal stresses in ceramic total knee components, *The Knee* 19 (2012) 846–850. <https://doi.org/10.1016/j.knee.2012.03.014>.
- [21] A.P. Krueger, G. Singh, F.T. Beil, B. Feuerstein, W. Ruether, C.H. Lohmann, Ceramic femoral component fracture in total knee arthroplasty: an analysis using fractography, fourier-transform infrared microscopy, contact radiography and histology, *The Journal of Arthroplasty* 29 (2014) 1001–1004. <https://doi.org/10.1016/j.arth.2013.11.003>.
- [22] C. Schwartz, How to reduce osteopenia in total knee arthroplasty?, *European journal of orthopaedic surgery & traumatology orthopedie traumatologie* 29 (2019) 139–145. <https://doi.org/10.1007/s00590-018-2290-z>.
- [23] J. Wolff, The classic: on the theory of fracture healing. 1873, *Clinical Orthopaedics and Related Research* 468 (2010) 1052–1055. <https://doi.org/10.1007/s11999-010-1240-9>.
- [24] H.M. Frost, Bone's mechanostat: a 2003 update, *The anatomical record. Part A, Discoveries in molecular, cellular, and evolutionary biology* 275 (2003) 1081–1101. <https://doi.org/10.1002/ar.a.10119>.
- [25] A. Galas, L. Banci, B. Innocenti, The Effects of Different Femoral Component Materials on Bone and Implant Response in Total Knee Arthroplasty: A Finite Element Analysis, *Materials (Basel)* 16 (2023). <https://doi.org/10.3390/ma16165605>.
- [26] L. de Ruyter, K. Rankin, M. Browne, A. Briscoe, D. Janssen, N. Verdonshot, Decreased stress shielding with a PEEK femoral total knee prosthesis measured in validated computational models, *Journal of Biomechanics* 118 (2021) 110270. <https://doi.org/10.1016/j.jbiomech.2021.110270>.
- [27] D.W. Lee, H. Du Ro, H.-S. Han, M.C. Lee, Titanium Alloy Knee Implant Is Associated with Higher Bone Density over Cobalt Chromium: A Prospective Matched-Pair Case-Control Study, *Clinics in Orthopedic Surgery* 15 (2023) 581–588. <https://doi.org/10.4055/cios22082>.
- [28] D. Vogel, M. Wehmeyer, M. Kebbach, H. Heyer, R. Bader, Stress and strain distribution in femoral heads for hip resurfacing arthroplasty with different materials: A finite element analysis, *Journal of the Mechanical Behavior of Biomedical Materials* 113 (2021) 104115. <https://doi.org/10.1016/j.jmbbm.2020.104115>.
- [29] J.Y. Rho, M.C. Hobatho, R.B. Ashman, Relations of mechanical properties to density and CT numbers in human bone, *Medical Engineering & Physics* 17 (1995) 347–355. [https://doi.org/10.1016/1350-4533\(95\)97314-f](https://doi.org/10.1016/1350-4533(95)97314-f).
- [30] E.F. Morgan, H.H. Bayraktar, T.M. Keaveny, Trabecular bone modulus-density relationships depend on anatomic site, *Journal of Biomechanics* 36 (2003) 897–904. [https://doi.org/10.1016/s0021-9290\(03\)00071-x](https://doi.org/10.1016/s0021-9290(03)00071-x).
- [31] H.H. Bayraktar, E.F. Morgan, G.L. Niebur, G.E. Morris, E.K. Wong, T.M. Keaveny, Comparison of the elastic and yield properties of human femoral trabecular and cortical bone tissue, *Journal of Biomechanics* 37 (2004) 27–35. [https://doi.org/10.1016/s0021-9290\(03\)00257-4](https://doi.org/10.1016/s0021-9290(03)00257-4).
- [32] M. Bahraminasab, B.B. Sahari, K.L. Edwards, F. Farahmand, M. Arumugam, Aseptic loosening of femoral components – Materials engineering and design considerations, *Materials & Design* 44 (2013) 155–163. <https://doi.org/10.1016/j.matdes.2012.07.066>.

- [33] M. Bahraminasab, B.B. Sahari, K.L. Edwards, F. Farahmand, T.S. Hong, H. Naghibi, Material tailoring of the femoral component in a total knee replacement to reduce the problem of aseptic loosening, *Materials & Design* 52 (2013) 441–451. <https://doi.org/10.1016/j.matdes.2013.05.066>.
- [34] E. Mick, J. Tinschert, A. Mitrovic, R. Bader, A Novel Technique for the Connection of Ceramic and Titanium Implant Components Using Glass Solder Bonding, *Materials (Basel)* 8 (2015) 4287–4298. <https://doi.org/10.3390/ma8074287>.
- [35] M. Bahraminasab, S. Arab, N. Doostmohammadi, Cytotoxicity and Ion Release of Functionally Graded Al₂O₃- Ti Orthopedic Biomaterial, *Journal of Biomimetics, Biomaterials and Biomedical Engineering* 54 (2022) 103–118. <https://doi.org/10.4028/www.scientific.net/JBBBE.54.103>.
- [36] M. Bahraminasab, S. Arab, S. Ghaffari, Osteoblastic cell response to Al₂O₃-Ti composites as bone implant materials, *BiolImpacts BI* 12 (2022) 247–259. <https://doi.org/10.34172/bi.2021.2330>.
- [37] M. Bahraminasab, S. Arab, M. Safari, A. Talebi, F. Kavakebian, N. Doostmohammadi, In vivo performance of Al₂O₃-Ti bone implants in the rat femur, *Journal of Orthopaedic Surgery and Research* 16 (2021) 79. <https://doi.org/10.1186/s13018-021-02226-7>.
- [38] M. Bahraminasab, M. Bozorg, S. Ghaffari, F. Kavakebian, Electrochemical corrosion of Ti-Al₂O₃ biocomposites in Ringer's solution, *Journal of Alloys and Compounds* 777 (2019) 34–43. <https://doi.org/10.1016/j.jallcom.2018.09.313>.
- [39] M. Bahraminasab, S. Ghaffari, H. Eslami-Shahed, Al₂O₃-Ti functionally graded material prepared by spark plasma sintering for orthopaedic applications, *Journal of the Mechanical Behavior of Biomedical Materials* 72 (2017) 82–89. <https://doi.org/10.1016/j.jmbbm.2017.04.024>.
- [40] M. Mitrovic DE 10 2015 016 895 B3, 2015.
- [41] M. Mitrovic, A. Zothner DE102011015299A1, 2012.
- [42] Q. Sun, L. Yang, W. Yang, H. Ji, M. Li, Y. Li, Microstructure evolution and bonding mechanism of ZrO₂ ceramic and Ti-6Al-4V alloy joints brazed by Bi₂O₃-B₂O₃-ZnO glass paste, *Journal of the European Ceramic Society* 42 (2022) 5953–5963. <https://doi.org/10.1016/j.jeurceramsoc.2022.06.016>.
- [43] M. Niinomi, Mechanical properties of biomedical titanium alloys, *Materials Science and Engineering: A* 243 (1998) 231–236. [https://doi.org/10.1016/S0921-5093\(97\)00806-X](https://doi.org/10.1016/S0921-5093(97)00806-X).
- [44] C. Schulze, M. Weinmann, C. Schweigel, O. Keßler, R. Bader, Mechanical Properties of a Newly Additive Manufactured Implant Material Based on Ti-42Nb, *Materials (Basel)* 11 (2018). <https://doi.org/10.3390/ma11010124>.
- [45] S. Ozan, J. Lin, Y. Li, R. Ipek, C. Wen, Development of Ti-Nb-Zr alloys with high elastic admissible strain for temporary orthopedic devices, *Acta Biomaterialia* 20 (2015) 176–187. <https://doi.org/10.1016/j.actbio.2015.03.023>.
- [46] C.M. Lee, C.P. Ju, J.H. Chern Lin, Structure-property relationship of cast Ti-Nb alloys, *Journal of Oral Rehabilitation* 29 (2002) 314–322. <https://doi.org/10.1046/j.1365-2842.2002.00825.x>.
- [47] S. Pilz, T. Gustmann, F. Günther, M. Zimmermann, U. Kühn, A. Gebert, Controlling the Young's modulus of a β-type Ti-Nb alloy via strong texturing by LPBF, *Materials & Design* 216 (2022) 110516. <https://doi.org/10.1016/j.matdes.2022.110516>.
- [48] J. Johannsen, C. Lauhoff, M. Stenzel, C. Schnitter, T. Niendorf, M. Weinmann, Laser beam powder bed fusion of novel biomedical titanium/niobium/tantalum alloys: Powder synthesis, microstructure evolution and mechanical properties, *Materials & Design* 233 (2023) 112265. <https://doi.org/10.1016/j.matdes.2023.112265>.
- [49] A.H. Hussein, M.A.-H. Gepreel, M.K. Gouda, A.M. Hefnawy, S.H. Kandil, Biocompatibility of new Ti-Nb-Ta base alloys, *Materials Science and Engineering: C, Materials for Biological Applications* 61 (2016) 574–578. <https://doi.org/10.1016/j.msec.2015.12.071>.
- [50] R. Soni, S. Pande, S. Salunkhe, H. Natu, E. Abouel Nasr, R. Shanmugam, H.M.A.M. Hussein, In Vitro and Electrochemical Characterization of Laser-Cladded Ti-Nb-Ta Alloy for Biomedical Applications, *Crystals* 12 (2022) 954. <https://doi.org/10.3390/cryst12070954>.

- [51] C. Lauhoff, J. Johannsen, A. Bolender, A. Engelhardt, M. Stenzel, M. Weinmann, T. Niendorf, On the effect of energy input on microstructure evolution and mechanical properties of laser beam powder bed fusion processed Ti-27Nb-6Ta biomedical alloy, *Materials Science and Engineering: A* (2024) 147363. <https://doi.org/10.1016/j.msea.2024.147363>.
- [52] P.A.B. Kuroda, L.M. Da Silva, K.D.S.J. Sousa, T.A.G. Donato, C.R. Grandini, Preparation, structural, microstructural, mechanical, and cytotoxic characterization of Ti-15Nb alloy for biomedical applications, *Artificial organs* 44 (2020) 811–817. <https://doi.org/10.1111/aor.13624>.
- [53] S. Ozan, J. Lin, Y. Li, C. Wen, New Ti-Ta-Zr-Nb alloys with ultrahigh strength for potential orthopedic implant applications, *Journal of the Mechanical Behavior of Biomedical Materials* 75 (2017) 119–127. <https://doi.org/10.1016/j.jmbbm.2017.07.011>.
- [54] J.P. Luo, J.F. Sun, Y.J. Huang, J.H. Zhang, Y.D. Zhang, D.P. Zhao, M. Yan, Low-modulus biomedical Ti-30Nb-5Ta-3Zr additively manufactured by Selective Laser Melting and its biocompatibility, *Materials Science and Engineering: C, Materials for Biological Applications* 97 (2019) 275–284. <https://doi.org/10.1016/j.msec.2018.11.077>.
- [55] W. Kong, S.C. Cox, Y. Lu, V. Villapun, X. Xiao, W. Ma, M. Liu, M.M. Attallah, Microstructural Evolution, Mechanical Properties, and Preosteoblast Cell Response of a Post-Processing-Treated Ti-5Zr β Ti Alloy Manufactured via Selective Laser Melting, *ACS Biomaterials Science & Engineering* 8 (2022) 2336–2348. <https://doi.org/10.1021/acsbiomaterials.1c01277>.
- [56] J. Ni, H. Ling, S. Zhang, Z. Wang, Z. Peng, C. Benyshek, R. Zan, A.K. Miri, Z. Li, X. Zhang, J. Lee, K.-J. Lee, H.-J. Kim, P. Tebon, T. Hoffman, M.R. Dokmeci, N. Ashammakhi, X. Li, A. Khademhosseini, Three-dimensional printing of metals for biomedical applications, *Materials Today: Bio* 3 (2019) 100024. <https://doi.org/10.1016/j.mtbio.2019.100024>.
- [57] F. Trevisan, F. Calignano, A. Aversa, G. Marchese, M. Lombardi, S. Biamino, D. Ugues, D. Manfredi, Additive manufacturing of titanium alloys in the biomedical field: processes, properties and applications, *Journal of Applied Biomaterials & Functional Materials* 16 (2018) 57–67. <https://doi.org/10.5301/jabfm.5000371>.
- [58] S. Singh, S. Ramakrishna, Biomedical applications of additive manufacturing: Present and future, *Current Opinion in Biomedical Engineering* 2 (2017) 105–115. <https://doi.org/10.1016/j.cobme.2017.05.006>.
- [59] X. Luo, T. Song, A. Gebert, K. Neufeld, I. Kaban, H. Ma, W. Cai, H. Lu, D. Li, N. Li, Y. Li, C. Yang, Programming Crystallographic Orientation in Additive-Manufactured Beta-Type Titanium Alloy, *Advanced science (Weinheim, Baden-Wuerttemberg, Germany)* 10 (2023) e2302884. <https://doi.org/10.1002/adv.202302884>.
- [60] C. Liu, Y. Wang, Y. Zhang, L.-C. Zhang, L. Wang, Deformation mechanisms of additively manufactured TiNbTaZrMo refractory high-entropy alloy: The role of cellular structure, *International Journal of Plasticity* 173 (2024) 103884. <https://doi.org/10.1016/j.ijplas.2024.103884>.
- [61] J.-O. Sass, A. Jakobi, A. Mitrovic, C. Ganz, J. Wilken, U. Burmeister, H. Lang, R. Bader, D. Vogel, Bending strength of ceramic compounds bonded with silicate-based glass solder, *Materials Testing* 63 (2021) 593–598. <https://doi.org/10.1515/mt-2020-0098>.
- [62] J.-O. Sass, U. Burmeister, C. Ganz, A. Mitrovic, H. Lang, R. Bader, D. Vogel, Fracture strength of monolithic and glass-soldered ceramic subcomponents of 5-unit fixed dental prosthesis, *Journal of Prosthodontics Official Journal of the American College of Prosthodontists* 32 (2023) e71-e80. <https://doi.org/10.1111/jopr.13586>.
- [63] F04 Committee, ASTM F1044-05(2017)e1: Test Method for Shear Testing of Calcium Phosphate Coatings and Metallic Coatings, ASTM International, West Conshohocken, PA.
- [64] F04 Committee, ASTM F1160-14(2017)e1: Test Method for Shear and Bending Fatigue Testing of Calcium Phosphate and Metallic Medical and Composite Calcium Phosphate/Metallic Coatings, ASTM International, West Conshohocken, PA.
- [65] ISO 14243-3:2014-11 Implants for surgery, Wear of total knee-joint prostheses, Part 3: Loading and displacement parameters for wear-testing machines with displacement control and corresponding environmental conditions for test, Beuth Verlag GmbH, Berlin.

- [66] D. Kluess, R. Souffrant, W. Mittelmeier, A. Wree, K.-P. Schmitz, R. Bader, A convenient approach for finite-element-analyses of orthopaedic implants in bone contact: modeling and experimental validation, *Computer Methods and Programs in Biomedicine* 95 (2009) 23–30. <https://doi.org/10.1016/j.cmpb.2009.01.004>.
- [67] A. Sauer, A. Maas, S. Ottawa, A. Giurea, T.M. Grupp, Towards a New, Pre-Clinical, Subject-Independent Test Model for Kinematic Analysis after Total Knee Arthroplasty—Influence of the Proximo-Distal Patella Position and Patellar Tendon Stiffness, *Applied Sciences* 11 (2021) 10322. <https://doi.org/10.3390/app112110322>.
- [68] E. Schileo, E. Dall'ara, F. Taddei, A. Malandrino, T. Schotkamp, M. Baleani, M. Viceconti, An accurate estimation of bone density improves the accuracy of subject-specific finite element models, *Journal of Biomechanics* 41 (2008) 2483–2491. <https://doi.org/10.1016/j.jbiomech.2008.05.017>.
- [69] C. Oefner, S. Herrmann, M. Kebbach, H.-E. Lange, D. Kluess, M. Woiczinski, Reporting checklist for verification and validation of finite element analysis in orthopedic and trauma biomechanics, *Medical Engineering & Physics* 92 (2021) 25–32. <https://doi.org/10.1016/j.medengphy.2021.03.011>.
- [70] S. Berahmani, D. Janssen, N. Verdonschot, Experimental and computational analysis of micromotions of an uncemented femoral knee implant using elastic and plastic bone material models, *Journal of Biomechanics* 61 (2017) 137–143. <https://doi.org/10.1016/j.jbiomech.2017.07.023>.
- [71] J.-O. Sass, K. Johnson, J.-B. Darques, L. Buerstenbinder, I. Soodmand, R. Bader, M. Kebbach, Influence of posterior cruciate ligament tension on tibiofemoral and patellofemoral joint contact mechanics in cruciate-retaining total knee replacement: a combined musculoskeletal multibody and finite-element simulation, *Computer Methods in Biomechanics and Biomedical Engineering* (2024) 1–13. <https://doi.org/10.1080/10255842.2024.2329946>.
- [72] M. Kebbach, M. Darowski, S. Krueger, C. Schilling, T.M. Grupp, R. Bader, A. Geier, Musculoskeletal Multibody Simulation Analysis on the Impact of Patellar Component Design and Positioning on Joint Dynamics after Unconstrained Total Knee Arthroplasty, *Materials (Basel)* 13 (2020). <https://doi.org/10.3390/ma13102365>.
- [73] J.Y. Rho, R.B. Ashman, C.H. Turner, Young's modulus of trabecular and cortical bone material: ultrasonic and microtensile measurements, *Journal of Biomechanics* 26 (1993) 111–119. [https://doi.org/10.1016/0021-9290\(93\)90042-D](https://doi.org/10.1016/0021-9290(93)90042-D).
- [74] T. Ishimoto, K. Hagihara, K. Hisamoto, S.-H. Sun, T. Nakano, Crystallographic texture control of beta-type Ti–15Mo–5Zr–3Al alloy by selective laser melting for the development of novel implants with a biocompatible low Young's modulus, *Scripta Materialia* 132 (2017) 34–38. <https://doi.org/10.1016/j.scriptamat.2016.12.038>.
- [75] J. Stráský, P. Harcuba, K. Václavová, K. Horváth, M. Landa, O. Srba, M. Janeček, Increasing strength of a biomedical Ti-Nb-Ta-Zr alloy by alloying with Fe, Si and O, *Journal of the Mechanical Behavior of Biomedical Materials* 71 (2017) 329–336. <https://doi.org/10.1016/j.jmbbm.2017.03.026>.
- [76] Q. Sui, P. Li, K. Wang, X. Yin, L. Liu, Y. Zhang, Q. Zhang, S. Wang, L. Wang, Effect of Build Orientation on the Corrosion Behavior and Mechanical Properties of Selective Laser Melted Ti-6Al-4V, *Metals* 9 (2019) 976. <https://doi.org/10.3390/met9090976>.
- [77] S. Vercaigne, J.G. Wolke, I. Naert, J.A. Jansen, Histomorphometrical and mechanical evaluation of titanium plasma-spray-coated implants placed in the cortical bone of goats, *Journal of Biomedical Materials Research* 41 (1998) 41–48. [https://doi.org/10.1002/\(sici\)1097-4636\(199807\)41:1<41:aid-jbm5>3.0.co;2-q](https://doi.org/10.1002/(sici)1097-4636(199807)41:1<41:aid-jbm5>3.0.co;2-q).
- [78] K. Ozeki, T. Yuhta, H. Aoki, I. Nishimura, Y. Fukui, Push-out strength of hydroxyapatite coated by sputtering technique in bone, *Biomedical Materials and Engineering* 11 (2001) 63–68.
- [79] M. Müller, F.F. Hennig, T. Hothorn, R. Stangl, Bone-implant interface shear modulus and ultimate stress in a transcortical rabbit model of open-pore Ti6Al4V implants, *Journal of Biomechanics* 39 (2006) 2123–2132. <https://doi.org/10.1016/j.jbiomech.2005.05.036>.
- [80] J. Li, H. Liao, B. Fartash, L. Hermansson, T. Johnsson, Surface-dimpled commercially pure titanium implant and bone ingrowth, *Biomaterials* 18 (1997) 691–696. [https://doi.org/10.1016/s0142-9612\(96\)00185-8](https://doi.org/10.1016/s0142-9612(96)00185-8).

- [81] C.K. Chang, J.S. Wu, D.L. Mao, C.X. Ding, Mechanical and histological evaluations of hydroxyapatite-coated and noncoated Ti6Al4V implants in tibia bone, *Journal of Biomedical Materials Research* 56 (2001) 17–23. [https://doi.org/10.1002/1097-4636\(200107\)56:1<17:aid-jbm1063>3.0.co;2-t](https://doi.org/10.1002/1097-4636(200107)56:1<17:aid-jbm1063>3.0.co;2-t).
- [82] J. Zelle, D. Janssen, S. Peeters, C. Brouwer, N. Verdonshot, Mixed-mode failure strength of implant-cement interface specimens with varying surface roughness, *Journal of Biomechanics* 44 (2011) 780–783. <https://doi.org/10.1016/j.jbiomech.2010.10.037>.
- [83] ISO 13179-1:2021 Implants for surgery, Coatings on metallic surgical implants, Part 1: Plasma-sprayed coatings derived from titanium or titanium-6 aluminum-4 vanadium alloy powders, Beuth Verlag GmbH, Berlin.
- [84] V.Z.C. Vásquez, M. Ozcan, E.T. Kimpara, Evaluation of interface characterization and adhesion of glass ceramics to commercially pure titanium and gold alloy after thermal- and mechanical-loading, *Dental Materials* 25 (2009) 221–231. <https://doi.org/10.1016/j.dental.2008.07.002>.
- [85] T. van Vu, G.-J. Oh, H.-P. Lim, K.-D. Yun, S.-K. Ryu, E.-K. Yim, J.G. Fisher, J.-S. Ban, S.-W. Park, Shear Bond Strength of Zirconia to Titanium Implant Using Glass Bonding, *Journal of Nanoscience and Nanotechnology* 19 (2019) 967–969. <https://doi.org/10.1166/jnn.2019.15913>.
- [86] Y.S. Zhukova, Y.A. Pustov, A.S. Konopatsky, M.R. Filonov, Characterization of electrochemical behavior and surface oxide films on superelastic biomedical Ti–Nb–Ta alloy in simulated physiological solutions, *Journal of Alloys and Compounds* 586 (2014) S535–S538. <https://doi.org/10.1016/j.jallcom.2013.01.151>.
- [87] J. Hey, M. Kasaliyska, A. Kiesow, R. Schweyen, C. Arnold, Retentive Force of Glass-Ceramic Soldered Customized Zirconia Abutment Copings with Prefabricated Titanium Bases, *Materials (Basel)* 13 (2020). <https://doi.org/10.3390/ma13143193>.
- [88] D. Travessa, M. Ferrante, The Al₂O₃-titanium adhesion in the view of the diffusion bonding process, *Journal of Materials Science* 37 (2002) 4385–4390. <https://doi.org/10.1023/A:1020669022776>.
- [89] B. Gibbesch, G. Elssner, G. Petzow, Microstructure of interface regions and mechanical properties of Ti/Al₂O₃ and Ti-alloy/Al₂O₃ joints for dental implants, *Clinical Materials* 5 (1990) 177–189. [https://doi.org/10.1016/0267-6605\(90\)90017-P](https://doi.org/10.1016/0267-6605(90)90017-P).
- [90] B. Gibbesch, G. Elssner, G. Petzow, Investigation of Ti/Al₂O₃ joints with intermediate tantalum and niobium layers, *Biomaterials* 13 (1992) 455–461. [https://doi.org/10.1016/0142-9612\(92\)90166-L](https://doi.org/10.1016/0142-9612(92)90166-L).
- [91] M.N. Rahaman, T. Huang, B.S. Bal, Y. Li, In vitro testing of Al₂O₃-Nb composite for femoral head applications in total hip arthroplasty, *Acta Biomaterialia* 6 (2010) 708–714. <https://doi.org/10.1016/j.actbio.2009.07.025>.
- [92] G. Bergmann, A. Bender, F. Graichen, J. Dymke, A. Rohlmann, A. Trepczynski, M.O. Heller, I. Kutzner, Standardized loads acting in knee implants, *PLOS ONE* 9 (2014) e86035. <https://doi.org/10.1371/journal.pone.0086035>.
- [93] V. Sansone, D. Pagani, M. Melato, The effects on bone cells of metal ions released from orthopaedic implants. A review, *Clinical cases in mineral and bone metabolism the official journal of the Italian Society of Osteoporosis, Mineral Metabolism, and Skeletal Diseases* 10 (2013) 34–40. <https://doi.org/10.11138/ccmbm/2013.10.1.034>.
- [94] B. Scharf, C.C. Clement, V. Zolla, G. Perino, B. Yan, S.G. Elci, E. Purdue, S. Goldring, F. Macaluso, N. Cobelli, R.W. Vachet, L. Santambrogio, Molecular analysis of chromium and cobalt-related toxicity, *Scientific Reports* 4 (2014) 5729. <https://doi.org/10.1038/srep05729>.
- [95] J.R.W. Cruisen, M.C. Koper, J. Jelsma, M. Heymans, I.C. Heyligers, B. Grimm, N.M.C. Mathijssen, M.G.M. Schotanus, Prosthetic hip-associated cobalt toxicity: a systematic review of case series and case reports, *EFORT open reviews* 7 (2022) 188–199. <https://doi.org/10.1530/EOR-21-0098>.
- [96] J. Markhoff, E. Mick, A. Mitrovic, J. Pasold, K. Wegner, R. Bader, Surface modifications of dental ceramic implants with different glass solder matrices: in vitro analyses with human primary osteoblasts and epithelial cells, *BioMed Research International* 2014 (2014) 742180. <https://doi.org/10.1155/2014/742180>.

- [97] B. Uivaraseanu, C.M. Vesa, D.M. Tit, O. Maghiar, T.A. Maghiar, C. Hozan, A.C. Nechifor, T. Behl, F.L. Andronie-Cioara, J.M. Patrascu, S. Bungau, Highlighting the advantages and benefits of cementless total knee arthroplasty (Review), *Experimental and Therapeutic Medicine* 23 (2022) 58. <https://doi.org/10.3892/etm.2021.10980>.
- [98] S. Berahmani, D. Janssen, D. Wolfson, K. Rivard, M. de Waal Malefijt, N. Verdonshot, The effect of surface morphology on the primary fixation strength of uncemented femoral knee prosthesis: a cadaveric study, *The Journal of Arthroplasty* 30 (2015) 300–307. <https://doi.org/10.1016/j.arth.2014.09.030>.
- [99] S. Sequeira, M.H. Fernandes, N. Neves, M.M. Almeida, Development and characterization of zirconia–alumina composites for orthopedic implants, *Ceramics International* 43 (2017) 693–703. <https://doi.org/10.1016/j.ceramint.2016.09.216>.
- [100] J.-F. Roulet, K.L. Schepker, A. Truco, H.-C. Schwarz, M.G. Rocha, Biaxial flexural strength, crystalline structure, and grain size of new commercially available zirconia-based ceramics for dental appliances produced using a new slip-casting method, *Journal of the Mechanical Behavior of Biomedical Materials* 114 (2021) 104180. <https://doi.org/10.1016/j.jmbbm.2020.104180>.
- [101] I. Bendich, C.M. Lawrie, V. Riegler, R.L. Barrack, R.M. Nunley, The Impact of Component Design and Fixation on Stress Shielding After Modern Total Knee Arthroplasty, *The Journal of Arthroplasty* 37 (2022) S221-S225. <https://doi.org/10.1016/j.arth.2022.01.074>.
- [102] L. de Ruitter, D. Janssen, A. Briscoe, N. Verdonshot, The mechanical response of a polyetheretherketone femoral knee implant under a deep squatting loading condition, *Proceedings of the Institution of Mechanical Engineers. Part H, Journal of engineering in medicine* 231 (2017) 1204–1212. <https://doi.org/10.1177/0954411917738805>.
- [103] J. Järvenpää, T. Soininvaara, J. Kettunen, H. Miettinen, H. Kröger, Changes in bone mineral density of the distal femur after total knee arthroplasty: a 7-year DEXA follow-up comparing results between obese and nonobese patients, *The Knee* 21 (2014) 232–235. <https://doi.org/10.1016/j.knee.2013.03.004>.

Verwendete Originalarbeiten zur kumulativen Dissertation

Folgende drei Originalarbeiten wurden für die kumulative Dissertation herangezogen:

- [I] **Sass, J.-O.**, Sellin, M.-L., Kauertz, E., Johannsen, J., Weinmann, M., Stenzel, M., Frank, M., Vogel, D., Bader, R., Jonitz-Heincke, A., 2024. Advanced Ti-Nb-Ta Alloys for Bone Implants with Improved Functionality. *Journal of Functional Biomaterials* 15 (2). 10.3390/jfb15020046. (IF = 5,0)

- [II] **Sass, J.-O.**, Henke, P., Mitrovic, A., Weinmann, M., Kluess, D., Johannsen, J., Sellin, M.-L., Lembke, U., Reimer, D., Lork, C., Jonitz-Heincke, A., Bader, R., 2024. Multifunctional Hybrid Material for Endoprosthetic Implants Based on Alumina-Toughened Zirconia Ceramics and Additively Manufactured TiNbTa Alloys. *Materials* 17 (8), 1838. 10.3390/ma17081838. (IF = 3,1)

- [III] **Sass, J.-O.**, Kebbach, M., Lork, C., Johannsen, J., Weinmann, M., Stenzel, M., Bader, R., 2024. Computational biomechanical study on hybrid implant materials for the femoral component of total knee replacements. *Journal of the Mechanical Behavior of Biomedical Materials*, 106681. 10.1016/j.jmbbm.2024.106681. (IF = 3,3)

Abbildungsverzeichnis

- Abbildung 1.** Übersicht der additiv mittels Laserstrahlschmelzen gefertigten Proben: A) Darstellung der Fertigungsausrichtungen 0° , 45° , 90° (z: Aufbaurichtung), B) zylindrische Proben für die Kompressionsversuche der Ti-Nbx-Ta6 ($x = 20, 27, 35$ Gew.-%) Legierungen und C) offen-poröse Proben aus Ti-Nb20-Ta6 oder Ti-Al6-V4 sowie die kubisch flächenzentrierte Einheitszelle. 4
- Abbildung 2.** Übersichtsdarstellung der A) Hybridproben für die Schertestung und B) des Funktionsdemonstrators der Gleitflächen des Tibiofemoralgelenkes der Femurkomponente einer bikondylären Knieendoprothese (Angaben in mm). 5
- Abbildung 3.** Darstellung der Randbedingungen der Finite-Elemente Modelle: A) zementfreie Implantation (K_{RP} : Knochenreferenzpunkt (fest eingespannt), F_{RP} : Referenzpunkt der Femurkomponente (Translation von 0,5 mm in y Richtung; restliche Freiheitsgrade nicht eingeschränkt), Anwendung der Reduktion einer initialen Oberflächendurchdringung von 0,5 mm, B) zweibeinige Kniebeuge (K_{RP} : Knochenreferenzpunkt (Freiheitsgrade aus der muskuloskelettalen Mehrkörpersimulation), T_{RP} : Referenzpunkt des Tibia-Inlays (fest eingespannt), K_{TF} : Koordinatensystem des tibiofemorales Gelenkes, K_{PF} : Koordinatensystem des patellofemorales Gelenkes, wobei Freiheitsgrade der Patellakomponente auf den Koordinatenursprung aufgebracht wurden und aus der muskuloskelettalen Mehrkörpersimulation entommen wurden) und Kennzeichnung definierter Bereiche für die Auswertung der Dehnungsenergiedichte (Kochen ROI 1 bis 5). Die Referenzpunkte sind mit den gekennzeichneten Flächen der Modellkomponenten gekoppelt. Die Richtungen entsprechen der anterior-posterioren Richtung (x), der superior-inferior Richtung (y) und der medio-lateralen Richtung (z). 8
- Abbildung 4.** Rückstreuелектроненаналысе von Ti-Nbx-Ta6 ($x = 20, 27, 35$ Gew.-%) Legierungen, die additiv mittels Laserstrahlschmelzen in 0° (oben) und 90° Fertigungsausrichtung (unten) hergestellt wurden. Plättchenartige Strukturen (nur Ti-Nb20-Ta6), längliche, säulenförmige Körner (bei 90°) und Schmelzbadgrenzen sind durch weiße Pfeile, gestrichelte Linien bzw. weiße Dreiecke hervorgehoben. 10
- Abbildung 5.** Darstellung A) repräsentativer Spannungs-Dehnungs-Kurven der durch Laserstrahlschmelzen additiv gefertigten Ti-Nbx-Ta6 ($x = 20, 27, 35$ Gew.-%) Legierungen in 0° , 45° und 90° Fertigungsausrichtung (z: Aufbaurichtung) und der offen-porösen Ti-Nb20-Ta6 und Ti-Al6-V4 Proben, B) beispielhafte elektronenmikroskopische Aufnahmen der Bruchflächen von Ti-Nb20-Ta6 Proben in B) 0° und C) 45° Fertigungsausrichtung sowie Kennzeichnung der spezifischen Bruchmuster des Verformungsbruchs (Wabenstruktur) und des Sprödbruchs (Spaltflächen). 11
- Abbildung 6.** Elektronenmikroskopische Struktur- und Elementanalyse der Grenzfläche des durch ein silikatisches Glaslot gefügten Ti-Nb35-Ta6/ATZ Hybridwerkstoffes, wobei Ti-Nb35-Ta6 additiv durch Laserstrahlschmelzen gefertigt wurde. Es werden die Elemente Sauerstoff, Kalium, Silizium, Aluminium und Natrium als Hauptbestandteile des Glaslotes dargestellt. 12

Abbildung 7. Mikroskopische Analyse der Bruchflächen der durch die Glaslottechnologie gefertigten Hybridwerkstoffe: A) Keramische Bruchfläche einer Ti/ATZ Probe für die Verdeutlichung des kohäsiven und adhäsiven Mischversagens, B) Ti-Nb35-Ta6 Bruchfläche einer Ti-Nb35-Ta6/ATZ Probe für die Verdeutlichung der sphärischen Poren im Glaslot und C) Reintitan Bruchfläche einer Ti/ATZ Probe zur Verdeutlichung einer vernetzten oder verzweigten Struktur der Fehlstellen im Glaslot.....13

Abbildung 8. Spannungsverteilungen (Werte angegeben in MPa) der zementfreien Implantation der Femurkomponenten aus Ti-Nb35-Ta6/ATZ Hybridwerkstoffen mit bzw. ohne offen-poröser Oberflächenstruktur und aus monolithischer ATZ Keramik (Referenz). Gekennzeichnet sind die maximalen Spannungen während der simulierten Implantation.14

Abbildung 9. Temperaturfelder der relativen Änderung der Dehnungsenergiedichte (ΔSED [%]) für die verschiedenen Knochenregionen (ROI 1 bis 5, rot gekennzeichnet) im Vergleich zur Femurkomponente auf Basis einer monolithischen ATZ Keramik als Funktion des Implantatwerkstoffes (Hybridwerkstoff aus Ti-Al6-V4/ATZ und Ti-Nb35-Ta6/ATZ mit dichter bzw. offen-poröser Oberflächenstruktur sowie monolithischem Co-Cr28-Mo6).15

Tabellenverzeichnis

Tabelle 1. Übersicht der linear-elastischen Materialeigenschaften des Knochens, der Femurkomponenten und des Tibia-Inlays [III]..... 7

Tabelle 2. Zusammenfassung der mechanischen Eigenschaften (C: Kompressionsmodul, $\sigma_{c,0.2}$: Dehngrenze, UCS: Kompressionsfestigkeit, ϵ_B : Bruchdehnung, EAS: Relation von Elastizität zur Dehngrenze) der durch Laserstrahlschmelzen additiv gefertigten Ti-Nbx-Ta6 ($x = 20, 27, 35$ Gew.-%) Legierungen in Abhängigkeit des Niob-Gehaltes und der Fertigungsausrichtung (FA) sowie die Eigenschaften der offen-porösen Proben aus Ti-Nb20-Ta6 und Ti-Al6-V4.....12

Abkürzungsverzeichnis

Abb.	Abbildung
ATZ	Aluminiumoxid verstärkte Zirkonoxidkeramik (<i>Alumina-Toughened Zirconia</i>)
Co-Cr-Mo	Kobalt-Chrom-Molybdän
EAS	Maximal ertragbare elastische Dehnung (engl. <i>elastic admissible strain</i>)
FE	Finite Elemente
Gew. %	Gewichtsprozent
HU	Hounsfield Units
PEEK	Polyetheretherketon
ROI	engl. <i>regions of interest</i>
Tab.	Tabelle
Ti/Nb	Titan-Niob
Ti/Nb/Ta	Titan-Niob-Tantal
Ti/Nb/Ta/Zr	Titan-Niob-Tantal-Zirkonium
Ti/Nb/Zr	Titan-Niob-Zirkonium
UHMW-PE	Ultrahochmolekulares Polyethylen
ZTA	Zirkonoxid-verstärkte Aluminiumoxidkeramik (engl. <i>Zirconia-Toughened Alumina</i>)

Lebenslauf**Persönliche Daten**

Name: Jan-Oliver Saß
 Geburtsdatum: 18.11.1994
 Geburtsort: Rathenow
 Staatsangehörigkeit: deutsch
 Kontakt: jan-oliver.sass@med.uni-rostock.de

Berufserfahrung

02/2024 – heute **Bestellung zum Strahlenschutzbeauftragten**
 gemäß §70 StrlSchG für die transportable Tiermedizinische Röntgeneinrichtung HF 80 ML ultra leicht mit Leonardo Vet 1210, Forschungslabor für Biomechanik und Implantattechnologie

02/2020 – heute **Wissenschaftlicher Mitarbeiter**
 Universitätsmedizin Rostock, Orthopädische Klinik und Poliklinik
 Forschungslabor für Biomechanik und Implantattechnologie
 Arbeitsgruppe: Experimentelle Biomechanik

11/2018 – 11/2019 **Wissenschaftliche Hilfskraft**
 Universitätsmedizin Rostock, Orthopädische Klinik und Poliklinik
 Forschungslabor für Biomechanik und Implantattechnologie

11/2016 – 10/2018 **Wissenschaftliche Hilfskraft**
 Universitätsmedizin Rostock
 Institut für Biomedizinische Technik

11/2015 – 07/2016 **Wissenschaftliche Hilfskraft**
 Universitätsmedizin Rostock, Orthopädische Klinik und Poliklinik
 Forschungslabor für Biomechanik und Implantattechnologie

08/2016 – 10/2016 **Industriefachpraktikum**
 Albutec GmbH Rostock

07/2014 – 09/2014 **Industriegrundpraktikum**
 Siemens AG (6 Wochen) und OHST GmbH (2 Wochen)

Akademischer Werdegang

Seit 07/2020 **Promotionsphase**
 Universitätsmedizin Rostock, Orthopädische Klinik und Poliklinik
 Forschungslabor für Biomechanik und Implantattechnologie
 Dissertation: „Biomechanische Charakterisierung neuartiger Hybridwerkstoffe für Knieendoprothesen basierend auf Oxidkeramiken und Titan/Niob/Tantal-Legierungen“

10/2017 – 11/2019 **Masterstudium Biomedizinische Technik**
 Universität Rostock
 Abschluss: M. Sc. (Note: 1,1)
 Master-Thesis: „Untersuchung der Betriebsfestigkeit von Transkatheter-Aortenklappenprothesen,“ (Note: 1,0)

10/2014 – 10/2017 **Bachelorstudium Biomedizinische Technik**
 Universität Rostock
 Abschluss: B. Sc. (Note: 1,6)
 Bachelor-Thesis: „Designentwicklung einer polymerbasierten Transkatheter-Herzklappenprothese unter Anwendung der numerischen Simulation“ (Note: 1,1)

08/2007 – 06/2013 **Allgemeine Hochschulreife**
 Friedrich-Ludwig-Jahn Gymnasium Rathenow
 Note: 1,2

Kompetenzen

Softwarekenntnisse	Professionaler Umgang mit Microsoft Office Anwendungen Professionaler Umgang mit Finite-Elemente Analysen in Abaqus Professionaler Umgang mit Rekonstruktionssoftware medizinischer Bilddaten (Mimics, AMIRA) Fortgeschrittener Umgang mit SPSS Statistics, GraphPad Prism Fortgeschrittener Umgang mit MATLAB Fortgeschrittener Umgang mit Creo Parametrics Fortgeschrittener Umgang mit Geomagic Studios
Fremdsprachen	Englisch fließend in Wort und Schrift

Preise und Auszeichnungen

2023	1. Platz des Nachwuchs-Wissenschaftspreises der Deutschen Kniegesellschaft für den Beitrag „Hammersdorfer, N., Ferner, F., Sass, J.-O. , Hembus, J., Lutter, C., 2023. Biomechanical assessment of additional contralateral stabilization techniques for distal femoral torsional osteotomies. 12. Jahreskongress der Deutschen Kniegesellschaft“
2016	Auszeichnung als Beststudent der Fakultät für Maschinenbau und Schifftechnik der Universität Rostock durch die Ingenieurskammer MV

Liste der Originalarbeiten und Konferenzbeiträge**Originalarbeiten**

1. Ferner, F., Hammersdorfer, N., Hembus, J., **Saß, J.-O.**, Bader, R., Klinder, A., Hiepe, L., Holl, N., Lutter, C., 2024. Hinge screw or no hinge stabilization provides decreased stability compared to hinge plate in a biomechanical evaluation of distal femoral derotational osteotomies. *Knee surgery, sports traumatology, arthroscopy: official journal of the ESSKA*. 10.1002/ksa.12251.
2. Gabler, C., **Saß, J.-O.**, Gierschner, S., Lindner, T., Bader, R., Tischer, T., 2018. In Vivo Evaluation of Different Collagen Scaffolds in an Achilles Tendon Defect Model. *BioMed research international* 2018, 6432742. 10.1155/2018/6432742.
3. Graw, C.L., Waletzko-Hellwig, J., **Sass, J.-O.**, Jackszis, M., Frerich, B., Bader, R., Dau, M., 2023. A new manufacturing process for allogeneic bone plates based on high hydrostatic pressure-treated granules for jaw augmentation. *Materials Testing* 65 (8), 1155–1166. 10.1515/mt-2023-0004.
4. Lutter, C., Hiller, N., **Sass, J.-O.**, Hembus, J., Jones, G., Vogel, D., Groß, J., Bader, R., Tischer, T., 2024. Refixation of the anterior cruciate ligament: A biomechanical analysis of suture techniques in a porcine model. *J. Exp. Orthop.* 11 (1). 10.1002/jeo2.12011.
5. **Sass, J.-O.**, Burmeister, U., Ganz, C., Mitrovic, A., Lang, H., Bader, R., Vogel, D., 2022. Fracture strength of monolithic and glass-soldered ceramic subcomponents of 5-unit fixed dental prosthesis. *Journal of Prosthodontics: official journal of the American College of Prosthodontists*. 10.1111/jopr.13586.
6. **Sass, J.-O.**, Hembus, J., Fuhrmann, E., Vogel, D., Bauer, E., Link, H.D., Bader, R., 2023. Pre-clinical characterization of a novel flexible surface stem design for total knee replacements. *Proceedings of the Institution of Mechanical Engineers. Part H, Journal of engineering in medicine* 237 (10), 1154–1166. 10.1177/09544119231197596.
7. **Sass, J.-O.**, Henke, P., Mitrovic, A., Weinmann, M., Kluess, D., Johannsen, J., Sellin, M.-L., Lembke, U., Reimer, D., Lork, C., Jonitz-Heincke, A., Bader, R., 2024. Multifunctional Hybrid Material for Endoprosthetic Implants Based on Alumina-Toughened Zirconia Ceramics and Additively Manufactured TiNbTa Alloys. *Materials* 17 (8), 1838. 10.3390/ma17081838.
8. **Sass, J.-O.**, Jakobi, A., Mitrovic, A., Ganz, C., Wilken, J., Burmeister, U., Lang, H., Bader, R., Vogel, D., 2021. Bending strength of ceramic compounds bonded with silicate-based glass solder. *Materials Testing* 63 (7), 593–598. 10.1515/mt-2020-0098.
9. **Sass, J.-O.**, Johnson, K., Darques, J.-B., Buerstenbinder, L., Soodmand, I., Bader, R., Kebbach, M., 2024. Influence of posterior cruciate ligament tension on tibiofemoral and patellofemoral joint contact mechanics in cruciate-retaining total knee replacement: a combined musculoskeletal multibody and finite-element simulation. *Computer Methods in Biomechanics and Biomedical Engineering*, 1–13. 10.1080/10255842.2024.2329946.
10. **Sass, J.-O.**, Kebbach, M., Lork, C., Johannsen, J., Weinmann, M., Stenzel, M., Bader, R., 2024. Computational biomechanical study on hybrid implant materials for the femoral component of total knee replacements. *Journal of the Mechanical Behavior of Biomedical Materials*, 106681. 10.1016/j.jmbbm.2024.106681.
11. **Sass, J.-O.**, Saemann, M., Kebbach, M., Soodmand, E., Wree, A., Bader, R., Kluess, D., 2024. The Morphology of the Femur Influences the Fracture Risk during Stumbling and Falls on the Hip—A Computational Biomechanical Study. *Life* 14 (7), 841. 10.3390/life14070841.
12. **Sass, J.-O.**, Sellin, M.-L., Kauertz, E., Johannsen, J., Weinmann, M., Stenzel, M., Frank, M., Vogel, D., Bader, R., Jonitz-Heincke, A., 2024. Advanced Ti-Nb-Ta Alloys for Bone Implants with Improved Functionality. *Journal of Functional Biomaterials* 15 (2). 10.3390/jfb15020046.

13. Waletzko-Hellwig, J., **Sass, J.-O.**, Bader, R., Frerich, B., Dau, M., 2024. Evaluation of integrity of allogeneic bone processed with high hydrostatic pressure: a pilot animal study. *Biomater Res.* 10.34133/bmr.0067.

Konferenzbeiträge

1. Becker, A.-K., Soodmand, I., **Sass, J.-O.**, Jabs, C., Kebbach, M., Dau, M., Bader, R. Kopplung von muskuloskelettaler Mehrkörpersimulation und Finite-Elemente-Analyse zur Modellierung des menschlichen Kausystems. 13. Kongress der Deutschen Gesellschaft für Biomechanik (DGfB).
2. Becker, A.-K., Soodmand, I., **Sass, J.-O.**, Jabs, C., Kebbach, M., Dau, M., Bader, R., 2023. Musculoskeletal multibody simulation provides personalized boundary conditions for finite element modeling of the human masticatory system. 5th International Conference on Biomedical Technology.
3. Becker, J., Tischer, T., Hembus, J., **Sass, J.-O.**, Bader, R., Lutter, C., 2024. Außenmeniskusnähte mit all-inside Fixierung an der Popliteusehne: eine biomechanische Evaluation. 41th AGA Kongress.
4. Hammersdorfer, N., Ferner, F., **Sass, J.-O.**, Hembus, J., Lutter, C., 2023. Biomechanical assessment of additional contralateral stabilization techniques for distal femoral torsional osteotomies. 12. Jahreskongress der Deutschen Kniegesellschaft.
5. Ausgezeichnet mit dem 1. Platz des Nachwuchs-Wissenschaftspreises der Deutschen Kniegesellschaft
6. Henke, P., Ruehrmund, L., Kebbach, M., **Sass, J.-O.**, Soodmand, I., Kleist, E., Woernle, C., Bader, R., 2022. Feasibility study to transfer musculoskeletal model data to a 6 DOF joint simulator. 27th Congress of the European Society of Biomechanics.
7. Johnson, K., **Sass, J.-O.**, Buerstenbinder, L., Darques, J.B., Soodmand, I., Bader, R., Kebbach, M., 2022. Posterior cruciate ligament tension and tibial component malrotation in total knee replacement. 27th Congress of the European Society of Biomechanics.
8. Saemann, M., Maeruan, K., **Sass, J.-O.**, Mauck, J., Schulze, C., Kluess, D., Bader, R., 2019. Influence of different boundary conditions and averaging algorithms on mechanical behavior in FE modeling of the proximal femur. EMBC2019: 41st Annual International Conference of the IEEE Engineering in Medicine and Biology Society 2019.
9. **Sass, J.-O.**, Henke, P., Kluess, D., Lork, C., Johannsen, J., Lembke, U., Pfuetzner, D., Weinmann, M., Stenzel, M., Bader, R., 2024. Mechanische Charakterisierung eines multifunktionalen hybriden Implantatwerkstoffes aus ATZ und additiv gefertigter Ti-35Nb-6Ta Legierung. 13. Kongress der Deutschen Gesellschaft für Biomechanik (DGfB).
10. **Sass, J.-O.**, Kluess, D., Lork, C., Kauertz, E., Lembke, U., Johannsen, J., Weinmann, M., Stenzel, M., Vogel, D., Bader, R., 2024. Mechanical and biological characterization of hybrid material compounds of Al₂O₃-toughened ZrO₂ ceramics and additively manufactured Ti-35Nb-6Ta. 12th World Biomaterials Congress (WBC 2024).
11. **Sass, J.-O.**, Lork, C., Kebbach, M., Bader, R., 2024. Finite-Elemente-Analyse hybrider Keramik-Titan-Materialien für die Knieendoprothetik. 13. Kongress der Deutschen Gesellschaft für Biomechanik (DGfB).
12. **Sass, J.-O.**, Saemann, M., Bader, R., Sander, M., Kluess, D., 2020. Einfluss morphologischer Parameter auf die Steifigkeit des proximalen humanen Femurs bei den Lastfällen Stolpern und seitlicher Sturz auf die Hüfte - Eine Finite-Elemente-Analyse. Deutscher Kongress für Orthopädie und Unfallchirurgie. 10.1055/s-0040-1717814.
13. **Sass, J.-O.**, Sellin, M.-L., Johannsen, J., Weinmann, M., Stenzel, M., Vogel, D., Jonitz-Heincke, A., Bader, R., 2024. Mechanical and biological properties of an additively manufactured Ti-20Nb-6Ta implant material with open porous structure. 12th World Biomaterials Congress (WBC 2024).

14. **Sass, J.-O.**, Sellin, M.-L., Kauertz, E., Johannsen, J., Weinmann, M., Stenzel, M., Vogel, D., Jonitz-Heincke, A., Bader, R., 2023. Mechanical functionality and biocompatibility of Ti-Nb-Ta alloys additively manufactured by laser beam powder bed fusion. 29th Annual Meeting of the German Society for Biomaterials (DGBM).
15. **Sass, J.-O.**, Vogel, D., Ganz, C., Lembke, U., Bader, R., 2022. Computational study of a ceramic-titanium material compound for hybrid knee endoprotheses. 5th International Conference on Hybrid Materials and Structures.
16. Soodmand, I., **Sass, J.-O.**, Becker, A.-K., Jabs, C., Kebbach, M., Dau, M., Bader, R. Influence of bone quality and dental implant material on stress distribution within the surrounding bone. VPH2024 - Data-Driven Simulation Technologies for Clinical Decision-Making.
17. Weinmann, M., Stenzel, M., **Sass, J.-O.**, Sellin, M.-L., Lork, C., Pfuetzner, D., Lembke, U., Kluess, D., Bader, R., 2023. Development of materials for additively manufactured hybrid knee implants. AMMM 2023: Additive Manufacturing Meets Medicine.

Danksagung

An dieser Stelle möchte ich mich herzlich bei den Menschen bedanken, die mich in der Zeit meiner Promotion wesentlich begleitet und unterstützt haben.

Ich beginne mit dem Dank bei Herrn Prof. Dr. med. habil. Dipl.-Ing. Rainer Bader für die Möglichkeit, die Promotion im Forschungslabor für Biomechanik und Implantattechnologie (FORBIOMIT) an der Orthopädischen Klinik und Poliklinik der Universitätsmedizin Rostock anfertigen zu können. Ich möchte mich bei ihm für die konstruktiven Diskussionen und Vorschläge bedanken, die zum Abschluss dieser Arbeit beigetragen haben sowie für die zahlreichen weiteren spannenden Projekte und Aufgaben, an denen ich mitwirken durfte. Weiterhin möchte ich mich bei allen im BMBF-Projekt HYTIMOX beteiligten Projektpartnern und insbesondere bei Frau Dr. Cornelia Lork, Herrn Dr. Markus Weinmann und Herrn Jan Johannsen für die Zusammenarbeit bedanken.

Ein großer Dank gilt allen gegenwärtigen und ausgeschiedenen Mitarbeitern und Mitarbeiterinnen des FORBIOMIT. Ich schätze es sehr, auch über die Arbeit hinaus gute Freundschaften gewonnen zu haben. Besonders möchte ich mich bei den Kolleginnen und Kollegen aus meiner Arbeitsgruppe, Frau Dr. Jessica Hembus, Herr Paul Henke und Herr Dr. Danny Vogel bedanken, die mich stets mit guten Hinweisen und konstruktiven Diskussionen unterstützt haben.

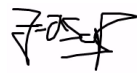
Des Weiteren möchte ich meinen Eltern, Großeltern, meiner Schwester und meinem Schwager für den Rückhalt und Unterstützung während meines bisherigen Werdeganges bedanken. Ganz besonders bedanke ich mich bei meiner wunderbaren Lebenspartnerin und Verlobten Karla, die mir in den stressigen und anspruchsvollen Phasen der Promotion zur Seite stand und auf die ich mich immer verlassen kann.

Erklärung

Hiermit erkläre ich, dass ich mich bisher keinem Promotionsverfahren unterzogen oder um dessen Zulassung beworben habe. Die eingereichte Dissertation wurde an keiner anderen Hochschule eingereicht.

Ich erkläre, dass ich die eingereichte Dissertation selbständig und ohne fremde Hilfe verfasst, andere als die von mir angegebenen Quellen und Hilfsmittel nicht benutzt und die den benutzten Werken wörtlich oder inhaltlich entnommenen Stellen als solche kenntlich gemacht habe.

Rostock, den 11.07.2025

Unterschrift: 

Jan-Oliver Saß

Article

Advanced Ti–Nb–Ta Alloys for Bone Implants with Improved Functionality

Jan-Oliver Sass ^{1,*}, Marie-Luise Sellin ¹, Elisa Kauertz ¹, Jan Johannsen ², Markus Weinmann ³,
Melanie Stenzel ³, Marcus Frank ^{4,5}, Danny Vogel ¹, Rainer Bader ^{1,5} and Anika Jonitz-Heincke ¹

¹ Research Laboratory for Biomechanics and Implant Technology, Department of Orthopaedics, Rostock University Medical Center, Doberaner Straße 142, 18057 Rostock, Germany;

marie-luise.sellin@med.uni-rostock.de (M.-L.S.); elisa.kauertz@uni-rostock.de (E.K.);

danny.vogel@med.uni-rostock.de (D.V.); rainer.bader@med.uni-rostock.de (R.B.);

anika.jonitz-heincke@med.uni-rostock.de (A.J.-H.)

² Fraunhofer Research Institution for Additive Manufacturing Technologies IAPT, Am Schleusenengraben 14, 21029 Hamburg, Germany; jan.johannsen@iapt.fraunhofer.de

³ TANIOBIS GmbH, Im Schleeke 78-91, 38642 Goslar, Germany; markus.weinmann@taniobis.com (M.W.); melanie.stenzel@taniobis.com (M.S.)

⁴ Medical Biology and Electron Microscopy Center, Rostock University Medical Center, Strempelstraße 14, 18057 Rostock, Germany; marcus.frank@med.uni-rostock.de

⁵ Department Life, Light and Matter, University of Rostock, 18051 Rostock, Germany

* Correspondence: jan-oliver.sass@med.uni-rostock.de; Tel.: +49-381-494-9338

Abstract: The additive manufacturing of titanium–niobium–tantalum alloys with nominal chemical compositions Ti–xNb–6Ta (x = 20, 27, 35) by means of laser beam powder bed fusion is reported, and their potential as implant materials is elaborated by mechanical and biological characterization. The properties of dense specimens manufactured in different build orientations and of open porous Ti–20Nb–6Ta specimens are evaluated. Compression tests indicate that strength and elasticity are influenced by the chemical composition and build orientation. The minimum elasticity is always observed in the 90° orientation. It is lowest for Ti–20Nb–6Ta (43.2 ± 2.7 GPa) and can be further reduced to 8.1 ± 1.0 GPa for open porous specimens ($p < 0.001$). Furthermore, human osteoblasts are cultivated for 7 and 14 days on as-printed specimens and their biological response is compared to that of Ti–6Al–4V. Build orientation and cultivation time significantly affect the gene expression profile of osteogenic differentiation markers. Incomplete cell spreading is observed in specimens manufactured in 0° build orientation, whereas widely stretched cells are observed in 90° build orientation, i.e., parallel to the build direction. Compared to Ti–6Al–4V, Ti–Nb–Ta specimens promote improved osteogenesis and reduce the induction of inflammation. Accordingly, Ti–xNb–6Ta alloys have favorable mechanical and biological properties with great potential for application in orthopedic implants.

Keywords: implant material; β -titanium alloy; mechanical properties; biological properties; laser beam powder bed fusion



Citation: Sass, J.-O.; Sellin, M.-L.; Kauertz, E.; Johannsen, J.; Weinmann, M.; Stenzel, M.; Frank, M.; Vogel, D.; Bader, R.; Jonitz-Heincke, A. Advanced Ti–Nb–Ta Alloys for Bone Implants with Improved Functionality. *J. Funct. Biomater.* **2024**, *15*, 46. <https://doi.org/10.3390/jfb15020046>

Academic Editors: Vadim Sheremetyev, Veronika Polyakova and Sergey Anikeev

Received: 8 January 2024

Revised: 8 February 2024

Accepted: 15 February 2024

Published: 17 February 2024



Copyright: © 2024 by the authors. Licensee MDPI, Basel, Switzerland. This article is an open access article distributed under the terms and conditions of the Creative Commons Attribution (CC BY) license (<https://creativecommons.org/licenses/by/4.0/>).

1. Introduction

Adequate mechanical properties, high corrosion resistance, biocompatibility, and sufficient osteogenesis are required for implant materials in direct bone contact [1]. Implants in direct contact with bone made of Ti–6Al–4V (values are always given in wt. %) have shown good long-term results in clinical use [2,3], though there is growing concern about potential damage to human cells from released aluminum and vanadium ions [2–5]. In addition, the mismatch in Young’s modulus between Ti–6Al–4V and human bone results in stress shielding of the adjacent bone stock, which, in the worst case, can lead to aseptic implant loosening [6]. To inhibit the release of cytotoxic metal ions into the human organism and to improve the mechanical fit between bone and implant, recent developments have focused

on low-modulus β -type titanium (Ti) alloys being composed exclusively of biocompatible components [4,7–14].

Biomedical β -type Ti alloys are typically formed in binary system Ti–Nb [7,13,15], ternary systems Ti–Nb–Ta [16–18], Ti–Nb–Zr [10], and Ti–Ta–Zr [19], and quaternary systems such as Ti–Nb–Ta–Zr [8,9,11,20] and Ti–Nb–Zr–Sn [21,22]. Entirely β -type Ti alloys may have a Young's modulus as low as 33 GPa [21], while Ti–6Al–4V has a Young's modulus of approximately 114 GPa [23]. Niobium and tantalum are particularly promising alloying elements. They stabilize the β -phase in Ti base alloys, form highly corrosion-resistant passive oxide layers, and are biocompatible [13,16,17,24–26].

In addition to the intrinsic material properties, processability is a key feature of implant materials. In this context, additive manufacturing (AM) technologies, such as laser beam powder bed fusion (PBF-LB/M), are becoming increasingly important for the fabrication of patient-specific bone implants [27–29] with open porous structures [30–33]. AM allows a high degree of design freedom in the development of new implants [27] but it must be taken into account that the layer-wise manufacturing process is highly anisotropic. Accordingly, additively manufactured parts may exhibit different properties if produced in different build orientations, influencing mechanical performance [15,22,34–37] and the biological response of human cells [38].

Ti–6Al–4V is by far the best-studied alloy system for application in AM of orthopedic and dental implants, and numerous reviews have been published on this topic [39–42]. The ultimate tensile strength (UTS) and elongation of additively manufactured Ti–6Al–4V varied in the range of approximately 850–1150 MPa and 3–20% [43], respectively, indicating sufficient strength and mostly also sufficient ductility. In addition, it has been observed that the rough surfaces typically formed in additively manufactured Ti–6Al–4V materials do not interfere with osteogenesis [38,44].

However, a critical issue is the material stiffness, i.e., lack of sufficient elasticity of Ti–6Al–4V, regardless of whether it was manufactured conventionally or additively. To overcome this issue, some of the above-mentioned β -type Ti alloys were recently examined for their suitability for AM. It turned out that the most relevant mechanical properties, such as strength and elasticity, were like those observed for conventionally processed materials [7,11,15,45]. Furthermore, the mechanical behavior of β -type Ti alloys can be tailored to achieve desired properties (e.g., low Young's modulus) by controlling relevant process parameters such as build direction and scanning speed [15,37]. In addition, PBF-LB/M parts possess surface characteristics that allow direct use as a bone implant, without the need of time- and cost-intensive post-processing strategies [28,38]. Since the surface topography is, among other parameters, influenced by the build orientation [38], understanding of its impact is mandatory.

Our intention was to perform a research study on the AM of highly bio-tolerant Ti base alloys. For this purpose, we chose the titanium–niobium–tantalum (Ti–Nb–Ta) alloy system in the Ti-rich domain, since relatively small changes in the Ti:Nb ratio have a significant effect on the phase formation and accordingly mechanical properties [46,47].

Pre-alloyed Ti–xNb–6Ta AM powders with $x = 20, 27, 35$ (wt. %) were prepared using the electrode induction melting inert gas atomization (EIGA) process and fully characterized. The powders were consolidated using PBF-LB/M, and the resulting specimens have been previously investigated for microstructure and tensile strength [18]. The present follow-up study aims to further determine the mechanical properties using compression tests, also considering the build orientation of the specimens in the AM process in 0° , 45° , and 90° . Furthermore, the biological response of cultivated human osteoblasts with specimens prepared in 0° and 90° build orientation was investigated. The results are compared to additively manufactured Ti–6Al–4V specimens. Finally, open porous Ti–20Nb–6Ta specimens with a face-centered cubic lattice-structure were additively manufactured to investigate the potential improvement of the bone-implant interaction compared with those printed fully dense.

2. Materials and Methods

2.1. Specimen Manufacturing by Laser Beam Powder Bed Fusion

Ti–Nb–Ta spherical powders with nominal chemical compositions of Ti–20Nb–6Ta, Ti–27Nb–6Ta, and Ti–35Nb–6Ta wt. % were produced by the EIGA process, which was conducted under purified argon (4.6, Linde GmbH, Pullach, Germany) atmosphere from pre-alloyed electrodes (TANIOBIS GmbH, Goslar, Germany). For details on the experimentally determined chemical composition, we refer to Johannsen et al. [18].

The raw Ti–Nb–Ta powder materials were sieved through 150 μm meshes, and the remaining powders were transferred into an air classifier for deagglomeration and the removal of fine particles < 10 μm to improve their handling, i.e., to avoid dusting during the manufacturing process and to improve flow properties. The remaining powder was sieved with ultrasonic vibration through 63 μm stainless steel mesh.

Particle size distributions (PSD) determined using a Master Sizer 2000 (Malvern, Worcestershire, UK) indicated that there is no evidence of particles <15 μm . D95 was between 63 μm and 69 μm for the different powders. In addition, a commercially available titanium grade 23 powder (Ti64-53/20, Tekna Plasma Europe, Macon, France) was used for manufacturing the reference Ti–6Al–4V specimens.

The Ti–Nb–Ta specimens were produced using a DMP350 Flex (3D Systems Corp., Rock Hill, SC, USA) equipped with a 1 kW single-mode laser (YLR-1000-WC-Y14, IPG Laser GmbH, Burbach, Germany), whereas Ti–6Al–4V was processed using a SLM500 Quad (Nikon SLM Solutions AG, Lübeck, Germany). Argon gas was used during fabrication to prevent oxidation. A stripe-based scanning strategy [18] was used with hatch distances of 69 μm for the Ti–Nb–Ta alloys and 100 μm for Ti–6Al–4V.

The process parameters for the AM of all Ti–Nb–Ta alloys were adopted from Johannsen et al. (Table 1) [18], providing specimens with densities >99.96% and microstructures with a homogeneous element distribution. Process parameters for AM of Ti–6Al–4V specimens were taken from an IAPT (Research Institution for Additive Manufacturing Technologies IAPT, Hamburg, Germany) database (Table 1). In addition, Ti–6Al–4V specimens were subjected to a stress relief annealing under vacuum (800 °C, 2 h). Such heat treatment was not required for the additively manufactured Ti–Nb–Ta specimens and was, therefore, not performed.

Table 1. Process parameters and resulting density during laser beam powder bed fusion of Ti–xNb–6Ta (x = 20, 27, 35) alloys and Ti–6Al–4V specimens and the resulting relative density shown as mean and standard deviation (in brackets).

Material	Scanning Speed [mm/s]	Laser Power [W]	Layer Thickness [mm]	Resulting Density [%]
Ti–20Nb–6Ta	1250	170	0.30	99.96 (0.01) ^a
Ti–27Nb–6Ta	1350	170	0.30	99.97 (0.01) ^a
Ti–35Nb–6Ta	1500	170	0.30	99.97 (0.01) ^a
Ti–6Al–4V	1200	240	0.60	>99.7 ^b

^a Density analysis of Ti–Nb–Ta alloys conducted by Johannsen et al. [18] with similar processing parameters and Ti–Nb–Ta powders. ^b Not specifically measured for this study, but typical value of the established process at the Fraunhofer Research Institution for Additive Manufacturing Technologies IAPT, Hamburg, Germany.

2.1.1. Specimens for Mechanical Characterization

Cylindrical specimens were fabricated at 0°, 45°, and 90° (90° corresponds to parallel orientation to the direction of construction) for compression testing of all dense Ti–Nb–Ta alloys using the process parameters described above. Accordingly, nine different groups were investigated: [Ti–20Nb–6Ta, Ti–27Nb–6Ta, Ti–35Nb–6Ta] \times [0°, 45°, 90°] with n = 5 specimens each.

Similar to a report by Schulze et al. [7], their dimensions were $d \times l = 10.7 \text{ mm} \times 16.0 \text{ mm}$ in the as-printed state. The specimens were milled to $d \times l = 6.9 \text{ mm} \times 10.4 \text{ mm}$

(Figure 1A). A black and white speckle pattern was applied to the surface of the specimens for local strain measurement using digital image correlation (DIC).

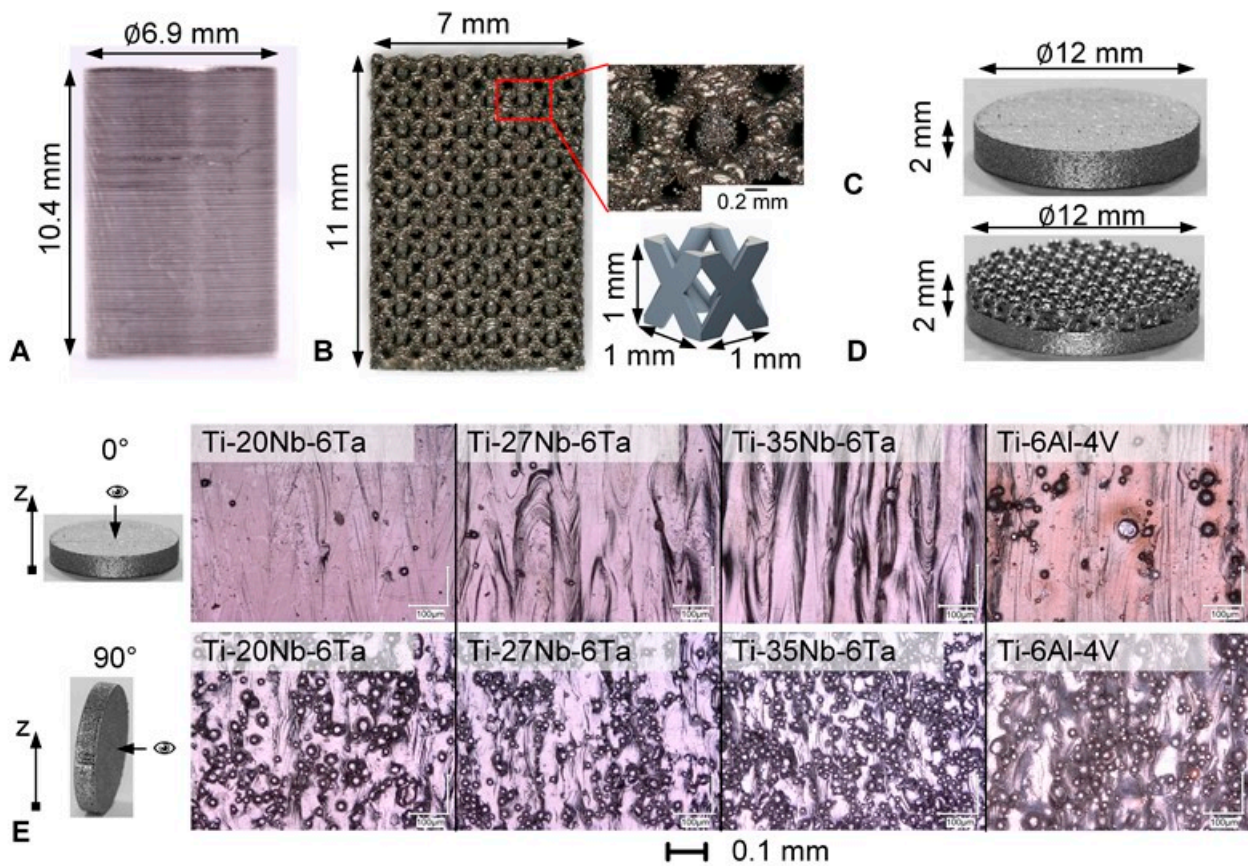


Figure 1. Overview of specimens manufactured by laser beam powder bed fusion for mechanical and biological characterization. (A) Machined, dense cylindrical specimens for mechanical characterization, (B) rectangular open porous lattice-structured specimen for mechanical characterization, magnified view of the structure and the CAD design of the face-centered cubic unit cell, (C) cylindrical dense specimens for biological characterization, (D) open porous lattice-structured specimen for biological characterization with one layer of the defined unit cells, and (E) digital microscopic images (200-times magnification) of as-printed surfaces in 0° and 90° build orientation (z indicating build direction) of the Ti-xNb-6Ta (x = 20, 27, 35) and Ti-6Al-4V specimens.

Open porous lattice-structured specimens were designed in Creo Parametrics 6.0.3.0 (PTC Inc., Boston, MA, USA) using a $1 \times 1 \times 1 \text{ mm}^3$ face-centered cubic unit cell with longitudinal struts comparable to Li et al. [30]. The strut diameter was 0.3 mm, and the resulting pore size was 0.6 mm, leading to a porosity of 70%. These values were designed based on previous studies where the defined pore size and porosity were reported to provide good osseointegration [33]. For the compression tests, n = 5 rectangular specimens ($7 \times 7 \times 11 \text{ mm}^3$) of Ti-20Nb-6Ta and Ti-6Al-4V were manufactured by PBF-LB/M. The rectangular specimens and the designed unit cell are shown in Figure 1B.

μ CT scans with a resolution of 9 μm were obtained (Skyscan1076, Bruker, Billerica, MA, USA) to define the porosity of the manufactured open porous specimens for mechanical characterization. The voltage and current were set at 95 kV and 104 μA , and a 0.5 mm aluminum filter was used. The porosity of the specimens was measured using Materialise Mimics 25.0 (Materialise NV, Leuven, Belgium). In addition, strut thickness and pore size were measured using a digital microscope (VHX-6000, Keyence Corporation, Osaka, Japan) at 10 different locations (5 on frontal and 5 on top view) on each specimen. Since the manufacturing of the Ti-20Nb-6Ta specimens resulted in an increase in strut thickness and

corresponding decrease in pore size and total porosity, the Ti-6Al-4V specimens had to be adjusted (strut diameter of 0.39 mm) to have an almost similar geometry for comparability of the results. The measured geometric parameters are shown in Table 2.

Table 2. Measured dimensions as mean value and standard deviation (in brackets) of the strut thickness and pore size (each in frontal and top view) as well as the porosity measured by μ CT scans of the open porous lattice-structured Ti-20Nb-6Ta and Ti-6Al-4V specimens.

Material	Strut Thickness [mm]				Pore Size [mm]				Porosity [%]	
	Front		Top		Front		Top			
Ti-20Nb-6Ta	0.47	(0.04)	0.43	(0.05)	0.47	(0.06)	0.54	(0.05)	49.47	(0.49)
Ti-6Al-4V	0.44	(0.02)	0.46	(0.02)	0.58	(0.02)	0.55	(0.02)	47.36	(1.30)

2.1.2. Specimens for Biological Characterization

The biological characterization was performed with both densely and open porous lattice-structured specimens. Cylindrical dense specimens ($d = 12$ mm, $h = 2$ mm) were fabricated in 0° and 90° build orientation, leading to six different groups [Ti-20Nb-6Ta, Ti-27Nb-6Ta, Ti-35Nb-6Ta] \times [$0^\circ, 90^\circ$] with $n = 38$ specimens each. Additionally, specimens made of Ti-6Al-4V serving as a reference were manufactured in 0° and 90° build orientations. The surfaces were not further processed and are referred to as “as-printed” in the following. Open porous lattice-structured specimens were manufactured consisting of one layer of the above-described face-centered cubic unit cells (Figure 1D). Accordingly, the specimens were 12 mm in diameter and 2 mm in height, i.e., 1 mm of dense structure and 1 mm of open porous lattice structure. Prior to their biological testing, all specimens were cleaned in an ultrasonic bath to remove residual powder and heat-sterilized at 180°C for 135 min.

The surface roughness of the dense specimens was analyzed with a laser-scanning microscope (VK-X250, Keyence Germany GmbH, Neu-Isenburg, Germany) with 20 times magnification, $\lambda_S = 8$, and $\lambda_C = 25$. The roughness values are summarized in Table 3, and light microscopic images are shown in Figure 1E. The light microscopic images demonstrated melt tracks and partly melted particles on the surface.

Table 3. Measured surface roughness (Ra: average roughness, Rz: arithmetical mean deviation of the profile) of the specimens for biological characterization in 0° and 90° build orientation (BO) shown as mean and standard deviation (in brackets).

Material	Ti-20Nb-6Ta		Ti-27Nb-6Ta		Ti-35Nb-6Ta		Ti-6Al-4V									
	BO [$^\circ$]		0	90	0	90	0	90								
Ra [μm]	4.0	(0.7)	5.7	(0.8)	6.6	(1.3)	8.0	(2.0)	9.0	(1.9)	8.6	(1.6)	5.9	(0.9)	11.6	(1.0)
Rz [μm]	34.7	(8.1)	47.9	(5.2)	56.2	(13.7)	63.5	(9.7)	77.1	(16.3)	68.9	(9.8)	68.1	(11.7)	103.5	(18.3)

2.2. Microstructural Characterization

In a previous study, the microstructure of the Ti-Nb-Ta alloys was described in detail [18]. Here we give a brief summary of the main findings, as they are crucial for understanding the present observations. Furthermore, the microstructure as a function of the orientation in the build chamber was studied by backscattered electron analysis (BSA). In addition, energy-dispersive X-ray spectroscopy (EDX) images of Ti-27Nb-6Ta in 0° and 90° orientation are shown in Figure A1 to illustrate the chemical homogeneity.

2.3. Mechanical Characterization

The cylindrical specimens were compressively loaded with 0.005 mm/s in a universal testing machine (100 kN Landmark[®], MTS Systems Corporation, Eden Prairie, MN, USA).

The test was terminated when the specimen failed (drop in the force–displacement curve) or when a compressive stress of 1900 MPa was reached. Furthermore, the elongation in load direction was measured using a 2D-DIC system (camera: isi-sys GmbH, Kassel, Germany; image recording: ViC Snap, Correlated Solutions Inc, Irmo, SC, USA), and the data were analyzed in GOM Suite 2021 (Carl Zeiss GOM Metrology GmbH, Braunschweig, Germany). The DIC-based elongation was used to calculate the compressive modulus (C in GPa). In addition, the compressive yield strength at 0.2% plastic strain ($\sigma_{C,0.2}$ in MPa), the ultimate compression strength (UCS), plastic elongation at break (ϵ_B in %), and the elastic admissible strain (EAS) were evaluated. The EAS is defined as an indicator of mechanical biofunctionality and was calculated as the ratio of the yield strength to the modulus [10,15]. This parameter has been used previously and is recommended for assessing the suitability of an implant material from a mechanical point of view [10,15]. Representative areas of the fracture surfaces were analyzed by a field emission scanning electron microscope (SEM, MERLIN[®] VP Compact, Co. Zeiss, Oberkochen, Germany). The specimens were mounted on an Al-SEM carrier with adhesive conductive carbon tape (Plano GmbH, Wetzlar, Germany).

The open porous lattice-structured specimens were compressively loaded until failure using a universal testing machine (Z050-50kN, Zwick Roell, Ulm, Germany) with a crosshead speed of 0.005 mm/s. Force–displacement curves were obtained using a tactile extensometer (digiClip Extensometer, Zwick Roell, Ulm, Germany), and mechanical properties were evaluated similar to those of densely manufactured specimens. For the calculation, the nominal cross-section of $7 \times 7 \text{ mm}^2$ was used. The apparent stiffness of the open porous lattice-structured specimens is further designated as compressive modulus.

2.4. Biological Characterization

2.4.1. Cell Biological Experiments

The biological characterization of dense and open porous lattice-structured specimens was performed with eight independent human osteoblast cell cultures (female: $n = 4$, mean age: 77 ± 3.7 years; male: $n = 4$, mean age: 78 ± 2.4 years). The local ethics committee approved the collection of cells after written informed consent of the patients (ethical approval of University of Rostock from 12/06/2018, registration no.: A2010-0010). The protocols for cell isolation from the cancellous bone of femoral heads of patients undergoing primary hip replacement and subsequent cultivation were previously reported [48]. Human osteoblasts from passage 4 were used for experiments. For this purpose, the cells were cultivated under standard cell culture conditions in a humidified atmosphere of 37°C and 5% CO_2 in calcium-free Dulbecco's Modified Eagle Medium (DMEM) containing 10% fetal calf serum (FCS; both: PAN-Biotech, Aidenbach, Germany), 1% amphotericin B, 1% penicillin–streptomycin, and 1% HEPES buffer (all: Sigma-Aldrich, Munich, Germany). To maintain the osteogenic phenotype, 10 mM β -glycerophosphate, $50 \mu\text{g} \times \text{mL}^{-1}$ ascorbic acid, and 100 nM dexamethasone were added to the cell culture medium (all: Sigma-Aldrich, Munich, Germany). Each cell number of 250,000 cells per 50 μL cell culture medium was seeded on top of the cleaned and sterilized specimens, allowing initial adherence over 30 min. Afterward, the cell-seeded specimens were incubated with 1 mL cell culture medium with additives as described before. To enhance the mineralization capacity of the human osteoblasts, the cell culture medium was supplemented with calcium chloride dehydrate ($\text{CaCl}_2 \cdot 2 \times \text{H}_2\text{O}$, final concentration: $1.8 \text{ mmol} \times \text{L}^{-1}$). The cultivation of osteoblasts on the dense and open porous specimens was conducted over 7 and 14 days. In the latter case, the medium was changed after 7 days.

To analyze the cell spreading after 7 days on the surface of densely manufactured specimens, the samples were washed with phosphate-buffered saline (PBS; Biochrom AG, Berlin, Germany), and cells were fixed with fixation buffer (1% paraformaldehyde, 2.5% glutaraldehyde, 0.1 M sodium phosphate buffer, pH 7.3) and stored at 4°C . Fixed samples were washed with sodium phosphate buffer (0.1 M) and subsequently dehydrated in an ascending series of ethanol prior critical point drying using CO_2 as an intermedium

(Emitech K850, Quorum Technologies LTD, East Sussex, UK). The specimens were sputter coated with a thin layer of gold with a thickness of approximately 15 nm under vacuum in an argon atmosphere (SCD 500 Leica, Wetzlar Germany). Using a field emission scanning electron microscope (MERLIN VP Compact, Carl Zeiss, Oberkochen Germany), the surface spreading of osteoblasts was imaged from selected regions (applied detector: HE-SE2; accelerating voltage 10.0 kV and 5.0 kV, working distance 3.9 mm).

2.4.2. Analysis of Cell Mediators Involved in Bone Formation, Remodeling, and Inflammation

The biological response of human osteoblasts on the specimens was characterized after 7 and 14 days of cultivation. Different mediators involved in osteogenesis, bone remodeling, and inflammation were analyzed by quantifying specific mRNA transcripts or by quantifying secreted proteins in the supernatants.

For gene expression analyses, the RNA of cells seeded on top of the specimens was isolated with the innuPREP RNA Mini Kit 2.0 (Analytik Jena, Jena, Germany) according to the manufacturer’s instructions. Only for cell lysis was the protocol modified with regard to a more prolonged incubation with the lysis buffer. Here, the osteoblasts have been lysed for 15 min under constant shaking to enhance the quality of isolated RNA. Before RNA was transcribed into cDNA using the High-Capacity cDNA Reverse Transcription Kit (Applied Biosystems, Foster City, CA, USA) according to the manufacturer’s instructions, its concentration was measured with a microplate reader and the NanoQuant™ Plate (both: Tecan Trading AG, Maennedorf, Switzerland). Afterward, 50 ng (for the dense specimens) or 100 ng (for the open porous specimens) RNA was used for the reverse transcription protocol (total volume of RNA and Mastermix was 20 µL). The PCR was performed using the following protocol: 10 min at 25 °C, 120 min at 37 °C, and 5 min at 85 °C in a thermocycler (Analytik Jena, Jena, Germany). Finally, all samples were diluted with 20 µL of RNase-free water and stored at –20 °C until further use.

Relative quantification of gene expression of defined genes was determined with the innuMIX qPCR DSGreen Standard in a qTower 2.0 (both: Analytik Jena AG, Jena, Germany). All primers used for analysis are listed in Table 4.

Table 4. Overview of the genes of interest and their primer sequences.

Primer	Sequences (5′–3′)
Actin Beta (<i>ACTB</i>)	fwd: CTCCTGGGCATGGAGTC rev: AGCACTGTGTTGGCGTACAG
Alkaline Phosphatase, Biomineralization Associated (<i>ALPL</i>)	fwd: CATTGTGACCACCACGAGAG rev: CCATGATCACGTC AATGTCC
Bone Gamma-Carboxyglutamate Protein (<i>BGLAP</i>)	fwd: TCAGCCAACTCGTCACAGTC rev: GGTGCAGCCTTTGTGTCC
Collagen Type I Alpha 1 Chain (<i>COL1A1</i>)	fwd: ACGAAGACATCCCACCAATC rev: AGATCACGTCATCGCACAAC
Interleukin 6 (<i>IL6</i>)	fwd: TGGATTCAATGAGGAGACTTGCC rev: CTGGCATTGTGGTTGGGTC
Matrix Metalloproteinase 1 (<i>MMP1</i>)	fwd: AGAGCAGATGTGGACCATGC rev: TCCCGATGATCTCCCCTGAC
Runt-related Transcription Factor 2 (<i>RUNX2</i>)	fwd: CGCCTCACAACAACCACAG rev: ACTGCTTGCAGCCTTAAATGAC
Secreted Phosphoprotein 1, Osteopontin (<i>SPP1</i>)	fwd: AACGCCGACCAAGGAAAAC rev: GCACAGGTGATGCCTAGGAG
Secreted protein acidic and rich in cysteine, Osteonectin (<i>SPARC</i>)	fwd: CTGGACTACATCGGGCCTTG rev: ATGGATCTTCTTACCCGCAG
Tissue inhibitor of metalloproteinase-1 (<i>TIMP1</i>)	fwd: ATTGCTGGAAAAC TGCAGGATG rev: GTCCACAAGCAATGAGTGCC

For each gene of interest, a master mix with the respective forward and reverse primer at 0.5 µL each, 3 µL of distilled water, and 5 µL of innuMIX qPCR DSGreen was prepared.

Afterward, 1 μL of template cDNA was pipetted onto the bottom of a 96-well PCR plate in duplicates, and a volume of 9 μL of the master mix was added. RNase-free water served as a negative control. The PCR plate was sealed, and qPCR followed the protocol: 2 min at 95 °C, 40 cycles of 5 s at 95 °C, and 25 s at 60 °C. A cycle threshold (Ct) of 30 was set as the interpretation limit. The $\Delta\Delta\text{Ct}$ method was performed using the Equation (1), where $\Delta\Delta\text{Ct}$ values are depicted as $2^{-\Delta\Delta\text{Ct}}$.

$$\Delta\Delta\text{Ct} = \Delta\text{Ct}_{\text{Ti-xNb-6Ta}} - \Delta\text{Ct}_{\text{Ti-6Al-4V}} \quad (1)$$

The amount of secreted proteins in the supernatants was determined via enzyme-linked immunosorbent assays. Specifically, the protein levels of cross-linked C-telopeptides of type I collagen (CICP, MicroVue Quidel, San Diego, CA, USA), interleukin (IL-) 6, and IL-8 (Thermo Fisher Scientific Inc., Waltham, MA, USA) were quantified according to the manufacturer's instructions. Absorbance was measured at 405 nm (CICP) or 450 nm (IL-6, IL-8) using a microplate reader (Tecan Trading AG, Maennedorf, Switzerland). Defined standard curves were used to calculate the protein concentrations, respectively. Finally, the protein concentration of the samples was related to the total protein content, which was determined with the Qubit Protein Assay Kit and Qubit 1.0 (both: Invitrogen, Waltham, MA, USA).

2.5. Statistical Evaluation

The statistical analysis and graphical illustration were performed in GraphPad Prism 9.2 (GraphPad Software, San Diego, CA, USA). Unless otherwise noted, data are presented as single values with median and interquartile range (figures) or mean and standard deviation (tables). Compression test results of $n = 5$ specimens for each group were tested for significance using the Mann–Whitney U test. Pairwise comparisons were made for each alloy according to build orientation and for each build orientation according to niobium content (e.g., Ti–20Nb–6Ta 0° vs. Ti–20Nb–6Ta 45° and vs. Ti–20Nb–6Ta 90°; Ti–20Nb–6Ta 0° vs. Ti–27Nb–6Ta 0° and vs. Ti–35Nb–6Ta 0°). For the biological analyses, a minimum of four different osteoblastic donors was used, and comparisons between experimental groups were performed using a paired or unpaired *t*-test. The level of significance was $p < 0.05$ for all tests.

3. Results

3.1. Microstructure Characterization

A detailed study on the chemical composition (Energy-dispersive X-ray spectroscopy, EDS) and phase composition (X-Ray diffraction analysis) of Ti–20Nb–6Ta, Ti–27Nb–6Ta, and Ti–35Nb–6Ta has already been published in [18]. All three Ti–Nb–Ta alloys possess a homogenous element distribution, which was also observed in specimens of this present study (see Appendix A for an example). In line with pure Nb, Ti–35Nb–6Ta revealed reflections attributed to the bcc β -phase. Increasing the Ti content leads to significant changes in the phase constitution and the appearance of more complicated diffraction patterns. While the reflections in the diffractogram of Ti–27Nb–6Ta could not be assigned unequivocally to specific phases, those of Ti–20Nb–6Ta clearly indicated the formation of an orthorhombic α'' -phase. It was supposed that, accordingly, the microstructure of Ti–27Nb–6Ta contains both α'' - and β -phase shares. A comparison of the microstructure using light microscopy visualized another difference in Ti–20Nb–6Ta on the one hand and Ti–27Nb–6Ta as well as Ti–35Nb–6Ta on the other hand. While the latter displayed typical features of additively manufactured specimens, c.f. melt pool boundaries and elongated columnar grains in build direction, the light microscopic images of Ti–20Nb–6Ta additionally exhibited platelet-like structures. However, those could not be differentiated by means of energy-dispersive X-ray spectroscopy.

The BSA images of Ti–20Nb–6Ta, Ti–27Nb–6Ta, and Ti–35Nb–6Ta additively built in 0° and 90° direction shown in Figure 2 confirm the previous observations from the light microscopic investigations. The chemical, i.e., phase composition, has a significant

influence on the morphology of the additively manufactured samples. Regardless of the chemical composition, melt pool boundaries, indicated by white triangles, are clearly visible in both 0° and 90° build orientations. In addition, the 90° images show elongated columnar grains oriented along the build orientation (grain boundaries are indicated by white dotted lines), reflecting the high anisotropy of the AM process due to epitaxial solidification. In contrast to Ti-27Nb-6Ta and Ti-35Nb-6Ta, the microstructure of Ti-20Nb-6Ta additionally shows plate-like segregations, which is fully consistent with the observations made by light microscopy [18]. Their size is difficult to determine from the available BSE images, but their thickness can be estimated to be 1–2 μm.

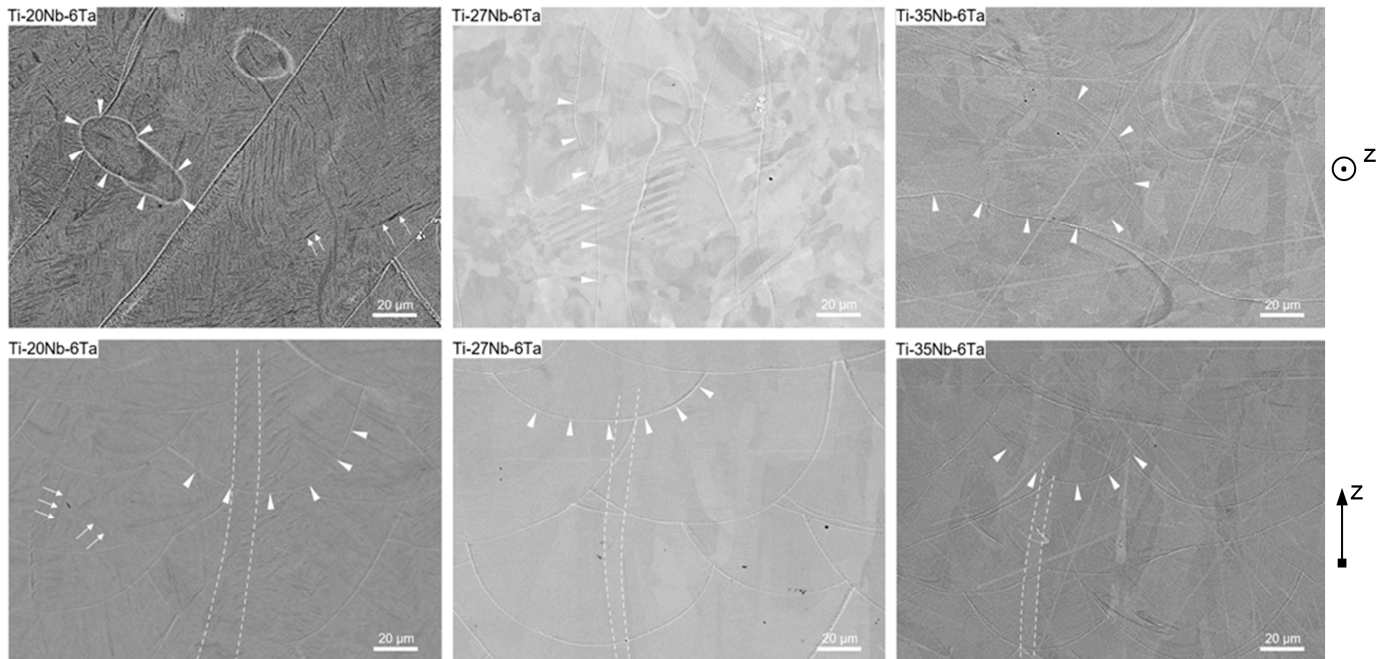


Figure 2. Backscattered electron analysis (BSE) of Ti-20Nb-6Ta, Ti-27Nb-6Ta, and Ti-35Nb-6Ta additively built in 0° (top) and 90° direction (bottom). Platelet-like structures (only Ti-20Nb-6Ta), elongated (columnar) grains (in 90°) and melt pool boundaries are highlighted by white arrows, dotted lines, and white triangles, respectively. The BSE images of Ti-35Nb-6Ta also feature scratches, which could not be removed by polishing.

3.2. Mechanical Characterization by Compression Testing

Stress–strain curves of one dense and one open porous specimen, representative of each group, are shown in Figure 3A. Specimens containing 20 wt. % and 27 wt. % of niobium fractured at ~45° to the load axis. Ti-35Nb-6Ta specimens did not fracture up to 1900 MPa compressive stress applied. Dimples and cleavage facets were observed on the fracture surfaces of Ti-20Nb-6Ta (Figure 3B,C), indicating the mixed behavior of ductile failure and brittle fracture, respectively. Only the fracture surfaces of the 0° and 45° Ti-20Nb-6Ta specimens could be examined, as the fractured parts of the other specimens adhered to each other, although the macroscopic fracture was visible. The open porous lattice-structured specimens also fracture at ~45° to the load axis, and the fractured pieces adhered to each other. Open porous Ti-20Nb-6Ta specimens showed ductile behavior with a pronounced plateau after yielding. In contrast, open porous Ti-6Al-4V specimens were less ductile with stepwise fracture of the lattice structure (Figure 3A).

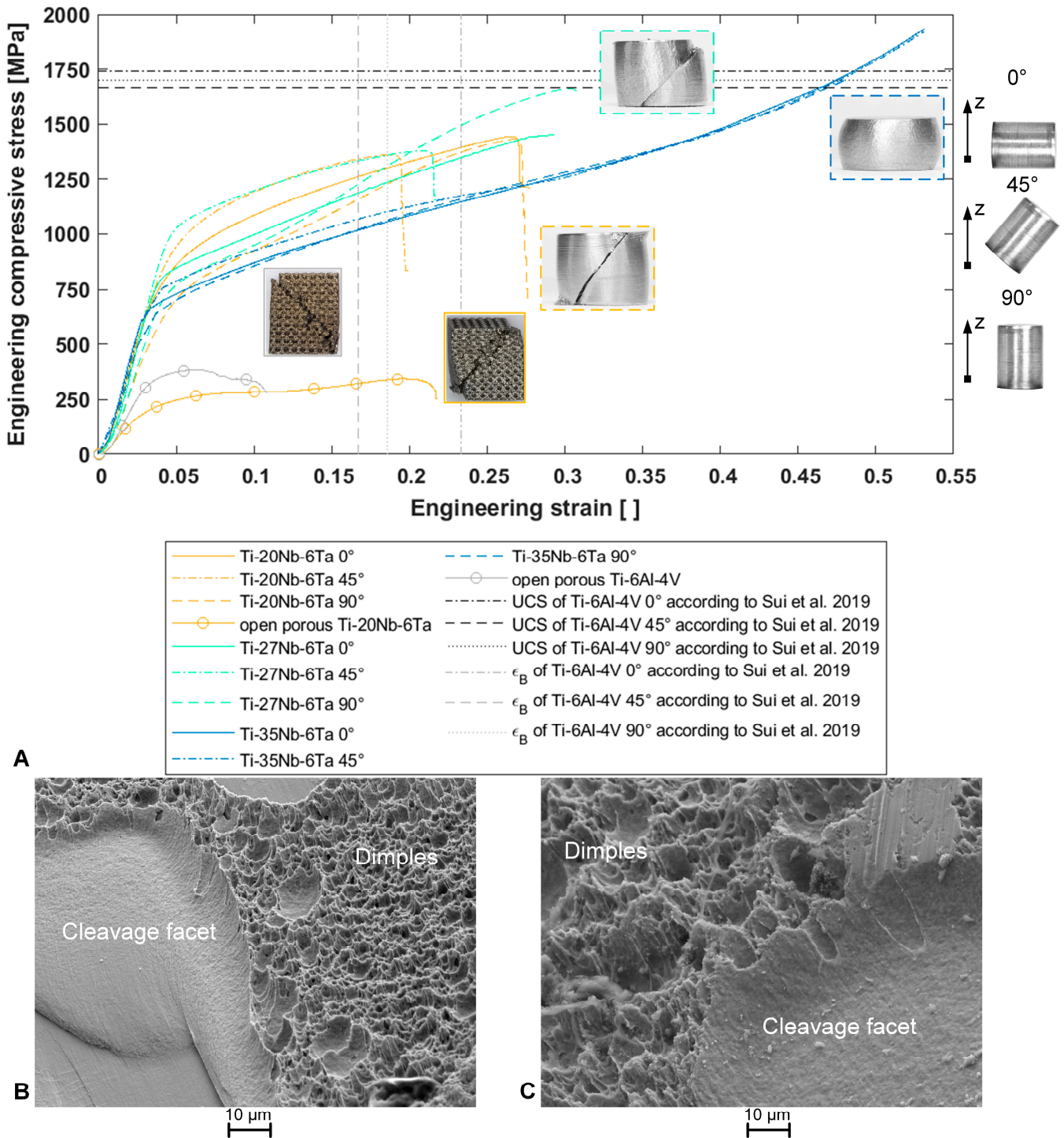


Figure 3. (A) Representative stress–strain curves and fracture images of dense Ti- x Nb-6Ta ($x = 20, 27, 35$) specimens in different build orientations ($0^\circ, 45^\circ, 90^\circ$) and open porous lattice structured Ti-20Nb-6Ta and Ti-6Al-4V specimens, where all specimens were manufactured by laser beam powder bed fusion of pre-alloyed spherical powders. Ultimate compressive strength (UCS) and elongation at break (ϵ_B) of Ti-6Al-4V in different build orientations according to Sui et al., 2019 [31] are shown for comparison, and the right image illustrates the orientation of the specimens in the build chamber (z : build direction). (B,C) Exemplary fracture images obtained by field emission scanning electron microscopy of the fracture surfaces at $1000\times$ magnification of dense Ti-20Nb-6Ta specimens in (B) 0° and (C) 45° build orientation.

Both the alloy composition, i.e., Ti:Nb ratio and the build orientation, affected the mechanical properties of the Ti-Nb-Ta alloys. The experimentally determined mechanical properties are graphically presented in Figure 4 and exact values of the mechanical properties, including mean and standard deviation and calculated elastic admissible strains, are given in Table 5.

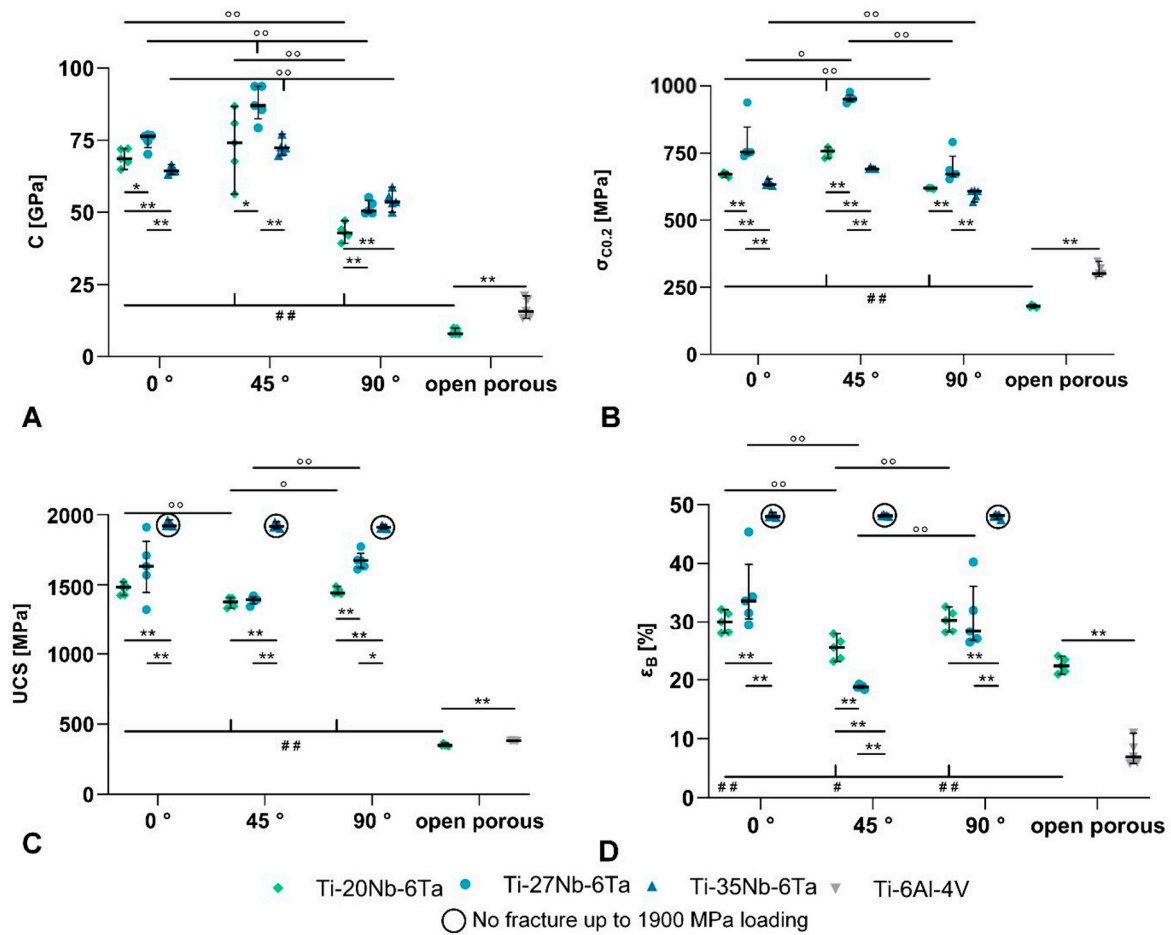


Figure 4. Measured compressive mechanical properties. (A) C: compression module, (B) $\sigma_{C0.2}$: compressive yield strength, (C) UCS: ultimate compressive strength, and (D) ϵ_B : elongation at break of the dense Ti-xNb-6Ta (x = 20, 27, 35) alloys additively manufactured by laser beam powder bed fusion in 0°, 45°, and 90° build orientation as well as the open porous lattice-structured Ti-20Nb-6Ta and Ti-6Al-4V specimens. Results of the pairwise Mann-Whitney U tests (n = 5) are indicated as follows: ° $p < 0.05$, °° $p < 0.01$ (effect of build direction); * $p < 0.05$, ** $p < 0.01$ (effect of material); # $p < 0.05$, ## $p < 0.01$ (effect of specimen structure).

For each alloy, the compressive modulus and yield strength as a function of the build orientation can be ordered as follows: $90^\circ < 0^\circ < 45^\circ$. Accordingly, the Ti-20Nb-6Ta in 90° build orientation showed the highest elastic admissible strain. The ultimate compressive strength and elongation at the breaks of Ti-20Nb-6Ta and Ti-27Nb-6Ta were minimal in 45° build orientation, and parameters increased with the niobium content. Also, for these two alloys, specimens manufactured in 45° build orientation showed the lowest strength and elongation at break, whereas small differences were visible between 0° and 90° build orientation. Ti-35Nb-6Ta showed a dissimilar behavior, the highest yield strength in 45° build orientation, and no fracture in all build orientations until a maximum compressive stress of 1900 MPa.

Table 5. Mechanical properties (C: compression module, $\sigma_{C0.2}$: compressive yield strength, UCS: ultimate compressive strength, ϵ_B : elongation at break, EAS: elastic admissible strain as ratio of $\sigma_{C0.2}$ to C) of the dense Ti-xNb-6Ta (x = 20, 27, 35) alloys additively manufactured by laser beam powder bed fusion in 0°, 45°, and 90° build orientation (BO) as well as of open porous lattice-structured Ti-20Nb-6Ta and Ti-6Al-4V specimens.

Nb [wt. %]	BO [°]	C [GPa]	$\sigma_{C0.2}$ [MPa]	UCS [MPa]	ϵ_B [%]	EAS []
Densely manufactured						
20	0	69.0 (2.7)	670.1 (6.3)	1467.8 (37.1)	29.9 (1.9)	0.97 (0.03)
	45	73.2 (10.6)	751.8 (15.6)	1374.6 (30.2)	25.3 (1.7)	1.05 (0.17)
	90	43.1 (2.6)	619.1 (2.0)	1453.3 (21.0)	30.2 (1.7)	1.44 (0.09)
27	0	74.9 (2.5)	787.3 (76.1)	1629.1 (191.8)	34.9 (5.5)	1.05 (0.11)
	45	87.9 (5.4)	954.4 (13.6)	1389.6 (23.9)	18.8 (0.3)	1.09 (0.07)
	90	51.7 (2.1)	695.1 (49.1)	1673.6 (55.7)	30.8 (5.1)	1.35 (0.11)
35 ^a	0	64.5 (1.1)	636.7 (8.2)	-	48.1 (0.3)	0.99 (0.02)
	45	72.6 (2.5)	693.4 (3.1)	-	48.1 (0.1)	0.96 (0.03)
	90	54.2 (2.9)	597.2 (17.0)	-	48.1 (0.3)	1.12 (0.02)
Open porous lattice-structured						
Ti-20Nb-6Ta		8.7 (1.0)	179.2 (4.5)	351.7 (7.5)	22.5 (1.0)	0.48 (0.07)
Ti-6Al-4V		16.7 (3.2)	312.0 (20.0)	381.7 (2.0)	7.63 (1.9)	0.53 (0.08)

^a No fracture up to ~1900 MPa compressive stress applied.

The compressive modulus of open porous lattice-structured Ti-20Nb-6Ta specimens compared to dense Ti-20Nb-6Ta specimens was reduced from 61.7 ± 12.9 GPa (averaged over different build orientations) to 8.7 ± 1.0 GPa. Open porous Ti-20Nb-6Ta specimens showed significantly lower compressive modulus and strength values but increased ductility compared to similar Ti-6Al-4V specimens.

3.3. Biological Characterization

Within the biological characterization, the influence of the chemical composition, build orientation during PBF-LB/M, and cultivation time was considered.

Regarding the influence of the build orientation of the Ti-Nb-Ta specimens on cell growth, it is evident that the cell settlement depends on it (Figure 5A). Scanning electron microscopy showed that the surfaces manufactured perpendicular to the building direction (0°) appeared smoother. Here, the osteoblasts, when examined in areas of high cell counts, had an elongated and spindle-shaped appearance and were located close together in clusters. This growth behavior of the cells resulted in a low degree of cell spreading and incomplete coverage of the surface. In contrast, cells exhibited a flat, stretched-out morphology on the surfaces of specimens manufactured in 90° build orientation, covering most of the material surface area. The surface morphology of specimens manufactured in 0° and 90° build orientation showed differences, i.e., 90° specimens showed a higher amount of partly melted particles on the surface. These were firmly attached to the surface and were caused by incomplete melting during the PBF-LB/M process. These elevations were clearly surrounded by the cells. Comparing the respective alloys with each other, it is noticeable that cell spreading on Ti-20Nb-6Ta was more pronounced than on Ti-27Nb-6Ta and Ti-35Nb-6Ta. Finally, osteoblasts seeded on Ti-6Al-4V samples for comparison showed a large number of round cells for both build orientations, with the 90° build orientation having a greater influence.

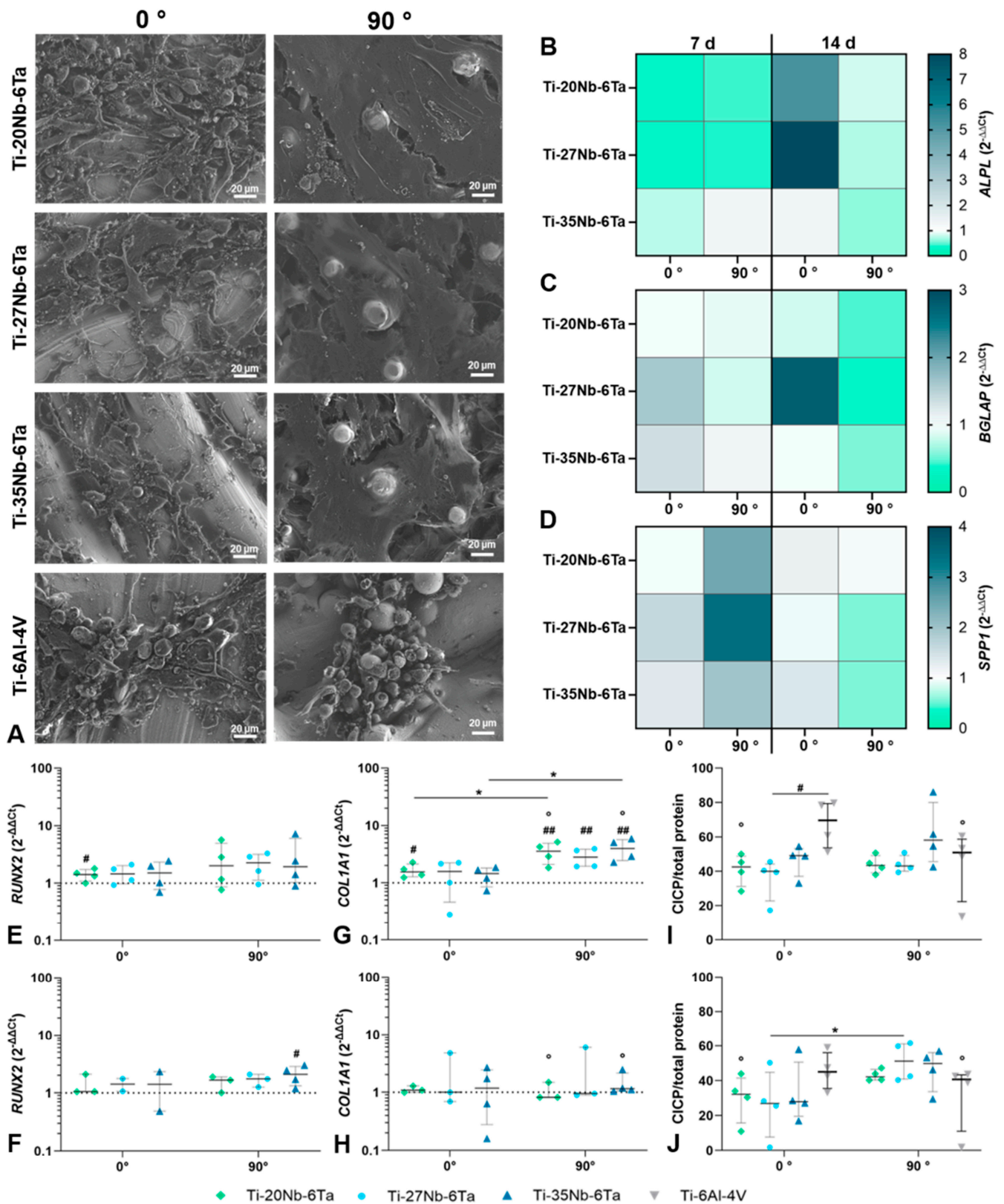


Figure 5. Biological characterization of the dense Ti-xNb-6Ta (x = 20, 27, 35) or Ti-6Al-4V specimens under consideration of cell spreading and induction of osteoblastic differentiation. (A) The population of the surfaces of the specimens with 0° and 90° build orientation with human osteoblasts

was determined after seven days via field emission scanning electron microscopy. Bar corresponds to 20 μm . (B–J) The differentiation capacity of human osteoblasts on the different surfaces of specimens was determined via gene expression analyses and quantification of C1CP after seven and fourteen days. (B–D) Heatmaps of ALPL, BGLAP, and SPP1 gene expression. Color coding corresponds to the median of at least two independent pre-osteoblast donors, with a white background corresponding to the gene expression level of osteoblasts on Ti-6Al-4V (“1”). A downregulated gene expression rate is displayed in green, with “0” corresponding to only low expression. Conversely, up-regulation is highlighted with a blue color code. (E–H) Gene expression levels of RUNX2 and COL1A1 after seven (E,G) and fourteen days (F,H). Data are depicted as individual values with median, minimum, and maximum ($n \geq 2$). Gene expression rates of osteoblasts on Ti-6Al-4V specimens served as controls (dotted line at “1”). (I,J) Protein amount of cross-linked C-telopeptides of Type 1 collagen (C1CP) after seven (I) and fourteen days (J) related to total protein (ng/mg, $n = 4$). Statistical significance was determined via unpaired (gene expression) and paired (protein quantification) *t*-test with * $p < 0.05$ (effect of build orientation); # $p < 0.05$, ## $p < 0.01$ (effect of the Ti alloy); ° $p < 0.05$ (effect of cultivation time).

In addition to the cell spreading on the surface of the specimens, the build orientation and the cultivation time significantly affected the gene expression profile of osteogenic differentiation markers. For ALP, BGLAP, and SPP1, differences to the Ti-6Al-4V control were apparent, but no statistical differences were shown by the build orientation or cultivation time due to a high donor variability (Figure 5B–D). RUNX2 mRNA was induced on the Ti-Nb-Ta specimens after 7 d of cultivation without differences between build orientations (Figure 5E,F). However, after 14 days, a trend of reduced RUNX2 mRNA was more present in osteoblasts cultivated on 0° build orientation specimens. Regarding the gene expression influenced by the niobium content, a significant induction of RUNX2 was observed for Ti-20Nb-6Ta after 7 d ($p = 0.0411$ compared to Ti-6Al-4V) and for Ti-35Nb-6Ta after 14 d ($p = 0.0158$ compared to Ti-6Al-4V). The gene expression of COL1A1 was significantly influenced by the build orientation and cultivation time. After 7 d of cultivation, compared to osteoblasts on Ti-6Al-4V references, a significant increase in COL1A1 mRNA was determined for Ti-20Nb-6Ta with 0° build orientation ($p = 0.0118$) and for all Ti-xNb-6Ta specimens with 90° build orientation ($p = 0.0019$ [Ti-20Nb-6Ta], $p = 0.0021$ [Ti-27Nb-6Ta], $p = 0.0011$ [Ti-35Nb-6Ta]). In osteoblasts cultivated on Ti-20Nb-6Ta ($p = 0.0350$) and Ti-35Nb-6Ta ($p = 0.0133$), a significantly higher gene expression rate in 90° was present compared to 0° build orientation. After 14 d, the COL1A1 mRNA was on the same transcript level as those for Ti-6Al-4V. This reduction was significantly different for osteoblasts cultivated on Ti-20Nb-6Ta ($p = 0.0129$) and Ti-35Nb-6Ta ($p = 0.0148$) specimens (Figure 5G,H). The release of the cross-linked C-telopeptides of Type 1 collagen (C1CP) was reduced in osteoblasts cultivated on Ti-xNb-6Ta after 7 d compared to those on Ti-6Al-4V (Figure 5I). This reduction was significant for osteoblasts on Ti-27Nb-6Ta 0° build orientation ($p = 0.0110$). After 14 days, a decreased release of C1CP was apparent for osteoblasts cultivated on 0° specimens. In contrast, on 90° samples, C1CP synthesis rates remained stable except for osteoblasts on Ti-6Al-4V with significantly reduced C1CP protein levels ($p = 0.0126$ compared to 7 d, Figure 5J). Significantly higher C1CP protein was determined for osteoblasts cultivated on Ti-27Nb-6Ta specimens with 90° compared to 0° build orientation ($p = 0.0477$).

Gene expression analysis was further used to determine the bone-destructive metalloprotease MMP1 and its natural inhibitor TIMP1. The induction of MMP1 mRNA after 7 days was particularly influenced by the build orientation (Figure 6A). While in specimens with 0° orientation, increased values were found for osteoblasts cultivated on Ti-20Nb-6Ta and Ti-27Nb-6Ta, cells on 90°-oriented samples showed significantly reduced gene expression ($p = 0.0184$ [Ti-20Nb-6Ta compared to Ti-6Al-4V], $p = 0.0250$ [Ti-27Nb-6Ta compared to Ti-6Al-4V]). A significant difference between the build orientations was only detected for Ti-20Nb-6Ta ($p = 0.0239$). Furthermore, MMP1 was not affected on Ti-35Nb-6Ta test samples in 0° orientation, whereas a non-significant reduction was detected on 90° specimens (Figure 6A). After 14 days, a similar trend was observed to that observed

after 7 days (Figure 6B). *MMP1* gene expression was significantly increased on Ti-20Nb-6Ta ($p = 0.0018$) specimens with 0° orientation compared to Ti-6Al-4V, while a significant reduction was evident at 90° orientation ($p = 0.0422$). In addition, the build orientation significantly affected cells cultivated on Ti-20Nb-6Ta ($p = 0.0124$). Moreover, a significant difference in niobium content was also observed after 14 days: osteoblasts on Ti-27Nb-6Ta at 0° orientation showed significantly less *MMP1* mRNA than Ti-20Nb-6Ta ($p = 0.0332$). In contrast to *MMP1*, the gene expression of *TIMP1* was not strongly affected (Figure 6C,D): after 7 days of cultivation, *TIMP1* mRNA of cells was unchanged on all Ti-Nb-Ta alloys with 0° orientation compared to cells on Ti-6Al-4V. On 90° -oriented surfaces, there was a trend toward decreased gene expression levels depending on the niobium content, but no significant differences could be determined (Figure 6C). A similar gene expression profile was also detected after 14 days, with *TIMP1* mRNA significantly reduced in osteoblasts on Ti-27Nb-6Ta with 0° orientation ($p = 0.0312$) and on Ti-20Nb-6Ta with 90° orientation ($p = 0.0315$; Figure 6D).

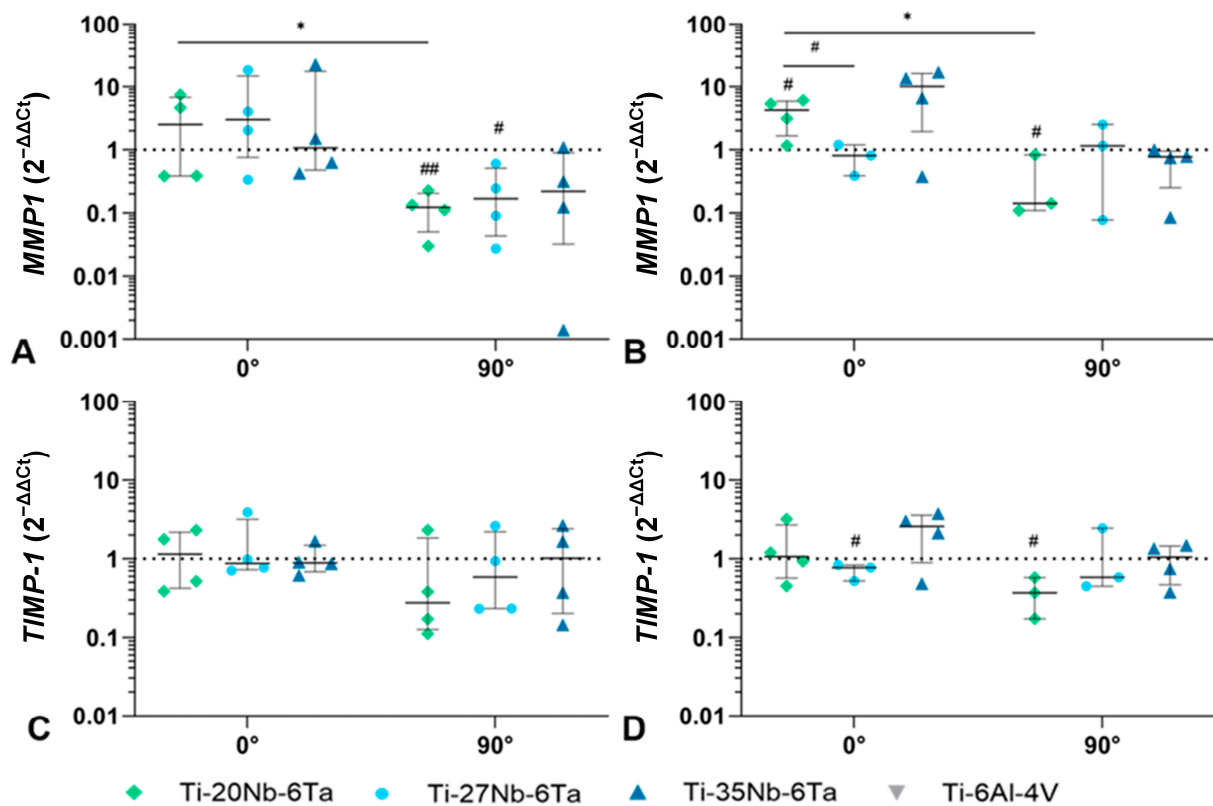


Figure 6. Gene expression analysis of *MMP1* (A,B) and *TIMP1* (C,D) of osteoblasts cultivated on dense Ti-xNb-6Ta ($x = 20, 27, 35$) or Ti-6Al-4V specimens after 7 (A,C) and 14 days (B,D). Data are depicted as individual values with median, minimum, and maximum ($n \geq 3$). Statistical significance was determined by an unpaired *t*-test with * $p < 0.05$ (effect of build orientation); # $p < 0.05$, ## $p < 0.01$ (effect of the material).

Further, the release of interleukin (IL-6 and IL-8) was determined to evaluate the pro-inflammatory potential of Ti-Nb-Ta specimens. For IL-6, significantly higher protein levels ($p = 0.0022$ [Ti-20Nb-6Ta], $p = 0.0343$ [Ti-27Nb-6Ta], $p = 0.0005$ [Ti-35Nb-6Ta] compared to 90°) were determined for osteoblasts cultivated on specimens in 0° build orientation after 7 d. Moreover, a significantly lower protein synthesis rate than those of osteoblasts on Ti-6Al-4V was apparent for Ti-27Nb-6Ta ($p = 0.0072$) and Ti-35Nb-6Ta ($p = 0.0207$). Osteoblasts on Ti-20Nb-6Ta released significantly less IL-6 than cells on Ti-35Nb-6Ta ($p = 0.0367$). Additionally, cells on 90° -oriented Ti-Nb-Ta specimens secreted IL-6 to a lesser extent than osteoblasts on Ti-6Al-4V (Figure 7A). After 14 d, IL-6 secretion remained

constant for osteoblasts on 0° Ti-Nb-Ta specimens. However, the IL-6 release of cells on Ti-35Nb-Ta was higher than those on Ti-6Al-4V ($p = 0.0207$). Although the release of IL-6 decreased after 14 days for osteoblasts on 90° Ti-6Al-4V, there was a higher synthesis rate for cells on 90°-oriented Ti-Nb-Ta specimens, with significant differences for osteoblasts on Ti-20Nb-6Ta ($p = 0.0212$) and Ti-27Nb-6Ta ($p = 0.010$, Figure 7B). For IL-8, significantly higher protein synthesis rates on day 7 were present for osteoblasts on specimens with 0° build orientation ($p = 0.0094$ [Ti-20Nb-6Ta], $p = 0.0274$ [Ti-27Nb-6Ta], $p = 0.0076$ [Ti-35Nb-6Ta]; compared to 90°). On samples with 90° build orientation, significantly reduced IL-8 was determined for osteoblasts on Ti-Nb-Ta compared to those on Ti-6Al-4V ($p = 0.0424$ [Ti-20Nb-6Ta], $p = 0.0073$ [Ti-27Nb-6Ta], $p = 0.0301$ [Ti-35Nb-6Ta]; Figure 7C). On day 14, constant IL-8 protein was detectable for osteoblasts on 0° oriented test specimens (Figure 7D). Although there was a significant increase in IL-8 protein for osteoblasts on 90° oriented Ti-Nb-Ta specimens ($p = 0.0250$ [Ti-20Nb-6Ta], $p = 0.0128$ [Ti-27Nb-6Ta], $p = 0.0104$ [Ti-35Nb-6Ta]; compared to 7 d), the amount of IL-8 was decreased compared to cells cultivated on Ti-6Al-4V (Ti-35Nb-6Ta: $p = 0.0448$).

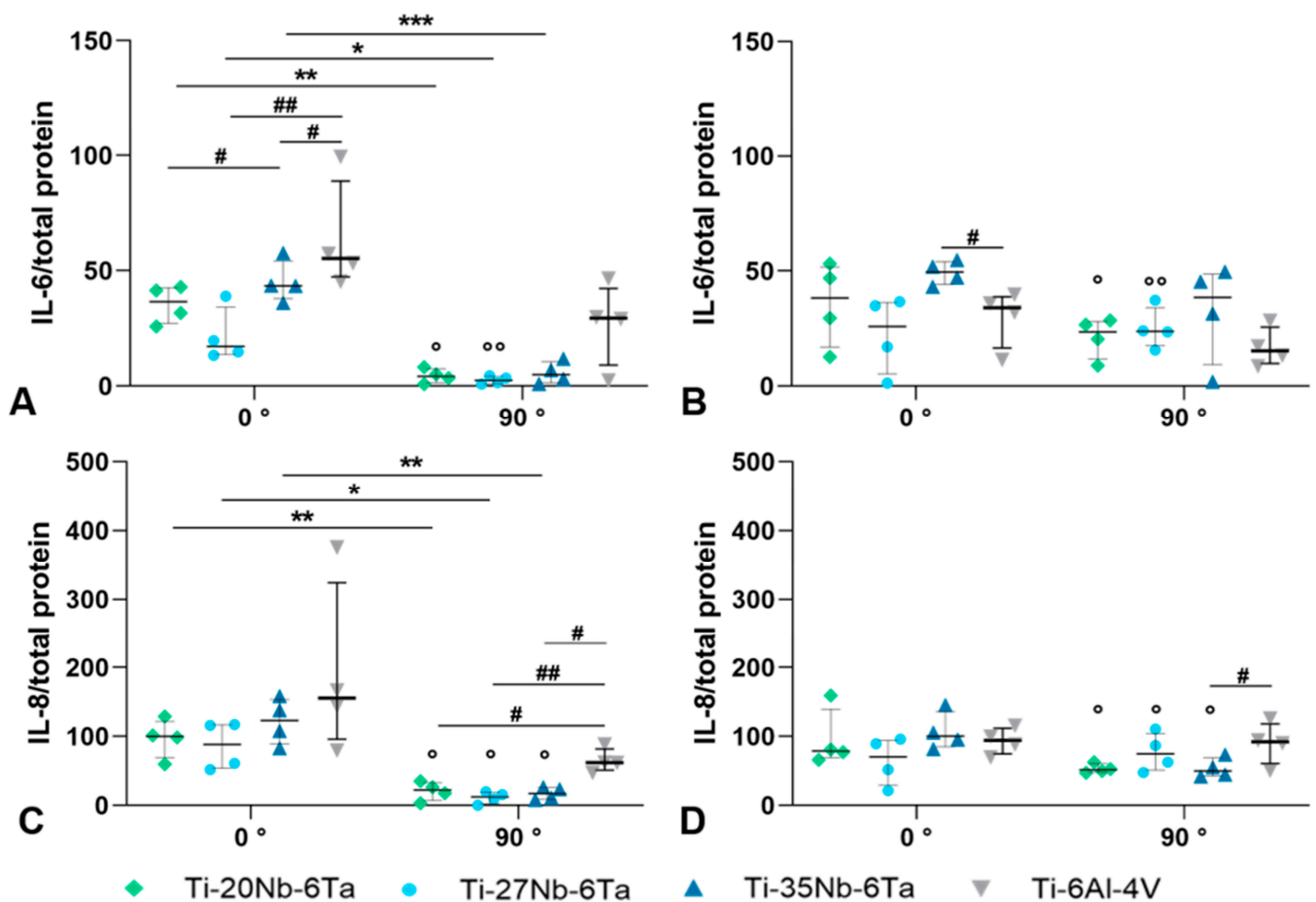


Figure 7. Induction of inflammation in human osteoblasts seeded on Ti-xNb-6Ta ($x = 20, 27, 35$) or Ti-6Al-4V specimens. The release of interleukin (IL-) 6 (A,B) and IL-8 (C,D) was determined via ELISA after 7 (A,C) and 14 days (B,D). Protein amounts were related to total protein ($\text{pg} \times \text{mg}^{-1}$, $n = 4$). Statistical significance was determined by a paired *t*-test with * $p < 0.05$, ** $p < 0.01$, *** $p < 0.001$ (effect of build orientation); # $p < 0.05$, ## $p < 0.01$ (effect of the material); ° $p < 0.05$, °° $p < 0.01$ (effect of cultivation time).

The biological characterization of open porous Ti-20Nb-6Ta specimens was performed with regard to the differentiation capacity, induction of inflammation, and bone remodeling of human osteoblasts. It was compared to similar specimens made of Ti-6Al-4V. A time-

dependent induction of the osteoblastic differentiation was apparent in osteoblasts on Ti-20Nb-6Ta. In detail, significantly enhanced *RUNX2* transcripts were determined after 14 d compared to osteoblasts seeded on Ti-6Al-4V ($p = 0.0415$, Figure 8A). For *COL1A1*, an increased gene expression was observed in both time intervals ($p = 0.0314$ [day 7, compared to Ti-6Al-4V]) with higher but non-significant values after 14 days. Regarding the induction of bone remodeling, mRNA transcript levels of the collagenase *MMP1* and its natural inhibitor *TIMP1* were determined, indicating decreased *MMP1* transcripts ($p = 0.0418$ [day 14, compared to Ti-6Al-4V]) and a time-dependent increase of *TIMP1* gene expression. Moreover, a significant decrease in IL-6 gene expression after 14 days ($p = 0.0327$, compared to 7 days) was observed in osteoblasts cultivated on open porous Ti-20Nb-6Ta specimens.

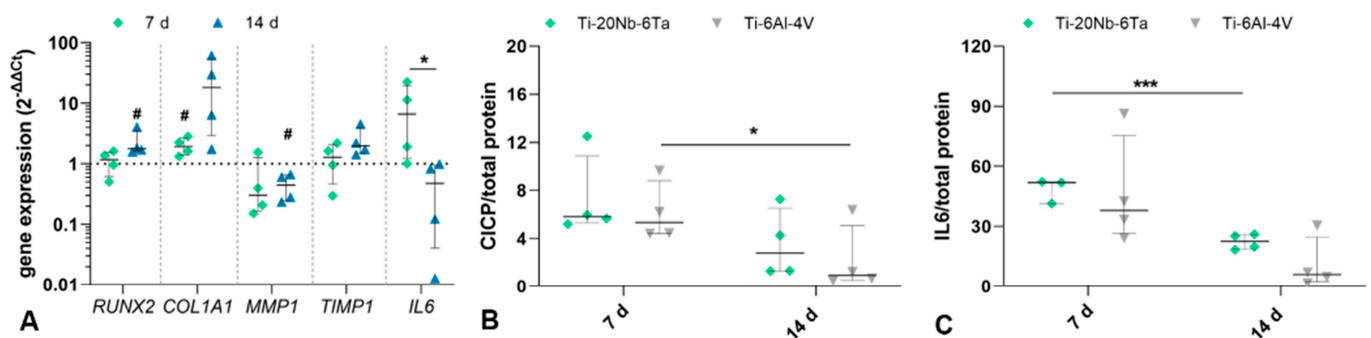


Figure 8. Biological characterization of open porous lattice-structured specimens (Ti-20Nb-6Ta vs. Ti-6Al-4V). The differentiation capacity, the induction of inflammation, and the induction of bone remodeling in human osteoblasts cultivated on open porous specimens were determined via gene expression analyses and protein quantification after 7 and 14 days. (A) Gene expression levels of *RUNX2*, *COL1A1*, *IL6*, *MMP1*, and *TIMP1* are depicted as individual values with median, minimum, and maximum ($n = 4$). Gene expression rates of osteoblasts on Ti-6Al-4V specimens served as controls (dotted line at “1”). Protein amount of (B) cross-linked C-telopeptides of Type 1 collagen (C1CP in ng/mg; $n \geq 3$) and (C) interleukin 6 (IL-6 in $\text{pg} \times \text{mg}^{-1}$) related to total protein. Statistical significance was determined by a paired (gene expression, C1CP) and an unpaired (IL-6) *t*-test with * $p < 0.05$, *** $p < 0.001$ (effect of cultivation time); # $p < 0.05$ (effect of the material).

In addition to gene expression analyses, the release of C1CP and IL-6 in cell culture supernatant was also determined. No differences in the amount of C1CP from osteoblasts on Ti-20Nb-6Ta and Ti-6Al-4V could be detected. A time-dependent decrease in protein was detected for both open porous specimens, although this was significant only for osteoblasts on Ti-6Al-4V ($p = 0.0148$, Figure 8B). A similar trend was also found for the secretion of IL-6, with a significant decrease in the amount of protein for Ti-20Nb-6Ta ($p = 0.0009$, Figure 8C).

4. Discussion

In this study, we characterized the mechanical and biological properties of Ti- x Nb-6Ta ($x = 20, 27, 35$) alloys manufactured by PBF-LB/M. The influence of build orientation during manufacturing on different properties was evaluated. In addition to fully dense specimens, open porous Ti-20Nb-6Ta specimens with a defined lattice structure were also characterized and compared to Ti-6Al-4V specimens.

The compressive modulus of the Ti-Nb-Ta alloys ranged from 43.7 ± 2.7 GPa (Ti-20Nb-6Ta, 90°) to 85.9 ± 2.7 GPa (Ti-27Nb-6Ta, 45°). Even though this is significantly higher than that of human cortical (18.6 GPa [49]) or cancellous bone (0.2–4.5 GPa [50]), it is distinctly reduced compared to Ti-6Al-4V (Young’s modulus: ~ 114 GPa [22]). In addition to the compressive modulus, the elastic admissible strain, which is defined as the ratio of yield strength to elasticity, is a useful parameter for assessing the potential of an implant material [10]. Elastic admissible strains of, e.g., Ti-42Nb are 0.95–1.54% [7,15], of various

Ti–Nb–Zr alloys 1.08–1.31% [10], of various Ti–Nb–Ta–Zr alloys 0.71–1.27% [9], and of Ti–6Al–4V ~0.8% [23]. Ti–Nb–Ta alloys investigated in this study showed elastic admissible strains between 0.96% and 1.44%, thus indicating a high ratio of compressive modulus and yield strength. Specimens built in 90° orientation showed the highest admissible strain for each alloy and are ranked as follows: Ti–20Nb–6Ta > Ti–27Nb–6Ta > Ti–35Nb–6Ta.

Both the niobium content and the build orientation of the Ti–Nb–Ta specimens affected the compressive mechanical properties. As reported by Johannsen et al. [18], the Ti:Nb ratio in Ti–Nb–Ta alloys influences the microstructure and the phase composition of the powders and the additively manufactured parts. It was reported that Ti–20Nb–6Ta is mostly composed of an orthorhombic α'' martensite phase whereas Ti–35Nb–6Ta crystallizes entirely in a bcc β -phase. Ti–27Nb–6Ta is characterized by a structure in which probably ω -, α'' -, and/or β -phases coexist.

Since the specimens in the present study were manufactured using the same powder feedstock and the AM process parameters developed in [18], it is obvious that identical microstructures were obtained compared to those published. This can be concluded from Figure 2 in which the microstructures of three Ti–Nb–Ta samples are compared by BSE analysis. Independent of the orientation in the built chamber, the BSE analysis of Ti–20Nb–6Ta shows platelet-like features, whereas Ti–27Nb–6Ta and Ti–35Nb–6Ta do not. This is in full agreement with the results of the previous light microscopic investigations in [18].

The different microstructures of the additively manufactured specimens cause different fracture behavior. Ti–35Nb–6Ta with a bcc structure did not fracture under compressive load. This is a behavior frequently observed for entirely β -phase Ti alloys such as Ti–42Nb [7] or Ti–Nb–Zr (Nb + Zr > 59 wt. %) [10]. For Ti–Nb–Ta–Zr alloys with a mixed β - and ω -phase, fracture at 45° to the load axis and the adhesion of the fractured pieces have been reported [8], identical to our observations. The compressive fracture of Ti–6Al–4V–5Nb consisting of an α' – β mixed phase with appearance of dimples and cleavage facets was reported by Sui et al. [51].

In addition to the chemical composition, the build orientation and scanning strategy during PBF-LB/M of β -Ti alloys influences the microstructure and, thus, the mechanical properties [15,37,52]. It is well understood that during fabrication, elongated columnar β -grains may form along the build direction [15,52] and that their formation is strongly influenced by the scanning strategy and the depths of the melt pools [37,52]. In line with the observations of Pilz et al. [15], Young's modulus (in our case compressive modulus) can be ordered as follows from highest to lowest: 45° > 0° > 90° (build orientation). In AM, the epitaxial growth of crystals is influenced by the movement of melt pools, which in turn depends on spatial and temporal variations in the temperature gradient. This can be used to program a preferred crystallographic orientation to feature desired properties [37]. The lowest stiffness of an additive manufactured part is achieved by parallel alignment of the <001> crystal direction to the load direction [15]. The results of our study indicate the possibility of the Ti–Nb–Ta alloys to be used as material for bone implant applications and that the stiffness, which is crucial in terms of implant-to-bone load transfer, can be tailored by the build orientation.

Although the findings of the present study are in general agreement with those of Pilz et al. [15], they did not observe significant differences in strength and ductility in specimens manufactured with different build orientations. The ductility of conventionally manufactured metal specimens can be traced back to grain sliding. In additively manufactured specimens, this effect can be severely limited due to the smaller crystallite sizes, the occurrence of melt pool boundaries and the cellular structure [36,53]. Liu et al. [53] investigated the deformation mechanism of a high-entropy alloy, Ti–Nb–Ta–Zr–Mo, produced by additive manufacturing. Their results suggested that the strength and ductility of the alloy resulted from a complex microstructure that included dislocations, solidification cell patterns, and grain boundaries. The study highlighted that the occurrence of dislocation slip, either within a single cell or across multiple cells, played a critical role. Despite the homogeneous element distribution of the Ti–Nb–Ta alloys, they have unique 1–2 μm thick

melt pool boundaries with a slight chemical segregation of Ti- and Nb/Ta-rich zones and platelet-like structures in Ti–20Nb–6Ta [18]. In the context of the complex deformation mechanisms of other β -type Ti alloys, we relate the dependence of strength and ductility on build orientation and chemical composition to the microstructure. However, a detailed investigation of the deformation behavior comparable to that of Liu et al. [53] was beyond the scope of our present study, but should be addressed in future research.

To further reduce the mechanical mismatch in elasticity between human bone and implant material and to improve the bone-implant interaction, open porous lattice-structured Ti–20Nb–6Ta specimens with a face-centered unit cell were additively manufactured (Figure 1). They have a compressive stiffness of 8.7 ± 1.0 GPa, which is in the range of human bone. Even though this is higher than the stiffness of porous structures reported in other studies [30,32], the observed yield (179.2 ± 4.5 MPa) and ultimate compressive strength (351.7 ± 7.5 MPa) are higher than in these studies and higher than the strength of human bone [54]. Compared to porous Ti–6Al–4V specimens with similar structure, Ti–20Nb–6Ta possesses a significantly lower compressive modulus but also lower strength, most probably due to the different intrinsic material properties. Nevertheless, it can be concluded that AM of open porous structured Ti–20Nb–6Ta is a suitable approach for the physical functionalization of orthopedic implants to enhance the bone–implant interaction.

Commonly used Ti–6Al–4V implants have significant disadvantages with regard to the toxicity of Al and V, when dissolved in the human organism [2–5]. In contrast, binary or ternary alloys with Ti, Nb and /or Ta as alloying constituents exhibit excellent biocompatibility and high corrosion resistance [55]. Last but not least, tantalum, with its low toxicity and high corrosion resistance, is an ideal candidate for bone regeneration [24,56]. In previous studies, we confirmed that both Ti–Nb alloys possess good biocompatibility [57] and that tantalum scaffolds are excellent substrates for bone cells depositing [58]. Accordingly, Ti–Nb–Ta alloys appear to be materials for the application as bone substitutes, promoting osteogenesis.

The surfaces of PBF-LB/M processed specimens typically have considerable roughness due to incompletely melted particles [28], and the surface properties are influenced by, among other parameters, the build orientation [38]. However, Ginestra et al. [38] reported a limited influence of the build orientation ($0^\circ, 15^\circ, 30^\circ, 45^\circ$) on the long-term osseointegrative behavior, with roughnesses (R_a) ranging from 17.4 ± 1.8 μm to 24.4 ± 3.1 μm . In line with previous studies [38,44], we demonstrated that as-printed surfaces do not impair osteogenesis and, therefore, no post-processing is necessarily required. In contrast to the observations of Ginestra et al. [38], based on the particular structuring of the surfaces in this study (0° and 90° build orientation) preferential osteoblast settlement was observed in 90° specimens. This is due to the microstructuring, which has a direct effect on cell–cell interactions [44] and on the actin cytoskeleton and its remodeling, which is associated with direct mechanotransduction, leading to the increased expression of osteogenic markers such as *RUNX2*, *SPP1*, and other genes [59–61]. In fact, we could detect an upregulation of osteogenic genes with dependence on the build orientation but also with dependence on the niobium content. The latter also correlates with cell morphology and, accordingly, with the distribution of the actin cytoskeleton. Our results are thus also consistent with the study by Lauria et al. [62], who demonstrated that a nanoporous Ti–45Nb surface may be associated with an increased surface nanostructure, which was beneficial for MG-63 osteosarcoma cell settlement, pseudopodia formation, and osteogenic differentiation. Further, osteogenic differentiation on Ti–Nb–Ta alloy is also apparent on the open-porous lattice structures. In particular, a strong time-dependent effect is found, characterized by an increase in *RUNX2* and *COL1A1*. Considering the optimal osseointegration of implant structures, a coordinated remodeling of the surrounding bone tissue is essential, a process regulated by a balanced activity of MMPs and TIMPs. In our study, a clearly reduced impact on bone destruction is evident on the open-porous Ti–20Nb–6Ta lattice structures, as the gene expression of *MMP-1* is diminished and, at the same time, *TIMP1* mRNA is induced in a time-dependent manner. This was also evident in osteoblasts cultivated

on dense specimens in 90° orientation. Thus, the results demonstrate that either surface structuring or the material composition has a beneficial effect on the MMP1/TIMP1 ratio through the absence of induced bone resorption processes. We have already observed a similar effect in a previous study where we found a clear correlation of the MMP1/TIMP1 ratio to the build orientation of Ti-6Al-4V specimens [63]. In addition to a possible surface structuring due to the build orientation, we were able to determine effects on *MMP1* and *TIMP1* gene expression depending on the niobium content. Here, a content of 35 wt. % Nb resulted in a clear increase in *MMP1* and *TIMP1* transcript levels, but without a significant difference to the other test specimens. This effect may be due to the increased deposition of type 1 collagen and related matrix remodeling processes. However, this remains to be proven in further studies.

Since the surfaces are initially settled by mesenchymal stem cells and osteoblasts after implantation, the osseointegrative process is also associated with the release of pro-inflammatory mediators leading to the differentiation of the stroma cells. Indeed, we determined an enhanced release of IL-6 within the 14 days of cultivation, in particular on Ti-Nb-Ta alloys with 90° surface orientation and open porous Ti-20Nb-6Ta test specimens compared to Ti-6Al-4V. At the same time, the release of IL-8 was clearly reduced on Ti-Nb-Ta alloys with 90° surface orientation. The higher content of IL-6 might not only be associated with inflammation since it was proven that the IL-6-dependent coupling mechanism also mediates bone formation [64]. Therefore, we assume that the release of IL-6 by human osteoblasts correlates directly with the osteogenic differentiation capacity of these cells seen in enhanced *RUNX2* and *COL1A1* gene expression. Besides bone-forming cells, macrophages are among the cells involved in the initial inflammatory response after implantation. In particular, the macrophage phenotype plays an important role in this process, significantly influencing the pro- or anti-inflammatory implant environment [65].

The study has some limitations. We have determined the compressive modulus of the Ti-Nb-Ta alloys and compared the results with the tensile modulus of other materials because the compressive modulus is rarely reported. However, since the Poisson's ratio of titanium alloys is about 0.33, it can be concluded that the compressive modulus and the Young's modulus are in a very similar range. Nevertheless, the tensile properties need to be investigated in future studies. In our present study, BSE measurements were performed to characterize the influence of the build orientation on the microstructure, and in addition, the previous results of Johannsen et al. [18] with similar Ti-Nb-Ta alloys and processing strategies were summarized and used to discuss the observed mechanical properties. However, a detailed investigation of the microstructure as a function of build orientation and processing strategy using XRD and EBSD to fully understand the deformation behavior is part of subsequent studies. Overall, it is not possible to conclude from this study whether the amount of niobium significantly influences biocompatibility and osteogenic differentiation, as there were only minor differences in cell behavior. Rather, build orientation seems to influence cell behavior through the structuring of the surface. In addition to the build orientation, the surface properties are influenced by laser power, scanning speed, and hatch distance. Therefore, future studies could optimize the surface properties by systematically analyzing the influence of the process strategy on the surface.

Despite these limitations, the results obtained have provided further insight into the essential properties of additively manufactured Ti-Nb-Ta alloys and have also identified further research questions. These include a comprehensive analysis of mechanical (tensile) properties as a function of build orientation, taking into account the detailed investigation of the microstructure. The influence of annealing on additively manufactured Ti-Nb-Ta has not been investigated, but it may be interesting in terms of structural changes and their influence on mechanical properties. Furthermore, the influence of differently structured surfaces on cell interaction, the specific macrophage response to Ti-Nb-Ta alloys, the surface properties in terms of the characterization of passive oxide layers, e.g., by XPS, and metal ion release in physiological solutions should be characterized in future studies.

5. Conclusions

Ti-xNb-6Ta (x = 20, 27, 35) alloys are promising materials for use in additively manufactured bone implants. The mechanical properties of Ti-Nb-Ta specimens produced by PBF-LB/M are controlled by the chemical composition of the alloy and the orientation of the specimen in the build chamber. Ti-Nb-Ta alloys have lower compressive moduli (Ti-20Nb-6Ta, 90°: 43 GPa) compared to commonly used Ti-6Al-4V (~114 GPa) implant materials, which reduces the mechanical mismatch with human bone and, thus, suppresses the tendency for stress shielding. The elasticity can be further reduced by fabricating open porous specimens (Ti-20Nb-6Ta: 8.7 GPa), thereby minimizing the mechanical mismatch with bone tissue. The biological properties were mainly influenced by the build orientation and cultivation time. As-printed surfaces of the Ti-Nb-Ta alloys promoted improved osteogenesis and reduced inflammation compared to Ti-6Al-4V. In conclusion, Ti-Nb-Ta alloys show great potential for use in orthopedic and dental implants, outperforming commonly used implant materials such as Ti-6Al-4V in the aspects investigated.

Author Contributions: Conceptualization, J.-O.S., J.J., M.W., M.S., D.V., R.B., and A.J.-H.; data curation, J.-O.S., M.-L.S., E.K., and M.F.; formal analysis, J.-O.S., M.-L.S., E.K., and A.J.-H.; funding acquisition, J.J., M.W., M.S., D.V., R.B., and A.J.-H.; investigation, J.-O.S., M.-L.S., E.K., and A.J.-H.; methodology, J.-O.S., M.-L.S., J.J., and A.J.-H.; project administration, J.-O.S., D.V., and R.B.; software, J.-O.S., M.-L.S., and A.J.-H.; supervision, D.V., R.B., and A.J.-H.; visualization, J.-O.S., M.-L.S., M.F., and A.J.-H.; writing—original draft, J.-O.S., and A.J.-H.; writing—review and editing, J.-O.S., M.-L.S., E.K., J.J., M.W., M.S., M.F., D.V., and R.B. All authors have read and agreed to the published version of the manuscript.

Funding: This work was supported by the German Federal Ministry of Education and Research (HYTIMOX, grant number: 03XP0279D), which had no role in study design; in the collection, analysis, and interpretation of data; in the writing of the report; and in the decision to submit the article for publication.

Institutional Review Board Statement: The study was conducted in accordance with the Declaration of Helsinki, and approved by the local ethics committee of University of Rostock (protocol code: A2010-0010 and date of approval: 12/06/2018).

Informed Consent Statement: Informed consent was obtained from all subjects involved in the study.

Data Availability Statement: The raw data supporting the conclusions of this article will be made available by the authors on request.

Acknowledgments: We would like to thank Christopher Benz and Martin Radke of the Institute of Structural Mechanics (University of Rostock, Rostock, Germany) and Nicolas Rabot for their support during mechanical characterization. We thank Armin Springer and Karoline Schulz of the Electron Microscopy Centre for their support with electron microscopy and sample preparation. Additionally, we want to thank the European Union and the state of Mecklenburg-West Pomerania (Germany) for providing the laser-scanning microscope (VK-X250, reference number GHS-15-0016) and digital microscope (VHX-6000, reference number GHS-16-0002).

Conflicts of Interest: M.W. and M.S. are employees of TANIOBIS GmbH. The authors declare no conflicts of interest.

Appendix A

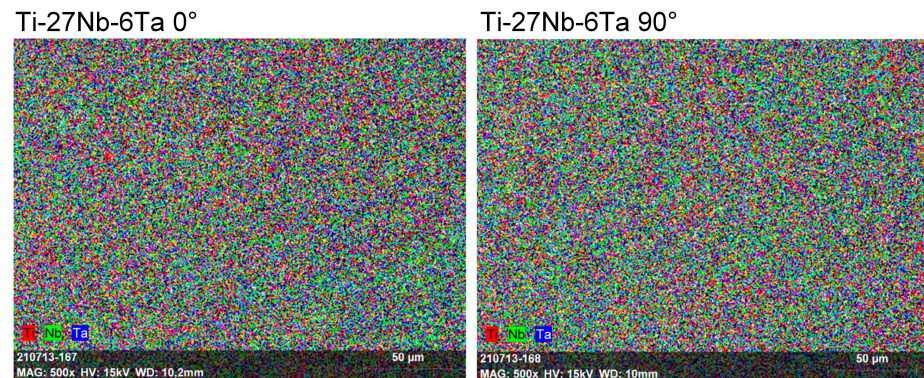


Figure A1. Energy dispersive X-ray spectroscopy images of Ti-27Nb-6Ta produced by laser beam powder bed fusion in 0° and 90° build orientation. The specimens have a chemically homogeneous distribution of elements.

References

- Pandey, A.; Awasthi, A.; Saxena, K.K. Metallic implants with properties and latest production techniques: A review. *Adv. Mater. Process. Technol.* **2020**, *6*, 405–440. [[CrossRef](#)]
- Farrahnour, A.; Zuhailawati, H. Review on the mechanical properties and biocompatibility of titanium implant: The role of niobium alloying element. *Int. J. Mater. Res.* **2021**, *112*, 505–513. [[CrossRef](#)]
- Gomes, C.C.; Moreira, L.M.; Santos, V.J.S.V.; Ramos, A.S.; Lyon, J.P.; Soares, C.P.; Santos, F.V. Assessment of the genetic risks of a metallic alloy used in medical implants. *Genet. Mol. Biol.* **2011**, *34*, 116–121. [[CrossRef](#)] [[PubMed](#)]
- Okazaki, Y.; Rao, S.; Ito, Y.; Tateishi, T. Corrosion resistance, mechanical properties, corrosion fatigue strength and cytocompatibility of new Ti alloys without Al and V. *Biomaterials* **1998**, *19*, 1197–1215. [[CrossRef](#)] [[PubMed](#)]
- Costa, B.C.; Tokuhara, C.K.; Rocha, L.A.; Oliveira, R.C.; Lisboa-Filho, P.N.; Costa Pessoa, J. Vanadium ionic species from degradation of Ti-6Al-4V metallic implants: In vitro cytotoxicity and speciation evaluation. *Mater. Sci. Eng. C Mater. Biol. Appl.* **2019**, *96*, 730–739. [[CrossRef](#)] [[PubMed](#)]
- Savio, D.; Bagno, A. When the Total Hip Replacement Fails: A Review on the Stress-Shielding Effect. *Processes* **2022**, *10*, 612. [[CrossRef](#)]
- Schulze, C.; Weinmann, M.; Schweigel, C.; Keßler, O.; Bader, R. Mechanical Properties of a Newly Additive Manufactured Implant Material Based on Ti-42Nb. *Materials* **2018**, *11*, 124. [[CrossRef](#)] [[PubMed](#)]
- Ozan, S.; Lin, J.; Li, Y.; Wen, C. New Ti-Ta-Zr-Nb alloys with ultrahigh strength for potential orthopedic implant applications. *J. Mech. Behav. Biomed. Mater.* **2017**, *75*, 119–127. [[CrossRef](#)] [[PubMed](#)]
- Stráský, J.; Harcuba, P.; Václavová, K.; Horváth, K.; Landa, M.; Srba, O.; Janeček, M. Increasing strength of a biomedical Ti-Nb-Ta-Zr alloy by alloying with Fe, Si and O. *J. Mech. Behav. Biomed. Mater.* **2017**, *71*, 329–336. [[CrossRef](#)] [[PubMed](#)]
- Ozan, S.; Lin, J.; Li, Y.; Ipek, R.; Wen, C. Development of Ti-Nb-Zr alloys with high elastic admissible strain for temporary orthopedic devices. *Acta Biomater.* **2015**, *20*, 176–187. [[CrossRef](#)]
- Luo, J.P.; Sun, J.F.; Huang, Y.J.; Zhang, J.H.; Zhang, Y.D.; Zhao, D.P.; Yan, M. Low-modulus biomedical Ti-30Nb-5Ta-3Zr additively manufactured by Selective Laser Melting and its biocompatibility. *Mater. Sci. Eng. C Mater. Biol. Appl.* **2019**, *97*, 275–284. [[CrossRef](#)]
- Ahmed, T.; Rack, H.J. Martensitic transformations in Ti-(16–26 at%) Nb alloys. *J. Mater. Sci.* **1996**, *31*, 4267–4276. [[CrossRef](#)]
- Zhang, Y.; Sun, D.; Cheng, J.; Tsoi, J.K.H.; Chen, J. Mechanical and biological properties of Ti-(0–25 wt%)Nb alloys for biomedical implants application. *Regen. Biomater.* **2020**, *7*, 119–127. [[CrossRef](#)]
- Munir, K.; Lin, J.; Wright, P.F.A.; Ozan, S.; Li, Y.; Wen, C. Mechanical, corrosion, nanotribological, and biocompatibility properties of equal channel angular pressed Ti-28Nb-35.4Zr alloys for biomedical applications. *Acta Biomater.* **2022**, *149*, 387–398. [[CrossRef](#)] [[PubMed](#)]
- Pilz, S.; Gustmann, T.; Günther, F.; Zimmermann, M.; Kühn, U.; Gebert, A. Controlling the Young's modulus of a β -type Ti-Nb alloy via strong texturing by LPBF. *Mater. Des.* **2022**, *216*, 110516. [[CrossRef](#)]
- Hussein, A.H.; Gepreel, M.A.-H.; Gouda, M.K.; Hefnawy, A.M.; Kandil, S.H. Biocompatibility of new Ti-Nb-Ta base alloys. *Mater. Sci. Eng. C Mater. Biol. Appl.* **2016**, *61*, 574–578. [[CrossRef](#)] [[PubMed](#)]
- Wei, T.Y.; Huang, J.C.; Chao, C.-Y.; Wei, L.L.; Tsai, M.T.; Chen, Y.H. Microstructure and elastic modulus evolution of TiTaNb alloys. *J. Mech. Behav. Biomed. Mater.* **2018**, *86*, 224–231. [[CrossRef](#)]
- Johannsen, J.; Lauhoff, C.; Stenzel, M.; Schnitter, C.; Niendorf, T.; Weinmann, M. Laser beam powder bed fusion of novel biomedical Titanium/Niobium/Tantalum alloys: Powder synthesis, microstructure evolution and mechanical properties. *Mater. Des.* **2023**, *233*, 112265. [[CrossRef](#)]





19. Kuroda, P.A.B.; de Freitas Quadros, F.; Sousa, K.D.S.J.; Donato, T.A.G.; de Araújo, R.O.; Grandini, C.R. Preparation, structural, microstructural, mechanical and cytotoxic characterization of as-cast Ti-25Ta-Zr alloys. *J. Mater. Sci. Mater. Med.* **2020**, *31*, 19. [[CrossRef](#)]
20. Kong, W.; Cox, S.C.; Lu, Y.; Villapun, V.; Xiao, X.; Ma, W.; Liu, M.; Attallah, M.M. Microstructural Evolution, Mechanical Properties, and Preosteoblast Cell Response of a Post-Processing-Treated Ti-25Zr β Ti Alloy Manufactured via Selective Laser Melting. *ACS Biomater. Sci. Eng.* **2022**, *8*, 2336–2348. [[CrossRef](#)]
21. Hao, Y.L.; Li, S.J.; Sun, S.Y.; Zheng, C.Y.; Hu, Q.M.; Yang, R. Super-elastic titanium alloy with unstable plastic deformation. *Appl. Phys. Lett.* **2005**, *87*, 91906. [[CrossRef](#)]
22. Challis, V.J.; Xu, X.; Halfpenny, A.; Cramer, A.D.; Saunders, M.; Roberts, A.P.; Sercombe, T.B. Understanding the effect of microstructural texture on the anisotropic elastic properties of Selective Laser Melted Ti-24Nb-4Zr-8Sn. *Acta Mater.* **2023**, *254*, 119021. [[CrossRef](#)]
23. Niinomi, M. Mechanical properties of biomedical titanium alloys. *Mater. Sci. Eng. A* **1998**, *243*, 231–236. [[CrossRef](#)]
24. Eisenbarth, E.; Velten, D.; Müller, M.; Thull, R.; Breme, J. Biocompatibility of beta-stabilizing elements of titanium alloys. *Biomaterials* **2004**, *25*, 5705–5713. [[CrossRef](#)]
25. Song, Y.; Xu, D.S.; Yang, R.; Li, D.; Wu, W.T.; Guo, Z.X. Theoretical study of the effects of alloying elements on the strength and modulus of β -type bio-titanium alloys. *Mater. Sci. Eng. A* **1999**, *260*, 269–274. [[CrossRef](#)]
26. Soni, R.; Pande, S.; Salunkhe, S.; Natu, H.; Abouel Nasr, E.; Shanmugam, R.; Hussein, H.M.A.M. In Vitro and Electrochemical Characterization of Laser-Cladded Ti-Nb-Ta Alloy for Biomedical Applications. *Crystals* **2022**, *12*, 954. [[CrossRef](#)]
27. Ni, J.; Ling, H.; Zhang, S.; Wang, Z.; Peng, Z.; Benyshek, C.; Zan, R.; Miri, A.K.; Li, Z.; Zhang, X.; et al. Three-dimensional printing of metals for biomedical applications. *Mater. Today Bio.* **2019**, *3*, 100024. [[CrossRef](#)]
28. Trevisan, F.; Calignano, F.; Aversa, A.; Marchese, G.; Lombardi, M.; Biamino, S.; Ugues, D.; Manfredi, D. Additive manufacturing of titanium alloys in the biomedical field: Processes, properties and applications. *J. Appl. Biomater. Funct. Mater.* **2018**, *16*, 57–67. [[CrossRef](#)]
29. Singh, S.; Ramakrishna, S. Biomedical applications of additive manufacturing: Present and future. *Curr. Opin. Biomed. Eng.* **2017**, *2*, 105–115. [[CrossRef](#)]
30. Li, Y.; Ding, Y.; Munir, K.; Lin, J.; Brandt, M.; Atrens, A.; Xiao, Y.; Kanwar, J.R.; Wen, C. Novel β -Ti35Zr28Nb alloy scaffolds manufactured using selective laser melting for bone implant applications. *Acta Biomater.* **2019**, *87*, 273–284. [[CrossRef](#)]
31. Gao, X.; Fraulob, M.; Haiat, G. Biomechanical behaviours of the bone-implant interface: A review. *J. R. Soc. Interface* **2019**, *16*, 20190259. [[CrossRef](#)]
32. Günther, F.; Pilz, S.; Hirsch, F.; Wagner, M.; Kästner, M.; Gebert, A.; Zimmermann, M. Shape optimization of additively manufactured lattices based on triply periodic minimal surfaces. *Addit. Manuf.* **2023**, *73*, 103659. [[CrossRef](#)]
33. Song, C.; Liu, L.; Deng, Z.; Lei, H.; Yuan, F.; Yang, Y.; Li, Y.; Yu, J. Research progress on the design and performance of porous titanium alloy bone implants. *J. Mater. Res. Technol.* **2023**, *23*, 2626–2641. [[CrossRef](#)]
34. Antony, A.A.; Meyer, J.; Prangnell, P.B. Effect of build geometry on the β -grain structure and texture in additive manufacture of Ti6Al4V by selective electron beam melting. *Mater. Charact.* **2013**, *84*, 153–168. [[CrossRef](#)]
35. Simonelli, M.; Tse, Y.Y.; Tuck, C. Effect of the build orientation on the mechanical properties and fracture modes of SLM Ti-6Al-4V. *Mater. Sci. Eng. A* **2014**, *616*, 1–11. [[CrossRef](#)]
36. Sui, Q.; Li, P.; Wang, K.; Yin, X.; Liu, L.; Zhang, Y.; Zhang, Q.; Wang, S.; Wang, L. Effect of Build Orientation on the Corrosion Behavior and Mechanical Properties of Selective Laser Melted Ti-6Al-4V. *Metals* **2019**, *9*, 976. [[CrossRef](#)]
37. Luo, X.; Song, T.; Gebert, A.; Neufeld, K.; Kaban, I.; Ma, H.; Cai, W.; Lu, H.; Li, D.; Li, N.; et al. Programming Crystallographic Orientation in Additive-Manufactured Beta-Type Titanium Alloy. *Adv. Sci. (Weinheim)* **2023**, *10*, e2302884. [[CrossRef](#)]
38. Ginestra, P.; Ferraro, R.M.; Zohar-Hauber, K.; Abeni, A.; Giliani, S.; Ceretti, E. Selective Laser Melting and Electron Beam Melting of Ti6Al4V for Orthopedic Applications: A Comparative Study on the Applied Building Direction. *Materials* **2020**, *13*, 5584. [[CrossRef](#)]
39. Avila, J.D.; Bose, S.; Bandyopadhyay, A. Additive manufacturing of titanium and titanium alloys for biomedical applications. In *Titanium in Medical and Dental Applications*; Elsevier: Amsterdam, The Netherlands, 2018; pp. 325–343, ISBN 9780128124567.
40. Harun, W.; Manam, N.S.; Kamariah, M.; Sharif, S.; Zulkifly, A.H.; Ahmad, I.; Miura, H. A review of powdered additive manufacturing techniques for Ti-6al-4v biomedical applications. *Powder Technol.* **2018**, *331*, 74–97. [[CrossRef](#)]
41. Aufa, A.N.; Hassan, M.Z.; Ismail, Z. Recent advances in Ti-6Al-4V additively manufactured by selective laser melting for biomedical implants: Prospect development. *J. Alloys Compd.* **2022**, *896*, 163072. [[CrossRef](#)]
42. Wysocki, B.; Maj, P.; Sitek, R.; Buhagiar, J.; Kurzydłowski, K.; Świąszkowski, W. Laser and Electron Beam Additive Manufacturing Methods of Fabricating Titanium Bone Implants. *Appl. Sci.* **2017**, *7*, 657. [[CrossRef](#)]
43. Nguyen, H.D.; Pramanik, A.; Basak, A.K.; Dong, Y.; Prakash, C.; Debnath, S.; Shankar, S.; Jawahir, I.S.; Dixit, S.; Buddhi, D. A critical review on additive manufacturing of Ti-6Al-4V alloy: Microstructure and mechanical properties. *J. Mater. Res. Technol.* **2022**, *18*, 4641–4661. [[CrossRef](#)]
44. Ponader, S.; Vairaktaris, E.; Heinel, P.; Wilmowsky, C.V.; Rottmair, A.; Körner, C.; Singer, R.F.; Holst, S.; Schlegel, K.A.; Neukam, F.W.; et al. Effects of topographical surface modifications of electron beam melted Ti-6Al-4V titanium on human fetal osteoblasts. *J. Biomed. Mater. Res. A* **2008**, *84*, 1111–1119. [[CrossRef](#)]

45. Ivanov, E.; Del Rio, E.; Kapchemnko, I.; Nyström, M.; Kotila, J. Development of Bio-Compatible Beta Ti Alloy Powders for Additive Manufacturing for Application in Patient-Specific Orthopedic Implants. *KEM* **2018**, *770*, 9–17. [[CrossRef](#)]
46. Kim, H.Y.; Fu, J.; Tobe, H.; Kim, J.I.; Miyazaki, S. Crystal Structure, Transformation Strain, and Superelastic Property of Ti–Nb–Zr and Ti–Nb–Ta Alloys. *Shap. Mem. Superelast.* **2015**, *1*, 107–116. [[CrossRef](#)]
47. Miyazaki, S.; Kim, H.Y.; Hosoda, H. Development and characterization of Ni-free Ti-base shape memory and superelastic alloys. *Mater. Sci. Eng. A* **2006**, *438–440*, 18–24. [[CrossRef](#)]
48. Lochner, K.; Fritsche, A.; Jonitz, A.; Hansmann, D.; Mueller, P.; Mueller-Hilke, B.; Bader, R. The potential role of human osteoblasts for periprosthetic osteolysis following exposure to wear particles. *Int. J. Mol. Med.* **2011**, *28*, 1055–1063. [[CrossRef](#)]
49. Rho, J.Y.; Ashman, R.B.; Turner, C.H. Young's modulus of trabecular and cortical bone material: Ultrasonic and microtensile measurements. *J. Biomech.* **1993**, *26*, 111–119. [[CrossRef](#)]
50. Morgan, E.F.; Bayraktar, H.H.; Keaveny, T.M. Trabecular bone modulus-density relationships depend on anatomic site. *J. Biomech.* **2003**, *36*, 897–904. [[CrossRef](#)]
51. Sui, Q.; Meng, L.; Wang, S.; Li, P.; Yin, X.; Wang, L. Effect of Nb addition on mechanical properties and corrosion behavior of Ti6Al4V alloy produced by selective laser melting. *J. Mater. Res.* **2020**, *35*, 571–579. [[CrossRef](#)]
52. Ishimoto, T.; Hagihara, K.; Hisamoto, K.; Sun, S.-H.; Nakano, T. Crystallographic texture control of beta-type Ti–15Mo–5Zr–3Al alloy by selective laser melting for the development of novel implants with a biocompatible low Young's modulus. *Scr. Mater.* **2017**, *132*, 34–38. [[CrossRef](#)]
53. Liu, C.; Wang, Y.; Zhang, Y.; Zhang, L.-C.; Wang, L. Deformation mechanisms of additively manufactured TiNbTaZrMo refractory high-entropy alloy: The role of cellular structure. *Int. J. Plast.* **2024**, *173*, 103884. [[CrossRef](#)]
54. Reilly, D.T.; Burstein, A.H. The elastic and ultimate properties of compact bone tissue. *J. Biomech.* **1975**, *8*, 393–405. [[CrossRef](#)]
55. do Prado, R.F.; Esteves, G.C.; Santos, E.L.D.S.; Bueno, D.A.G.; Cairo, C.A.A.; de Vasconcellos, L.G.O.; Sagnori, R.S.; Tessarin, F.B.P.; Oliveira, F.E.; de Oliveira, L.D.; et al. In vitro and in vivo biological performance of porous Ti alloys prepared by powder metallurgy. *PLoS ONE* **2018**, *13*, e0196169. [[CrossRef](#)]
56. Wang, H.; Su, K.; Su, L.; Liang, P.; Ji, P.; Wang, C. Comparison of 3D-printed porous tantalum and titanium scaffolds on osteointegration and osteogenesis. *Mater. Sci. Eng. C Mater. Biol. Appl.* **2019**, *104*, 109908. [[CrossRef](#)]
57. Markhoff, J.; Weinmann, M.; Schulze, C.; Bader, R. Influence of different grained powders and pellets made of Niobium and Ti-42Nb on human cell viability. *Mater. Sci. Eng. C Mater. Biol. Appl.* **2017**, *73*, 756–766. [[CrossRef](#)]
58. Jonitz, A.; Lochner, K.; Lindner, T.; Hansmann, D.; Marrot, A.; Bader, R. Oxygen consumption, acidification and migration capacity of human primary osteoblasts within a three-dimensional tantalum scaffold. *J. Mater. Sci. Mater. Med.* **2011**, *22*, 2089–2095. [[CrossRef](#)]
59. Vermeulen, S.; Tahmasebi Birgani, Z.; Habibovic, P. Biomaterial-induced pathway modulation for bone regeneration. *Biomaterials* **2022**, *283*, 121431. [[CrossRef](#)]
60. Liu, S.; Zhang, L.; Li, Z.; Gao, F.; Zhang, Q.; Bianco, A.; Liu, H.; Ge, S.; Ma, B. Materials-Mediated In Situ Physical Cues for Bone Regeneration. *Adv. Funct. Mater.* **2023**, *34*, 2306534. [[CrossRef](#)]
61. Chen, C.; Zhu, Y.; Wang, R.; Han, Y.; Zhou, H. Effect of Controlled Microtopography on Osteogenic Differentiation of Mesenchymal Stem Cells. *J. Healthc. Eng.* **2022**, *2022*, 7179723. [[CrossRef](#)]
62. Lauria, I.; Kutz, T.N.; Böke, F.; Rütten, S.; Zander, D.; Fischer, H. Influence of nanoporous titanium niobium alloy surfaces produced via hydrogen peroxide oxidative etching on the osteogenic differentiation of human mesenchymal stromal cells. *Mater. Sci. Eng. C Mater. Biol. Appl.* **2019**, *98*, 635–648. [[CrossRef](#)] [[PubMed](#)]
63. Weißmann, V.; Drescher, P.; Seitz, H.; Hansmann, H.; Bader, R.; Seyfarth, A.; Klinder, A.; Jonitz-Heincke, A. Effects of Build Orientation on Surface Morphology and Bone Cell Activity of Additively Manufactured Ti6Al4V Specimens. *Materials* **2018**, *11*, 915. [[CrossRef](#)] [[PubMed](#)]
64. Sims, N.A.; Jenkins, B.J.; Quinn, J.M.W.; Nakamura, A.; Glatt, M.; Gillespie, M.T.; Ernst, M.; Martin, T.J. Glycoprotein 130 regulates bone turnover and bone size by distinct downstream signaling pathways. *J. Clin. Investig.* **2004**, *113*, 379–389. [[CrossRef](#)] [[PubMed](#)]
65. Ji, Z.; Wan, Y.; Wang, H.; Yu, M.; Zhao, Z.; Wang, T.; Ma, G.; Fan, S.; Liu, Z. Effects of surface morphology and composition of titanium implants on osteogenesis and inflammatory responses: A review. *Biomed. Mater.* **2023**, *18*, 042002. [[CrossRef](#)]

Disclaimer/Publisher's Note: The statements, opinions and data contained in all publications are solely those of the individual author(s) and contributor(s) and not of MDPI and/or the editor(s). MDPI and/or the editor(s) disclaim responsibility for any injury to people or property resulting from any ideas, methods, instructions or products referred to in the content.

Article

Multifunctional Hybrid Material for Endoprosthetic Implants Based on Alumina-Toughened Zirconia Ceramics and Additively Manufactured TiNbTa Alloys

Jan-Oliver Sass ^{1,*}, Paul Henke ¹ , Aurica Mitrovic ², Markus Weinmann ³ , Daniel Kluess ^{1,4} , Jan Johannsen ⁵ , Marie-Luise Sellin ¹, Ulrich Lembke ⁶, Daniel Reimer ⁷, Cornelia Lork ², Anika Jonitz-Heincke ¹ and Rainer Bader ¹

¹ Research Laboratory for Biomechanics and Implant Technology, Department of Orthopaedics, Rostock University Medical Center, Doberaner Straße 142, D-18057 Rostock, Germany; paul.henke@med.uni-rostock.de (P.H.)

² ZM Praezisionsdentaltechnik GmbH, Breite Str. 16, D-18057 Rostock, Germany; cornelia.lork@zm-dental.de (C.L.)

³ TANIOBIS GmbH, Im Schleeke 78-91, D-38642 Goslar, Germany; markus.weinmann@taniobis.com

⁴ INNOPROFF GmbH, Joachim-Jungius-Straße 9, D-18059 Rostock, Germany

⁵ Fraunhofer Research Institution for Additive Manufacturing Technologies IAPT, Am Schleusengraben 14, D-21029 Hamburg, Germany; jan.johannsen@iapt.fraunhofer.de

⁶ DOT GmbH, Charles-Darwin-Ring 1A, D-18059 Rostock, Germany

⁷ FMZ GmbH, Charles-Darwin-Ring 3A, D-18059 Rostock, Germany

* Correspondence: jan-oliver.sass@med.uni-rostock.de; Tel.: +49-381-494-9338

Abstract: Aseptic implant loosening after a total joint replacement is partially influenced by material-specific factors when cobalt–chromium alloys are used, including osteolysis induced by wear and corrosion products and stress shielding. Here, we aim to characterize a hybrid material consisting of alumina-toughened zirconia (ATZ) ceramics and additively manufactured Ti-35Nb-6Ta (TiNbTa) alloys, which are joined by a glass solder. The structure of the joint, the static and fatigue shear strength, the influence of accelerated aging, and the cytotoxicity with human osteoblasts are characterized. Furthermore, the biomechanical properties of the functional demonstrators of a femoral component for total knee replacements are evaluated. The TiNbTa-ATZ specimens showed a homogenous joint with statistically distributed micro-pores and a slight accumulation of Al-rich compounds at the glass solder–TiNbTa interface. Shear strengths of 26.4 ± 4.2 MPa and 38.2 ± 14.4 MPa were achieved for the TiNbTa-ATZ and Ti-ATZ specimens, respectively, and they were not significantly affected by the titanium material used, nor by accelerated aging ($p = 0.07$). All of the specimens survived 10^7 cycles of shear loading to 10 MPa. Furthermore, the TiNbTa-ATZ did not impair the proliferation and metabolic activity of the human osteoblasts. Functional demonstrators made of TiNbTa-ATZ provided a maximum bearable extension–flexion moment of 40.7 ± 2.2 Nm. The biomechanical and biological properties of TiNbTa-ATZ demonstrate potential applications for endoprosthetic implants.

Keywords: joint arthroplasty; total knee replacement; implant; aseptic loosening; material joining; alumina-toughened zirconia; beta titanium; glass soldering; additive manufacturing



Citation: Sass, J.-O.; Henke, P.; Mitrovic, A.; Weinmann, M.; Kluess, D.; Johannsen, J.; Sellin, M.-L.; Lembke, U.; Reimer, D.; Lork, C.; et al. Multifunctional Hybrid Material for Endoprosthetic Implants Based on Alumina-Toughened Zirconia Ceramics and Additively Manufactured TiNbTa Alloys. *Materials* **2024**, *17*, 1838. <https://doi.org/10.3390/ma17081838>

Academic Editors: Ghais Kharmanda and Ke Yang

Received: 14 March 2024

Revised: 10 April 2024

Accepted: 11 April 2024

Published: 16 April 2024



Copyright: © 2024 by the authors. Licensee MDPI, Basel, Switzerland. This article is an open access article distributed under the terms and conditions of the Creative Commons Attribution (CC BY) license (<https://creativecommons.org/licenses/by/4.0/>).

1. Introduction

Aseptic implant loosening is the main reason for the revision of total joint replacements [1]. Implant-material-related complications are associated with wear particles, corrosion products, and the mechanical mismatch of the materials to the human bone [2,3]. Metal wear particles can stimulate osteoclastic bone resorption [2] and released metal ions, e.g., from cobalt–chromium and titanium alloys (Co^{2+} , Cr^{3+} , Al^{3+} , and V^{2+}), may cause adverse local [4–6] and systematic biological responses [7–11]. Commonly used implant materials lead to the mechanical loading alteration of the periprosthetic bone (i.e., stress shielding). The mechanical stimulus on the bone tissue and cells is reduced; thus, the bone

remodeling is shifted toward resorption [2,3]. These effects lead to periprosthetic bone loss, thereby potentially causing osteolysis, implant loosening, and increased periprosthetic fracture risk [12].

Multifunctional hybrid implant materials have been investigated to address these issues [13–21]. These materials are supposed to combine the advantageous properties of oxide ceramics at the articulating surfaces of the artificial joint and titanium (Ti) alloys at the bone–implant interface. Thus, high wear and corrosion resistance with a lower risk of stress shielding and improved osseointegration can be achieved [13,15,17,22]. In previous studies, functionally graded materials manufactured by spark plasma sintering have been investigated [13–17,22]. They are composed of a pure ceramic phase (e.g., Al_2O_3 or Y_2O_3 -stabilized ZrO_2), graded ceramic–titanium phases with continuously decreasing ceramic content, and a titanium or Ti-6Al-4V phase. Other approaches have used laser-engineered net shaping to manufacture Ti6Al4V- Al_2O_3 [18] hybrids or glass solders to join solid ceramic- and titanium-based components [20,21].

The glass soldering of bioceramics such as Al_2O_3 or ZrO_2 and commercially pure titanium (cp-Ti) was originally intended for dental applications [23], but it has since demonstrated applicability to endoprosthetic implant materials like alumina-toughened zirconia (ATZ) ceramics and Ti-6Al-4V [21]. Processing such hybrid materials involves the application of a biocompatible silica-based glass [21,24] to the joining surfaces, as well as a subsequent firing to melt the glass solder. The main reasons for a stable and durable connection are the formation of reaction layers during a firing that is comparable to other metal–ceramic composites [20,25], and the mechanical interlocking between glass solder and the ceramic or the metal part [20]. For example, Mick et al. [21] used a glass solder (main components: SiO_2 , Al_2O_3 , Na_2O , and KO_2) to fabricate Ti6Al4V-ATZ hybrid materials, and they reported a bending strength of 118 ± 33 MPa. In addition, Markhoff et al. [26] showed a good interaction of human osteoblasts with a similar glass solder that was applied as a coating on ATZ bulk material. Nevertheless, the transformation of this technology to endoprosthetic implants, such as the femoral component of a total knee replacement, presents challenges in joining larger- and complex-shaped surfaces.

While the number of ceramic systems for endoprosthetic implant applications is limited so far, a variety of metallic implant materials is available. In this regard, Ti and its alloys are state-of-the-art materials that feature good biocompatibility, i.e., cell tolerance and osseointegration [27–30]. Standard titanium materials are commercially pure Ti (cp-Ti) and Ti-6Al-4V [27,30], where the latter provides high survival rates for endoprosthetic implants [31]. However, both suffer from their stiffness, which is expressed by a high elastic modulus of ~ 110 GPa [27], which thus poses a major stress shielding risk [32,33]. It has also been discussed that released aluminum and vanadium ions potentially cause adverse biological effects in the organism [9,11,34].

Consequently, extensive studies have been performed to explore advanced biocompatible Ti-based alloys, featuring a favorable combination of high elasticity (a low Young's modulus), high strength, good fatigue properties, and biocompatibility. Hence, binary, ternary, quaternary, and even multi-component high-entropy Ti base alloys have been developed for use as metallic implant materials [35–51].

The most thoroughly investigated binary Ti alloy systems are Ti/Nb [35–38] and Ti/Ta [39–41,52]. Their phase composition and mechanical properties depend on the Ti:(Nb/Ta) ratio. Ti-rich alloys predominantly crystallize hexagonally with an α or α' crystal structure. Both Nb and Ta are so-called β stabilizers and, accordingly, Nb or Ta-rich alloys crystallize in the cubic-body-centered β structure [53,54]. Moreover, an orthorhombic α'' crystal structure and $\alpha + \beta$ compositions were reported. The mechanical properties of α and β can be quite different: alloys possessing the α phase are usually stronger, whereas those with β structure are more elastic, thereby providing better mechanical compatibility with the cortical and trabecular bone [27,28,55].

Combining Ti with both Nb and Ta leads to ternary Ti/Nb/Ta alloys. They have also attracted scientific attention, and the diversity of materials and compositions is much

higher than in binary subsystems. Some alloy compositions have even been proven to exhibit a shape memory effect or superelasticity [43,46]. Typical Ti/Nb/Ta alloys that have been investigated for biomedical applications are, e.g., β -phase Ti-25Nb-25Ta, which has been processed by cold crucible levitation melting [42]. This alloy revealed a low Young's modulus of about 55 GPa, as well as good ductility and strength, i.e., 20% elongation at fracture and about 530 MPa ultimate tensile strength. The Ti-30Nb-18Ta, which was arc-melted, solution-treated, and then 50% cold-rolled, predominantly consisted of the orthorhombic α'' martensitic phase embedded in a β -phase matrix [44]. An important finding was the efficient passivation of Ti-30Nb-18Ta due to the presence of Nb and Ta, which form chemically inert native oxide surfaces that protect the alloys from the further oxidation of, e.g., body fluids.

Recently, Ti/Nb/Ta alloys in the Ti-rich domain were described. Materials with a Ti-xNb-6Ta ($x = 20, 27, \text{ and } 35$) chemical composition were especially developed for application in additive manufacturing processes [45]. The goal was to produce patient-specific dental and orthopedic implants with the highest level of biocompatibility using laser beam powder bed fusion (PBF-LB/M). It turned out that the compressive modulus could be lowered to ~ 43 GPa in the case of Ti-20Nb-6Ta [47]. This is in the range of the most elastic Ti/Nb/Ta/Zr (TNTZ) [46,48,49,51,56] alloys, which are also referred to as gum metal [50] due to their high elasticity, or to Ti/Nb/Zr/Sn (TNZS), which possess similar characteristics [57,58]. However, the chemistry and controllability across the entire process chain is significantly simpler for ternary Ti/Nb/Ta alloys compared to TNTZ, which is an important factor with regard to commercial applications.

The present study aims to characterize hybrid TiNbTa-ATZ specimens using additively manufactured Ti-35Nb-6Ta components that are joined to ATZ using a biocompatible silica-based glass solder. The manufactured TiNbTa-ATZ joints were structurally and chemically analyzed by backscatter electron (BSE) microscopy and energy-dispersive X-ray spectroscopy (EDX). Furthermore, the hybrid material was characterized by mechanical testing (i.e., of static and fatigue shear stress), and the influence of artificially aging on static shear strength was analyzed. Hybrid Ti-ATZ specimens were used as a reference. In addition, the cytotoxicity of TiNbTa-ATZ specimens was evaluated and compared with Ti-ATZ and Co-28Cr-6Mo specimens using an elution assay and human osteoblasts. Furthermore, a simplified functional implant demonstrator of a hybrid material-based femoral component was fabricated, structurally characterized, and analyzed for its mechanical strength under biomechanical loading using gait cycles, as well as loading to failure.

2. Materials and Methods

2.1. Manufacturing of the Hybrid Material

The hybrid material specimens made of slip-casted ATZ (Koebel Engineering, Dachsen, Switzerland), and the TiNbTa were manufactured and joined by applying glass soldering. Hybrid Ti-ATZ materials were used as a reference since glass soldering was initially developed to join cp-Ti and zirconia-based oxide ceramics in the field of dentistry [23]. The TiNbTa components were additively manufactured using PBF-LB/M. The spherical TiNbTa powder was produced by electrode induction melting gas atomization (EIGA), which was conducted under a purified argon (4.6, Linde GmbH, Pullach, Germany) atmosphere from pre-alloyed electrodes (TANIOBIS GmbH, Goslar, Germany) [45]. In a previous study with similar powder, the measured chemical composition, which was determined by inductively coupled plasma optical emission spectroscopy (ICP-OES) was 58.87 wt. % Ti, 34.45 wt. % Nb, and 5.98 wt. % Ta [45]. PBF-LB/M was performed using a DMP350 Flex (3D Systems Corp., Rock Hill, SC, USA) equipped with a 1 kW single-mode laser (YLR-1000-WC-Y14, IPG Laser GmbH, Burbach, Germany) under an argon gas atmosphere to prevent oxidation. The scanning speed was $1500 \text{ mm} \times \text{s}^{-1}$, the laser power was 170 W, the layer thickness was 0.3 mm, and the hatch distance was 69 μm . Similar powder, devices, and process parameters led to dense parts with a homogenous element distribution and a monocrystalline β -phase [45]. After additive manufacturing, all TiNbTa components were

heat-treated for 4 h at 1200 °C in a vacuum. Within the preliminary tests, we observed that this was necessary to reduce the residual stresses during glass soldering. Furthermore, the end faces of the cylindrical TiNbTa specimens used for shear testing were machined to meet the parallelism requirements of the joining surfaces.

The main components of the silica-based glass solder (DCMhotbond fusio-12, DCM Dental Creative Management GmbH, Rostock, Germany) were SiO₂ (63–67 wt. %), Al₂O₃ (6–9 wt. %), K₂O (6–9 wt. %), and Na₂O (6–9 wt. %). The glass solder had a coefficient of thermal expansion (CTE) of $10.0 \times 10^{-6} \text{ K}^{-1}$, a melting temperature of 450 °C, and a bending strength at room temperature of $\geq 50 \text{ MP}$ (provided by ZM Praezisionsdentaltechnik GmbH, Rostock, Germany). The ATZ ceramics (provided by Koebel Engineering, Dachsen, Switzerland) had a CTE of $7.8\text{--}8.1 \times 10^{-6} \text{ K}^{-1}$. Further, the CTE of Ti-35Nb-6Ta (provided by TANIOWIS GmbH, Goslar, Germany) was temperature-dependent and ranged, in the relevant temperature regime of 20 °C to 450 °C (i.e., the melting point of the glass solder), from $8.2 \times 10^{-6} \text{ K}^{-1}$ to $9.3 \times 10^{-6} \text{ K}^{-1}$. Similar to previous studies [21,24], the soldering was performed in a furnace and according to the guidelines provided by DCM Dental Creative Management GmbH, Rostock, Germany. Before glass soldering, the joining surfaces were sandblasted (110 μm Al₂O₃ at 4 bar), cleaned in an ultrasonic bath in ethanol, and then primed with a thin layer of the glass solder. After sandblasting, the TiNbTa and cp-Ti components had an average roughness (measured using a VK-X250 laser scanning microscope, Keyence Corporation, Osaka, Japan) of $1.5 \pm 0.1 \mu\text{m}$ and $1.7 \pm 0.1 \mu\text{m}$, respectively. Finally, a glass solder paste was applied to the joining surfaces and fired at 820 °C for 5 min in a vacuum using a heating and cooling rate of $20 \text{ K}\cdot\text{min}^{-1}$. The joined interface of the TiNbTa-ATZ specimens was analyzed by BSE and EDX using an SEM JSM6490 (Jeol, Akishima, Tokyo, Japan) equipped with an X-Flash SEM 4010 (Bruker Nano GmbH, Berlin, Germany) for structural and chemical analysis.

2.2. Shear Testing, Artificial Aging, and Fracture Analysis

The static and dynamic shear testing of the hybrid materials was performed according to the relevant standards [59–61]. The dimensions of the shear test specimens are shown in Figure 1.

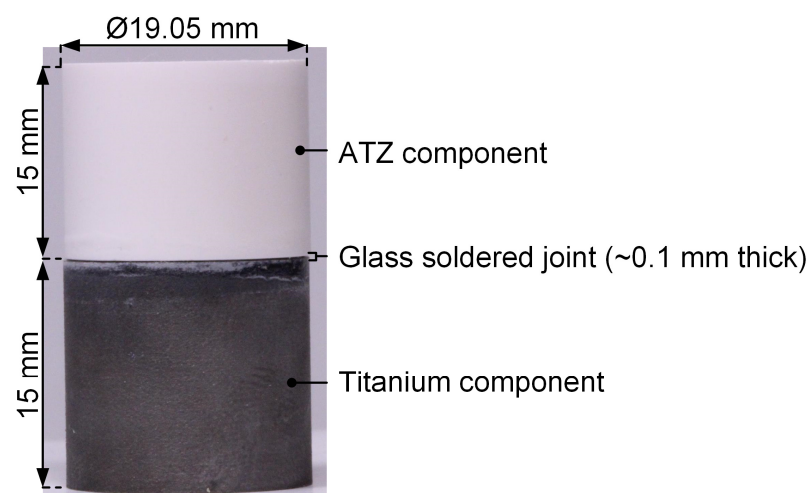


Figure 1. The shear specimens were based on hybrid materials consisting of an alumina-toughened zirconia (ATZ) ceramic and an additively manufactured Ti-35Nb-6Ta (TiNbTa) or a cp-Ti joined with a silica-based glass solder.

Furthermore, the influence of artificial aging (0.5 MPa, 70 °C, 14 days [62]) on the static shear strength was evaluated. Accordingly, six different groups (Table 1) were characterized, and each group contained $n = 5$ specimens.

Table 1. Overview of the mechanically tested groups, the used hybrid material, the test specifications, and the measured cross-section at the soldered joint.

Group	Material	Specifications	Cross-Section [mm ²]
1	TiNbTa-ATZ	Static shear test	279.4 ± 0.1
2	Ti-ATZ	Static shear test	280.0 ± 0.3
3	TiNbTa-ATZ	Accelerated aging followed by static shear test	281.0 ± 1.1
4	Ti-ATZ	Accelerated aging followed by static shear test	280.4 ± 0.4
5	TiNbTa-ATZ	Fatigue shear test	280.3 ± 0.8
6	Ti-ATZ	Fatigue shear test	281.9 ± 1.2

The static shear tests were conducted using a universal testing machine (Zwick 50kN RetroLine, Zwick Roell, Ulm, Germany). The specimens were loaded until fracture at a rate of 2.5 mm × min⁻¹. The fatigue tests were performed using an electro-dynamic testing machine (ElectroForce 3510, TA Instruments—Waters LLC, Eden Prairie, MN, USA) with a sinusoidal load between 1 MPa and 10 MPa and a frequency of 10 Hz [63]. Furthermore, 10⁷ cycles were defined as a successful test [59].

After mechanical testing, the fractured surfaces of all specimens were analyzed with a digital microscope (VHX-6000) and laser scanning microscope (VK-X250) (both obtained from Keyence Corporation, Osaka, Japan) to determine the causes of fracture.

2.3. Biological Characterization

For the biological characterization of the hybrid material specimens (TiNbTa-ATZ and Ti-ATZ), cytotoxicity measurements were performed by an elution assay, and commercially used Co-28Cr-6Mo specimens served as the negative control. The specimens had a diameter of 12 mm and were 5 mm in height. The heat-sterilized specimens were first covered with 838 µL of calcium-free Dulbecco's Modified Eagle's Medium (DMEM) per sample, and they were incubated at 37 °C and 5% CO₂ for 14 and 21 days. A medium control without samples was included. The medium eluates were stored at −20 °C until use.

For the cytotoxicity assays, human osteoblasts were isolated from the femoral heads of the patients undergoing total hip arthroplasty according to an established protocol by Lochner et al. [64]. Femoral heads were provided after informed consent was obtained from the patients. The study was approved by the ethics committee of the University Medical Center Rostock (A 2010-0010). Experiments were performed with human osteoblasts from a total of six donors (n = 8, female: n = 6, mean age: 61 ± 7.3 years; male: n = 2, mean age: 53.5 ± 3.5 years). Cells were cultured under standard culture conditions at 37 °C and 5% CO₂ in a calcium-free DMEM supplemented with 10% fetal calf serum (FCS; both: PAN-Biotech, Aidenbach, Germany), 1% amphotericin B, 1% penicillin-streptomycin, and 1% HEPES buffer (all: Sigma-Aldrich, Munich, Germany). To maintain the osteogenic phenotype, 10 mM of β-glycerophosphate, 50 µg × mL⁻¹ of ascorbic acid, and 100 nM of dexamethasone were added to the cell culture medium (all: Sigma-Aldrich, Munich, Germany). Moreover, 10,000 osteoblasts per well were seeded in a 96-well plate (Thermo Fisher Scientific Inc., Waltham, MA, USA).

The eluates of the hybrid materials, the Co-28Cr-6Mo specimens, and controls were thawed and diluted 1:1 with a fresh medium containing osteogenic additives to use them for the exposure of the osteoblastic cells. Osteoblasts were incubated with 150 µL of the diluted eluate for 24 h. Afterward, the viability of osteoblasts after incubation was evaluated via the metabolic activity assay water-soluble tetrazolium salt (WST-1; Takara Bio, Saint-Germain-en-Laye, France) and the CyQUANT™ NF Cell Proliferation Assay (ThermoFisher Scientific, Waltham, MA, USA). First, the metabolic activity was determined. Then, the diluted eluates were removed and the cells were washed with PBS. The cells were then incubated with a defined volume of WST-1/medium reagent (1:10 ratio) at 37 °C and 5% CO₂. After an incubation period of 30 min, 100 µL of the supernatants were transferred to a 96-well cell culture plate, and the absorbance at 450 nm (reference wavelength: 630 nm)

was measured in a microplate reader (Tecan Reader Infinite[®] 200 Pro, Tecan Trading AG, Maennedorf, Switzerland). To determine the absolute cell number, the CyQUANT[™] Cell Proliferation Assay was performed according to the manufacturer's guidelines. The same cells for which the metabolic activity was previously determined were used. Cells were covered with 100 μ L of 1 \times Dye Binding Solution (consisting of 1:500 Dye Reagent and 1 \times HBSS), incubated at 37 $^{\circ}$ C, and protected from light. After 60 min, the fluorescence intensity was measured at 530 nm (excitation wavelength: 485 nm) using the Tecan Infinite[®] 200 Pro reader. A cell number calibration curve was generated using pre-defined cell numbers in duplicate to relate the fluorescence signal to the actual cell number.

2.4. Biomechanical Characterization of Functional Demonstrators

2.4.1. Demonstrator Manufacturing

Based on the geometries of commercially available total knee endoprostheses [65], a simplified functional demonstrator was designed in Creo Parametrics 10.0.0.0 (PTC, Boston, MA, USA) to gain experience with more complex-shaped soldering components. The simplification was necessary to achieve the next development step. The functional demonstrator represented one condyle of the tibiofemoral joint (Figure 2) with an outer radius of 30 mm and a depth of 22.5 mm. Since a homogeneous joint gap is crucial for the glass soldering process, a frame and spacers were designed on the titanium component with a height of 0.1 mm. The titanium-based component was further designed to enable clamping of the functional demonstrator during the biomechanical testing, and geometric cutouts were designed to reduce the amount of heat absorption during the firing process. A detailed depiction of the dimensions is shown in Appendix A.

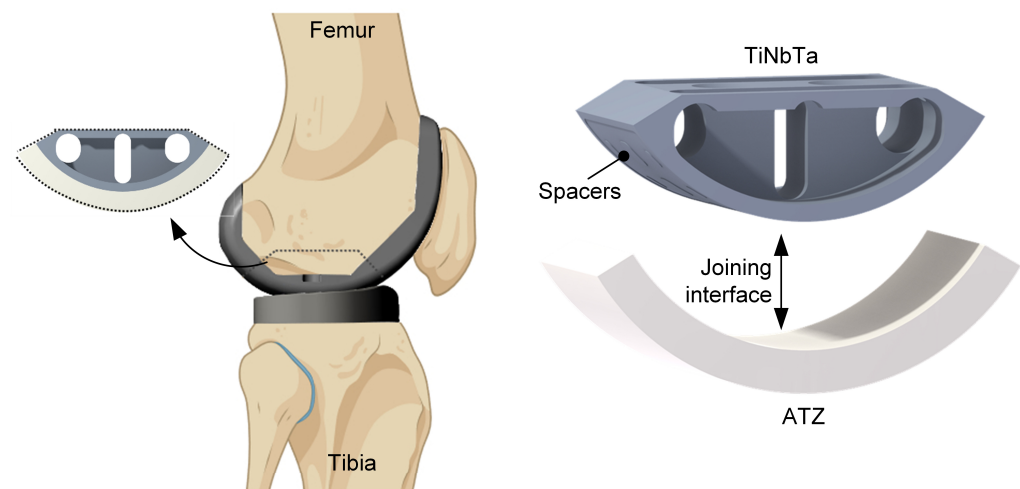


Figure 2. Design of the simplified functional demonstrator of a hybrid-material-based femoral component for a total knee replacement resembling a part of the tibiofemoral joint. The hybrid material is formed by a glass soldering of the additively manufactured TiNbTa to ATZ ceramics, and the joining surface of TiNbTa is functionalized with spacers that are 0.1 mm in height to ensure a homogeneous joint gap (created with Biorender.com).

For glass soldering, the joint surfaces were sandblasted (110 μ m Al_2O_3 at 4 bar) and cleaned with ethanol in an ultrasonic bath for 3 min. The average roughness values (measured by laser scanning microscopy) of the sandblasted TiNbTa (PBF-LB/M) and cp-Ti (CNC machined) components were $5.8 \pm 2.0 \mu\text{m}$ and $1.9 \pm 0.3 \mu\text{m}$, respectively. In general, the soldering followed the same procedure as described in Section 2.1, but a more extensive priming of the surfaces was conducted to omit the pore formation in the soldered joint. The first priming was performed by spray coating with the glass solder paste. A firing process of the individual parts was subsequently conducted to, respectively, establish the joint between the glass solder, the ATZ, and the titanium-based material. After the first priming

of the titanium-based component, the soldering surface was polished (600 μm and 1000 μm grit), covered with glass solder paste, and then fired again. This process was repeated two times to fill the room between the spacers with the glass solder. In Figure 3, the initial additively manufactured TiNbTa component along with the spray-coated specimen and the final stage of priming are illustrated.

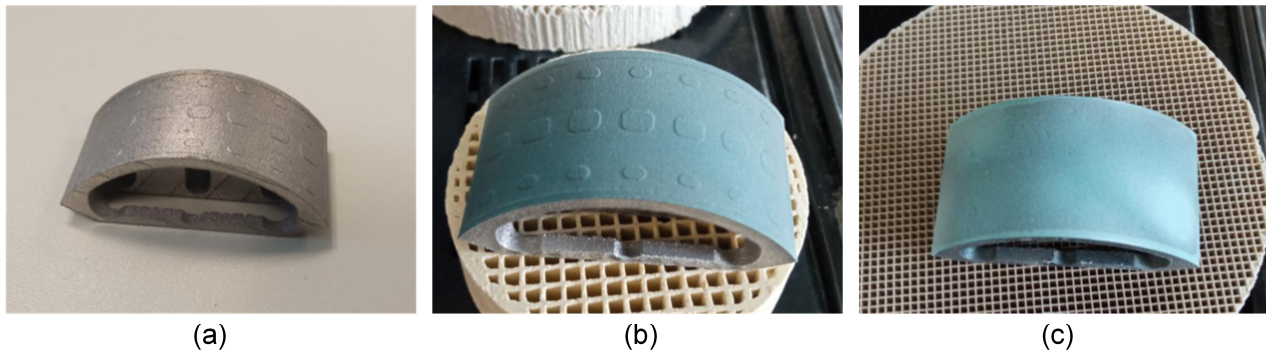


Figure 3. The consecutive steps taken to prime the Ti-based component (TiNbTa or cp-Ti) of the hybrid-material-based functional demonstrator with (a) an untreated specimen, (b) a specimen coated with the glass solder, and (c) a completely primed specimen by stepwise firing and polishing the glass solder to fill the gap between the designed spacers with the glass solder. The glass solder was dyed blue for better visualization.

The soldering of the ATZ and the TiNbTa or cp-Ti component was conducted at 820 $^{\circ}\text{C}$ for 5 min in a vacuum. The structure quality of the joint interface was analyzed by conducting an electron microscopy of a polished cross-section of the hybrid TiNbTa-ATZ specimen.

2.4.2. Biomechanical Characterization

The biomechanical characterization of the functional demonstrators comprised two consecutive tests. First, the specimens were loaded for 10,000 walking cycles; second, the same specimens were used to evaluate the maximum extension–flexion moment. Each group of either TiNbTa-ATZ or Ti-ATZ hybrids contained $n = 3$ specimens.

The 10,000 walking cycles were applied using a 6-degree-of-freedom joint simulator (VIVOTM, Advanced Mechanical Technology, Watertown, MA, USA), which was used in accordance with ISO standard 14243-3:2014 [61]. Therefore, the extension–flexion, internal–external rotation, and anterior–posterior translation were position-controlled, and the superior–inferior direction was force-controlled (axial force). The abduction–adduction rotation and medial–lateral translation remained unloaded. The functional demonstrators were articulated with cylindrical ultra-high-molecular-weight polyethylene specimens with a flat surface. Silicone oil (Typ 350, Caesar & Loretz GmbH, Hilden, Germany) served as a lubricant. The test setup and applied rheonomic constraints are shown in Figure 4a. Moreover, the specimens that survived the dynamic loading were rotationally loaded until failure with $0.1^{\circ} \times \text{s}^{-1}$ (Figure 4b) to simulate an extension–flexion moment. The ATZ component was constrained in the yz-plane (sagittal plane), and the moment was applied through the titanium component and the rotational center of the functional demonstrator.

2.5. Statistical Analysis

Statistical analysis of the results was performed in GraphPad Prism 9.2 (GraphPad Software, San Diego, CA, USA), and $p < 0.05$ was used as the level of significance. The results of the shear testing were checked for significant differences using the Mann–Whitney U Test. For the cytotoxicity tests, comparisons between the experimental groups were performed using 2-way ANOVA and the Bonferroni multiple comparison test. All data are presented as individual values with median and interquartile ranges.

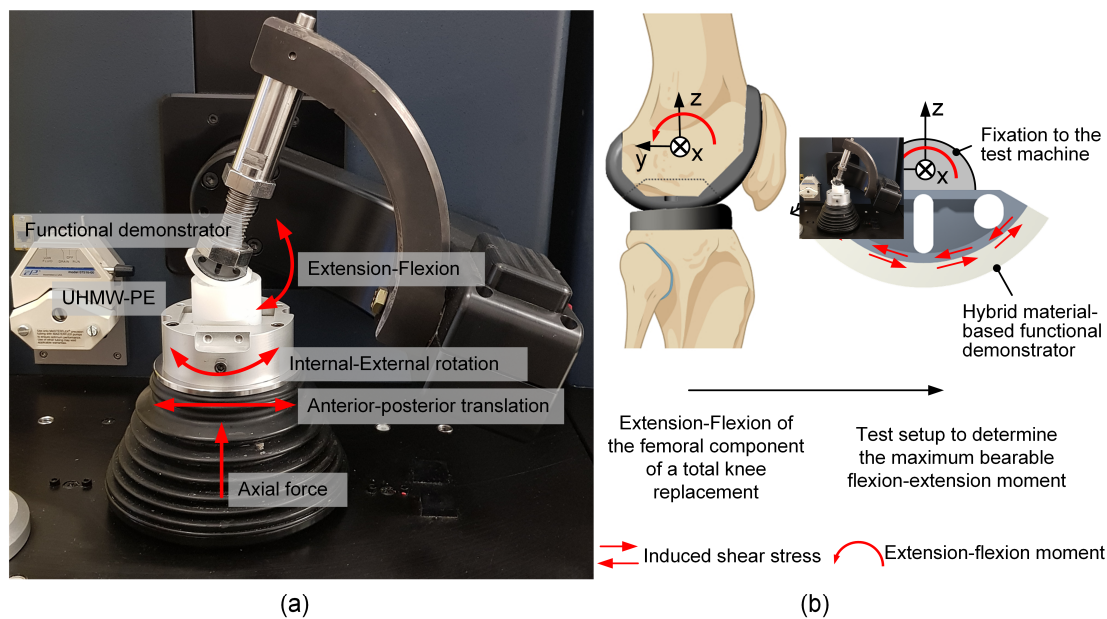


Figure 4. Biomechanical characterization of the hybrid-material-based (glass soldered TiNbTa-ATZ or Ti-ATZ) functional demonstrators of the femoral component of a total knee replacement: (a) biomechanical loading of the walking cycle in the VIVO™ joint simulator and (b) schematic illustration of the flexion movement of the tibiofemoral joint and the derived test setup to characterize the maximum bearable extension–flexion moment (created with Biorender.com).

3. Results

3.1. Structural, Chemical, and Mechanical Characterization

The structural and chemical analysis by electron microscopy of a polished cross-section of a TiNbTa-ATZ specimen is shown in Figure 5. The BSE image in Figure 5a points to the fact that the soldering occurred very homogeneously. The thickness of the solder was slightly below 100 μm . Occasionally, spherical pores were visible in the solder with diameters in the single-digit micro region, as evident from the magnified spot displayed in Figure 5d. The elemental mapping of the TiNbTa component (Figure 5b) displayed a homogenous element distribution of the constituting elements. In contrast to the as-atomized TiNbTa powder, no segregation in the Ti- or Nb/Ta-enriched dendrite-type structures was observed. The ATZ (Figure 5c) represents a two-phase material in which sub-micron Al_2O_3 particles were evenly embedded in a ZrO_2 matrix. The element mapping of the solder displayed in Figure 5e reveals a local accumulation of aluminum at the glass solder–TiNbTa interface. Besides these features, the glass solder was constituted by a homogenous SiO_2 , K_2O , and Na_2O matrix containing Al_2O_3 segregations (Figure 5f).

The static shear strength between the tested groups was not statistically different ($p = 0.07$) (see Figure 6a), and all specimens showed a brittle fracture behavior. The representative stress–displacement curves are shown in Appendix B. The static shear strength of the TiNbTa-ATZ and Ti-ATZ specimens (Group 1 vs. Group 2) was 26.4 ± 4.2 MPa and 38.2 ± 14.4 Mpa, respectively. The static shear strength of the artificially aged TiNbTa-ATZ and Ti-ATZ specimens (Group 3 vs. Group 4) was 32.1 ± 1.4 Mpa and 44.1 ± 9.7 Mpa, respectively. Both hybrid materials (Groups 5 and 6) survived 10^7 cycles at a 10 Mpa dynamic shear loading without fracture.

A mixed mode of failure in the Ti-based bulk material (cohesive failure) and failure in the glass solder (adhesive failure) was observed in different proportions (Figure 6b). Cohesive failure was visible as a deposition of the material on the ATZ component, as can be seen by the depth profile in Figure 6e. Furthermore, it was observed that specimens with a predominantly cohesive failure had higher shear strengths compared to the specimens that mainly fractured in the glass solder (Figure 6b). The pore formation locally hindered

the bonding of the materials, thereby causing imperfections in the soldered joint. These imperfections were randomly distributed across the surfaces and were either spherical (Figure 6f–h) or formed a networked or branched structure (Figure 6i–k).

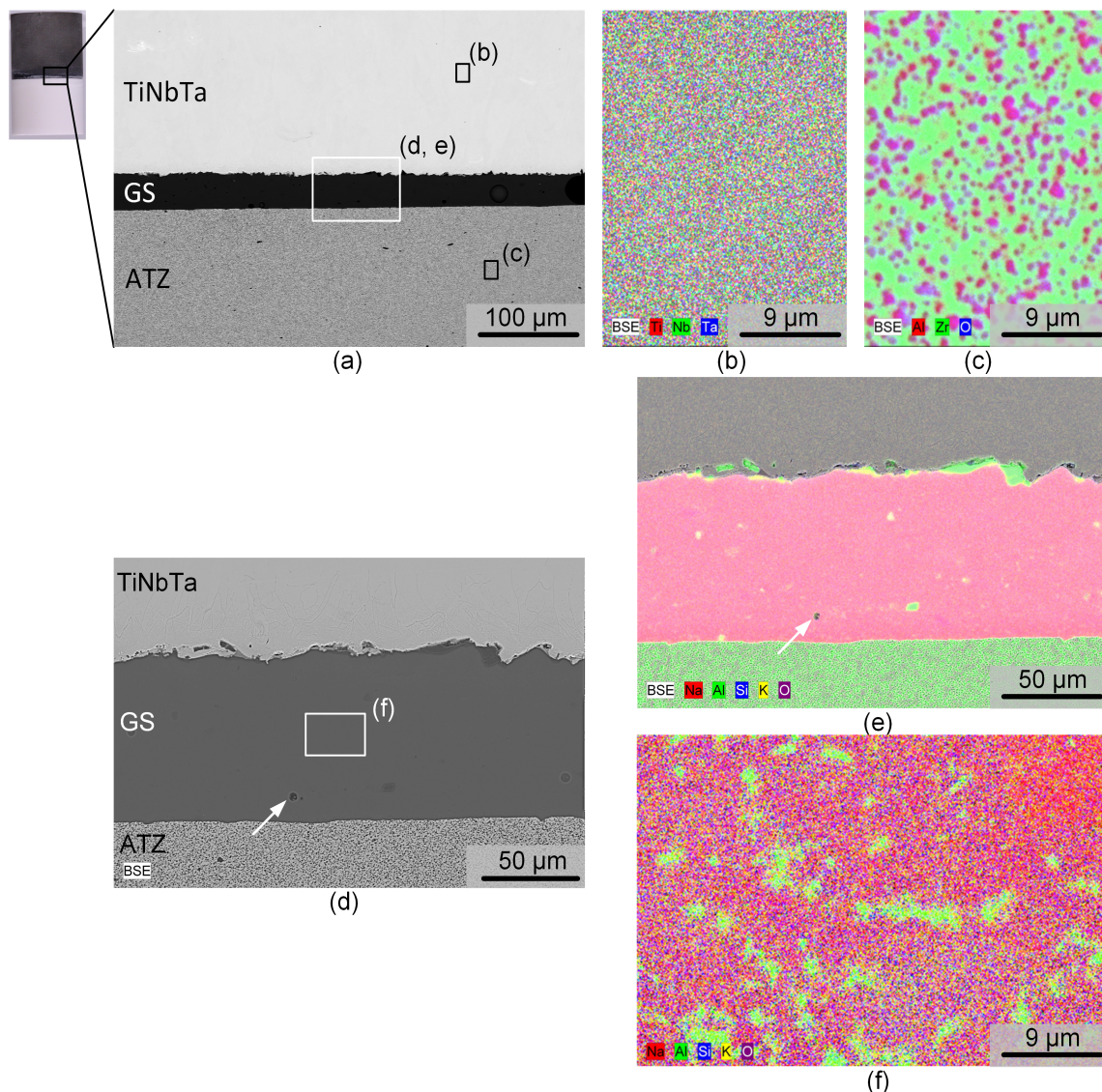


Figure 5. Electron microscopic images of a hybrid material of an alumina-toughened zirconia (ATZ) ceramic and additively manufactured Ti-35Nb-6Ta (TiNbTa) that were joined using a silica-based glass solder. (a,d) Backscatter electron microscopy of the investigated cross-section at different magnifications. (b,c,e,f) Element distribution in the TiNbTa alloy, (b) the ATZ ceramic, and (c) the glass solder (e,f). Pores are indicated by white arrows.

3.2. Biological Characterization

An eluate test was performed to indirectly determine the cytotoxicity of the hybrid materials. For this purpose, specimens of the hybrids and Co-28Cr-6Mo (the negative control) were incubated in osteoblastic cell culture medium over a period of 14 and 21 days. Afterward, the eluates were used for the cell experiments.

The eluates from the hybrid material specimens did not affect the proliferation of human osteoblasts (Figure 7a). No difference could be detected between the medium controls (dashed line) or between the incubation times of the eluates. However, a slight reduction in cell number was detected for the cells exposed to the 14-day eluates of the Co-28Cr-6Mo alloy.

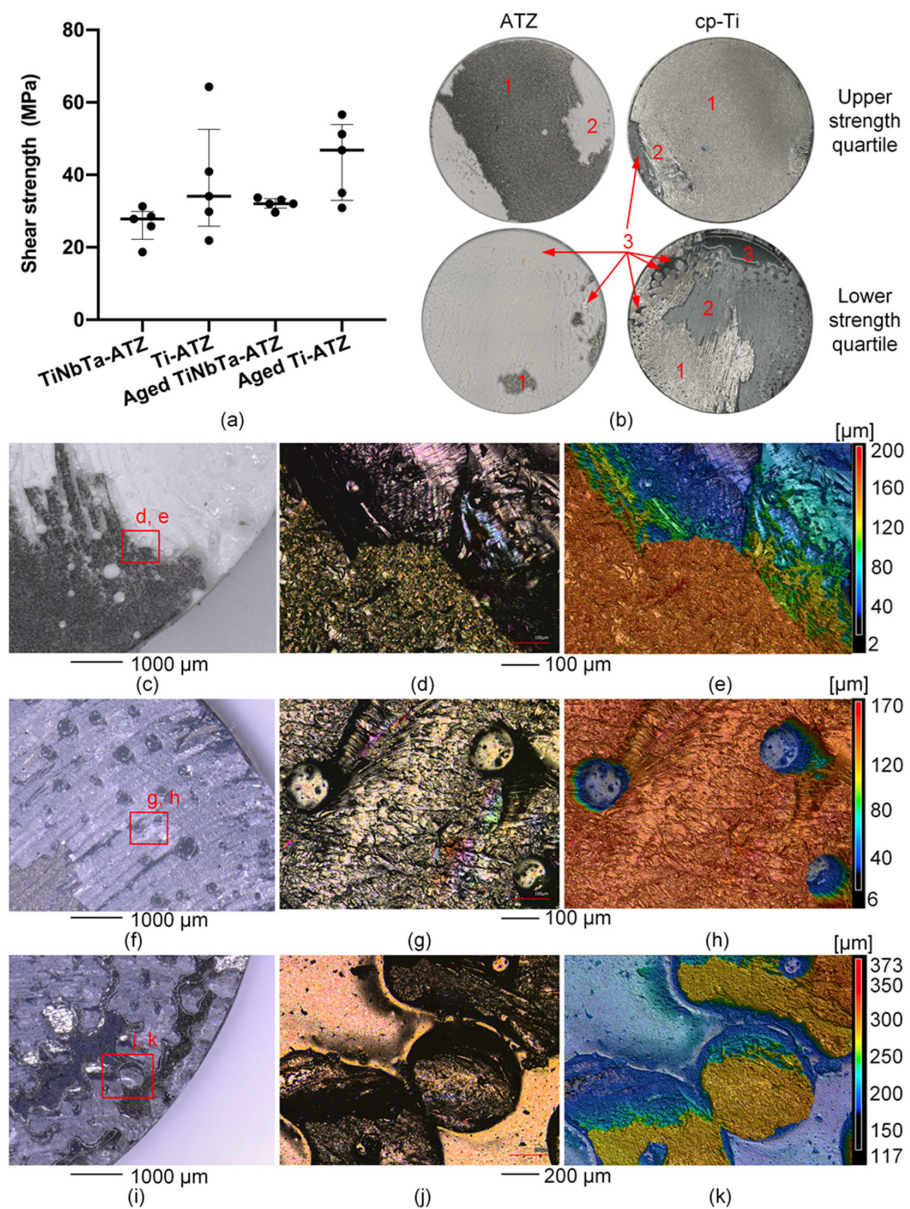


Figure 6. Results of the static shear testing and microscopy of the fracture surfaces of the glass-soldered TiNbTa-ATZ or Ti-ATZ hybrids. (a) The static shear strength (the data are presented as single values (indicated by bullets) with median and interquartile ranges). (b) The representative fracture surfaces of the specimens in the upper and lower quartile of the static strength (1: cohesive failure of the Ti-based component, 2: adhesive failure of the glass solder, and 3: imperfections in the glass solder due to spherical pores). (c–e) The microscopic images and depth profile of an ATZ fracture surface of a Ti-ATZ specimen indicating the cohesive failure of the cp-Ti, which led to the deposition of the bulk material on the ATZ surface. (d–h) The microscopic images and depth profile of a TiNbTa fracture surface of a Group 1 specimen indicating spherical pores in the glass solder. (i–k) The microscopic images and depth profile of an cp-Ti fracture surface of a Group 4 specimen indicating networked or branched structures in the glass solder.

The metabolic activity of osteoblasts was not influenced after exposure to the 14-day eluates (Figure 7b). In contrast, the incubation of cells with the 21-day eluates of the TiNbTa-ATZ specimens resulted in a significantly higher metabolic activity compared to those of Co-28Cr-6Mo ($p = 0.031$). Compared to the cells exposed to the 21-day negative control eluates, the eluates of the hybrid test specimens did not influence the metabolic activity.

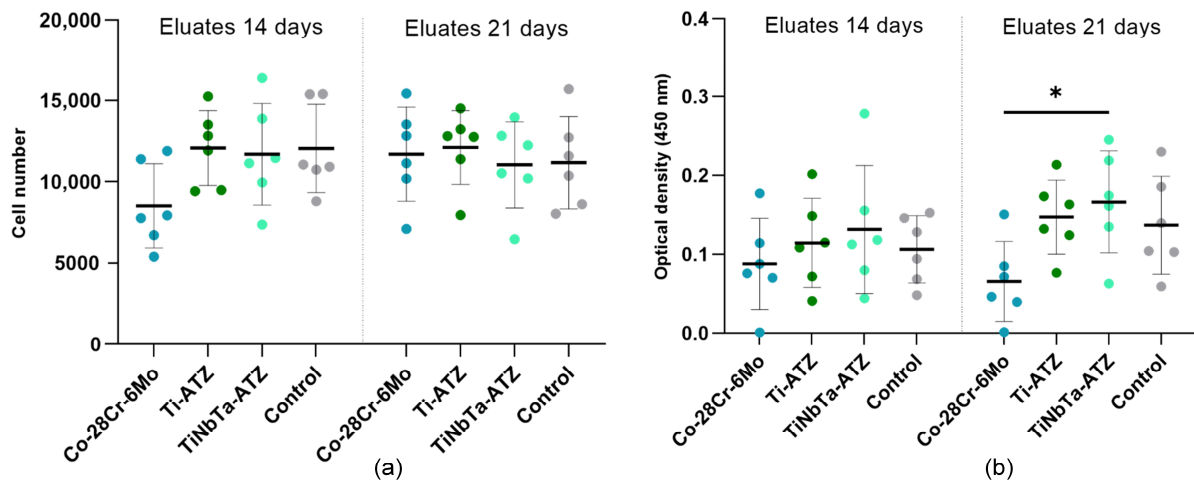


Figure 7. Cytotoxicity analysis of the glass-soldered, hybrid material specimens (TiNbTa-ATZ or Ti-ATZ) and Co-28Cr-6Mo (negative control) using elution testing. For this purpose, the specimens were incubated in a cell culture medium over 14 and 21 days. Afterward, the human osteoblasts were exposed to the eluates over a period of 24 h. Quantification of (a) the cell number by CyQUANT™ assay and (b) the metabolic activity by WST-1 assay. The osteoblasts in a cell culture medium served as the control. The data of six individual donors are presented as single values with median and interquartile ranges. Statistical significance was determined by two-way ANOVA followed by a Bonferroni multiple comparison test. * $p < 0.05$.

3.3. Biomechanical Characterization of the Demonstrator

Structural analysis of the soldered joint of a TiNbTa-ATZ functional demonstrator revealed a homogenous joint gap and pores within the glass solder (Figure 8), as already observed for the soldered cylindrical specimens (Figures 5 and 6). Due to the high quality of the bond, all specimens survived a fatigue test with 10,000-simulated gait cycles. The functional demonstrators showed a brittle fracture behavior, which is illustrated by the moment–rotation curves shown in Appendix B. The maximum extension–flexion moments of the functional demonstrators consisting of TiNbTa-ATZ and Ti-ATZ were 40.7 ± 2.2 Nm (individual values: 42.2 Nm, 42.3 Nm, 37.7 Nm) and 18.4 ± 3.8 Nm (individual values: 17.2 Nm, 14.5 Nm, 23.5 Nm), respectively. In accordance with the shear-induced fracture, all specimens showed a mixed cohesive and adhesive failure.

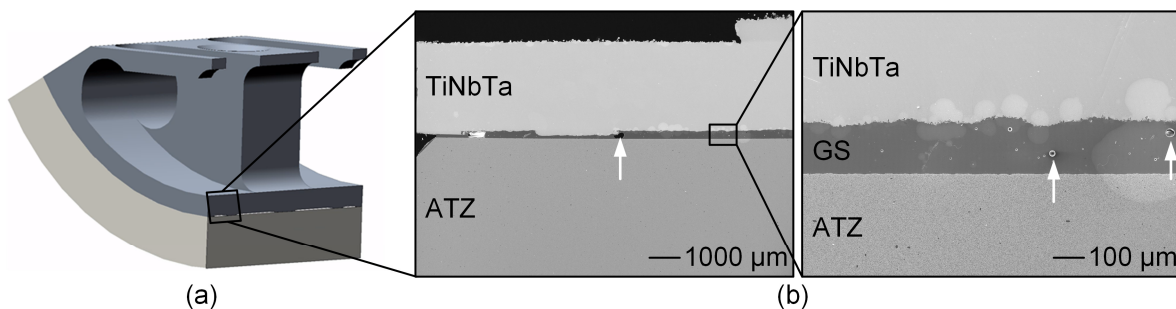


Figure 8. Structural analysis of the functional demonstrator of the femoral component of a total knee replacement made of alumina-toughened zirconia (ATZ) ceramic and additively manufactured Ti-35Nb-6Ta (TiNbTa) that were joined by a silica-based glass solder (GS): (a) illustration of the analyzed cross-section of the functional demonstrator and (b) the backscatter electron microscopy of the polished cross-section of the soldered joint. The examples of the pores in the glass solder are highlighted by white arrows.

4. Discussion

Multifunctional hybrid materials have been described as reducing the rate of material-related aseptic implant loosening in total joint replacements [13–21]. These hybrid materials are composed of an oxide ceramic at the articulating interfaces and a Ti-based material at the bone–implant interface. One feasible technology to combine oxide ceramics with Ti alloys is glass soldering [20,21,66,67]. Here, we investigated the static and fatigue shear strength, the influence of aging, and the cytotoxicity of hybrid material specimens consisting of a slip-casted ATZ and additively manufactured β -type Ti-35Nb-6Ta that were joined by a silica-based glass solder. In addition, the biomechanical performance of the functional demonstrators of a total knee replacement was analyzed under walking cycles, and load-to-failure testing was conducted under an extension–flexion loading.

The static shear strength of the TiNbTa-ATZ hybrid material (26.4 ± 4.2 MPa) did not differ significantly from that of Ti-ATZ (38.2 ± 14.4 MPa), and accelerated aging did not significantly affect the shear strength (see Figure 6a). In addition, all specimens demonstrated sufficient fatigue strength to withstand 10^7 dynamic shear loading cycles. A comparable study investigating Ti-ZrO₂ hybrid materials reported a shear strength of 16.8 ± 4.9 MPa [25], which is slightly below the values observed in this present study.

In order to be used as an implant material in cementless total joint replacements, the soldered joint of the hybrid material should not represent a predetermined fracture point. In the case of cementless titanium-based implants, the fixation strength between the bone and the implant surface determines the maximum load-bearing capacity. It has been reported that the bone–implant interface strength ranges from 0.5 MPa to 19.7 MPa [68–72]. In addition, in the standard to evaluate the shear strength of titanium-based plasma-sprayed coatings, 20 MPa has been defined as a minimum requirement [63]. Therefore, according to the measured properties, the investigated hybrid materials had sufficient strength to ensure that they do not form a flaw when used in endoprosthetic implants. However, during functional loading in vivo, the hybrid material is subjected to mixed tensile, shear, and compressive stresses [73]. Investigating the influence of the different stresses occurring simultaneously is complex and requires further studies that go beyond the content of the present study.

The microscopic investigations of the fracture surfaces (Figure 6) revealed that the strength of the hybrid material is determined by the adhesive failure along the interface between the glass solder and Ti-based material, as well as by the cohesive fracture of the glass solder, which is in line with previous observations [21,25,67]. Within the TiNbTa alloys, oxide films (e.g., TiO₂, Nb₂O₅, and Ta₂O₅), are formed [74,75], and the reaction of the chemical compounds in the surface layers with the glass solder is crucial in the formation of the material bond [20,21]. Hey et al. [76] described the formation of Ti₅Si₃ due to the reaction of SiO₂ with Ti using a comparable silica-based glass solder. Furthermore, in a study on the diffusion bonding of Al₂O₃ and cp-Ti, Travessa et al. [77] described that, at 800 °C, Al₂O₃ dissolves in the presence of titanium and further reacts with titanium to form an intermetallic Ti₃Al compound. In the process, oxygen diffuses into titanium, and Al-rich compounds accumulate at the interface, which was also observed in our study. In contrast, no chemical reaction in the Ti-30Ta and Ti-40Nb with Al₂O₃ has been reported [78,79], and also no measurable formation of an interfacial reaction phase of pure Nb with Al₂O₃ has been conducted [80]. Therefore, it seems reasonable that the material bond between the glass solder and TiNbTa was formed by the reaction of titanium with SiO₂ and Al₂O₃. Moreover, it has been previously described that the formed oxide layer in the titanium material or the interface between the oxide layer and the bulk material was responsible for the failure of the interfaces between the titanium and glass ceramics [21,67]. This was also shown in our present study by the visible deposition of the TiNbTa or cp-Ti on the ATZ fracture surface. The described chemical reactions should be verified in future research by focusing on the formation of the intermetallic reaction zone.

Transferring the knowledge gained from glass soldering to more complex and larger joining surfaces is crucial for the development of a hybrid material-based endoprosthetic

implant. To gain a first experience of the feasibility, we manufactured a simplified functional demonstrator resembling one condyle of the tibiofemoral joint (see Figure 2). As we already observed the pores in the soldered joints of the shear test specimens, we tried to reduce them by modifying the priming of the joining surfaces. To achieve a constant joint thickness, the titanium components were provided with spacers that were 0.1 mm in height. The dimensions of the functional demonstrator are shown in Figure 2 and Appendix A. Despite these efforts, pores were still visible in the joint gaps. Nevertheless, all specimens survived 10,000 walking cycles, and the TiNbTa-ATZ hybrids showed maximum extension–flexion moments of 40.7 ± 2.2 Nm. The rather small standard deviation indicates that the modification of the priming processes had a positive influence on the variations in the mechanical properties.

Given the absence of prior experiences with the investigated hybrid material regarding biomechanical loading scenarios, the walking cycles gave a first impression of the biomechanical performance of the implant demonstrator. We admit that 10,000 cycles are not enough to prove the fatigue strength under physiological loading. For example, the ISO standard 14,243 specifies 5×10^6 load cycles, which correspond to approximately five years of clinical use. In addition to the walking cycles, a subsequent loading to failure was used to determine the maximum extension–flexion moment. Bergmann et al. [81] reported data of an instrumented TKR and defined the EXTREME100 case as the maximum value suitable for studying mechanical safety under severe in vivo conditions. The flexion moments during walking and jogging were 25.9 Nm and 39.8 Nm, respectively; in addition, significantly higher values of 46.1 Nm and 59.1 Nm have been observed during squatting and stair descent, respectively [81]. Another study by Dreyer et al. [82] determined the peak values during various physiological motions in a comparable range (26 to 35 Nm). Considering that the maximum extension–flexion moment of the functional demonstrator was observed for a single condyle and that in vivo loads were measured for a bicondylar TKR, it seems that the bonding strength of the TiNbTa-ATZ hybrid meets the minimum requirement for an endoprosthetic implant. However, as mentioned above, the total knee endoprostheses were subjected to complex loadings by superimposed forces and moments. In addition, the material joint strength should provide a high safety factor that ensures mechanical functionality over a long period. The bonding strength of the complex-shaped hybrid material specimens should therefore be improved, e.g., by realizing a form fit of the ATZ and titanium components.

We observed a difference in the maximum extension–flexion moments of the TiNbTa-ATZ and Ti-ATZ functional demonstrators, although no significant differences were observed during the shear loading tests. For shear loading, the additive manufactured TiNbTa was machined to obtain parallel joining surfaces, which was afterward sandblasted (see Section 2.2). This procedure led to a similar roughness of the different specimens. However, the joining surfaces of the TiNbTa components of the functional demonstrator were not machined, and only sandblasting of the as-printed surface with similar process parameters to the cp-Ti components was used. For this reason, the TiNbTa components possessed a higher roughness than those of cp-Ti. In addition to the chemical bond, mechanical interlocking can also majorly contribute to bonding strength [20], which may have led to the increased joint strength in the rougher TiNbTa demonstrators. However, no study has investigated the influence of the surface roughness of additively manufactured TiNbTa components on bonding strength with a silica-based glass solder so far. Therefore, this might be one factor to improve, i.e., further increasing the bonding strength.

In addition to the mechanical properties, the cytotoxicity of the hybrid materials specimens is relevant for their later application as bone implants. In our present study, the TiNbTa-ATZ specimens did not impair the vitality of the human osteoblasts, whereas Co-28Cr-6Mo decreased the cell proliferation and metabolic activity (see Figure 7). The cytotoxic effect of the released Co- and Cr-ions on human cells has been previously demonstrated in various studies [4–8]. In contrast to Co-28Cr-6Mo, the glass solder and ATZ ceramics are highly biocompatible [26]. In addition, it has been shown that osteoblasts

cultured on TiNbTa exhibit a gene differentiation indicating bone formation [47], and Ti/Nb/Ta alloys are highly corrosion-resistant [74,75]. Furthermore, contrary to Ti-6Al-4V, where potentially harmful aluminum and vanadium ions are released [9–11,34], niobium and tantalum are highly biocompatible with no cytotoxic effects have been described so far [83]. In line with these previous findings, we demonstrated that the hybrid TiNbTa-ATZ material showed no cytotoxic effects *in vitro*; however, future studies may need to investigate the ion release in the long term.

Having said the above, this study has some limitations. We observed the pores in the soldered interface that reduce the mechanically loaded cross-section area. Such faults may cause local stress concentrations resulting in unexpected failure. The pores are based on entrapped gas, which might come from the evaporation of the polymer-based carrier suspension of the glass solder paste during firing. Minimizing the pore formation is a critical issue for the manufacturing of reliable bonding with glass solders [24,84]. The development of technological approaches to prevent these pores was beyond the scope of this present study. All the TiNbTa components were heat-treated before soldering to reduce the residual stresses during soldering; however, comprehensive investigation of the influence on the microstructure and mechanical properties was not performed in this study. Furthermore, despite measures (such as PBF-LB/M in an argon atmosphere and soldering in a vacuum) to prevent the oxidation of the TiNbTa component, the influence on the aforementioned properties cannot be completely ruled out. Moreover, oxygen might diffuse from the glass solder into the TiNbTa alloy. The influence of the manufacturing chain on the mechanical properties of the TiNbTa alloy is a part of ongoing studies, and it will be addressed in the future. In addition, the functional demonstrator represents a simplified implant design. Hence, the observations during biomechanical testing need to be verified with a more complex design that is closer to the currently used implants.

Further research should focus on parameter characterization for the bonding strength of TiNbTa-ATZ hybrid materials, e.g., by characterizing the influence of the surface roughness or the chemical composition of the glass solder and joining parameters.

5. Conclusions

Aseptic implant loosening of joint endoprostheses is partially affected by the currently used implant materials. This study described the manufacturing of the advanced TiNbTa-ATZ hybrid materials that potentially combine the high wear and corrosion resistance of the ATZ ceramics and enhanced osseointegration of TiNbTa alloys. The mechanical characterizations within shear tests and biomechanical loading scenarios that were applied to the functional demonstrators of the femoral component of total knee replacements revealed a sufficient enough mechanical strength to withstand acting loads during physiological motion. Furthermore, in line with the intrinsic properties of the specific materials, the TiNbTa-ATZ hybrid material showed no cytotoxic effect on human osteoblasts. Therefore, our data indicate the potential of hybrid TiNbTa-ATZ implant materials for use in joint endoprostheses.

Author Contributions: Conceptualization, J.-O.S., A.M., M.W., D.K., J.J., U.L., D.R., C.L., A.J.-H. and R.B.; methodology, J.-O.S., P.H., A.M., M.W., D.K., M.-L.S., U.L., D.R., C.L., A.J.-H. and R.B.; formal analysis, J.-O.S., M.-L.S. and A.J.-H.; investigation, J.-O.S., P.H., M.-L.S., D.K., M.W., A.J.-H. and R.B.; data curation, J.-O.S., P.H., M.-L.S., A.J.-H. and M.W.; writing—original draft preparation, J.-O.S., M.-L.S. and A.J.-H.; writing—review and editing, P.H., A.M., M.W., D.K., J.J., U.L., D.R., C.L. and R.B.; visualization, J.-O.S., M.-L.S. and A.J.-H.; supervision, D.K., A.J.-H. and R.B.; project administration, J.-O.S. and C.L.; funding acquisition, A.M., M.W., D.K., J.J., D.R., U.L., C.L., A.J.-H. and R.B. All authors have read and agreed to the published version of the manuscript.

Funding: This research study was supported by the German Federal Ministry of Education and Research (BMBF, grant number: 03XP0279D), which had no role in the study design; in the collection, analysis, and interpretation of data; in the writing of the report; and in the decision to submit the article for publication. The authors also gratefully thank the German Research Foundation (DFG) for funding the VIVO™ joint simulator (GZ: INST 2268/17-1 FUGG), as well as the European Union and the state of Mecklenburg-West Pomerania (Germany) for funding the laser scanning

microscope (VK-X250, grant number GHS-15-0016) and digital microscope (VHX-6000, grant number GHS-16-0002).

Institutional Review Board Statement: The biological characterization, using human osteoblasts, was conducted in accordance with the guidelines detailed in the Declaration of Helsinki. In addition, they study was approved by the Institutional Review Board (or ethics committee) of the University Medical Center Rostock (A 2010-0010).

Informed Consent Statement: Informed consent was obtained from all subjects involved in the study.

Data Availability Statement: The data presented in this study are available on request from the corresponding authors.

Acknowledgments: We would like to thank Christian Kaddick and Thuy Linh Le (both: Endolab GmbH, Riedering, Germany) for performing the artificial aging; Danny Vogel and Mario Jackszis (both: Research Laboratory for Biomechanics and Implant Technology, Rostock, Germany) for assistance during the biomechanical evaluation of the functional demonstrators; Robert Hauschild and Dirk Pfuetzner (both: FMZ GmbH, Rostock, Germany) for assistance during the design development of the functional demonstrator; and Melanie Stenzel (TANIOBIS GmbH, Goslar, Germany) for many inspiring discussions.

Conflicts of Interest: J.-O.S., P.H., D.K., J.J., M.-L.S., A.J.-H., and R.B., declare no conflicts of interest. A.M. and C.L. are employees of ZM Praezisionsdentaltechnik GmbH, M.W. is an employee of TANIOBIS GmbH, U.L. is an employee of DOT GmbH, and D.R. is an employee of FMZ GmbH.

Appendix A

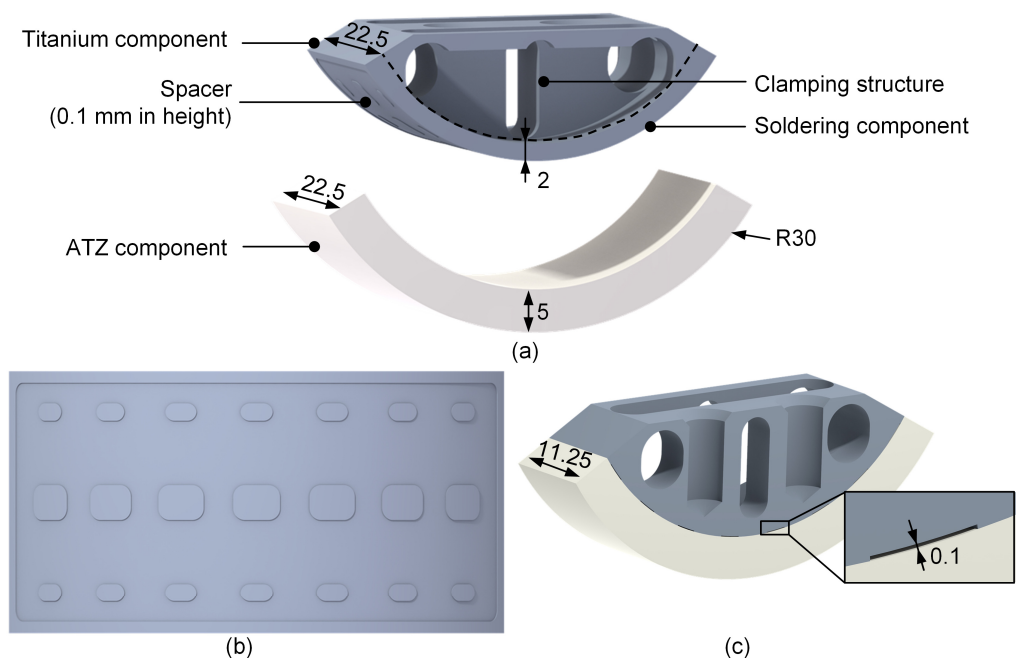


Figure A1. Depiction of the designed hybrid-material-based functional demonstrator of a total knee replacement showing (a) an explosion view and the dimensions of the components, (b) the designed spacers on the titanium component to obtain a homogenous joint gap, and (c) a cut view of the functional demonstrator to highlight the designed joining interface.

Appendix B

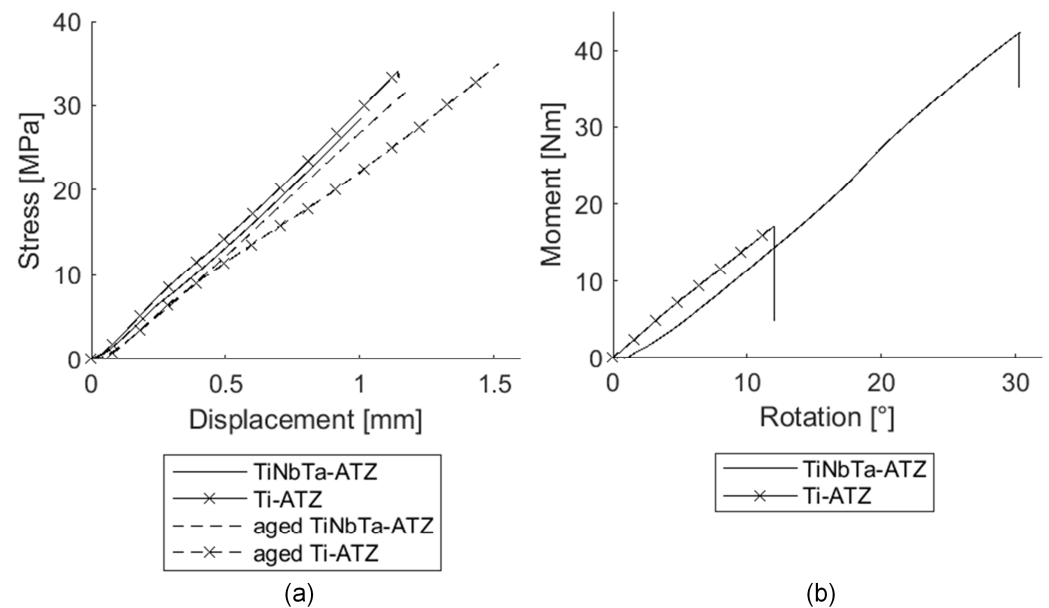


Figure A2. Representative results of the hybrid materials made of an alumina-toughened zirconia (ATZ) ceramic and an additive manufactured Ti-35Nb-6Ta (TiNbTa) or cp-Ti joined with a silica-based glass solder. (a) Stress–displacement curves of the static shear tests with the TiNbTa-ATZ (Group 1) and Ti-ATZ (Group 2) specimens, and (b) the representative moment–rotation curves of functional demonstrators of a total knee replacement made of TiNbTa-ATZ or Ti-ATZ hybrid material.

References

- Lewis, P.L.; Robertsson, O.; Graves, S.E.; Paxton, E.W.; Prentice, H.A.; W-Dahl, A. Variation and trends in reasons for knee replacement revision: A multi-registry study of revision burden. *Acta Orthop.* **2021**, *92*, 182–188. [[CrossRef](#)] [[PubMed](#)]
- Goodman, S.B.; Gallo, J. Periprosthetic Osteolysis: Mechanisms, Prevention and Treatment. *J. Clin. Med.* **2019**, *8*, 2091. [[CrossRef](#)]
- Järvenpää, J.; Soininvaara, T.; Kettunen, J.; Miettinen, H.; Kröger, H. Changes in bone mineral density of the distal femur after total knee arthroplasty: A 7-year DEXA follow-up comparing results between obese and nonobese patients. *Knee* **2014**, *21*, 232–235. [[CrossRef](#)] [[PubMed](#)]
- Jonitz-Heincke, A.; Sellin, M.-L.; Seyfarth, A.; Peters, K.; Mueller-Hilke, B.; Fiedler, T.; Bader, R.; Klinder, A. Analysis of Cellular Activity Short-Term Exposure to Cobalt and Chromium Ions in Mature Human Osteoblasts. *Materials* **2019**, *12*, 2771. [[CrossRef](#)] [[PubMed](#)]
- Sansone, V.; Pagani, D.; Melato, M. The effects on bone cells of metal ions released from orthopaedic implants. A review. *Clin. Cases Miner. Bone Metab.* **2013**, *10*, 34–40. [[CrossRef](#)] [[PubMed](#)]
- Scharf, B.; Clement, C.C.; Zolla, V.; Perino, G.; Yan, B.; Elci, S.G.; Purdue, E.; Goldring, S.; Macaluso, F.; Cobelli, N.; et al. Molecular analysis of chromium and cobalt-related toxicity. *Sci. Rep.* **2014**, *4*, 5729. [[CrossRef](#)] [[PubMed](#)]
- Crutsen, J.R.W.; Koper, M.C.; Jelsma, J.; Heymans, M.; Heyligers, I.C.; Grimm, B.; Mathijssen, N.M.C.; Schotanus, M.G.M. Prosthetic hip-associated cobalt toxicity: A systematic review of case series and case reports. *EFORT Open Rev.* **2022**, *7*, 188–199. [[CrossRef](#)] [[PubMed](#)]
- Glaß, H.; Jonitz-Heincke, A.; Petters, J.; Lukas, J.; Bader, R.; Hermann, A. Corrosion Products from Metallic Implants Induce ROS and Cell Death in Human Motoneurons In Vitro. *J. Funct. Biomater.* **2023**, *14*, 392. [[CrossRef](#)]
- Costa, B.C.; Tokuhara, C.K.; Rocha, L.A.; Oliveira, R.C.; Lisboa-Filho, P.N.; Costa Pessoa, J. Vanadium ionic species from degradation of Ti-6Al-4V metallic implants: In vitro cytotoxicity and speciation evaluation. *Mater. Sci. Eng. C Mater. Biol. Appl.* **2019**, *96*, 730–739. [[CrossRef](#)]
- Crapper, D.R.; Krishnan, S.S.; Dalton, A.J. Brain aluminum distribution in Alzheimer's disease and experimental neurofibrillary degeneration. *Science* **1973**, *180*, 511–513. [[CrossRef](#)]
- Gomes, C.C.; Moreira, L.M.; Santos, V.J.S.V.; Ramos, A.S.; Lyon, J.P.; Soares, C.P.; Santos, F.V. Assessment of the genetic risks of a metallic alloy used in medical implants. *Genet. Mol. Biol.* **2011**, *34*, 116–121. [[CrossRef](#)] [[PubMed](#)]
- Lee, D.W.; Du Ro, H.; Han, H.-S.; Lee, M.C. Titanium Alloy Knee Implant Is Associated with Higher Bone Density over Cobalt Chromium: A Prospective Matched-Pair Case-Control Study. *Clin. Orthop. Surg.* **2023**, *15*, 581–588. [[CrossRef](#)] [[PubMed](#)]
- Bahraminasab, M.; Arab, S.; Doostmohammadi, N. Cytotoxicity and Ion Release of Functionally Graded Al₂O₃- Ti Orthopedic Biomaterial. *J. Biomim. Biomater. Biomed. Eng.* **2022**, *54*, 103–118. [[CrossRef](#)]

14. Bahraminasab, M.; Arab, S.; Ghaffari, S. Osteoblastic cell response to Al₂O₃-Ti composites as bone implant materials. *Bioimpacts* **2022**, *12*, 247–259. [[CrossRef](#)] [[PubMed](#)]
15. Bahraminasab, M.; Arab, S.; Safari, M.; Talebi, A.; Kavakebian, F.; Doostmohammadi, N. In vivo performance of Al₂O₃-Ti bone implants in the rat femur. *J. Orthop. Surg. Res.* **2021**, *16*, 79. [[CrossRef](#)] [[PubMed](#)]
16. Bahraminasab, M.; Bozorg, M.; Ghaffari, S.; Kavakebian, F. Electrochemical corrosion of Ti-Al₂O₃ biocomposites in Ringer's solution. *J. Alloys Compd.* **2019**, *777*, 34–43. [[CrossRef](#)]
17. Bahraminasab, M.; Ghaffari, S.; Eslami-Shahed, H. Al₂O₃-Ti functionally graded material prepared by spark plasma sintering for orthopaedic applications. *J. Mech. Behav. Biomed. Mater.* **2017**, *72*, 82–89. [[CrossRef](#)] [[PubMed](#)]
18. Zhang, Y.; Bandyopadhyay, A. Direct fabrication of compositionally graded Ti-Al₂O₃ multi-material structures using Laser Engineered Net Shaping. *Addit. Manuf.* **2018**, *21*, 104–111. [[CrossRef](#)]
19. Moayedee, Y.; Nikzad, L.; Majidian, H. Exploration into the microstructural, mechanical, and biological characteristics of the functionally graded 3Y-TZP/Ti6Al4V system as a potential material for dental implants. *J. Mech. Behav. Biomed. Mater.* **2024**, *151*, 106380. [[CrossRef](#)]
20. Sun, Q.; Yang, L.; Yang, W.; Ji, H.; Li, M.; Li, Y. Microstructure evolution and bonding mechanism of ZrO₂ ceramic and Ti-6Al-4V alloy joints brazed by Bi₂O₃-B₂O₃-ZnO glass paste. *J. Eur. Ceram. Soc.* **2022**, *42*, 5953–5963. [[CrossRef](#)]
21. Mick, E.; Tinschert, J.; Mitrovic, A.; Bader, R. A Novel Technique for the Connection of Ceramic and Titanium Implant Components Using Glass Solder Bonding. *Materials* **2015**, *8*, 4287–4298. [[CrossRef](#)] [[PubMed](#)]
22. Bahraminasab, M.; Sahari, B.B.; Edwards, K.L.; Farahmand, F.; Hong, T.S.; Naghibi, H. Material tailoring of the femoral component in a total knee replacement to reduce the problem of aseptic loosening. *Mater. Des.* **2013**, *52*, 441–451. [[CrossRef](#)]
23. Mitrovic, M.; Zothner, A. Dentalimplantat. Patent DE102011015299A1, 27 September 2012.
24. Sass, J.-O.; Burmeister, U.; Ganz, C.; Mitrovic, A.; Lang, H.; Bader, R.; Vogel, D. Fracture strength of monolithic and glass-soldered ceramic subcomponents of 5-unit fixed dental prosthesis. *J. Prosthodont.* **2023**, *32*, e71–e80. [[CrossRef](#)]
25. van Vu, T.; Oh, G.-J.; Lim, H.-P.; Yun, K.-D.; Ryu, S.-K.; Yim, E.-K.; Fisher, J.G.; Ban, J.-S.; Park, S.-W. Shear Bond Strength of Zirconia to Titanium Implant Using Glass Bonding. *J. Nanosci. Nanotechnol.* **2019**, *19*, 967–969. [[CrossRef](#)]
26. Markhoff, J.; Mick, E.; Mitrovic, A.; Pasold, J.; Wegner, K.; Bader, R. Surface modifications of dental ceramic implants with different glass solder matrices: In vitro analyses with human primary osteoblasts and epithelial cells. *Biomed. Res. Int.* **2014**, *2014*, 742180. [[CrossRef](#)] [[PubMed](#)]
27. Niinomi, M.; Boehlert, C.J. Titanium Alloys for Biomedical Applications. In *Advances in Metallic Biomaterials*; Niinomi, M., Narushima, T., Nakai, M., Eds.; Springer: Berlin/Heidelberg, Germany, 2015; pp. 179–213. ISBN 978-3-662-46835-7.
28. Rack, H.J.; Qazi, J.I. Titanium alloys for biomedical applications. *Mater. Sci. Eng. C* **2006**, *26*, 1269–1277. [[CrossRef](#)]
29. Long, M.; Rack, H.J. Titanium alloys in total joint replacement—A materials science perspective. *Biomaterials* **1998**, *19*, 1621–1639. [[CrossRef](#)]
30. Kaur, M.; Singh, K. Review on titanium and titanium based alloys as biomaterials for orthopaedic applications. *Mater. Sci. Eng. C Mater. Biol. Appl.* **2019**, *102*, 844–862. [[CrossRef](#)]
31. Grimberg, A.; Luetzner, J.; Melsheimer, O.; Morlock, M.; Steinbrueck, A. The German Arthroplasty Registry—Annual Report. 2023. Available online: https://www.eprd.de/fileadmin/user_upload/Dateien/Publikationen/Berichte/AnnualReport2023-Web_2024-03-26_F.pdf (accessed on 9 April 2024).
32. Rho, J.Y.; Kuhn-Spearing, L.; Zioupos, P. Mechanical properties and the hierarchical structure of bone. *Med. Eng. Phys.* **1998**, *20*, 92–102. [[CrossRef](#)]
33. Choi, K.; Kuhn, J.L.; Ciarelli, M.J.; Goldstein, S.A. The elastic moduli of human subchondral, trabecular, and cortical bone tissue and the size-dependency of cortical bone modulus. *J. Biomech.* **1990**, *23*, 1103–1113. [[CrossRef](#)]
34. Matusiewicz, H. Potential release of in vivo trace metals from metallic medical implants in the human body: From ions to nanoparticles—A systematic analytical review. *Acta Biomater.* **2014**, *10*, 2379–2403. [[CrossRef](#)] [[PubMed](#)]
35. Kim, H.Y.; Miyazaki, S. Martensitic Transformation and Superelastic Properties of Ti-Nb Base Alloys. *Mater. Trans.* **2015**, *56*, 625–634. [[CrossRef](#)]
36. Kuroda, P.A.B.; Da Silva, L.M.; Sousa, K.D.S.J.; Donato, T.A.G.; Grandini, C.R. Preparation, structural, microstructural, mechanical, and cytotoxic characterization of Ti-15Nb alloy for biomedical applications. *Artif. Organs* **2020**, *44*, 811–817. [[CrossRef](#)] [[PubMed](#)]
37. Schulze, C.; Weinmann, M.; Schweigel, C.; Keßler, O.; Bader, R. Mechanical Properties of a Newly Additive Manufactured Implant Material Based on Ti-42Nb. *Materials* **2018**, *11*, 124. [[CrossRef](#)] [[PubMed](#)]
38. Pilz, S.; Gustmann, T.; Günther, F.; Zimmermann, M.; Kühn, U.; Gebert, A. Controlling the Young's modulus of a β-type Ti-Nb alloy via strong texturing by LPBF. *Mater. Des.* **2022**, *216*, 110516. [[CrossRef](#)]
39. Huang, S.; Sing, S.L.; de Looze, G.; Wilson, R.; Yeong, W.Y. Laser powder bed fusion of titanium-tantalum alloys: Compositions and designs for biomedical applications. *J. Mech. Behav. Biomed. Mater.* **2020**, *108*, 103775. [[CrossRef](#)]
40. Soro, N.; Brodie, E.G.; Abdal-hay, A.; Alali, A.Q.; Kent, D.; Dargusch, M.S. Additive manufacturing of biomimetic Titanium-Tantalum lattices for biomedical implant applications. *Mater. Des.* **2022**, *218*, 110688. [[CrossRef](#)]
41. Zhou, Y.L.; Niinomi, M.; Akahori, T. Effects of Ta content on Young's modulus and tensile properties of binary Ti-Ta alloys for biomedical applications. *Mater. Sci. Eng. A* **2004**, *371*, 283–290. [[CrossRef](#)]
42. Bertrand, E.; Gloriant, T.; Gordin, D.M.; Vasilescu, E.; Drob, P.; Vasilescu, C.; Drob, S.I. Synthesis and characterisation of a new superelastic Ti-25Ta-25Nb biomedical alloy. *J. Mech. Behav. Biomed. Mater.* **2010**, *3*, 559–564. [[CrossRef](#)]

43. Dubinskiy, S.; Prokoshkin, S.; Brailovski, V.; Inaekyan, K.; Korotitskiy, A. In situ X-ray diffraction strain-controlled study of Ti–Nb–Zr and Ti–Nb–Ta shape memory alloys: Crystal lattice and transformation features. *Mater. Charact.* **2014**, *88*, 127–142. [[CrossRef](#)]
44. Hussein, A.H.; Gepreel, M.A.-H.; Gouda, M.K.; Hefnawy, A.M.; Kandil, S.H. Biocompatibility of new Ti–Nb–Ta base alloys. *Mater. Sci. Eng. C Mater. Biol. Appl.* **2016**, *61*, 574–578. [[CrossRef](#)]
45. Johannsen, J.; Lauhoff, C.; Stenzel, M.; Schnitter, C.; Niendorf, T.; Weinmann, M. Laser beam powder bed fusion of novel biomedical titanium/niobium/tantalum alloys: Powder synthesis, microstructure evolution and mechanical properties. *Mater. Des.* **2023**, *233*, 112265. [[CrossRef](#)]
46. Kim, H.Y.; Fu, J.; Tobe, H.; Kim, J.I.; Miyazaki, S. Crystal Structure, Transformation Strain, and Superelastic Property of Ti–Nb–Zr and Ti–Nb–Ta Alloys. *Shap. Mem. Superelasticity* **2015**, *1*, 107–116. [[CrossRef](#)]
47. Sass, J.-O.; Sellin, M.-L.; Kauertz, E.; Johannsen, J.; Weinmann, M.; Stenzel, M.; Frank, M.; Vogel, D.; Bader, R.; Jonitz-Heincke, A. Advanced Ti–Nb–Ta Alloys for Bone Implants with Improved Functionality. *J. Funct. Biomater.* **2024**, *15*, 46. [[CrossRef](#)] [[PubMed](#)]
48. Furuta, T.; Kuramoto, S.; Hwang, J.; Nishino, K.; Saito, T. Elastic Deformation Behavior of Multi-Functional Ti–Nb–Ta–Zr–O Alloys. *Mater. Trans.* **2005**, *46*, 3001–3007. [[CrossRef](#)]
49. Gudkov, S.V.; Simakin, A.V.; Konushkin, S.V.; Ivannikov, A.Y.; Nasakina, E.O.; Shatova, L.A.; Kolmakov, A.G.; Sevostyanov, M.A. Preparation, structural and microstructural characterization of Ti–30Nb–10Ta–5Zr alloy for biomedical applications. *J. Mater. Res. Technol.* **2020**, *9*, 16018–16028. [[CrossRef](#)]
50. Saito, T.; Furuta, T.; Hwang, J.-H.; Kuramoto, S.; Nishino, K.; Suzuki, N.; Chen, R.; Yamada, A.; Ito, K.; Seno, Y.; et al. Multifunctional Alloys Obtained via a Dislocation-Free Plastic Deformation Mechanism. *Science* **2003**, *300*, 464–467. [[CrossRef](#)] [[PubMed](#)]
51. Sevostyanov, M.A.; Kolmakov, A.G.; Sergiyenko, K.V.; Kaplan, M.A.; Baikin, A.S.; Gudkov, S.V. Mechanical, physical–chemical and biological properties of the new Ti–30Nb–13Ta–5Zr alloy. *J. Mater. Sci.* **2020**, *55*, 14516–14529. [[CrossRef](#)]
52. Prigent, H.; Pellen-Mussi, P.; Cathelineau, G.; Bonnaure-Mallet, M. Evaluation of the biocompatibility of titanium–tantalum alloy versus titanium. *J. Biomed. Mater. Res.* **1998**, *39*, 200–206. [[CrossRef](#)]
53. Weng, W.; Biesiekierski, A.; Li, Y.; Wen, C. Effects of selected metallic and interstitial elements on the microstructure and mechanical properties of beta titanium alloys for orthopedic applications. *Materialia* **2019**, *6*, 100323. [[CrossRef](#)]
54. Kolli, R.; Devaraj, A. A Review of Metastable Beta Titanium Alloys. *Metals* **2018**, *8*, 506. [[CrossRef](#)]
55. Farrahnoor, A.; Zuhailawati, H. Review on the mechanical properties and biocompatibility of titanium implant: The role of niobium alloying element. *Int. J. Mater. Res.* **2021**, *112*, 505–513. [[CrossRef](#)]
56. Niinomi, M. Recent metallic materials for biomedical applications. *Metall. Mater. Trans. A* **2002**, *33*, 477–486. [[CrossRef](#)]
57. Fu, J.; Yamamoto, A.; Kim, H.Y.; Hosoda, H.; Miyazaki, S. Novel Ti-base superelastic alloys with large recovery strain and excellent biocompatibility. *Acta Biomater.* **2015**, *17*, 56–67. [[CrossRef](#)]
58. Hao, Y.L.; Li, S.J.; Sun, S.Y.; Zheng, C.Y.; Hu, Q.M.; Yang, R. Super-elastic titanium alloy with unstable plastic deformation. *Appl. Phys. Lett.* **2005**, *87*, 091906. [[CrossRef](#)]
59. F04 Committee. *Test Method for Shear and Bending Fatigue Testing of Calcium Phosphate and Metallic Medical and Composite Calcium Phosphate/Metallic Coatings*; ASTM International: West Conshohocken, PA, USA, 2018.
60. F04 Committee. *Test Method for Shear Testing of Calcium Phosphate Coatings and Metallic Coatings*; ASTM International: West Conshohocken, PA, USA, 2018.
61. ISO 14243-3:2014-11; Implants for Surgery, Wear of total Knee-Joint Prostheses, Part 3: Loading and Displacement Parameters for Wear-Testing Machines with Displacement Control and Corresponding Environmental Conditions for Test. Beuth Verlag GmbH: Berlin, Germany, 2014.
62. F02 Committee. *Guide for Accelerated Aging of Sterile Barrier Systems for Medical Devices*; ASTM International: West Conshohocken, PA, USA, 2021.
63. ISO 13179-1:2021; Implants for Surgery, Coatings on Metallic Surgical Implants, Part 1: Plasma-Sprayed Coatings Derived from Titanium or Titanium-6 Aluminum-4 Vanadium Alloy Powders. Beuth Verlag GmbH: Berlin, Germany, 2021.
64. Lochner, K.; Fritsche, A.; Jonitz, A.; Hansmann, D.; Mueller, P.; Mueller-Hilke, B.; Bader, R. The potential role of human osteoblasts for periprosthetic osteolysis following exposure to wear particles. *Int. J. Mol. Med.* **2011**, *28*, 1055–1063. [[CrossRef](#)]
65. Zietz, C.; Reinders, J.; Schwiesau, J.; Paulus, A.; Kretzer, J.P.; Grupp, T.; Utzschneider, S.; Bader, R. Experimental testing of total knee replacements with UHMW-PE inserts: Impact of severe wear test conditions. *J. Mater. Sci. Mater. Med.* **2015**, *26*, 134. [[CrossRef](#)]
66. Suansuwan, N.; Swain, M.V. Adhesion of porcelain to titanium and a titanium alloy. *J. Dent.* **2003**, *31*, 509–518. [[CrossRef](#)]
67. Vásquez, V.Z.C.; Ozcan, M.; Kimpara, E.T. Evaluation of interface characterization and adhesion of glass ceramics to commercially pure titanium and gold alloy after thermal- and mechanical-loading. *Dent. Mater.* **2009**, *25*, 221–231. [[CrossRef](#)]
68. Vercaigne, S.; Wolke, J.G.; Naert, I.; Jansen, J.A. Histomorphometrical and mechanical evaluation of titanium plasma-spray-coated implants placed in the cortical bone of goats. *J. Biomed. Mater. Res.* **1998**, *41*, 41–48. [[CrossRef](#)]
69. Ozeki, K.; Yuhta, T.; Aoki, H.; Nishimura, I.; Fukui, Y. Push-out strength of hydroxyapatite coated by sputtering technique in bone. *Biomed. Mater. Eng.* **2001**, *11*, 63–68.
70. Müller, M.; Hennig, F.F.; Hothorn, T.; Stangl, R. Bone-implant interface shear modulus and ultimate stress in a transcortical rabbit model of open-pore Ti6Al4V implants. *J. Biomech.* **2006**, *39*, 2123–2132. [[CrossRef](#)]

71. Li, J.; Liao, H.; Fartash, B.; Hermansson, L.; Johnsson, T. Surface-dimpled commercially pure titanium implant and bone ingrowth. *Biomaterials* **1997**, *18*, 691–696. [[CrossRef](#)]
72. Chang, C.K.; Wu, J.S.; Mao, D.L.; Ding, C.X. Mechanical and histological evaluations of hydroxyapatite-coated and noncoated Ti6Al4V implants in tibia bone. *J. Biomed. Mater. Res.* **2001**, *56*, 17–23. [[CrossRef](#)]
73. Zelle, J.; Janssen, D.; Peeters, S.; Brouwer, C.; Verdonschot, N. Mixed-mode failure strength of implant-cement interface specimens with varying surface roughness. *J. Biomech.* **2011**, *44*, 780–783. [[CrossRef](#)]
74. Zhukova, Y.S.; Pustov, Y.A.; Konopatsky, A.S.; Filonov, M.R. Characterization of electrochemical behavior and surface oxide films on superelastic biomedical Ti–Nb–Ta alloy in simulated physiological solutions. *J. Alloys Compd.* **2014**, *586*, S535–S538. [[CrossRef](#)]
75. Soni, R.; Pande, S.; Salunkhe, S.; Natu, H.; Abouel Nasr, E.; Shanmugam, R.; Hussein, H.M.A.M. In Vitro and Electrochemical Characterization of Laser-Cladded Ti–Nb–Ta Alloy for Biomedical Applications. *Crystals* **2022**, *12*, 954. [[CrossRef](#)]
76. Hey, J.; Kasaliyska, M.; Kiesow, A.; Schweyen, R.; Arnold, C. Retentive Force of Glass-Ceramic Soldered Customized Zirconia Abutment Copings with Prefabricated Titanium Bases. *Materials* **2020**, *13*, 3193. [[CrossRef](#)]
77. Travessa, D.; Ferrante, M. The Al₂O₃-titanium adhesion in the view of the diffusion bonding process. *J. Mater. Sci.* **2002**, *37*, 4385–4390. [[CrossRef](#)]
78. Gibbesch, B.; Elssner, G.; Petzow, G. Microstructure of interface regions and mechanical properties of Ti/Al₂O₃ and Ti-alloy/Al₂O₃ joints for dental implants. *Clin. Mater.* **1990**, *5*, 177–189. [[CrossRef](#)]
79. Gibbesch, B.; Elssner, G.; Petzow, G. Investigation of Ti/Al₂O₃ joints with intermediate tantalum and niobium layers. *Biomaterials* **1992**, *13*, 455–461. [[CrossRef](#)] [[PubMed](#)]
80. Rahaman, M.N.; Huang, T.; Bal, B.S.; Li, Y. In vitro testing of Al₂O₃-Nb composite for femoral head applications in total hip arthroplasty. *Acta Biomater.* **2010**, *6*, 708–714. [[CrossRef](#)] [[PubMed](#)]
81. Bergmann, G.; Bender, A.; Graichen, F.; Dymke, J.; Rohlmann, A.; Trepczynski, A.; Heller, M.O.; Kutzner, I. Standardized loads acting in knee implants. *PLoS ONE* **2014**, *9*, e86035. [[CrossRef](#)] [[PubMed](#)]
82. Dreyer, M.J.; Trepczynski, A.; Hosseini Nasab, S.H.; Kutzner, I.; Schütz, P.; Weisse, B.; Dymke, J.; Postolka, B.; Moewis, P.; Bergmann, G.; et al. European Society of Biomechanics S.M. Perren Award 2022: Standardized tibio-femoral implant loads and kinematics. *J. Biomech.* **2022**, *141*, 111171. [[CrossRef](#)]
83. Eisenbarth, E.; Velten, D.; Müller, M.; Thull, R.; Breme, J. Biocompatibility of beta-stabilizing elements of titanium alloys. *Biomaterials* **2004**, *25*, 5705–5713. [[CrossRef](#)]
84. Sass, J.-O.; Jakobi, A.; Mitrovic, A.; Ganz, C.; Wilken, J.; Burmeister, U.; Lang, H.; Bader, R.; Vogel, D. Bending strength of ceramic compounds bonded with silicate-based glass solder. *Mater. Test.* **2021**, *63*, 593–598. [[CrossRef](#)]

Disclaimer/Publisher’s Note: The statements, opinions and data contained in all publications are solely those of the individual author(s) and contributor(s) and not of MDPI and/or the editor(s). MDPI and/or the editor(s) disclaim responsibility for any injury to people or property resulting from any ideas, methods, instructions or products referred to in the content.



Computational biomechanical study on hybrid implant materials for the femoral component of total knee replacements

Jan-Oliver Sass^{a,*}, Maeruan Kebbach^a, Cornelia Lork^b, Jan Johannsen^c, Markus Weinmann^d, Melanie Stenzel^d, Rainer Bader^a

^a Research Laboratory for Biomechanics and Implant Technology, Department of Orthopedics, Rostock University Medical Center, Doberaner Straße 142, D-18057 Rostock, Germany

^b ZM Präzisionsdentaltechnik GmbH, Breite Straße 16, D-18055 Rostock, Germany

^c Fraunhofer Research Institution for Additive Manufacturing Technologies IAPT, Am Schleusengraben 14, D-21029 Hamburg, Germany

^d TANIÖBIS GmbH, Im Schleeke 87-91, D-38642 Goslar, Germany

ARTICLE INFO

Keywords:

Total knee replacement
Femoral component
Implant material
Beta titanium
Alumina-toughened zirconia ceramic
Uncemented fixation
Bone-implant interaction
Stress shielding
Finite element analysis

ABSTRACT

Multifunctional materials have been described to meet the diverse requirements of implant materials for femoral components of uncemented total knee replacements. These materials aim to combine the high wear and corrosion resistance of oxide ceramics at the joint surfaces with the osteogenic potential of titanium alloys at the bone-implant interface. Our objective was to evaluate the biomechanical performance of hybrid material-based femoral components regarding mechanical stress within the implant during cementless implantation and stress shielding (evaluated by strain energy density) of the periprosthetic bone during two-legged squat motion using finite element modeling. The hybrid materials consisted of alumina-toughened zirconia (ATZ) ceramic joined with additively manufactured Ti-6Al-4V or Ti-35Nb-6Ta alloys. The titanium component was modeled with or without an open porous surface structure. Monolithic femoral components of ATZ ceramic or Co-28Cr-6Mo alloy were used as reference. The elasticity of the open porous surface structure was determined within experimental compression tests and was significantly higher for Ti-35Nb-6Ta compared to Ti-6Al-4V (5.2 ± 0.2 GPa vs. 8.8 ± 0.8 GPa, $p < 0.001$). During implantation, the maximum stress within the ATZ femoral component decreased from 1568.9 MPa (monolithic ATZ) to 367.6 MPa (Ti-6Al-4V/ATZ), 560.9 MPa (Ti-6Al-4V/ATZ with an open porous surface), 474.9 MPa (Ti-35Nb-6Ta/ATZ), and 648.4 MPa (Ti-35Nb-6Ta/ATZ with an open porous surface). The strain energy density increased at higher flexion angles for all models during the squat movement. At $\sim 90^\circ$ knee flexion, the strain energy density in the anterior region of the distal femur increased by 25.7 % (Ti-6Al-4V/ATZ), 70.3 % (Ti-6Al-4V/ATZ with an open porous surface), 43.7 % (Ti-35Nb-6Ta/ATZ), and 82.5% (Ti-35Nb-6Ta/ATZ with an open porous surface) compared to monolithic ATZ. Thus, the hybrid material-based femoral component decreases the intraoperative fracture risk of the ATZ part and considerably reduces the risk of stress shielding of the periprosthetic bone.

1. Introduction

Femoral components used in total knee replacement (TKR) are commonly made of cobalt-chromium-molybdenum alloy such as Co-28Cr-6Mo. The main reason for implant revisions represents aseptic loosening (Grimberg et al., 2023), which in part is caused by wear-particle-related osteolysis (Crutsen et al., 2022; Drynda et al., 2018; Jonitz-Heincke et al., 2019; Yang et al., 2015) and periprosthetic bone resorption due to bone stress shielding (Järvenpää et al., 2014; Lee

et al., 2023; Mintzer et al., 1990). In this context, corrosion and wear-resistant oxide ceramics (e.g. alumina toughened zirconia (ATZ) ceramic, zirconia toughened alumina (ZTA) ceramic) have been introduced as alternative implant materials, showing good clinical results (Bergschmidt et al., 2016). However, femoral components based on oxide ceramics are prone to brittle fracture during high-impact events (Kluess et al., 2012; Krueger et al., 2014). Furthermore, they are bioinert materials allowing only contact osteogenesis but no firm osseointegration of the implant (Bedir et al., 2023). Therefore, the benefits of

* Corresponding author.

E-mail address: jan-oliver.sass@med.uni-rostock.de (J.-O. Sass).

<https://doi.org/10.1016/j.jmbbm.2024.106681>

Received 29 April 2024; Received in revised form 15 June 2024; Accepted 8 August 2024

Available online 10 August 2024

1751-6161/© 2024 The Authors. Published by Elsevier Ltd. This is an open access article under the CC BY license (<http://creativecommons.org/licenses/by/4.0/>).

uncemented implantation, such as improved component fixation through direct integration with the bone, preservation of bone stock, and reduced systemic side effects associated with debris and third-body wear, cannot be realized in cemented TKR (Uivaraseanu et al., 2022). Moreover, uncemented TKRs made of oxide ceramics similar lead to stress shielding of the periprosthetic bone since there is a mismatch in elasticity of the implant material and bone.

As an alternative, β -titanium (β -Ti) alloys were investigated (Farrahnor and Zuhailawati, 2021; Johannsen et al., 2023; Niinomi, 1998) which are providing a lower Young's modulus (higher elasticity) compared to Ti-6Al-4V, Co-28Cr-6Mo alloy and oxide ceramics (Niinomi, 1998), thus potentially reducing the stress shielding. The elasticity and excellent biocompatibility are traced back to the body-centered cubic crystal structure stabilized by biocompatible elements such as niobium, tantalum, and zirconium (Eisenbarth et al., 2004; Farrahnor and Zuhailawati, 2021; Niinomi, 1998). In addition to their suitable properties, certain β -Ti alloys, e.g. Ti-Nb (Pilz et al., 2022; Schulze et al., 2018), Ti-Nb-Ta (Johannsen et al., 2023; Sass et al., 2024c), and Ti-Nb-Ta-Zr (Luo et al., 2019; Ozan et al., 2017) can be additively manufactured, which is advantageous in terms of design freedom and fabrication of open porous surface structures, e.g. flexible surface designs (Sass et al., 2023), for enhanced implant-bone interaction (Ni et al., 2019; Song et al., 2023). However, titanium and its alloys have a lower wear resistance and, therefore, cannot be applied for high tribologically stressed implant parts (Kaur and Singh, 2019).

To address clinical issues with CoCrMo-based femoral components, PEEK (Post et al., 2022; Ruiter et al., 2017, 2021), multifunctional materials (Bahraminasab et al., 2017, 2019, 2021, 2022a, 2022b; Mick et al., 2015; Sass et al., 2024a; Sun et al., 2022) or wear-resistant coatings on titanium-based implants (Galas et al., 2023; Lee et al., 2023) have been investigated. In this regard, multifunctional materials are defined by the combination of a ceramic-based implant component in the articulating contact zone and a titanium-based implant component in the bone interface to meet the diverse requirements of an advanced implant material for TKR (Bahraminasab et al., 2017, 2019, 2021, 2022a, 2022b; Mick et al., 2015; Sass et al., 2024a; Sun et al., 2022). These materials may combine the advantageous properties by reducing the specific limitations of each monolithic material. Functionally graded materials with an increasing Ti-6Al-4V content from the pure oxide ceramic component to the bone interface, produced by spark laser sintering, have been investigated (Bahraminasab et al., 2017, 2019, 2021, 2022a, 2022b; Moayedee et al., 2024). Soldering ceramic and titanium components with a glass solder to create a hybrid material is another conceivable approach. Joining dissimilar materials is challenging but can be achieved (Mick et al., 2015; Sass et al., 2024a; Suansuwan and Swain, 2003; Sun et al., 2022; Vásquez et al., 2009). During a firing process, a material bond is formed by diffusion of elements and the formation of interlayers (Mick et al., 2015; Sass et al., 2024a; Sun et al., 2022; Vásquez et al., 2009) and mechanical interlocking (Sun et al., 2022). Despite promising results of joined orthopedic materials (Ti-6Al-4V/ATZ (Mick et al., 2015), Ti-35Nb-6Ta/ATZ (Sass et al., 2024a)), the concept of a hybrid material-based femoral component for TKR using glass soldering of subcomponents has not been studied.

Furthermore, previous studies investigating alternative implant materials for the femoral component of a TKR have been focused on the bone-implant interaction (Bahraminasab et al., 2013; Galas et al., 2023; Ruiter et al., 2021) to prove the reduced stress shielding but the mechanical loading of the femoral component induced during the implantation procedure has not been considered. Since Kluess et al. (2012) clearly described the risk of intraoperative fracture of ceramic femoral components caused by anterior-posterior opening ("wedge load"), it is essential to investigate the influence of the hybrid material in this loading scenario as well.

Hence, the present study aimed to analyze the biomechanical properties of a hybrid material-based femoral component for TKR using finite

element (FE) modeling. For this purpose, the hybrid material was realized by bonding ATZ ceramics to Ti-6Al-4V or Ti-35Nb-6Ta alloys. We investigated the stresses and strains within the femoral component and the periprosthetic bone under mechanical loading induced by the uncemented implantation and during a two-legged squat motion up to $\sim 90^\circ$ knee flexion. The squat motion was based on a numerical workflow, where a musculoskeletal multibody simulation (MMBS) of the lower extremity was sequentially linked to the FE model.

2. Materials and methods

2.1. Study overview

This study investigated the influence of the femoral component material on the biomechanical properties using a right cruciate-retaining TKR (Columbus®, Aesculap AG, Tuttlingen, Germany). The tibial insert and resurfaced patellar component were considered within the two-legged squat motion. Four different materials were defined for the femoral component: hybrid materials of ATZ and Ti-6Al-4V (Ti-6Al-4V/ATZ) or ATZ and Ti-35Nb-6Ta (Ti-35Nb-6Ta/ATZ), monolithic Co-28Cr-6Mo alloy, and monolithic ATZ ceramic. The Ti-35Nb-6Ta/ATZ hybrid material has been recently experimentally characterized and showed promising mechanical and biological properties (Sass et al., 2024a). The additively manufactured titanium components were completely dense or had an open porous surface structure. Implant loading during uncemented implantation and stress shielding within the periprosthetic bone during two-legged squat motion was evaluated by comparing the strain energy density in defined regions of interest (ROI). Most of the model input parameters were taken from the literature. Since no data were available on the elastic properties of open porous Ti-35Nb-6Ta lattice structures for the functionalized implant surface, mechanical tests of material specimens were carried out accordingly.

2.2. Experimental characterization of open porous lattice structures

2.2.1. Specimen preparation

For detailed information on the preparation of the pre-alloyed Ti-35Nb-6Ta powders and the process parameters, we refer to a previous study by Johannsen et al. (2023). In brief, the Ti-35Nb-6Ta specimens were produced by laser beam powder bed fusion (PBF-LB/M) using a DMP350 Flex (3D Systems Corp., Rock Hill, SC, USA) equipped with a 1 kW single-mode laser (YLR-1000-WC-Y14, IPG Laser GmbH, Burbach, Germany). Ti-6Al-4V specimens were prepared using a SLM500 Quad (SLM Solutions Group AG, Luebeck, Germany) (Sass et al., 2024c). The defined process led to chemical homogenous Ti-35Nb-6Ta specimens having a pure β crystal structure and densities $>99\%$ (Johannsen et al., 2023). Open porous lattice structures were designed with a $1 \times 1 \times 1 \text{ mm}^3$ face-centered cubic unit cell in Creo Parametrics 6.0.3.0 (PTC Inc., Boston, MA, USA) based on a previous study (Sass et al., 2024c). The strut diameter and resulting nominal porosity were 0.3 mm and 70 %, respectively. Rectangular specimens measuring $7 \times 7 \times 11 \text{ mm}^3$ were prepared for experimental compression tests (Fig. 1A).

2.2.2. Mechanical characterization

The open porous specimens ($n = 5$) were axially loaded to failure using a universal testing machine (Z050-50 kN, Zwick Roell, Ulm, Germany) at a crosshead speed of $0.005 \text{ mm} \times \text{s}^{-1}$ (Sass et al., 2024c). The stress-strain curves were obtained using a tactile extensometer (digiClip Extensometer, Zwick Roell, Ulm, Germany), and the compressive modulus (C), the compressive yield strength ($\sigma_{C,0.2}$) the ultimate compressive strength (UCS), and the elongation at break (ϵ) were evaluated. The test setup is shown in Fig. 1B.

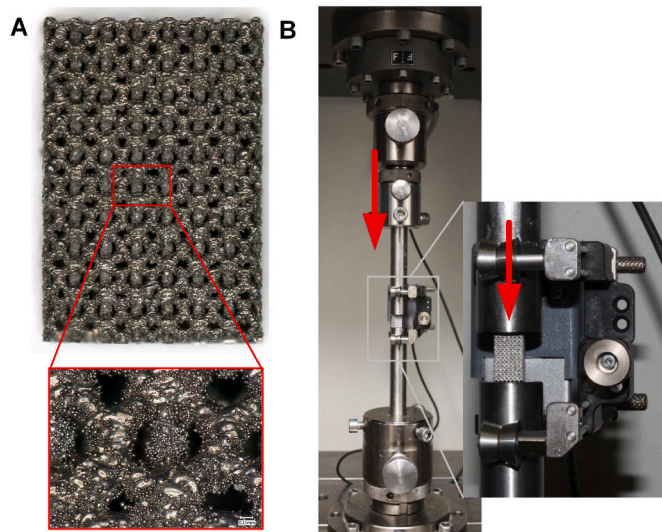


Fig. 1. A) Rectangular open porous specimen for axial compression test with a detailed view of the lattice structure and B) setup for mechanical testing indicating the compression force vector.

2.2.3. Statistical analysis

Statistical analysis of the experimental data was performed in SPSS statistics (v25, IBM Corp., Armonk, NY, USA), and the level of significance was $p < 0.05$ for all tests. All groups were tested for statistical significance using an independent *t*-test after evaluating its applicability regarding the groups' normal distribution and variance homogeneity.

2.3. Finite-element simulation

2.3.1. General model assumptions, material properties, and discretization strategy

Two quasi-static FE models were developed in Abaqus v2022 (Dassault Systèmes, Providence, RI, USA) using the implicit solver resembling the uncemented implantation and the two-legged squat motion. For both models, the CT scan of a human femur (male, 83 years old, body weight of 61 kg) was reconstructed using Mimics 25.0 (Materialise NV, Leuven, Belgium) and sectioned 10 mm above the femoral component. Virtual implantation of the femoral component was performed according to the surgical guidelines and was reviewed by an experienced orthopedic surgeon.

The established implant design was modified to create a biphasic design (Fig. 2) with fully constrained interfaces between the sub-components. This artificial design was used to study the hybrid material-based femoral components. The titanium component had a constant thickness of 3 mm (excluding the two pins). In addition, models with an open porous surface (1 mm thick) have been designed, which may enhance bone-implant interaction (Galas et al., 2023; Gao et al., 2019). Accordingly, the material interface was always defined by dense

material components.

The modeled material properties are summarized in Table 1. All materials were assumed to have isotropic and linear elastic material properties. Heterogeneous bone properties were based on the correlation between Young's modulus and Hounsfield units (HU) for the cortical (ash density $\geq 0.6 \text{ g} \times \text{cm}^{-3}$) and trabecular (ash density $< 0.6 \text{ g} \times \text{cm}^{-3}$) bone (Keyak and Falkinstein, 2003) of the distal femur in the superior-inferior direction (Rho et al., 1995). The correlation functions were chosen as they directly refer to bone specimens extracted from human distal femurs. A phantom-based calibration (QRM, Moehrendorf, Germany) was performed to define the correlation between apparent density and HU, and further, the apparent density was transformed into ash density (Schileo et al., 2008). In Abaqus v2022, a node-based assignment of Young's moduli was performed using a self-written plug-in (Mauck et al., 2016). Each node obtains an HU value derived from the CT data using the corresponding node coordinates. The HU values are considered as virtual temperatures to simulate the heterogeneous bone material properties in vivo by a linear-elastic temperature-dependent material model. The frequency of assigned Young's moduli, the curve of the Young's moduli as a function of the HU, and the assigned corresponding Young's moduli are shown in Fig. 3.

Femoral component materials (hybrid materials, Co-28Cr-6Mo alloy, ATZ ceramic) and UHMW-PE for the tibial insert and patellar component were assumed to be homogeneous. The open porous surface structure of the titanium part of the femoral component was represented by the experimentally determined compressive stiffness and not by modeling the actual geometry of the lattice structures. In addition to the elastic properties, UHMW-PE was modeled with a plastic material

Table 1

Defined material properties for finite element modeling (E_{Cort} : Young's modulus of the cortical bone, E_{Trab} : Young's modulus of the trabecular bone, ρ : ash density).

Material	Young's modulus [GPa]	Poisson's ratio	Reference
Bone	$E_{\text{Cort}} = -6.142 \times 0.014 \times \rho$ $E_{\text{Trab}} = 0.82 \times \rho^{1.27}$	0.4	Rho et al. (1995)
Co-28Cr-6Mo	240	0.3	Galas et al. (2023)
UHMW-PE	0.239	0.35	Sauer et al. (2021)
ATZ	261	0.27	Vogel et al. (2021)
Ti-6Al-4V	110	0.3	Niinomi (1998)
Open porous Ti-6Al-4V	8.8	0.3	Current study
Ti-35Nb-6Ta ^a	63	0.3	Sass et al. (2024c)
Open porous Ti-35Nb-6Ta	5.2	0.3	Current study

^a Averaged compressive modulus of specimens manufactured in three different build directions during laser beam powder bed fusion.

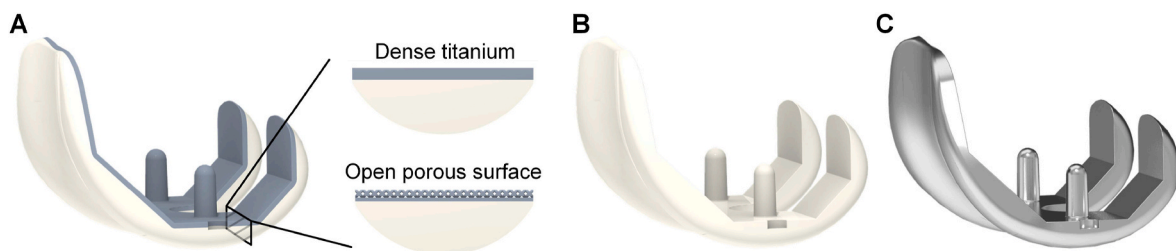


Fig. 2. Geometries of the analyzed femoral components of a total knee replacement (figures created in Creo Parametrics 6.0.3.0) made of A) a hybrid material of ATZ ceramic (articulating surface) and a titanium alloy (bone interacting surface), and section views of the hybrid material-based femoral component showing the titanium-based component with/without an open porous surface structure, B) monolithic ATZ ceramic and C) monolithic Co-28Cr-6Mo alloy.

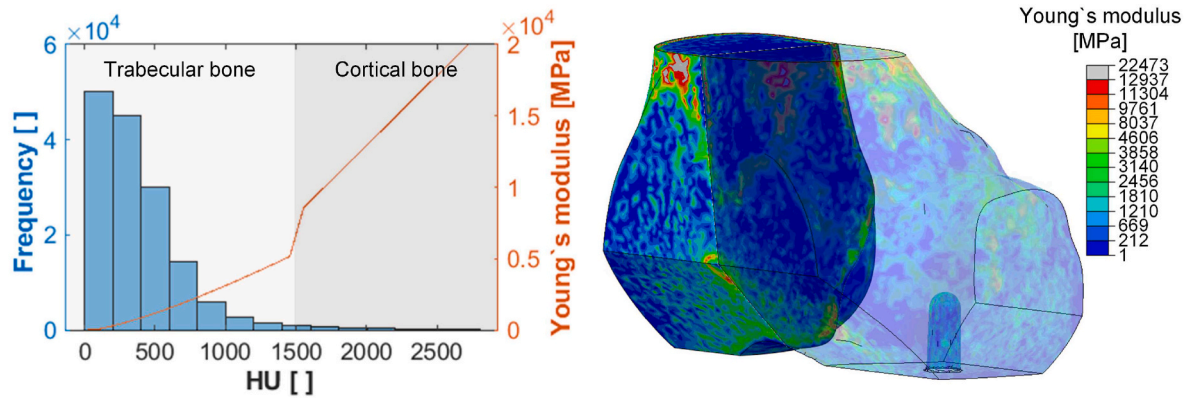


Fig. 3. Frequency and Young's moduli as a function of the Hounsfield unit (HU) according to Rho et al. (1995) of the distal femur used for the finite element analysis and the assigned heterogenous Young's moduli in Abaqus v2022 that corresponds to the HU.

behavior (yield strength: 25 MPa) (Sauer et al., 2021).

Quadratic tetrahedron elements (C3D10) were used to discretize the model. The element sizes were defined within a convergence analysis where the number of elements was incrementally increased. The maximum stress in the femoral component during uncemented implantation and the strain energy in the femoral bone during two-legged squat motion were evaluated. Convergence was defined as a change in the outcome measures of less than 5% compared to the next finer mesh. The defined element edge lengths of the model representing uncemented implantation were 1.4 mm for the ATZ component. The dense and open porous titanium components were meshed with an element edge length of 0.6 mm and 1.1 mm, respectively. The regions of maximum stress in the titanium components were finer meshed with an element edge length of 0.3 mm and a minimum of four elements across the thickness. In the squatting model, element edge lengths of 2.2 mm, 1.5 mm, and 2.2 mm were used for the ATZ component, the titanium components, and the femoral bone, respectively. In addition, the tibial insert and the patellar component were meshed with element edge lengths of 3 mm. Further details of the mesh and convergence study can be found in the Supplementary Material.

2.3.2. Boundary conditions and interaction properties during implantation

The assembly and the boundary conditions of the uncemented implantation are shown in Fig. 4A. Based on literature studies (Berahmani

et al., 2017; Post et al., 2022), an interference fit of 1 mm was created between bone and implant in the anterior-posterior direction. We did not model the implantation by forcing the implant onto the bone, but instead used the remove interference fit option in the contact module. In this step, the surface nodes of the bone (secondary surface) are moved incrementally toward the implant surface (main surface) (Berahmani et al., 2017). In addition, the implant was moved 0.5 mm distally to remove the superior-inferior interference fit. This translational constraint was applied to a coupled reference point (F_{RP}). The bone was fixed proximally throughout the simulation by fully constraining a coupled reference point (B_{RP}). The implantation results in maximum stresses in the lateral posterior radius, as shown in Fig. 4B.

The bone-implant contact was modeled as a hard surface-to-surface contact and with a frictionless penalty contact. Since the friction of the interface did not affect the results with the defined boundary conditions, we simplified the model with this assumption and reduced the run time and convergence errors caused by frictional contact.

2.3.3. Boundary and contact conditions of the two-legged squat motion

The model assembly and the boundary conditions of the two-legged squat motion are shown in Fig. 5. The boundary conditions were derived from a previously described MMBS (Kebbach et al., 2020, 2023; Tischer et al., 2023) and are shown in Fig. 5A. The squat motion was chosen because it covers a wide range of motion and has been previously used to

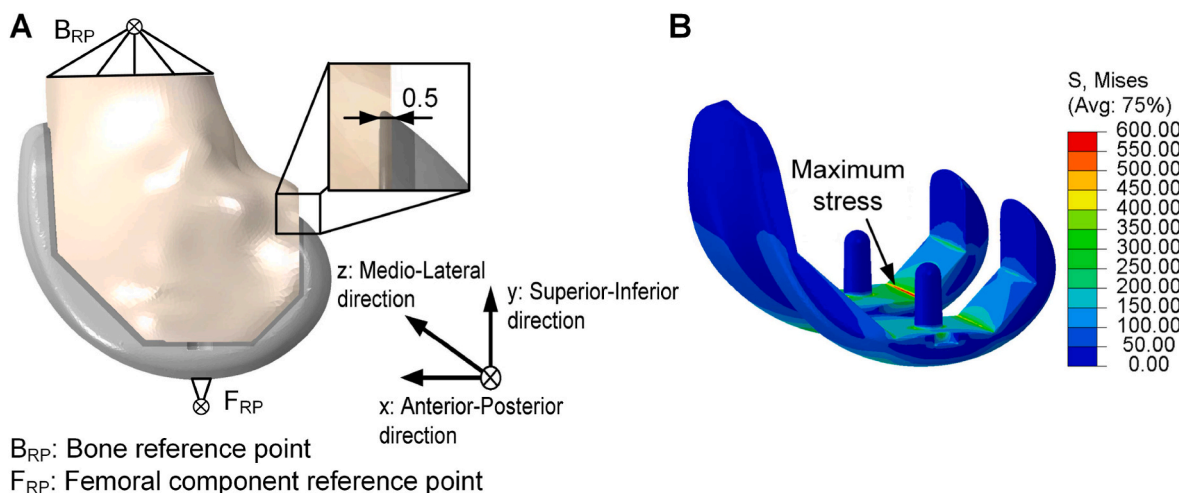


Fig. 4. Finite element model of the uncemented implantation of the femoral component: A) model assembly with initial position of the femoral component and femoral bone (total interference fit in anterior-posterior direction of 1 mm) and identification of the reference points (B_{RP}: fully constrained during loading, F_{RP}: displaced in superior-inferior direction for implantation, free translation in x-direction and constrained in z-direction and all rotational degrees of freedom) and B) location of the maximum von Mises stresses (in MPa) during the implantation.

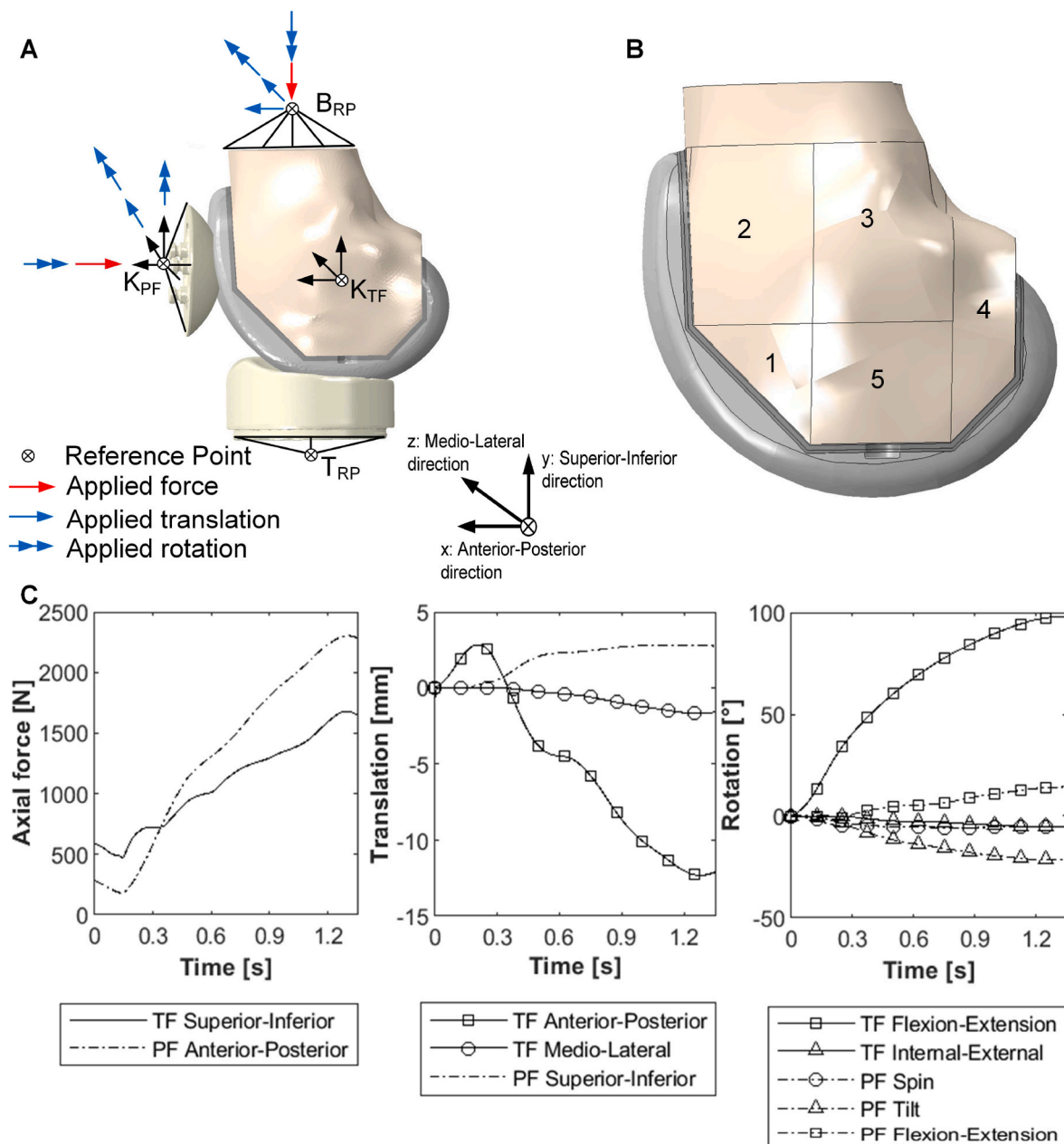


Fig. 5. Finite element model of the two-legged squat motion to $\sim 90^\circ$ of knee flexion: A) initial position of the femoral component, tibial insert and patellar component, where the defined local coordinate systems for the tibiofemoral (K_{TF}) and patellofemoral joint (K_{PF}), the reference points (B_{RP} , T_{RP}) and the applied boundary conditions derived from the musculoskeletal multibody simulation are indicated, B) defined regions of interest 1 to 5 to analyze the volumetric stress shielding by the strain energy density as a function of knee flexion angle and femoral component material, and C) tibiofemoral (TF) and patellofemoral (PF) joint forces, translations and rotations applied to the reference points.

study bone-implant load transfer in TKR (Ruiter et al., 2017; van Jonbergen et al., 2012). The FE model contains the tibial insert, the resurfaced patellar component, the femoral component, and the distal femur. The methodology to link the MMBS and FE analysis followed the workflow according to our previous work (Sass et al., 2024b).

The MMBS was based on the dataset of the 4th Grand Knee Challenge Competition (Fregly et al., 2012) and was built in SIMPACK V9.7 (Dassault Systèmes, Providence, RI, USA). The model used a non-linear force-strain relationship for relevant ligaments of the tibiofemoral and patellofemoral joint, and the articulating implant surfaces were constrained using a polygonal contact model. To calculate the muscle forces, joint coordinates from motion capturing were used in a forward dynamic MMBS using a computed muscle controller with static optimization and wrapping algorithm (Kebbach et al., 2020). Concerning

the implant design, the previous implant components were replaced with those described in section 2.1. The kinematics and contact forces of the tibiofemoral and patellofemoral joints (Fig. 5c) were calculated in the MMBS and then transferred to fixed local coordinate systems in Abaqus v2022 (tibiofemoral K_{TF} , patellofemoral K_{PF} , see Fig. 5A). The joint kinematics were further transferred to the bone reference point (B_{RP}), which was kinematically coupled to the distal cut surface of the femur. Five bone ROI (see Fig. 5B) were defined in the distal femur (Meneghini et al., 2015; Ruiter et al., 2021) to assess the influence of the implant material on volumetric stress shielding.

During the two-legged squat motion, the implant was assumed to be osseointegrated, which was modeled with a fully constrained interface (tie constraint) between the femoral component (main surface) and bone (secondary surface). In addition, ATZ ceramic or Co-28Cr-6Mo alloy

articulating surfaces in contact with UHMW-PE were modeled as hard surface-to-surface contact with a coefficient of friction of 0.04 (Godest et al., 2002).

2.3.4. Outcome measures

The maximum stress in the femoral component was evaluated during the uncemented implantation. This was performed separately for each model component in the hybrid material-based femoral components. Due to the different intrinsic material properties (brittle vs. ductile), the maximum principal stress was used for the ATZ ceramic, and the maximum von Mises stress was used for the Co-28Cr-6Mo alloy and the titanium alloys. During squatting, the relative change in strain energy density compared to the ATZ femoral component in the defined bone ROI was evaluated for each time step. The strain energy density has been described as a stimulus for bone remodeling (Carter et al., 1987; Huiskes et al., 1987) and has previously been used to study the influence of the implant material on volumetric stress shielding around the femoral component (Ruiter et al., 2021). The increase in the strain energy density compared to the defined reference indicates an improvement in the load transfer from the implant to the adjacent bone as the bone is subjected to higher strains.

3. Results

3.1. Mechanical characterization

Representative stress-strain curves of the open porous lattice structures are shown in Fig. 6. Specimens of both titanium alloys fractured at $\sim 45^\circ$ to the load axis, with Ti-35Nb-6Ta exhibiting extensive ductile behavior.

The determined mechanical properties and their level of significance are shown in Table 2. The Ti-35Nb-6Ta specimens showed a higher elasticity, ultimate compressive strength, and elongation at break but decreased yield strength compared to the Ti-6Al-4V specimens.

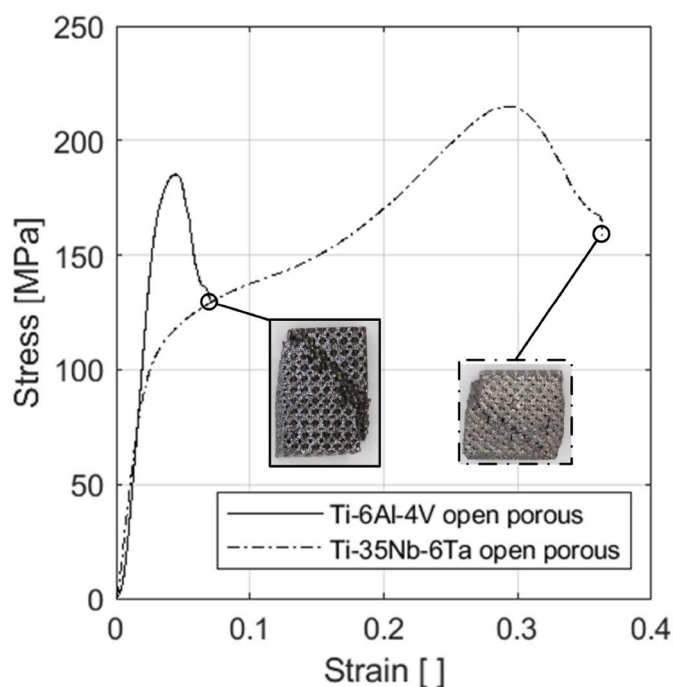


Fig. 6. Representative stress-strain curves of rectangular ($7 \times 7 \times 11 \text{ mm}^3$) open porous structured specimens made of Ti-6Al-4V or Ti-35Nb-6Ta and illustration of the macroscopic fracture.

3.2. Finite-element simulation of the implantation

The maximum stress during implantation was observed in the lateral, posterior radius of the uncemented femoral components and at the final position of the implantation since the anterior-posterior opening was the largest there. Fig. 7 compares the different stress distributions of the hybrid material-based femoral component made of Ti-35Nb-6Ta/ATZ with and without an open porous surface structure of the titanium part and of the monolithic ATZ femoral component.

The maximum principal stress in the monolithic ATZ femoral component amounted to 1568.9 MPa, and the maximum von Mises stress in the Co-28Cr-6Mo based femoral component was 1290.6 MPa. The maximum principal stress in the ATZ component decreased within the hybrid material-based femoral components to 367.6 MPa (-76.6%) for Ti-6Al-4V/ATZ, to 560.9 MPa (-64.3%) for Ti-6Al-4V/ATZ with an open porous surface structure, to 474.9 MPa (-69.7%) for Ti-35Nb-6Ta/ATZ, and to 648.4 MPa (-58.7%) for Ti-35Nb-6Ta/ATZ with an open porous surface structure. The maximum von Mises stresses in the titanium-based implant parts were 758.2 MPa (Ti-6Al-4V/ATZ), 636.5 MPa (Ti-6Al-4V/ATZ with an open porous surface structure), 506.2 MPa (Ti-35Nb-6Ta/ATZ), and 411.1 MPa (Ti-35Nb-6Ta/ATZ with an open porous surface structure). The maximum von Mises stress in the open porous surface layer was 52.6 MPa and 84.2 MPa in the Ti-35Nb-6Ta and Ti-6Al-4V implant components, respectively.

Accordingly, we observed that the stress within the ATZ part of a hybrid material-based femoral component is influenced by Young's modulus and the structural stiffness of the joined titanium part.

3.3. Finite element simulation of the squat motion

The strain energy density in the anterior region of the distal femur (ROI 1) as a function of the knee flexion angle is shown in Fig. 8 as a representative curve of the analyzed models during the two-legged squat motion. It can be seen that the strain energy density increased at higher flexion angles due to a higher axial joint force. In addition, the hybrid materials increased the strain energy density and, therefore, the load on the bone. The effect of the different implant materials is clearly pronounced in bone ROI 1 at approximately 35° of knee flexion. The strain energy density of the periprosthetic bone was influenced by both the titanium alloy used and the implant surface structure (dense or open porous).

The relative changes in strain energy density (ΔSED) within the bone ROIs of the different femoral component materials compared to monolithic ATZ ceramic are shown in Fig. 9. We observed minor differences between ATZ ceramic and Co-28Cr-6Mo alloy, based on their comparable Young's moduli (ATZ: 261 GPa vs. Co-28Cr-6Mo: 240 GPa). The hybrid materials distinctively increased the strain energy density in the anterior region of the periprosthetic bone (ROI 1 and 5). For example in the bone ROI 1 at $\sim 90^\circ$ of knee flexion, the strain energy density increased by 25.7% (Ti-6Al-4V/ATZ), 70.3% (Ti-6Al-4V/ATZ with an open porous surface), 43.7% (Ti-35Nb-6Ta/ATZ), 82.5% (Ti-35Nb-6Ta/ATZ with an open porous surface), and 4.8% (Co-28Cr-6Mo alloy) compared to monolithic ATZ.

4. Discussion

To avoid metal ion release, stress shielding, and subsequent aseptic implant loosening, current advances in implant materials for femoral components of TKR represent polymers such as PEEK (Post et al., 2022; Ruiter et al., 2017, 2021), functionally graded materials (Bahraminasab et al., 2017, 2021, 2022a, 2022b; Moayedee et al., 2024), or wear-resistant coatings on titanium-based implants (Galas et al., 2023; Lee et al., 2023). In line with these approaches, soldering of ceramic and titanium subcomponents to form a hybrid material is a promising approach in TKR that has been investigated in a recent experimental study of our group (Sass et al., 2024a). However, this study was limited

Table 2

Mechanical properties of the compressively loaded open porous lattice structures and the level of significance between Ti-35Nb-6Ta and Ti-6Al-4V specimens. C: compressive modulus, $\sigma_{c,0.2}$: compressive yield strength, UCS: compressive ultimate strength, ϵ : elongation at break.

	C [GPa]		$\sigma_{c,0.2}$ [MPa]		UCS [MPa]		ϵ [%]	
Ti-35Nb-6Ta	5.2	(0.2)	89.9	(0.6)	226.5	(32.2)	0.35	(0.03)
Ti-6Al-4V	8.8	(0.8)	163.1	(2.6)	183.7	(2.4)	0.12	(0.02)
p-value	<0.001		<0.001		0.029		<0.001	

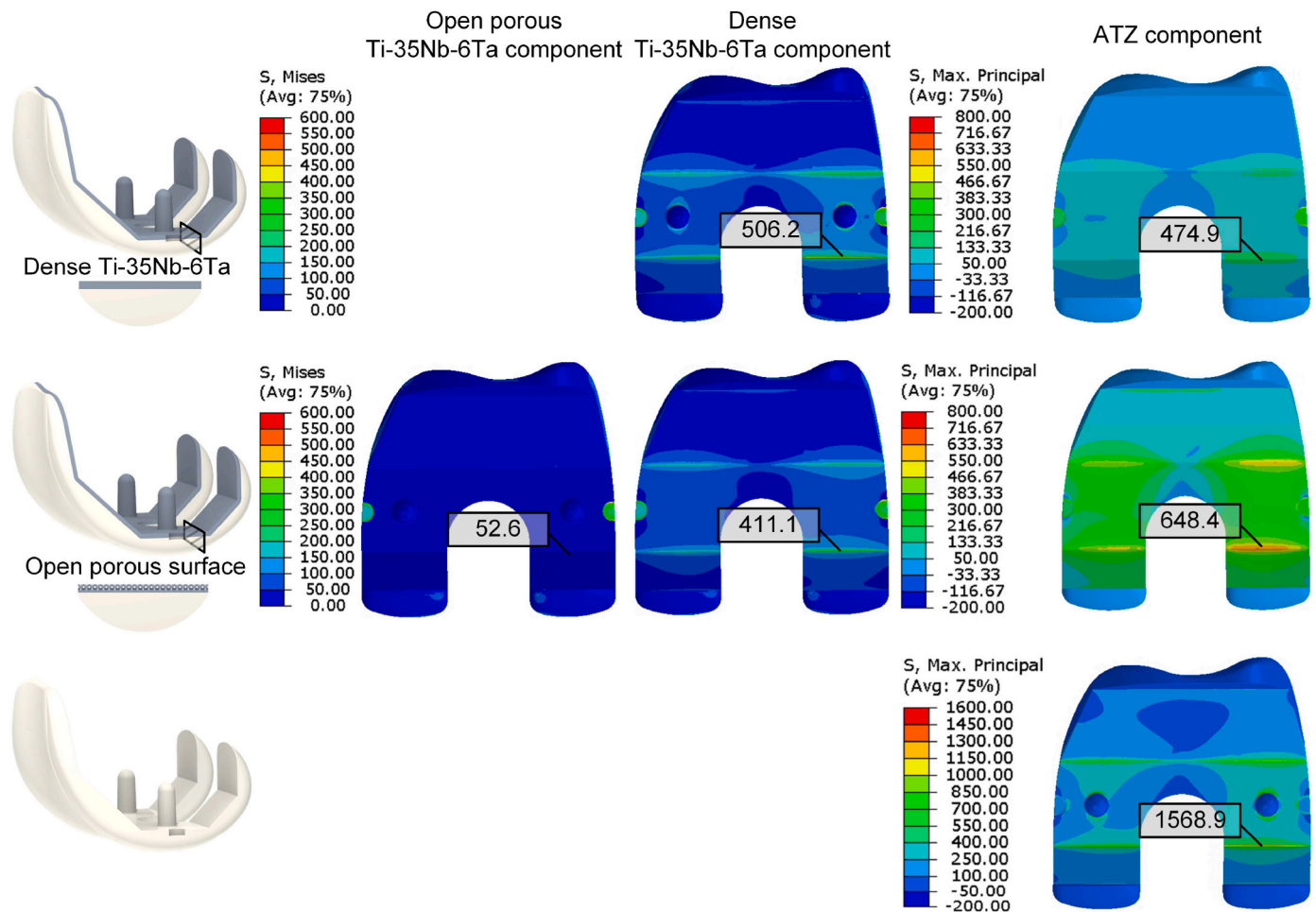


Fig. 7. Stress distributions (von Mises or maximum principal stress, both in MPa) of the finite element models simulating implantation of uncemented femoral components consisting of Ti-35Nb-6Ta/ATZ hybrid materials with/without an open porous surface structure, and monolithic ATZ.

by simplified geometries, and the performance during implantation and the bone-implant interactions have not been investigated so far. Hence, we used the FE analysis to evaluate the biomechanical properties of a hybrid material-based femoral component based on an oxide ceramic component in the articulating interfaces and a titanium-based component in the bone-implant interface. The titanium alloys were Ti-6Al-4V or Ti-35Nb-6Ta (pure β -Ti), which were modeled either completely dense or with an open porous surface structure. We analyzed implant loading scenarios by uncemented implantation and bone-implant interaction during two-legged squat motion.

Uncemented implantation of the femoral component has benefits compared to cemented fixation (Uivaraseanu et al., 2022) but is a high-impact event and results in an anterior-posterior opening of the femoral component, comparable to the loading of cemented implantation with distal under resection of the femur (Klues et al., 2012). Several studies have experimentally and numerically investigated the implantation of femoral components (Berahmani et al., 2015, 2017; Klues et al., 2010, 2012). During implantation, higher stresses in

ceramic-based femoral component compared with a femoral component made of Co-28Cr-6Mo alloy were observed and critical maximum principal stresses of up to ~2000 MPa were reported in the radius of the transition from the distal horizontal section to the anterior and posterior oblique sections (Klues et al., 2010, 2012). In our present study, a maximum principal stress of 1568.9 MPa has been demonstrated in the monolithic ATZ-based femoral component, which was comparable to these previous observations. Although ATZ ceramics have a relatively high fracture toughness compared to other ceramics (Bedir et al., 2023), it is characterized by brittle fracture (Roulet et al., 2021; Sequeira et al., 2017), and studies reported maximum flexural strength of 1394 MPa (Sequeira et al., 2017) and maximum biaxial strength of 1636 ± 302 MPa (Roulet et al., 2021). Therefore, the maximum principal stress in the monolithic ATZ femoral component in this study was within a critical range of material failure, indicating the risk of intraoperative fracture. The observed stress in the titanium components was below the yield strength of the materials (Sass et al., 2024c), and the stress in the open porous surface layer also did not exceed the yield strength. Thus,

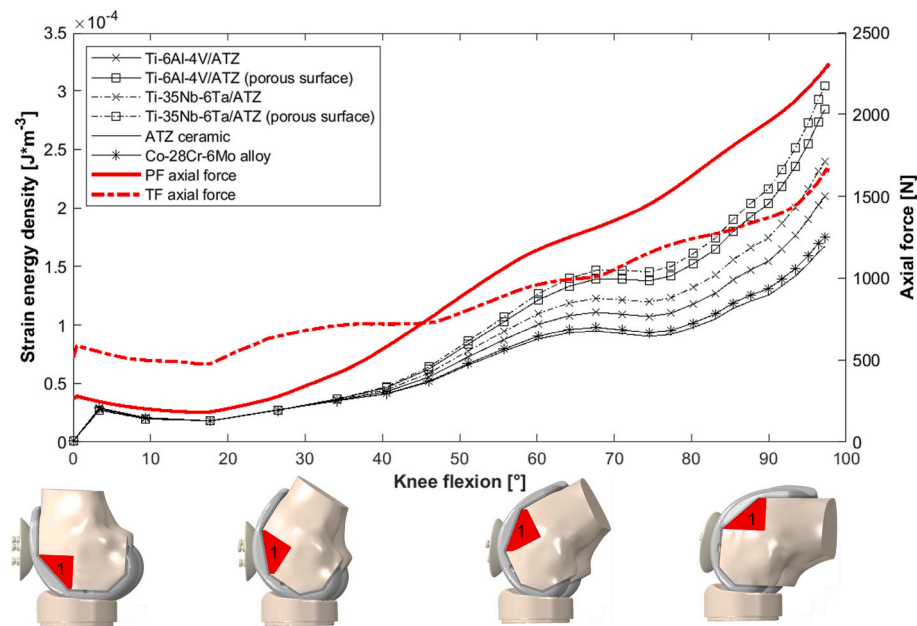


Fig. 8. Strain energy density in the bone region of interest one as a function of the knee flexion angle and the axial force distribution at the tibiofemoral (TF) and patellofemoral (PF) joints and comparison of the different femoral component materials (hybrid materials of Ti-6Al-4V/ATZ and Ti-35Nb-6Ta/ATZ with and without an open porous surface structure, monolithic ATZ ceramic and monolithic Co-28Cr-6Mo alloy).

the mechanical integrity of the titanium components was maintained during cementless implantation.

We found a distinctive stress reduction in the ATZ component within the hybrid material-based implants ranging from -76.6% to -58.7% , depending on the model configuration. Our observations showed that in the hybrid material concept, the titanium component shields the ATZ component from high stresses. This phenomenon depends on the area moment of inertia of the implant components. Accordingly, when the elasticity of the titanium alloy increases, the stress in the ATZ component increases as well, while the stress in the titanium component decreases. The design optimization of the components is crucial for sufficient implant safety during uncemented implantation since the area moment of inertia is determined by the intrinsic material properties and the geometrical property (e.g. wall thickness).

Stress shielding of the periprosthetic bone is caused by the altered load transfer to the distal femoral bone after TKR. Implant materials with a higher stiffness than bone led to a biomechanical situation in which forces are carried predominantly by the implant components and not by the bone. According to Wolff's law (Wolff, 2010), the altered bone loading induces stress-related bone resorption (Galas et al., 2023; Ruiter et al., 2021). We found that there were no differences between ATZ ceramic and Co-28Cr-6Mo alloy based femoral components in terms of stress shielding. This is reasonable because ATZ and Co-28Cr-6Mo have almost similar Young's moduli. Due to the higher elasticity of the titanium alloys, the hybrid femoral components reduced the stress shielding of the periprosthetic bone compared to monolithic ATZ and Co-28Cr-6Mo. Previous studies have investigated the effect of the implant material on the stress shielding (Bahraminasab et al., 2013; Galas et al., 2023; Ruiter et al., 2021) and confirm our current observations. A comparison of PEEK (Ruiter et al., 2021), Ti-6Al-4V with Ti-Nb-N coating (Galas et al., 2023), or a functionally graded material (Bahraminasab et al., 2013) indicated that stress shielding decreases with higher elasticity of the implant materials. Our results highlight the beneficial effects of β -Ti alloys such as Ti-35Nb-6Ta and the design of open porous implant surface structures to reduce the stress shielding within the periprosthetic bone. The applied lattice structures used for experimental characterization were only one example of various design possibilities. Despite achieving compressive stiffness in the range of

human bone, further optimization, or other designs should be considered.

Clinical studies have analyzed bone resorption after TKR with radiographic measurements of bone density (Bendich et al., 2022; Järvenpää et al., 2014; Lee et al., 2023; Mintzer et al., 1990; Yilmaz et al., 2021). These studies have demonstrated that the anterior part of the distal femoral bone is particularly affected. This region is comparable to our described bone ROI 1 and 5. The hybrid femoral components showed the highest improvement in implant-to-bone load transfer in this region, indicating potential to reduce clinically relevant bone resorption. In this context, a comparison of different implant materials has not been performed in clinical studies so far.

This computational study has limitations. The FE analysis was based on one femoral component design implanted in one femur. Therefore, anatomical variations or different bone conditions were not considered. For uncemented implantation, only one press-fit was considered, and the linear-elastic material assumptions of the bone may overestimate the implant load because the bone is plastically deformed during uncemented implantation (Berahmani et al., 2017). Cementless implanted ATZ ceramic or Co-28Cr-6Mo alloy-based femoral components necessarily require surface functionalization, e.g. titanium plasma spray coating, to achieve osseointegration, which was neglected in the simulations of this present study. Furthermore, the dynamic impaction during implantation was simplified to a static model, but we based our modeling on a previous study (Berahmani et al., 2017). In addition, the derived boundary conditions of the two-legged squat motion were based on a MMBS of the lower extremity, with its limitations described in detail by Keibach et al. (2020). In addition, no experimental study has been conducted to manufacture a hybrid material-based femoral component so far. Hence, because the numerical simulations have not been experimentally validated, the absolute results have to be interpreted with restrictions. However, general observations of the simulations are consistent with other previously published studies. Accordingly, this computational study should be considered as a systematic comparison of the different implant materials and as a first evaluation rather than as a determination of absolute values. Moreover, glass soldering is a viable technology for bonding ATZ ceramics to titanium materials, creating a material bond and mechanical interlock

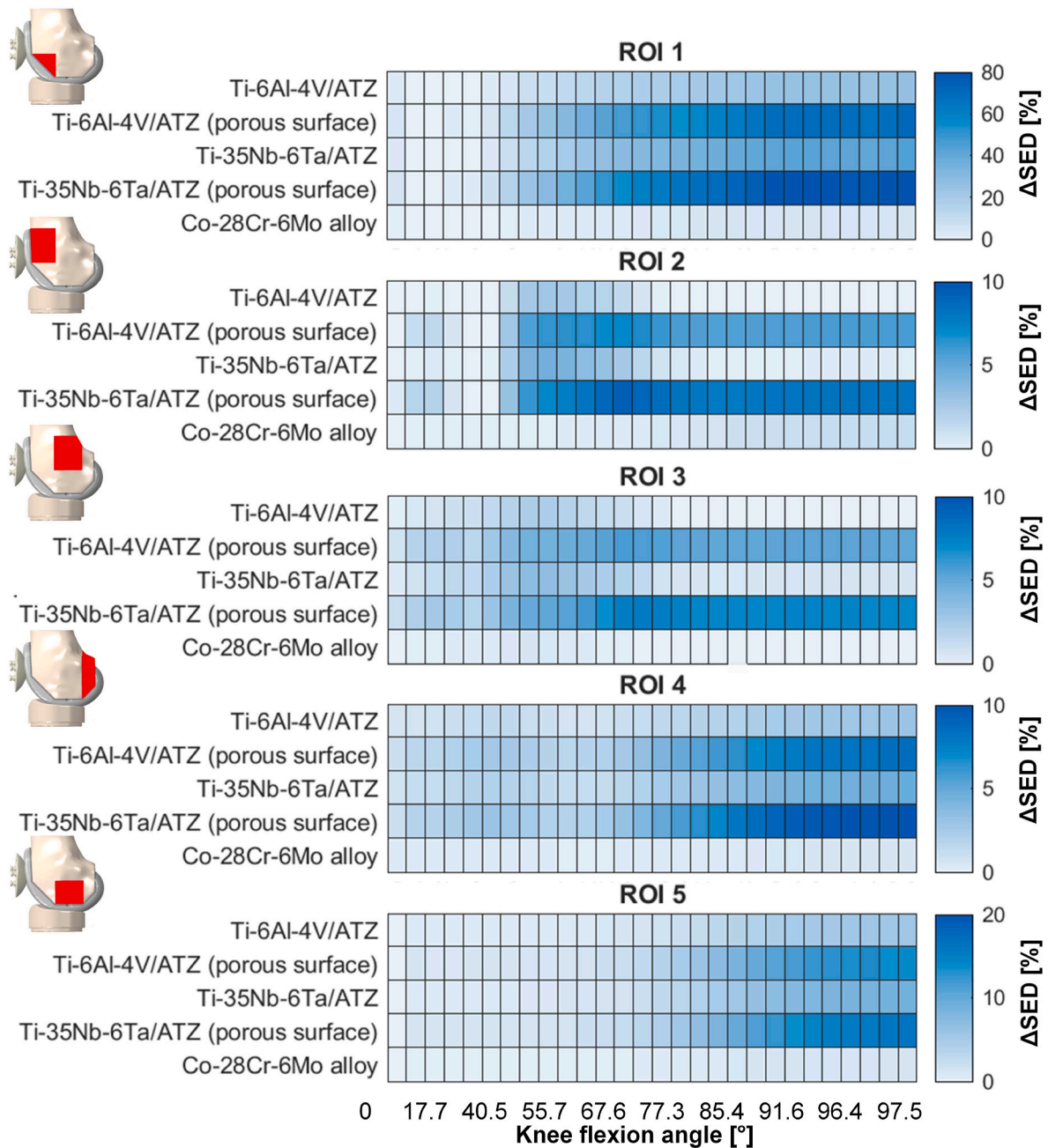


Fig. 9. Heat maps of the relative change in strain energy density (ΔSED [%]) for the different bone regions of interest (ROI) compared to the ATZ ceramic-based femoral component as a function of the implant material (hybrid materials of Ti-6Al-4V/ATZ and Ti-35Nb-6Ta/ATZ with dense or an open porous surface structure, and monolithic Co-28Cr-6Mo alloy).

during firing (Mick et al., 2015; Sass et al., 2024a; Suansuwan and Swain, 2003; Sun et al., 2022; Vásquez et al., 2009). In our present study, the soldered joint was considered only by constrained interfaces and not by volumetric modeling of the glass solder. However, the investigation of the interface stresses and the joint strength of the material bond are of great importance, since failure is likely to occur within the glass-solder or the titanium alloy surface (Sass et al., 2024a). In our previous study on the experimental characterization of TiNbTa/ATZ specimens, we concluded that a diffusion layer is formed at the glass-solder/TiNbTa interface (Sass et al., 2024a), and it is reasonable to assume that this has different material properties than the bulk TiNbTa alloy. Furthermore, thin joints (~0.1 mm (Sass et al., 2024a)) pose challenges in FE modeling, which could be solved by sub-modeling of certain locations.

The transfer of the glass soldering technology to Ti-35Nb-6Ta and the development of a functional demonstrator are part of subsequent studies. Future studies should focus on various aspects, including the press fit required to achieve primary stability, the influence of design specifications, and patient-specific factors such as bone quality and individual motion sequences. Assuming a glass-soldered bond between the materials, it is crucial to develop a reliable FE model of the material joint and to comprehensively analyze the factors influencing the joint strength. In addition, worst-case scenarios such as under-resection during implantation or dynamic impactions induced by falls or accidents could be considered to further evaluate the performance of hybrid implant materials.

5. Conclusion

The purpose of this computational study was to analyze hybrid materials for the uncemented femoral component by evaluating their biomechanical properties during implantation and two-legged squat motion. The hybrid material was based on ATZ ceramics for the articulating surface and different titanium alloys (Ti–6Al–4V or Ti–35Nb–6Ta) for the bone-implant interface. In the FE modeling, the hybrid femoral component showed a reduced fracture risk within the ceramic part compared to the monolithic ceramic implant for the investigated uncemented implantation. In addition, the stress shielding in the periprosthetic bone is mainly reduced in the anterior region, where bone resorption has been primarily observed in clinical studies. The combination of ATZ ceramics and titanium alloys in a multifunctional material potentially combines the high wear and corrosion resistance of ATZ ceramics with the osseointegration and high elasticity of the TiNbTa alloy. At the same time, limitations such as brittle fracture of the ceramic and poor wear resistance of the titanium alloy are reduced. Therefore, the hybrid implant material shows great potential for reducing material-related aseptic implant loosening after total knee replacement.

Declaration of generative AI in scientific writing

During the preparation of this work the author(s) used Grammarly and DeepL/write in order to correct typos and grammatical errors. After using this tool/service, the author(s) reviewed and edited the content as needed and take(s) full responsibility for the content of the publication.

Funding

This work was supported by the Federal Ministry of Education and Research BMBF, Germany (grant number: 03XP0279D), which had no role in study design; in the collection, analysis, and interpretation of data; in the writing of the report; and in the decision to submit the article for publication.

CRediT authorship contribution statement

Jan-Oliver Sass: Writing – original draft, Visualization, Validation, Supervision, Project administration, Methodology, Investigation, Formal analysis, Data curation, Conceptualization. **Maeruan Kebbach:** Writing – review & editing, Validation, Methodology, Data curation, Conceptualization. **Cornelia Lork:** Writing – review & editing, Project administration, Funding acquisition, Conceptualization. **Jan Johannsen:** Writing – review & editing, Resources, Methodology, Funding acquisition, Conceptualization. **Markus Weinmann:** Writing – review & editing, Resources, Methodology, Funding acquisition, Conceptualization. **Melanie Stenzel:** Writing – review & editing, Resources, Methodology, Funding acquisition, Conceptualization. **Rainer Bader:** Writing – review & editing, Supervision, Funding acquisition, Conceptualization.

Declaration of competing interest

The authors declare the following financial interests/personal relationships which may be considered as potential competing interests: The authors Jan-Oliver Sass, Jan Johannsen, Maeruan Kebbach, Rainer Bader declare that they have no known competing financial interests or personal relationships that could have appeared to influence the work reported in this paper.

Cornelia Lork reports a relationship with ZM Präzisionsdenteltechnik GmbH that includes: employment. Markus Weinmann reports a relationship with TANI OBIS GmbH that includes: employment. Melanie Stenzel reports a relationship with TANI OBIS GmbH that includes: employment.

Data availability

Data will be made available on request.

Acknowledgments

We would like to thank Christoph Lutter (Department of Orthopaedics, Rostock University Medical Center, Rostock, Germany) for his support in the virtual implantation of the femoral component.

Appendix A. Supplementary data

Supplementary data to this article can be found online at <https://doi.org/10.1016/j.jmbbm.2024.106681>.

References

- Bahraminasab, M., Arab, S., Doostmohammadi, N., 2022a. Cytotoxicity and ion release of functionally graded Al₂O₃-Ti orthopedic biomaterial. *JBBBE* 54, 103–118. <https://doi.org/10.4028/www.scientific.net/JBBBE.54.103>.
- Bahraminasab, M., Arab, S., Ghaffari, S., 2022b. Osteoblastic cell response to Al₂O₃-Ti composites as bone implant materials. *Bioimpacts: BI* 12 (3), 247–259. <https://doi.org/10.34172/bi.2021.2330>.
- Bahraminasab, M., Arab, S., Safari, M., Talebi, A., Kavakebian, F., Doostmohammadi, N., 2021. In vivo performance of Al₂O₃-Ti bone implants in the rat femur. *J. Orthop. Surg. Res.* 16 (1), 79. <https://doi.org/10.1186/s13018-021-02226-7>.
- Bahraminasab, M., Bozorg, M., Ghaffari, S., Kavakebian, F., 2019. Electrochemical corrosion of Ti-Al₂O₃ biocomposites in Ringer's solution. *J. Alloys Compd.* 777, 34–43. <https://doi.org/10.1016/j.jallcom.2018.09.313>.
- Bahraminasab, M., Ghaffari, S., Eslami-Shahed, H., 2017. Al₂O₃-Ti functionally graded material prepared by spark plasma sintering for orthopaedic applications. *J. Mech. Behav. Biomed. Mater.* 72, 82–89. <https://doi.org/10.1016/j.jmbbm.2017.04.024>.
- Bahraminasab, M., Sahari, B.B., Edwards, K.L., Farahmand, F., Hong, T.S., Naghibi, H., 2013. Material tailoring of the femoral component in a total knee replacement to reduce the problem of aseptic loosening. *Mater. Des.* 52, 441–451. <https://doi.org/10.1016/j.matdes.2013.05.066>.
- Bedir, T., Altan, E., Aranci-Ciftci, K., Gunduz, O., 2023. *Bioceramics*. In: Gunduz, O., Egles, C., Pérez, R.A., Fical, D., Ustundag, C.B. (Eds.), *Biomaterials and Tissue Engineering*, vol. 74. Springer International Publishing, Cham, pp. 175–203.
- Bendich, I., Lawrie, C.M., Riegler, V., Barrack, R.L., Nunley, R.M., 2022. The impact of component design and fixation on stress shielding after modern total knee arthroplasty. *J. Arthroplasty* 37 (6S), S221–S225. <https://doi.org/10.1016/j.arth.2022.01.074>.
- Berahmani, S., Janssen, D., Verdonschot, N., 2017. Experimental and computational analysis of micromotions of an uncemented femoral knee implant using elastic and plastic bone material models. *J. Biomech.* 61, 137–143. <https://doi.org/10.1016/j.jbiomech.2017.07.023>.
- Berahmani, S., Janssen, D., Wolfson, D., Rivard, K., Waal Malefijt, M. de, Verdonschot, N., 2015. The effect of surface morphology on the primary fixation strength of uncemented femoral knee prosthesis: a cadaveric study. *J. Arthroplasty* 30 (2), 300–307. <https://doi.org/10.1016/j.arth.2014.09.030>.
- Bergschmidt, P., Ellenrieder, M., Bader, R., Kluess, D., Finze, S., Schwemmer, B., Mittelmeier, W., 2016. Prospective comparative clinical study of ceramic and metallic femoral components for total knee arthroplasty over a five-year follow-up period. *Knee* 23 (5), 871–876. <https://doi.org/10.1016/j.knee.2016.06.001>.
- Carter, D.R., Fyhrie, D.P., Whalen, R.T., 1987. Trabecular bone density and loading history: regulation of connective tissue biology by mechanical energy. *J. Biomech.* 20 (8), 785–794. [https://doi.org/10.1016/0021-9290\(87\)90058-3](https://doi.org/10.1016/0021-9290(87)90058-3).
- Crutsen, J.R.W., Koper, M.C., Jelsma, J., Heymans, M., Heyligers, I.C., Grimm, B., Mathijssen, N.M.C., Schotanus, M.G.M., 2022. Prosthetic hip-associated cobalt toxicity: a systematic review of case series and case reports. *EFORT open reviews* 7 (3), 188–199. <https://doi.org/10.1530/EOR-21-0098>.
- Drynda, A., Drynda, S., Kekow, J., Lohmann, C.H., Bertrand, J., 2018. Differential effect of cobalt and chromium ions as well as CoCr particles on the expression of osteogenic markers and osteoblast function. *Int. J. Mol. Sci.* 19 (10) <https://doi.org/10.3390/ijms19103034>.
- Eisenbarth, E., Velten, D., Müller, M., Thull, R., Breme, J., 2004. Biocompatibility of beta-stabilizing elements of titanium alloys. *Biomaterials* 25 (26), 5705–5713. <https://doi.org/10.1016/j.biomaterials.2004.01.021>.
- Farrahnour, A., Zuhailawati, H., 2021. Review on the mechanical properties and biocompatibility of titanium implant: the role of niobium alloying element. *Int. J. Mater. Res.* 112 (6), 505–513. <https://doi.org/10.1515/ijmr-2020-8060>.
- Fregly, B.J., Besier, T.F., Lloyd, D.G., Delp, S.L., Banks, S.A., Pandy, M.G., D'Lima, D.D., 2012. Grand challenge competition to predict in vivo knee loads. *J. Orthop. Res.* : official publication of the Orthopaedic Research Society 30 (4), 503–513. <https://doi.org/10.1002/jor.22023>.
- Galas, A., Banci, L., Innocenti, B., 2023. The effects of different femoral component materials on bone and implant response in total knee arthroplasty: a finite element analysis. *Materials* 16 (16). <https://doi.org/10.3390/ma16165605>.

- Gao, X., Fraulob, M., Haiat, G., 2019. Biomechanical behaviours of the bone-implant interface: a review. *J. R. Soc., Interface* 16 (156), 20190259. <https://doi.org/10.1098/rsif.2019.0259>.
- Godest, A.C., Beaugonin, M., Haug, E., Taylor, M., Gregson, P.J., 2002. Simulation of a knee joint replacement during a gait cycle using explicit finite element analysis. *J. Biomech.* 35 (2), 267–275. [https://doi.org/10.1016/S0021-9290\(01\)00179-8](https://doi.org/10.1016/S0021-9290(01)00179-8).
- Grimberg, A., Lütznier, J., Melzheimer, O., Morlock, M., Steinbrück, A., 2023. *Arthroplasty Register Germany (EPRD) - Annual Report 2023: Mit Sicherheit Mehr Qualität. EPRD Deutsche Endoprothesenregister, Berlin, p. 175.*
- Huiskes, R., Weinans, H., Grootenboer, H.J., Dalstra, M., Fudala, B., Slooff, T.J., 1987. Adaptive bone-remodeling theory applied to prosthetic-design analysis. *J. Biomech.* 20 (11–12), 1135–1150. [https://doi.org/10.1016/0021-9290\(87\)90030-3](https://doi.org/10.1016/0021-9290(87)90030-3).
- Järvenpää, J., Soininvaara, T., Kettunen, J., Miettinen, H., Kröger, H., 2014. Changes in bone mineral density of the distal femur after total knee arthroplasty: a 7-year DEXA follow-up comparing results between obese and nonobese patients. *Knee* 21 (1), 232–235. <https://doi.org/10.1016/j.knee.2013.03.004>.
- Johannsen, J., Lauhoff, C., Stenzel, M., Schnitter, C., Niendorf, T., Weinmann, M., 2023. Laser beam powder bed fusion of novel biomedical titanium/niobium/tantalum alloys: powder synthesis, microstructure evolution and mechanical properties. *Mater. Des.* 233, 112265. <https://doi.org/10.1016/j.matdes.2023.112265>.
- Jonitz-Heincke, A., Sellin, M.-L., Seyfarth, A., Peters, K., Mueller-Hilke, B., Fiedler, T., Bader, R., Klinder, A., 2019. Analysis of cellular activity short-term exposure to cobalt and chromium ions in mature human osteoblasts. *Materials* 12 (17). <https://doi.org/10.3390/ma12172771>.
- Kaur, M., Singh, K., 2019. Review on titanium and titanium based alloys as biomaterials for orthopaedic applications. *Materials science & engineering. C, Materials for biological applications* 102, 844–862. <https://doi.org/10.1016/j.msec.2019.04.064>.
- Keibach, M., Darowski, M., Krueger, S., Schilling, C., Grupp, T.M., Bader, R., Geier, A., 2020. Musculoskeletal multibody simulation analysis on the impact of patellar component design and positioning on joint dynamics after unconstrained total knee arthroplasty. *Materials* 13 (10). <https://doi.org/10.3390/ma13102365>.
- Keibach, M., Geier, A., Darowski, M., Krueger, S., Schilling, C., Grupp, T.M., Bader, R., 2023. Computer-based analysis of different component positions and insert thicknesses on tibio-femoral and patello-femoral joint dynamics after cruciate-retaining total knee replacement. *Knee* 40, 152–165. <https://doi.org/10.1016/j.knee.2022.11.010>.
- Keyak, J.H., Falkinstein, Y., 2003. Comparison of in situ and in vitro CT scan-based finite element model predictions of proximal femoral fracture load. *Med. Eng. Phys.* 25 (9), 781–787. [https://doi.org/10.1016/S1350-4533\(03\)00081-X](https://doi.org/10.1016/S1350-4533(03)00081-X).
- Klueess, D., Bergschmidt, P., Mueller, I., Mittelmeier, W., Bader, R., 2012. Influence of the distal femoral resection angle on the principal stresses in ceramic total knee components. *Knee* 19 (6), 846–850. <https://doi.org/10.1016/j.knee.2012.03.014>.
- Klueess, D., Mittelmeier, W., Bader, R., 2010. Intraoperative impaction of total knee replacements: an explicit finite-element analysis of principal stresses in ceramic vs. cobalt-chromium femoral components. *Clin. Biomech.* 25 (10), 1018–1024. <https://doi.org/10.1016/j.clinbiomech.2010.08.002>.
- Krueger, A.P., Singh, G., Beil, F.T., Feuerstein, B., Ruether, W., Lohmann, C.H., 2014. Ceramic femoral component fracture in total knee arthroplasty: an analysis using fractography, fourier-transform infrared microscopy, contact radiography and histology. *J. Arthroplasty* 29 (5), 1001–1004. <https://doi.org/10.1016/j.arth.2013.11.003>.
- Lee, D.W., Du Ro, H., Han, H.-S., Lee, M.C., 2023. Titanium alloy knee implant is associated with higher bone density over cobalt chromium: a prospective matched-pair case-control study. *Clinics in orthopedic surgery* 15 (4), 581–588. <https://doi.org/10.4055/cios22082>.
- Luo, J.P., Sun, J.F., Huang, Y.J., Zhang, J.H., Zhang, Y.D., Zhao, D.P., Yan, M., 2019. Low-modulus biomedical Ti-30Nb-5Ta-3Zr additively manufactured by Selective Laser Melting and its biocompatibility. *Materials science & engineering. C, Materials for biological applications* 97, 275–284. <https://doi.org/10.1016/j.msec.2018.11.077>.
- Mauck, J., Wieding, J., Klueess, D., Bader, R., 2016. Numerical simulation of mechanically stimulated bone remodelling. *Current Directions in Biomedical Engineering* 2 (1), 643–647. <https://doi.org/10.1515/cdbme-2016-0141>.
- Meneghini, R.M., Mont, M.A., Backstein, D.B., Bourne, R.B., Dennis, D.A., Scuderi, G.R., 2015. Development of a modern knee society radiographic evaluation system and methodology for total knee arthroplasty. *J. Arthroplasty* 30 (12), 2311–2314. <https://doi.org/10.1016/j.arth.2015.05.049>.
- Mick, E., Tinschert, J., Mitrovic, A., Bader, R., 2015. A novel technique for the connection of ceramic and titanium implant components using glass solder bonding. *Materials* 8 (7), 4287–4298. <https://doi.org/10.3390/ma8074287>.
- Mintzer, C.M., Robertson, D.D., Rackemann, S., Ewald, F.C., Scott, R.D., Spector, M., 1990. Bone loss in the distal anterior femur after total knee arthroplasty. *Clin. Orthop. Relat. Res.* 260, 135–143.
- Moayedee, Y., Nikzad, L., Majidian, H., 2024. Exploration into the microstructural, mechanical, and biological characteristics of the functionally graded 3Y-TZP/Ti6Al4V system as a potential material for dental implants. *J. Mech. Behav. Biomed. Mater.* 151, 106380. <https://doi.org/10.1016/j.jmbmm.2024.106380>.
- Ni, J., Ling, H., Zhang, S., Wang, Z., Peng, Z., Benyshek, C., Zan, R., Miri, A.K., Li, Z., Zhang, X., Lee, J., Lee, K.-J., Kim, H.-J., Tebon, P., Hoffman, T., Dokmeci, M.R., Ashammakhi, N., Li, X., Khademhosseini, A., 2019. Three-dimensional printing of metals for biomedical applications. *Materials today. Bio* 3, 100024. <https://doi.org/10.1016/j.mtbio.2019.100024>.
- Niinomi, M., 1998. Mechanical properties of biomedical titanium alloys. *Mater. Sci. Eng.* 243 (1–2), 231–236. [https://doi.org/10.1016/S0921-5093\(97\)00806-X](https://doi.org/10.1016/S0921-5093(97)00806-X).
- Ozan, S., Lin, J., Li, Y., Wen, C., 2017. New Ti-Ta-Zr-Nb alloys with ultrahigh strength for potential orthopedic implant applications. *J. Mech. Behav. Biomed. Mater.* 75, 119–127. <https://doi.org/10.1016/j.jmbmm.2017.07.011>.
- Pilz, S., Gustmann, T., Günther, F., Zimmermann, M., Kühn, U., Gebert, A., 2022. Controlling the Young's modulus of a β -type Ti-Nb alloy via strong texturing by LPBF. *Mater. Des.* 216, 110516. <https://doi.org/10.1016/j.matdes.2022.110516>.
- Post, C.E., Bitter, T., Briscoe, A., Verdonschot, N., Janssen, D., 2022. A FE study on the effect of interference fit and coefficient of friction on the micromotions and interface gaps of a cementless PEEK femoral component. *J. Biomech.* 137, 111057. <https://doi.org/10.1016/j.jbiomech.2022.111057>.
- Rho, J.Y., Hobatho, M.C., Ashman, R.B., 1995. Relations of mechanical properties to density and CT numbers in human bone. *Med. Eng. Phys.* 17 (5), 347–355. [https://doi.org/10.1016/1350-4533\(95\)97314-f](https://doi.org/10.1016/1350-4533(95)97314-f).
- Roulet, J.-F., Schepker, K.L., Truco, A., Schwarz, H.-C., Rocha, M.G., 2021. Biaxial flexural strength, crystalline structure, and grain size of new commercially available zirconia-based ceramics for dental appliances produced using a new slip-casting method. *J. Mech. Behav. Biomed. Mater.* 114, 104180. <https://doi.org/10.1016/j.jmbmm.2020.104180>.
- Ruiter, L. de, Janssen, D., Briscoe, A., Verdonschot, N., 2017. The mechanical response of a polyetheretherketone femoral knee implant under a deep squatting loading condition. *Proceedings of the Institution of Mechanical Engineers. Part H. Journal of engineering in medicine* 231 (12), 1204–1212. <https://doi.org/10.1177/0954411917738805>.
- Ruiter, L. de, Rankin, K., Browne, M., Briscoe, A., Janssen, D., Verdonschot, N., 2021. Decreased stress shielding with a PEEK femoral total knee prosthesis measured in validated computational models. *J. Biomech.* 118, 110270. <https://doi.org/10.1016/j.jbiomech.2021.110270>.
- Sass, J.-O., Hembus, J., Fuhrmann, E., Vogel, D., Bauer, E., Link, H.D., Bader, R., 2023. Pre-clinical characterization of a novel flexible surface stem design for total knee replacements. *Proceedings of the Institution of Mechanical Engineers. Part H. Journal of engineering in medicine* 237 (10), 1154–1166. <https://doi.org/10.1177/09544119231197596>.
- Sass, J.-O., Henke, P., Mitrovic, A., Weinmann, M., Klueess, D., Johannsen, J., Sellin, M.-L., Lembke, U., Reimer, D., Lork, C., Jonitz-Heincke, A., Bader, R., 2024a. Multifunctional hybrid material for endoprosthetic implants based on alumina-toughened zirconia ceramics and additively manufactured TiNbTa alloys. *Materials* 17 (8), 1838. <https://doi.org/10.3390/ma17081838>.
- Sass, J.-O., Johnson, K., Darques, J.-B., Buerstenbinder, L., Soodmand, I., Bader, R., Keibach, M., 2024b. Influence of posterior cruciate ligament tension on tibiofemoral and patellofemoral joint contact mechanics in cruciate-retaining total knee replacement: a combined musculoskeletal multibody and finite-element simulation. *Computer Methods in Biomechanics and Biomedical Engineering*, pp. 1–13. <https://doi.org/10.1080/10255842.2024.2329946>.
- Sass, J.-O., Sellin, M.-L., Kauertz, E., Johannsen, J., Weinmann, M., Stenzel, M., Frank, M., Vogel, D., Bader, R., Jonitz-Heincke, A., 2024c. Advanced Ti-Nb-Ta alloys for bone implants with improved functionality. *J. Funct. Biomater.* 15 (2), 46. <https://doi.org/10.3390/jfb15020046>.
- Sauer, A., Maas, A., Ottawa, S., Giurea, A., Grupp, T.M., 2021. Towards a new, pre-clinical, subject-independent test model for kinematic analysis after total knee arthroplasty—Influence of the proximo-distal patella position and patellar tendon stiffness. *Appl. Sci.* 11 (21), 10322. <https://doi.org/10.3390/app112110322>.
- Schileo, E., Dall'ara, E., Taddei, F., Malandrino, A., Schotkamp, T., Baleani, M., Viceconti, M., 2008. An accurate estimation of bone density improves the accuracy of subject-specific finite element models. *J. Biomech.* 41 (11), 2483–2491. <https://doi.org/10.1016/j.jbiomech.2008.05.017>.
- Schulze, C., Weinmann, M., Schweigel, C., Keßler, O., Bader, R., 2018. Mechanical properties of a newly additive manufactured implant material based on Ti-42Nb. *Materials* 11 (1). <https://doi.org/10.3390/ma11010124>.
- Sequeira, S., Fernandes, M.H., Neves, N., Almeida, M.M., 2017. Development and characterization of zirconia-alumina composites for orthopedic implants. *Ceram. Int.* 43 (1), 693–703. <https://doi.org/10.1016/j.ceramint.2016.09.216>.
- Song, C., Liu, L., Deng, Z., Lei, H., Yuan, F., Yang, Y., Li, Y., Yu, J., 2023. Research progress on the design and performance of porous titanium alloy bone implants. *J. Mater. Res. Technol.* 23, 2626–2641. <https://doi.org/10.1016/j.jmrt.2023.01.155>.
- Suansuwan, N., Swain, M.V., 2003. Adhesion of porcelain to titanium and a titanium alloy. *J. Dent.* 31 (7), 509–518. [https://doi.org/10.1016/S0300-5712\(03\)00071-X](https://doi.org/10.1016/S0300-5712(03)00071-X).
- Sun, Q., Yang, L., Yang, W., Ji, H., Li, M., Li, Y., 2022. Microstructure evolution and bonding mechanism of ZrO₂ ceramic and Ti-6Al-4V alloy joints brazed by Bi₂O₃-B₂O₃-ZnO glass paste. *J. Eur. Ceram. Soc.* 42 (13), 5953–5963. <https://doi.org/10.1016/j.jeurceramsoc.2022.06.016>.
- Tischer, T., Geier, A., Lutter, C., Enz, A., Bader, R., Keibach, M., 2023. Patella height influences patellofemoral contact and kinematics following cruciate-retaining total knee replacement. *J. Orthop. Res. : official publication of the Orthopaedic Research Society* 41 (4), 793–802. <https://doi.org/10.1002/jor.25425>.
- Uivaraseanu, B., Vesa, C.M., Tit, D.M., Maghiar, O., Maghiar, T.A., Hozan, C., Nechifor, A.C., Behl, T., Andronice-Cioara, F.L., Patrascu, J.M., Bungau, S., 2022. Highlighting the advantages and benefits of cementless total knee arthroplasty. *Exp. Ther. Med.* 23 (1), 58. <https://doi.org/10.3892/etm.2021.10980> (Review).
- van Jonbergen, H.-P.W., Innocenti, B., Gervasi, G.L., Labey, L., Verdonschot, N., 2012. Differences in the stress distribution in the distal femur between patellofemoral joint replacement and total knee replacement: a finite element study. *J. Orthop. Surg. Res.* 7, 28. <https://doi.org/10.1186/1749-799X-7-28>.
- Vásquez, V.Z.C., Ozcan, M., Kimpara, E.T., 2009. Evaluation of interface characterization and adhesion of glass ceramics to commercially pure titanium and gold alloy after

- thermal- and mechanical-loading. *Dent. Mater.* : official publication of the Academy of Dental Materials 25 (2), 221–231. <https://doi.org/10.1016/j.dental.2008.07.002>.
- Vogel, D., Wehmeyer, M., Kebbach, M., Heyer, H., Bader, R., 2021. Stress and strain distribution in femoral heads for hip resurfacing arthroplasty with different materials: A finite element analysis. *Journal of the mechanical behavior of biomedical materials* 113, 104115. <https://doi.org/10.1016/j.jmbbm.2020.104115>.
- Wolff, J., 2010. The classic: on the theory of fracture healing. 1873. *Clin. Orthop. Relat. Res.* 468 (4), 1052–1055. <https://doi.org/10.1007/s11999-010-1240-9>.
- Yang, S., Zhang, K., Li, F., Jiang, J., Jia, T., Yang, S.-Y., 2015. Biological responses of preosteoblasts to particulate and ion forms of Co-Cr alloy. *J. Biomed. Mater. Res.* 103 (11), 3564–3571. <https://doi.org/10.1002/jbm.a.35501>.
- Yilmaz, M., Holm, C.E., Lind, T., Flivik, G., Odgaard, A., Petersen, M.M., 2021. Bone remodeling and implant migration of uncemented femoral and cemented asymmetrical tibial components in total knee arthroplasty - DXA and RSA evaluation with 2-year follow up. *Knee surgery & related research* 33 (1), 25. <https://doi.org/10.1186/s43019-021-00111-5>.